25

1

NASA CONTRACTOR REPORT

NASA CR-66664

NASA CR-66664

GPO PRICE $ _____

CFSTI PRICE(S) $ _____

Hard copy (HC) 3.00

Microfiche (MF) .65

ff 653 July 65

FINAL REPORT

STUDY OF DIRECT VERSUS ORBITAL ENTRY FOR MARS MISSIONS

Volume VI - Appendix D - Subsystem Studies and Parametric Data

Prepared by

MARTIN MARIETTA CORPORATION
DENVER, COLORADO

for

Langley Research Center

NATIONAL AERONATUICS AND SPACE ADMINISTRATION • WASHINGTON, D.C. • AUGUST 1968

NASA CR-66664

FINAL REPORT

STUDY OF DIRECT VERSUS ORBITAL ENTRY FOR MARS MISSIONS

VOLUME VI: APPENDIX D - SUBSYSTEM STUDIES AND PARAMETRIC DATA

By Raymond S. Wiltshire, William D. Van Arnam, Thomas R. Tracey, Frederick A. Jaeger, Parker S. Stafford, Michael Kardos, Arno C. Serold, Stephen G. Homic, Dean A. Schneebeck, and John W. Cox

Prepared under Contract No. NAS1-7976 by
MARTIN MARIETTA CORPORATION
Denver, Colorado

for

NATIONAL AERONAUTICS AND SPACE ADMINISTRATION

FOREWORD

This Final Report for the "Study of Direct Versus Orbital Entry for Mars Missions" (NASA Contract NAS1-7976) is provided in accordance with Part III A.4 of the contract schedule as amended. The report is in six volumes as follows:

NASA CR-66659 - Volume I - Summary;

NASA CR-66660 - Volume II - Parametric Studies, Final Analyses, and Conceptual Designs;

NASA CR-66661 - Volume III - Appendix A - Launch Vehicle Performance and Flight Mechanics;

NASA CR-66662 - Volume IV - Appendix B - Entry and Terminal Phase Performance Analysis;

NASA CR-66663 - Volume V - Appendix C - Entry Configuration Analysis;

NASA CR-66664 - Volume VI - Appendix D - Subsystem Studies and Parametric Data.

APPENDIX D

CONTENTS

APPENDIX D

APPENDIX D

APPENDIX D

APPENDIX D

APPENDIX D

APPENDIX D

SUBSYSTEM STUDIES AND PARAMETRIC DATA

APPENDIX D

1. PARAMETRIC WEIGHT EQUATIONS AND DERIVATION

This section of Appendix D presents the general weight equations showing the relationship of the various components that were fed into the machine program. The second part of the section covers the derivation of the component or subsystem equations complete with the empirical or theoretical curves used to develop the equations. Detail weight statements of the three point design configurations are included at the end of this section.

General Weight Equations

Basic parameters.-

$$D_{A/S} = \left(\frac{W_E}{32.2 \times 1.64 \times 0.785 B_E} \right)^{\frac{1}{2}}$$

$$= 0.155 \left(\frac{W_E}{B_E} \right)^{\frac{1}{2}}$$

where

W_E = entry weight

B_E = ballistic coefficient

$D_{A/S}$ = diameter aeroshell, ft

Soft lander. - To go from entry weight to capsule system weight:

$$W_S = W_E + W_{DP} + W_{DS} + W_C + W_A + W_{E/L} + W_{G/C-T}$$

where

W_S = capsule system weight

W_{DP} = deorbit propulsion system (including propellant) weight

W_{DS} = deorbit structure weight

W_C = canister weight

W_A = adapter weight

$W_{E/L}$ = adapter electrical weight

$W_{G/C-T}$ = terminal guidance weight.

To go from entry weight to landed equipment weight:

$$W_V = W_E - W_{A/S} - W_{A/D-E} - W_{ACS-E} - W_{S-A/S} - W_{BF}$$

where

W_V = verniered weight

$W_{A/S}$ = weight aeroshell

$W_{A/D-E}$ = weight aerodecelerator, expended

$W_{S-A/S}$ = weight science in A/S

W_{BF} = weight backface shield.

$$W_L = W_V - W_{VP-E}$$

where

W_L = landed weight

W_{VP-E} = weight vernier propellant.

$$W_{LE} = W_L - W_{LS} - W_{AD-F} - W_{VP-F} - W_{ACS-F} - W_{TE} - W_{TH} - W_{PY}$$

where

W_{LE} = weight landed equipment

W_{LS} = weight lander structure

$W_{A/D-F}$ = weight aerodecelerator, fixed

W_{VP-F} = weight vernier propulsion, fixed

W_{ACS-F} = weight ACS, fixed

W_{TE} = weight telecommunication cabling

W_{TH} = weight thermal control

W_{PY} = weight pyrotechnic control.

Thus, W_{LE} includes guidance and control, telecommunication, power, thermal control, and science.

Guidance and control: All guidance and control electronics and reference units are included. This includes the electronics and reference for the attitude control system, but not the propulsive portion, tanks, valves, nozzles, etc., of the ACS. The sequencer is included in guidance and control.

Telecommunication: All telemetry encoders, multiplexers, power supplies, and all rf transmitters, receivers, and antenna systems are included. The wiring from the encoders to the instruments is not included because this is input as a function of the aeroshell diameter, as W_{TE} above.

Power: All power control, wiring, separation disconnects, batteries, solar panels, or RTGs are included in this category.

Thermal control: All thermal control equipment not required for the entry phase of the mission is included in this category.

Science: All science equipment including SDS, supports, deployment mechanisms, and electrical cabling as required for specific instruments or experiments are in this category. An allowance of 13 lb for minimum entry science is included in the aeroshell and is not a part of W_{LE}.

Detail Parametric Weight Equations

Deorbit propulsion system weight, W_{DP}. - Special curves were plotted for various types of propulsion systems as a function of propellant required. The propellant required is an output of the performance machine program. The following input equations were generated as input to this subsystem.

Weight of engine mount (fig. D1)

$$W_{EM} = 0.07(\text{thrust})^{2/3} \quad \text{min. } 2.0 \text{ lb}$$

Fuel or oxidizer tank weight assuming titanium spheres based on general curve (fig. D2) and 30% nonoptimum factor:

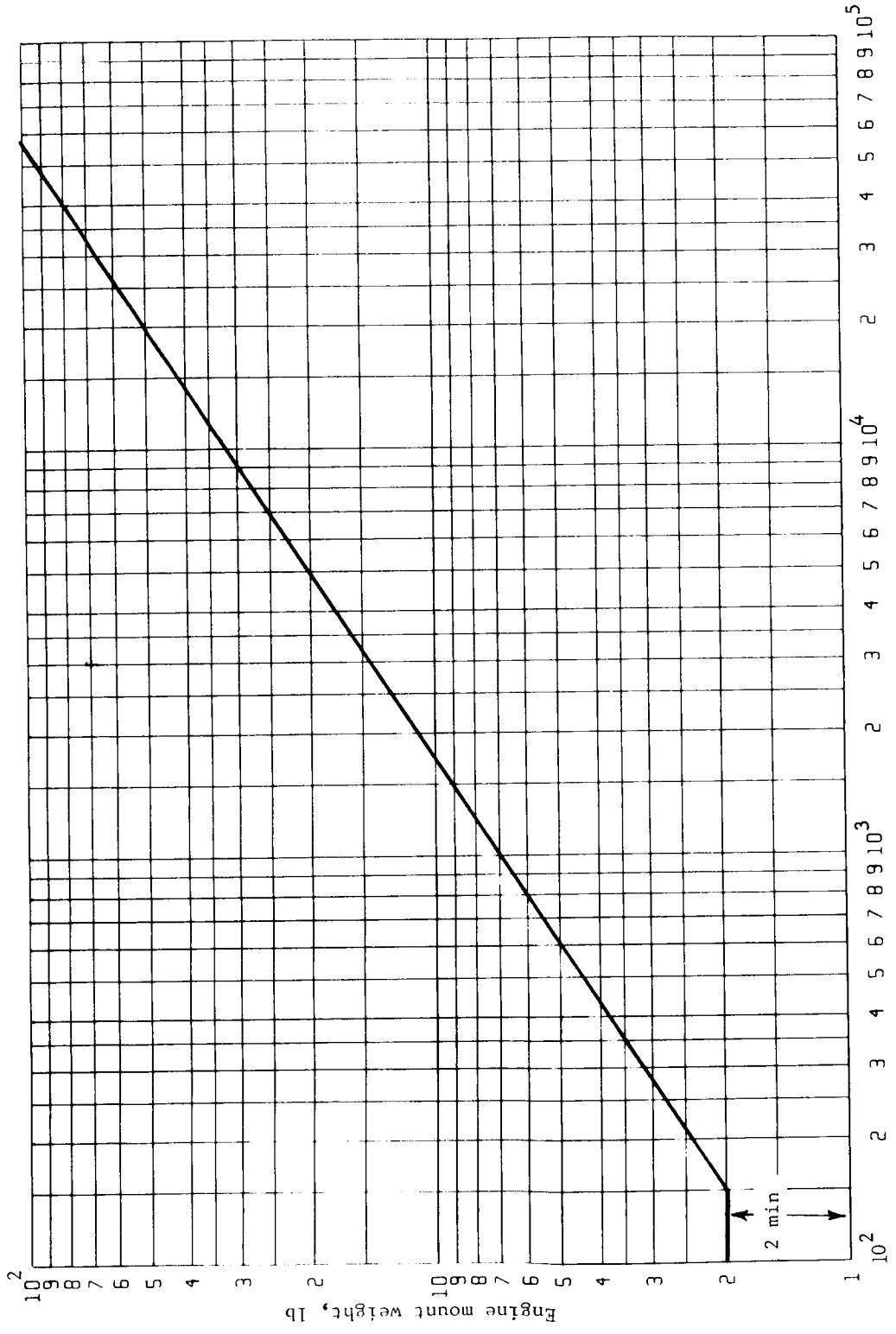

Figure D1.- Engine Mount Versus Engine Thrust

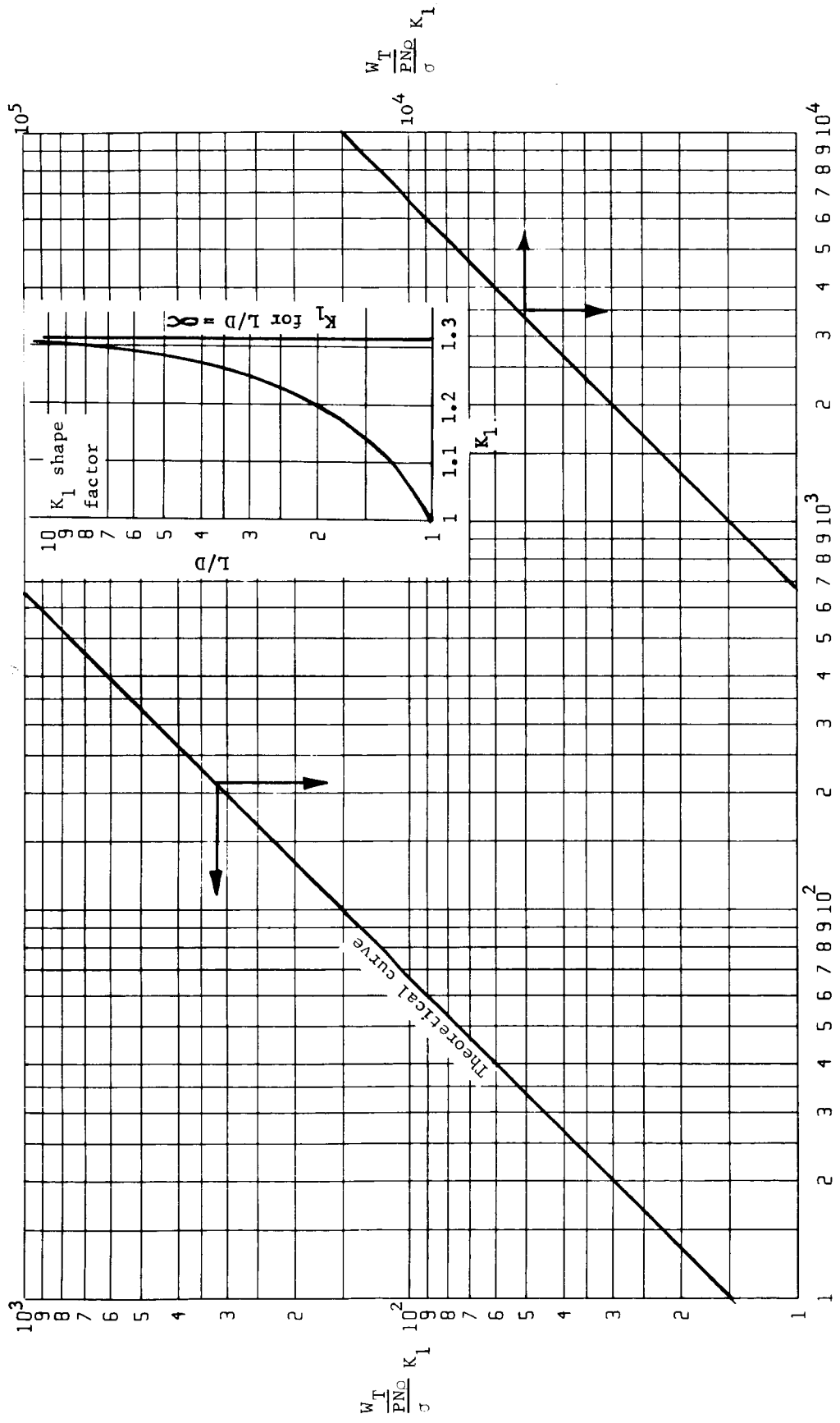

Figure D2.- General Tank Weights

APPENDIX D

$$W_t = 1.0 + 2.0 \frac{PN\ \rho V}{\sigma}$$

for $PNV^{1/3} > 10\ 600$ and

$$W_t = 1.0 + 0.0212\ V^{2/3}$$

for $PNV^{1/3} < 10\ 600$

where

P = operating pressure, psi

N = factor of safety

ρ = density titanium, 0.168

V = volume, cu in.

σ = ultimate tensile Ti = 165 000 minimum gage = 0.020.

Tank support/tank (propellant or gas) from figure D3:

$$W_s = 0.75 \left(W_P + W_t\right)^{0.5}$$

where

W_t = tank weight

W_P = propellant in tank.

Weight high pressure spheres N (based on nonoptimum of 18% fig. D2):

$$W_S = 1.77 \frac{PN\ \rho V}{\sigma}$$

Deorbit structure weight, W_{DS}. - Based on figure D4, based on Phase B structure data and other studies, plus 4 lb for separation bolts:

$$W_{DS} = 4 + 0.16 \left(W_E + W_{DP}\right)^{0.7}$$

Canister weight, W_C. - From figure D5, based on expansion of Phase B data plus cylindrical section for flaps:

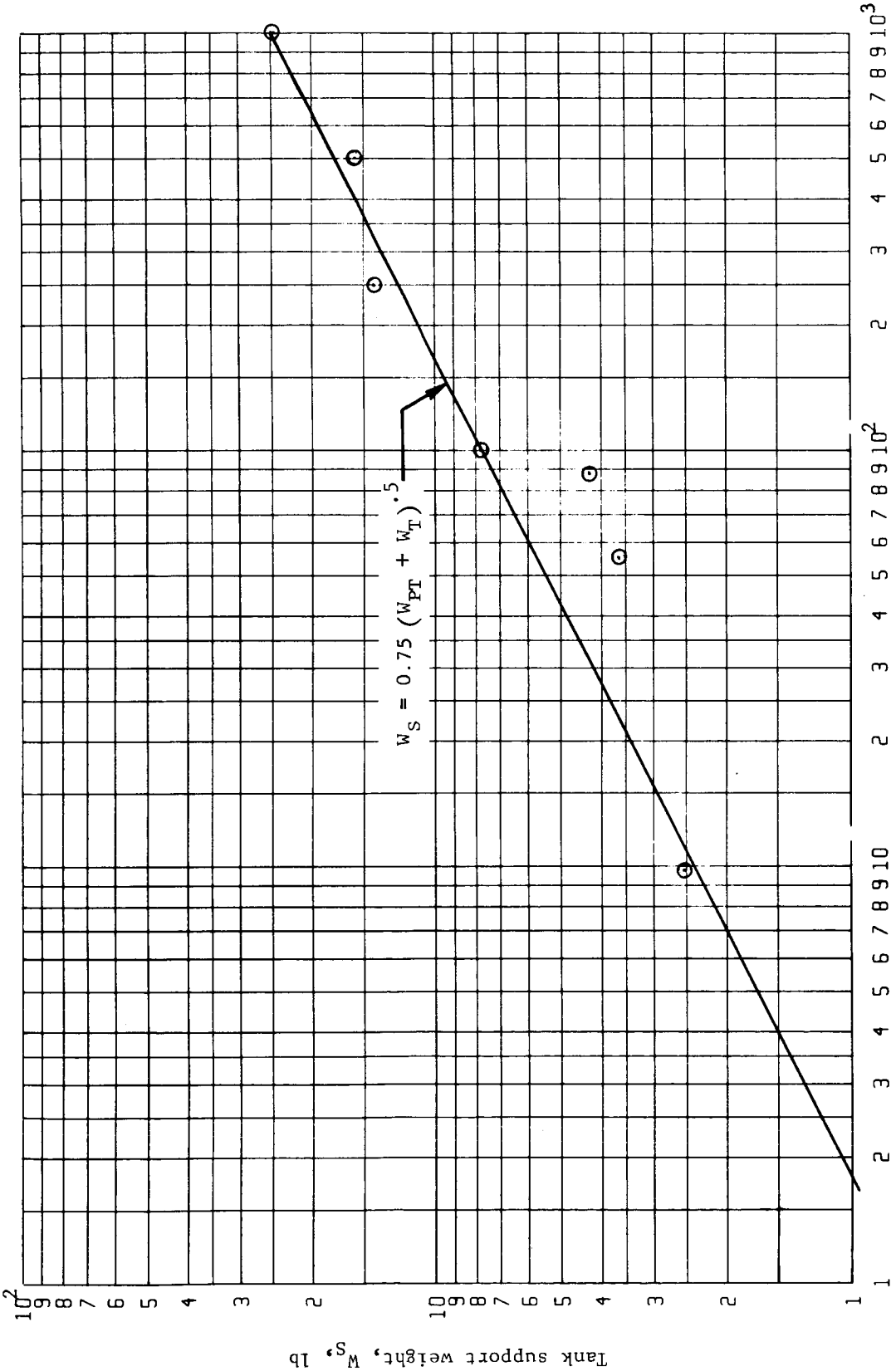

Figure D3.- Tank Support Versus Propellant and Tankage

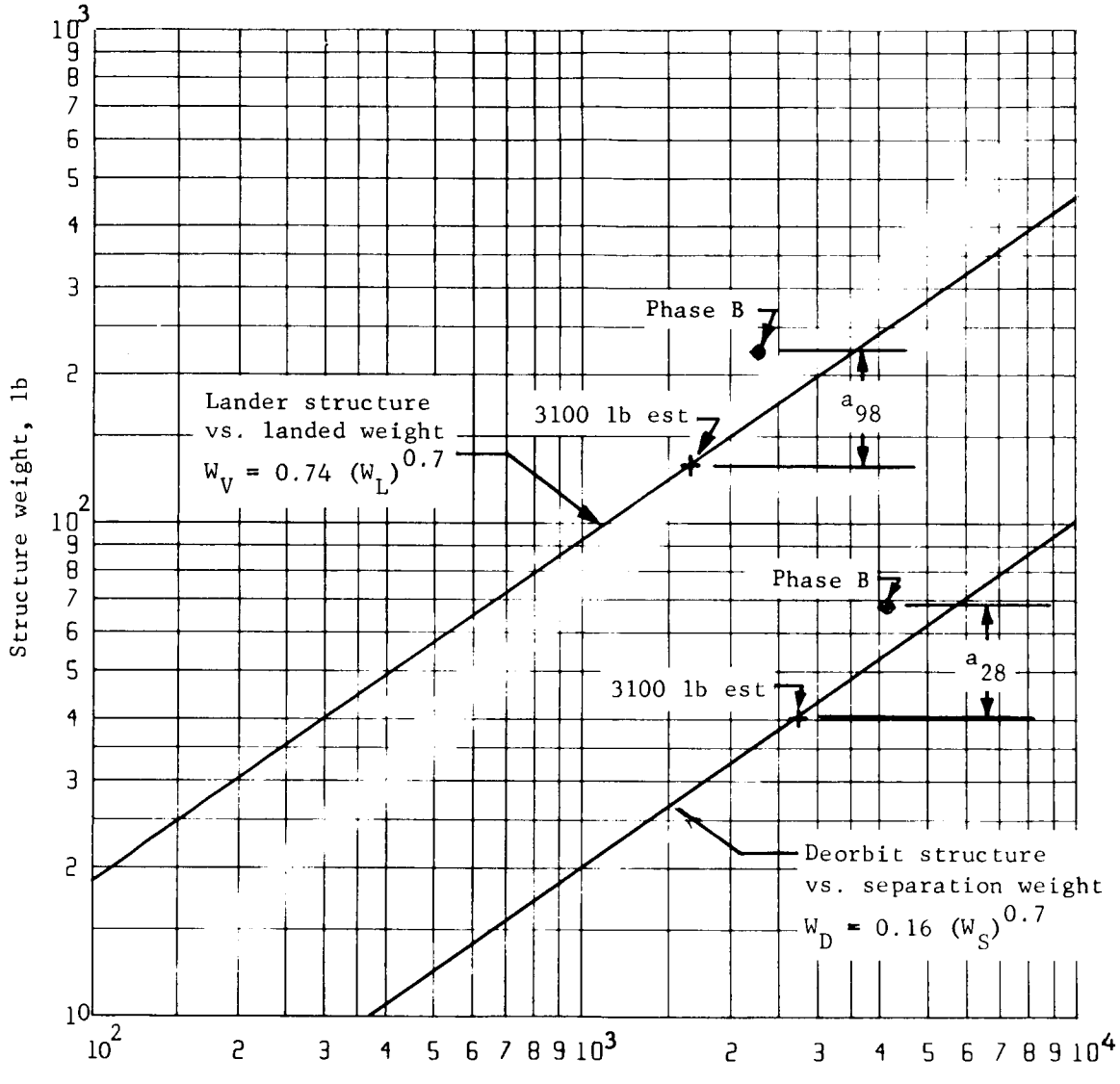

[a]Reduction for smaller size, no garage, no separate surface lab, and three engines.

Figure D4.- Structure Weight Versus Separation Weight or Landed Weight

APPENDIX D

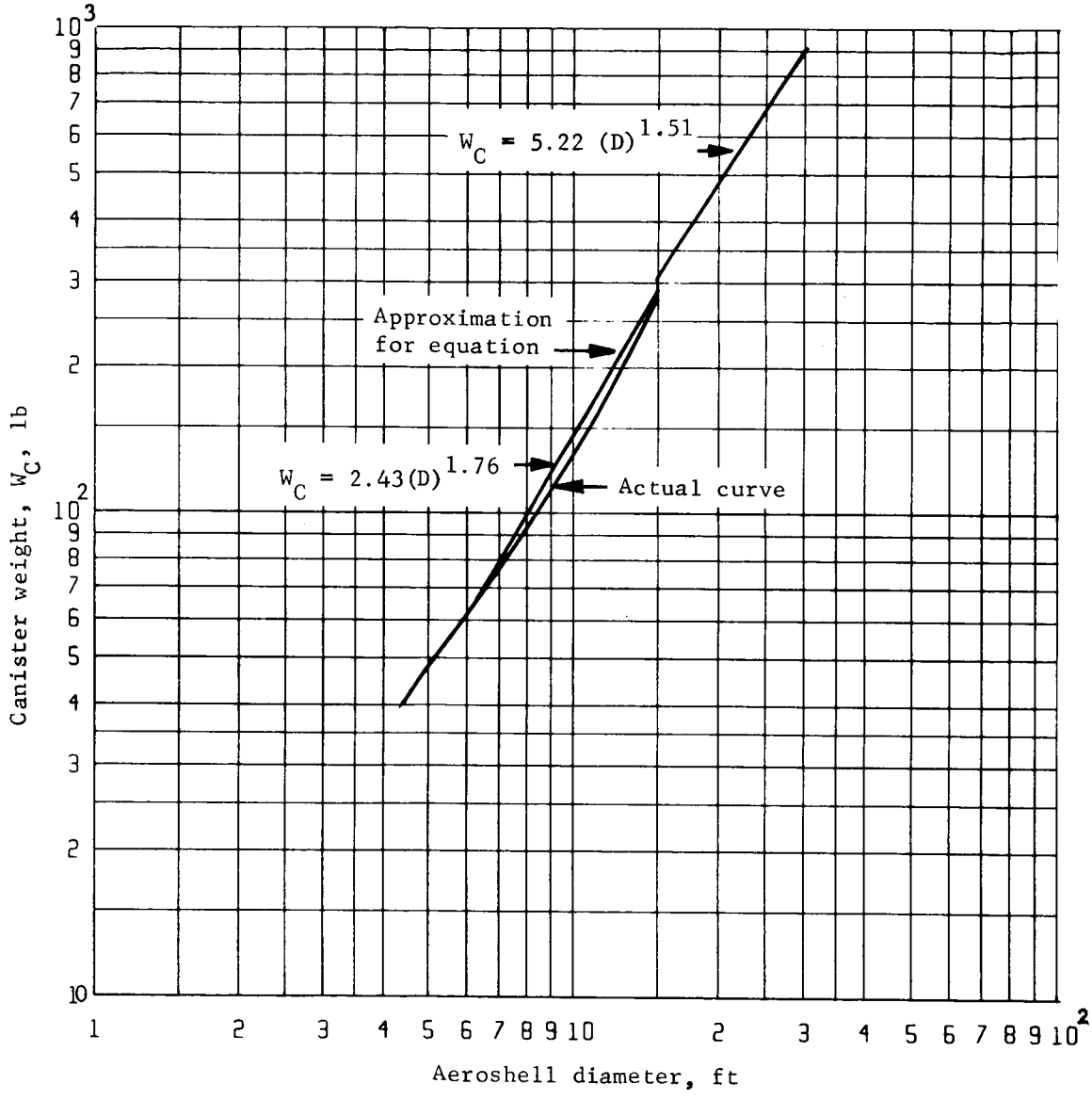

Figure D5.- Canister Weight Versus Aeroshell Diameter

1) Cylinder at 76 lb/ft;

2) One frame at 20 lb for all additions.

Further, for canisters with expanded flaps, the reference diameter had to be used. Figure D6 gives the relationship of effective area to reference diameter. Thus,

$$W_C = 2.34 \left(D_{A/S}\right)^{1.67}$$

for $D_{A/S} \leq 15$ ft, and

$$W_C = 5.22 \left(D_{A/S-F}\right)^{1.51}$$

for $D_{A/S-F} > 15$ ft.

To develop $D_{A/S-F}$ for an eight-flap configuration,

$$D_{A/S-F} = 0.536(A)^{0.645}$$

for $176 < A < 400$, and

$$D_{A/S-F} = 0.147(A)^{0.86}$$

for $A > 400$

where A = effective flap area.

Adapter weight, W_A. - The adapter is assumed of constant diameter to match the spacecraft. The amount of true load-bearing material is negligible. For aeroshells with flaps, an extension is added at the weight of 2 lb/in. Thus,

$$W_A = K = 18$$

for $D_{A/S} \leq 15$ ft

$$W_A = 18 + 12 \left(D_{A/S-F} - 15\right)$$

for $D_{A/S} > 15$ ft.

APPENDIX D

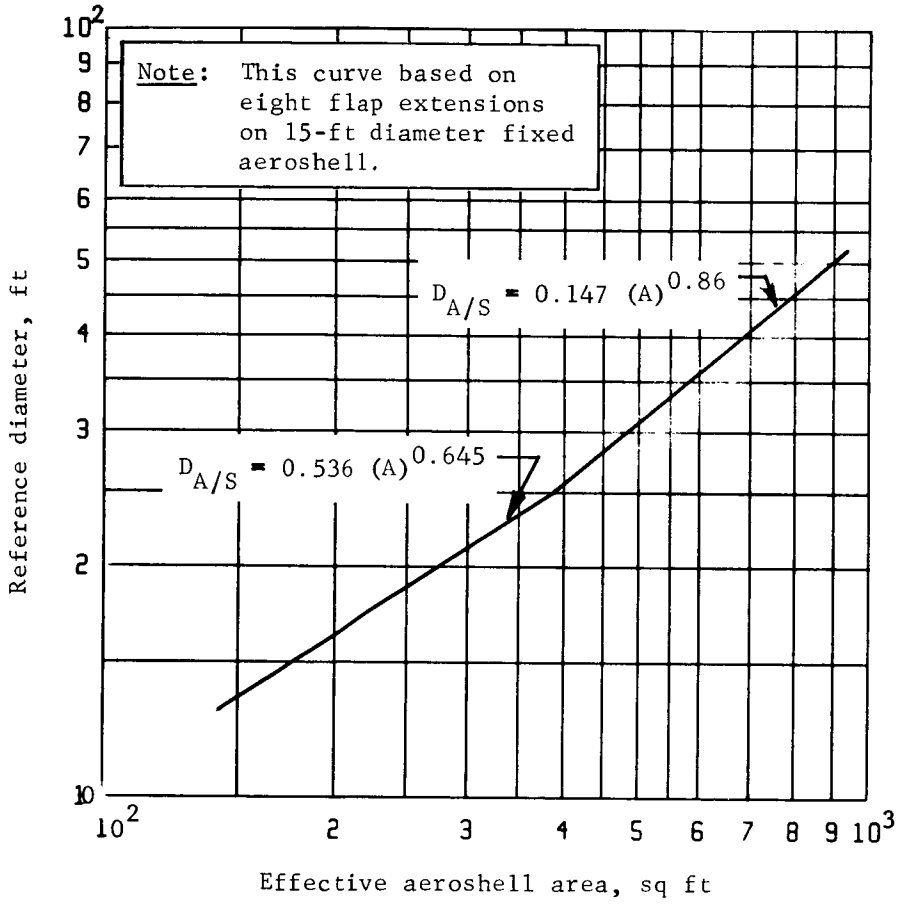

Figure D6.- Reference Diameter Versus Aeroshell Effective Diameter

APPENDIX D

Adapter electrical weight, $W_{E/L}$. - This weight is a constant, depending on the type of system electrical equipment in the adapter.

	Solar or battery	RTG
Status voltage regulator	3.5	3.5
Equipment voltage regulator	4.0	4.0
Power management control	3.0	3.0
Battery charger	2.0	---
Separation disconnect	2.0	2.0
Packaging and mount	4.0	4.0
Cabling	5.5	5.5
	24.0	22.0

Thus,

$$W_{E/L} = K = 24 \text{ for solar or battery}$$

$$= 22 \text{ for RTG}$$

Terminal guidance weight, $W_{G/C-T}$. - This is used only if terminal guidance is mounted on the capsule. The following equation includes supports and cabling as a function of $D_{A/S}$:

$$W_{G/C-T} = 36 + 1.1\ D_{A/S}$$

Aeroshell weight, $W_{A/S}$. - Aeroshell weight for orbital and direct entry is discussed below.

Orbital entry: For this case, the design was limited to fixed aeroshells of maximum diameter of 15 ft. Weight was developed in three parts:

$W_{A/S}$ = Weight of Structure + Weight of Ablator + Weight of Paint + Miscellaneous

The weight of the structure is from a printout, which is shown graphically in figure D7.

APPENDIX D

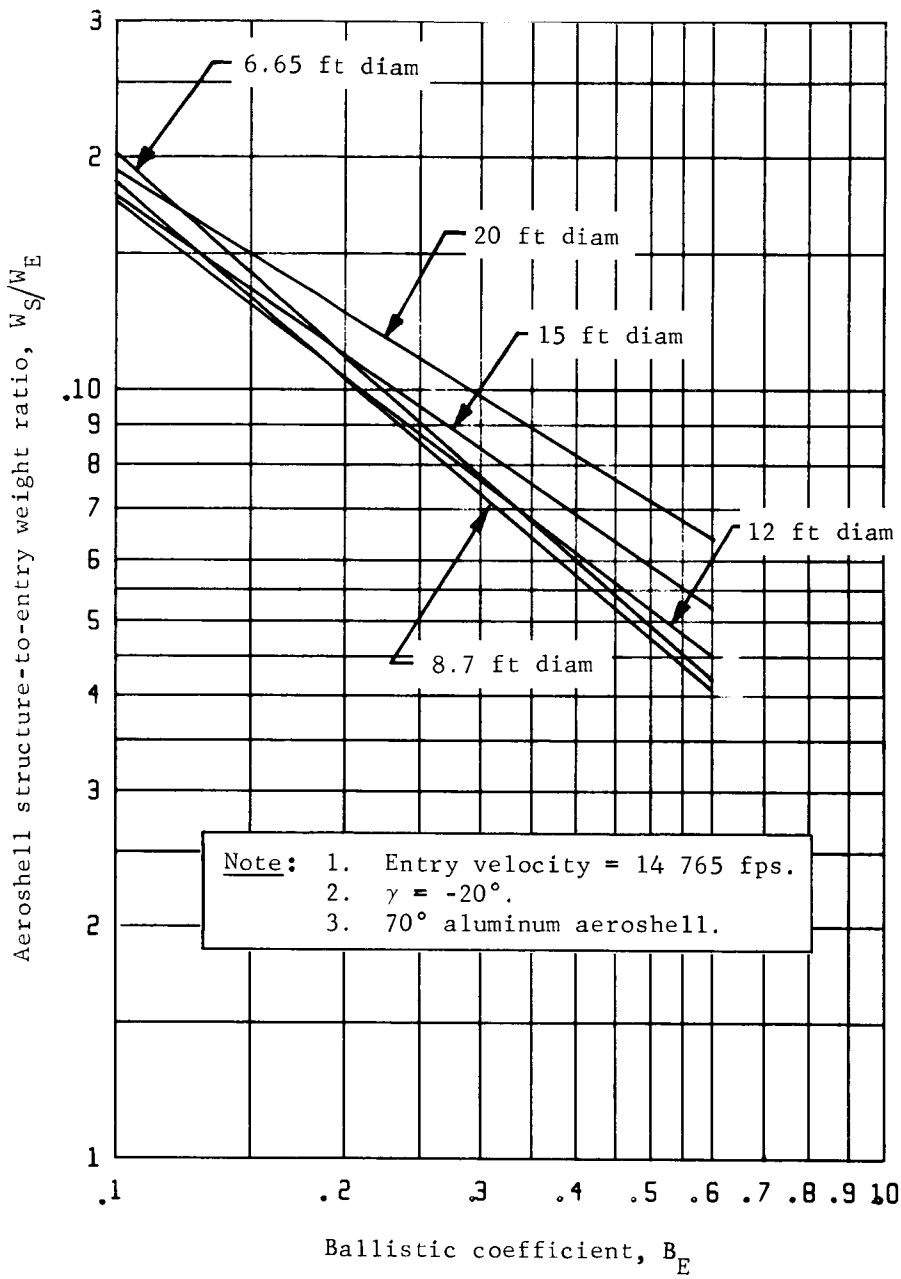

Figure D7.- Orbital Entry Aeroshell Structure Ratio Versus Ballistic Coefficient

APPENDIX D

For the weight of the ablator, the distribution follows the following general form (fig. D8):

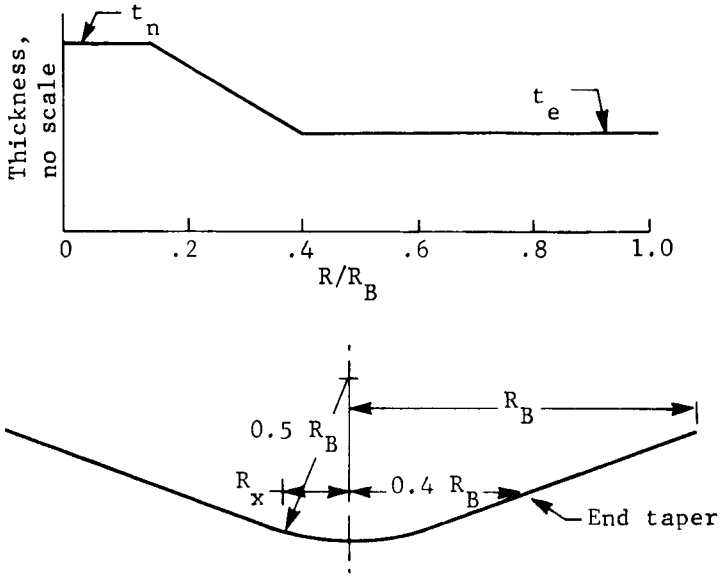

Figure D8.- Distribution of Ablator Weight, Orbital Entry

Figure D8.- Distribution of Ablator Weight, Orbital Entry

$$R_x = 0.5\ R_B \sin 20^\circ = 0.5\ 0.3420\ R_B = 0.171\ R_B$$

$$\text{Area of nose} = \pi\ 0.0603\ R_B^2 = 0.19\ R_B^2$$

$$\text{Volume of nose} = 0.19\ R_B^2\ t_n$$

$$\text{Volume of trans} = \pi\ (R_x + 0.4\ R_B)\ \frac{0.4\ R_B - R_x}{\cos 20^\circ} \times \frac{t_n + t_e}{2.5}$$

$$= \pi \times 0.571\ R_B \times 0.244\ R_B \times \frac{t_n + t_e}{2.5}$$

$$= 0.173\ R_B^2\ (t_n + t_e)$$

$$\text{Volume of edge} = \pi\ (R_B + 0.4\ R_B)\ \frac{R_B - 0.4R_B}{\cos 20} \times t_e$$

$$= \pi \times 1.4\ R_B\ (0.64\ R_B)\ t_e$$

$$= 2.81\ R_B^2\ t_e$$

APPENDIX D

$$\text{Total volume} = 0.19\ R_B^2\ t_n + 0.173\ R_B^2\ (t_n + t_e) + 2.81\ R_B^2\ t_e$$

$$= (0.363\ t_n + 2.983\ t_e)\ R_B^2$$

Ablator material SLS type at 0.0085 lb/cu in.

$$\text{Weight} = 1.05 \times 0.0085\ (0.363\ t_n + 2.983\ t_e)\ R_B$$

$$= 0.009\ (0.363\ t_n + 2.983\ t_e)\ R_B^2$$

Values of t_n and t_e come from figures D9 and D10, R_B is in inches. The value of t_n and t_e are taken for the 3σ lowest gamma (lowest negative value).

Paint and miscellaneous:

$$W = 3 + 0.025\ (D_{A/S})^2$$

Direct entry: Three similar parts make up the aeroshell weights for direct entry.

Structure weight is taken from printouts, which are shown graphically in figures D11 thru D14.

Ablator must be subdivided into two cases, based on the relationship of β and γ as shown below.

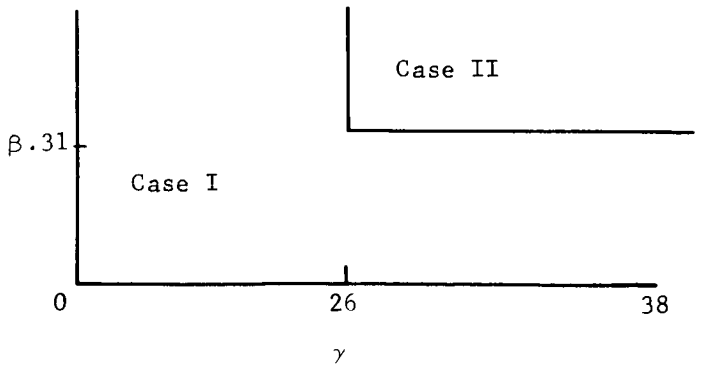

APPENDIX D

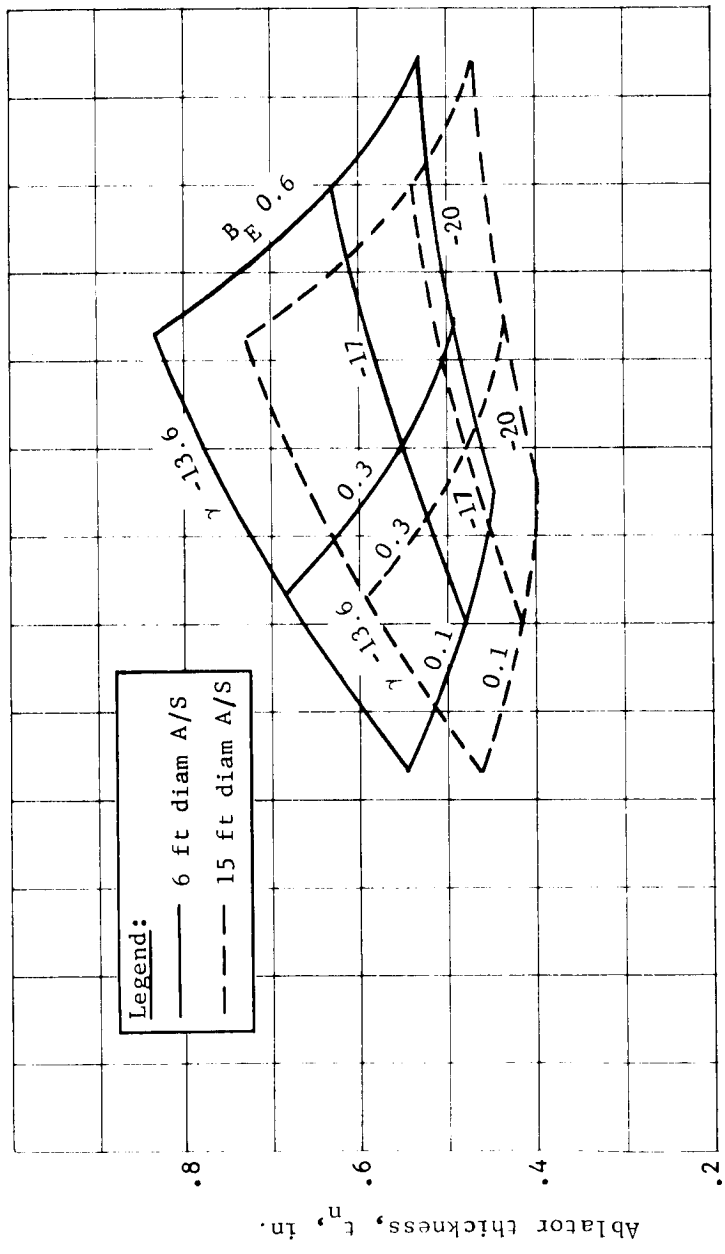

Figure D9.- Orbital Entry Nose Ablator Thickness

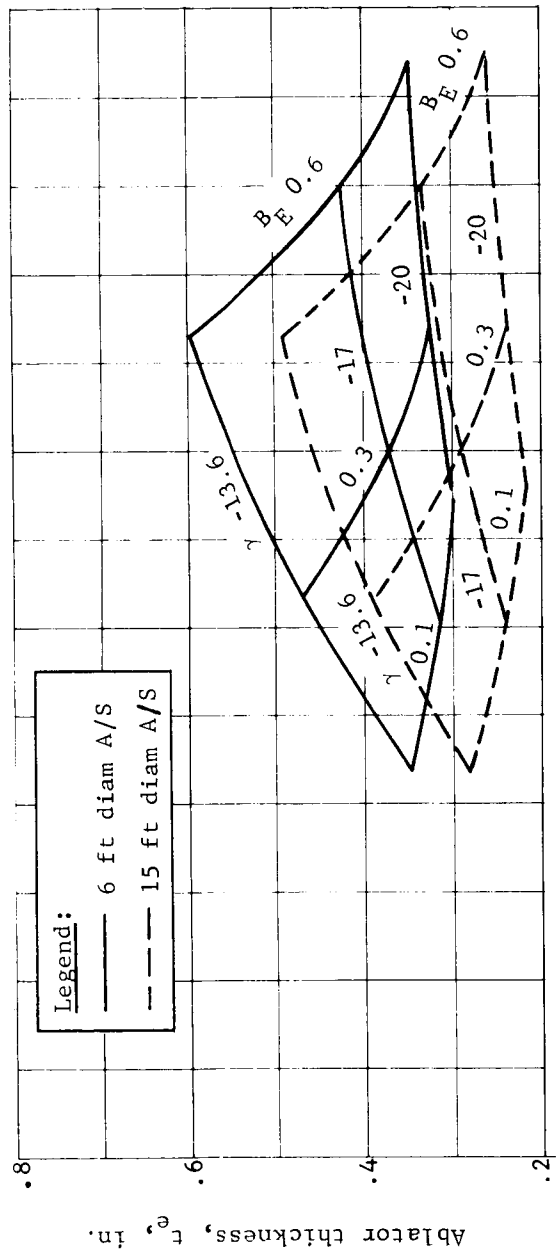

Figure D10.- Orbital Entry Edge Ablator Thickness

APPENDIX D

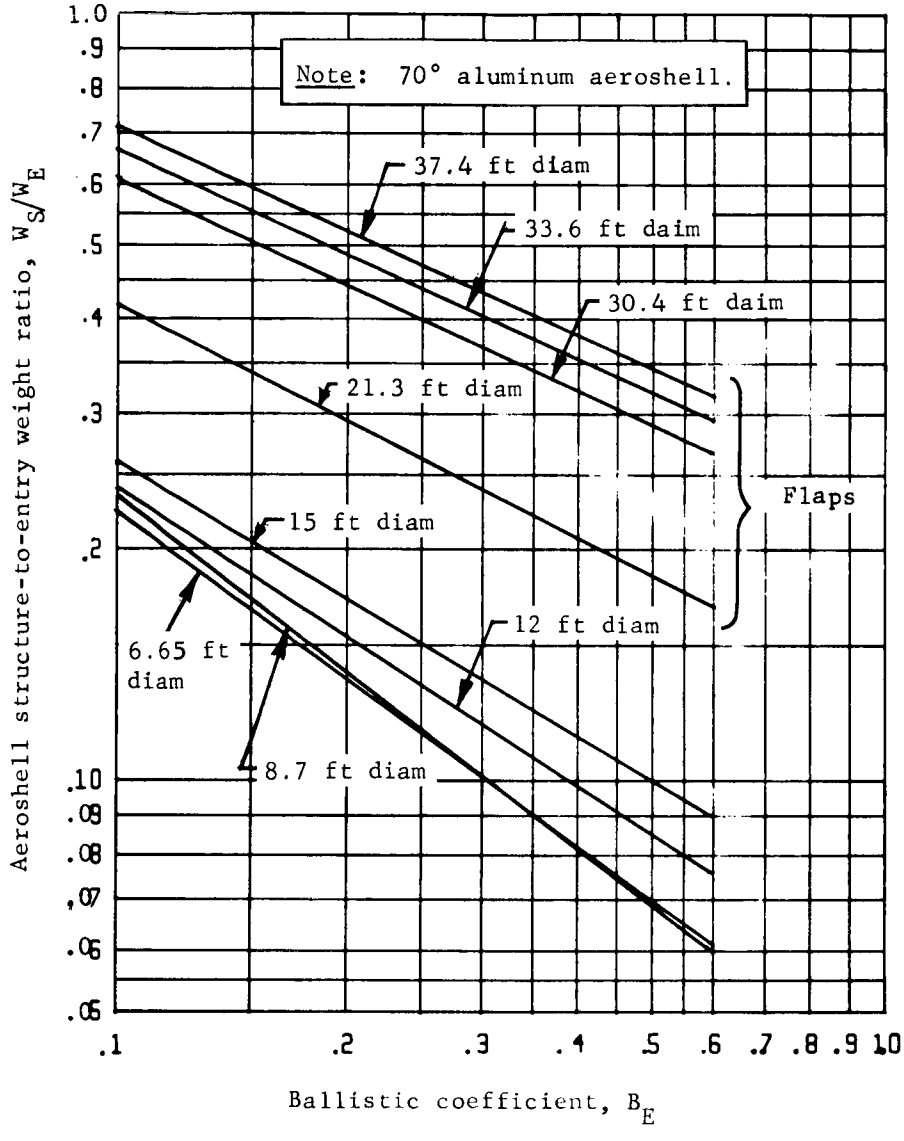

Figure D11.- Direct Entry Aeroshell Structure Ratio Versus Ballistic Coefficient, V_E = 21 000 fps, γ = -30°

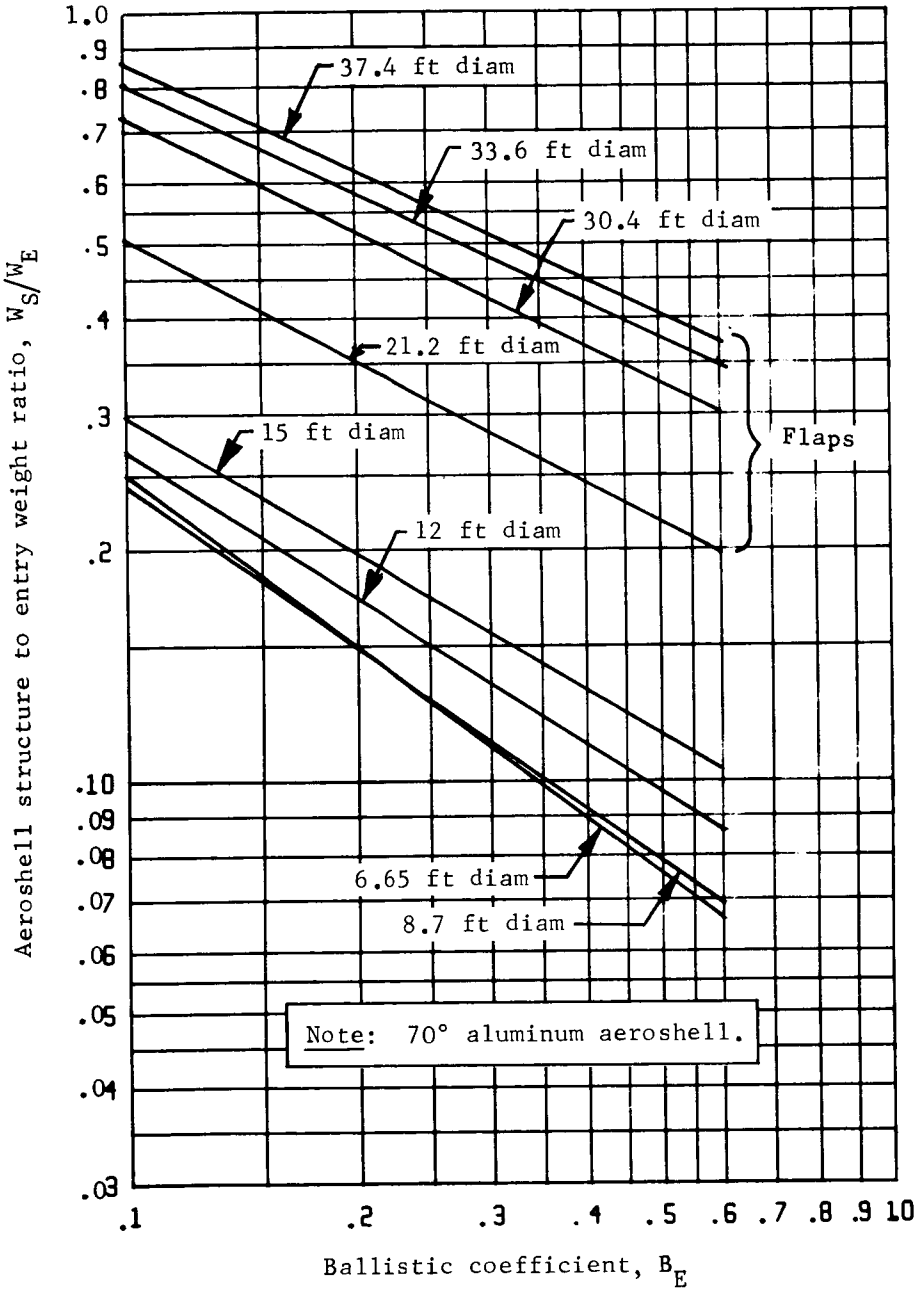

Figure D12.- Direct Entry Aeroshell Structure Ratio Versus Ballistic Coefficient, V_E = 21 000 fps, γ = -38°

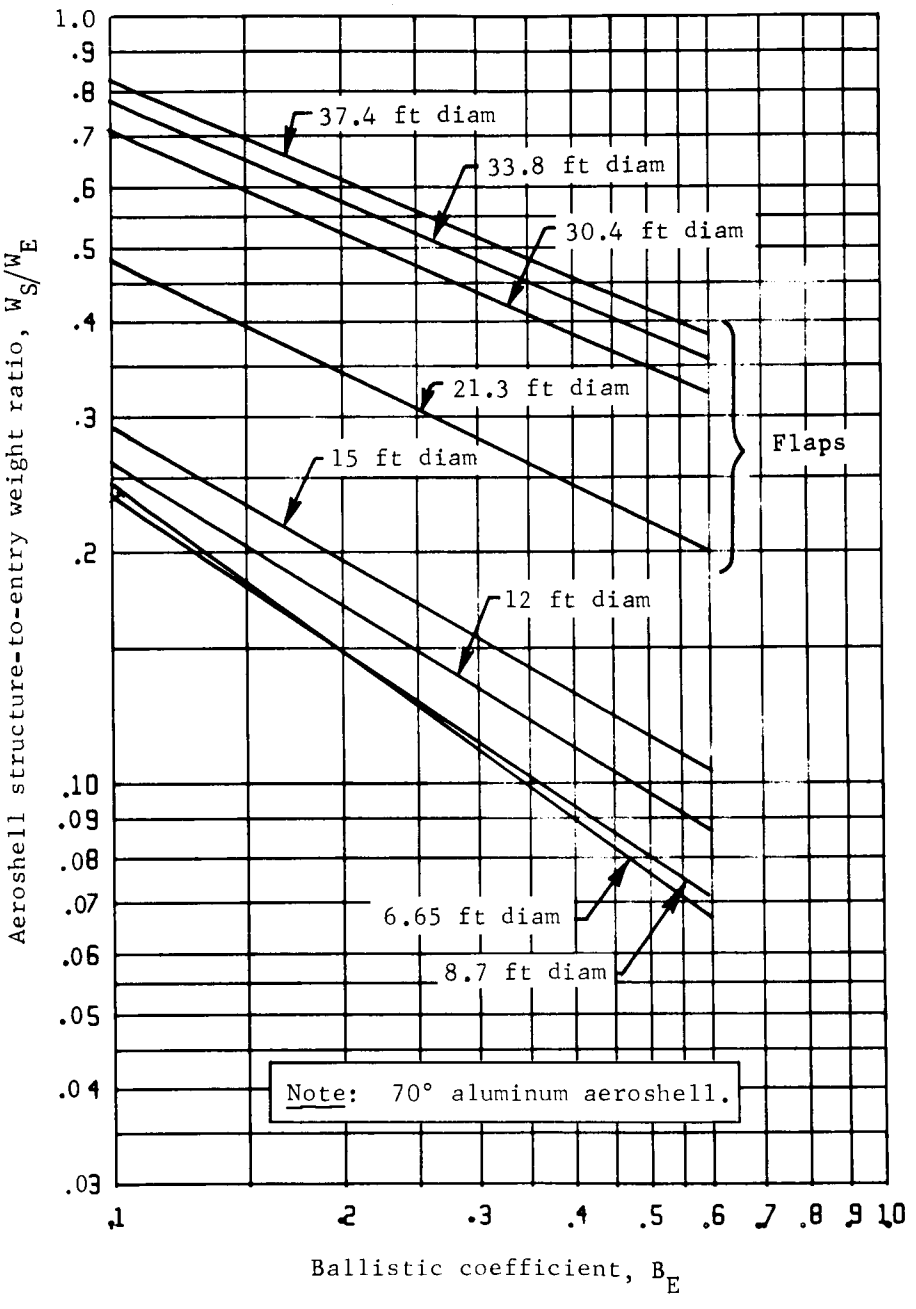

Figure D13.- Direct Entry Aeroshell Structure Ratio Versus Ballistic Coefficient, V_E = 24 000 fps, γ = -30°

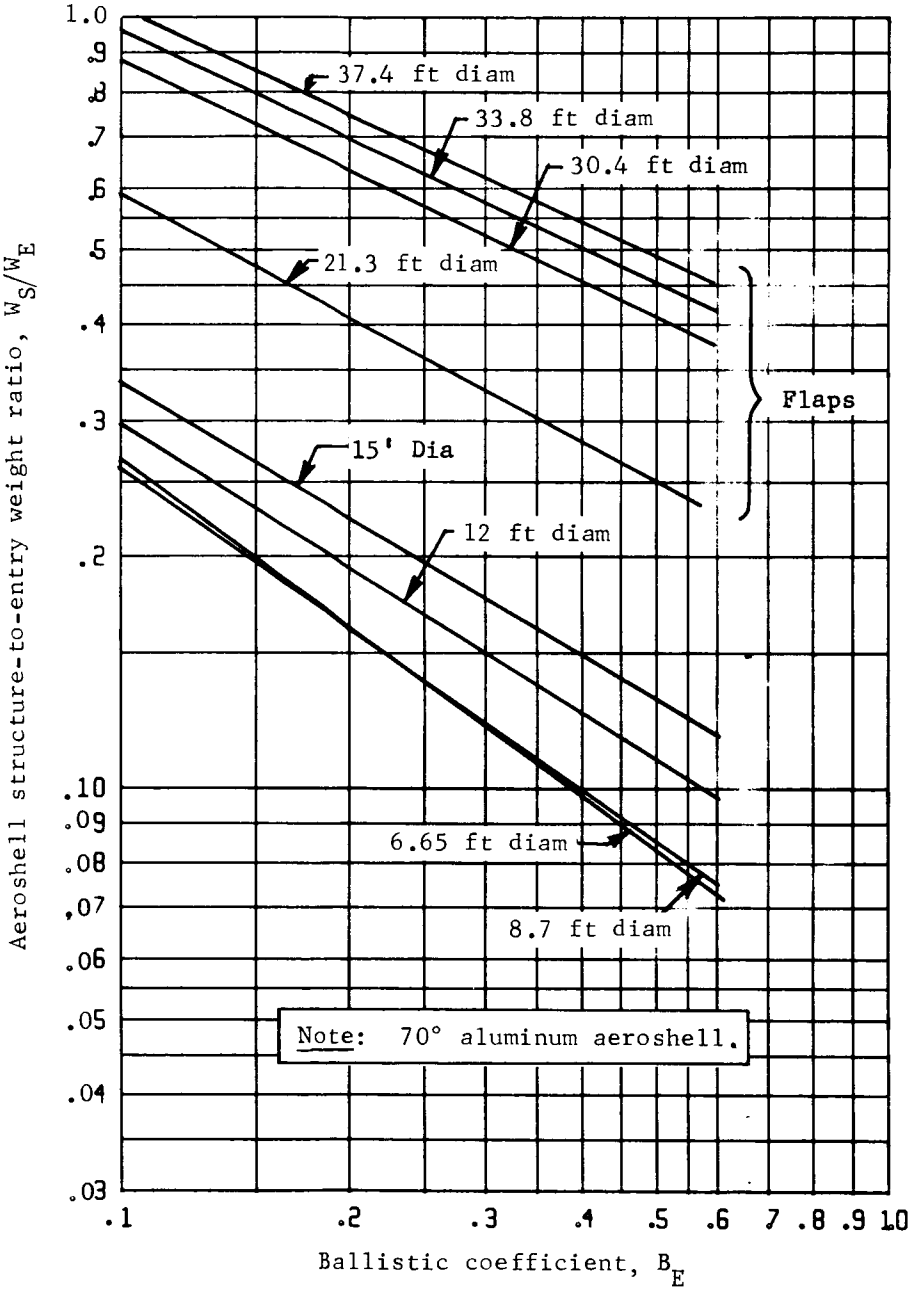

Figure D14.- Direct Entry Aeroshell Structure Ratio Versus Ballistic Coefficient, V_E = 24 000 fps, γ = -38°

APPENDIX D

For Case I, the equation for direct entry applies; for Case II, the distribution is as shown below.

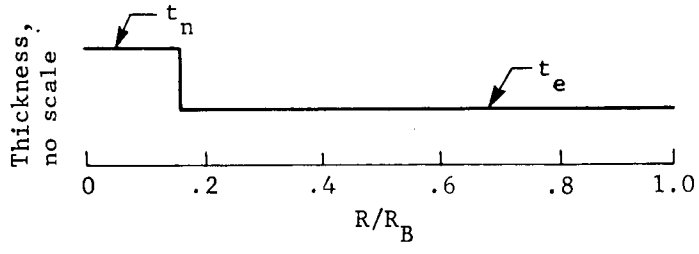

The material for t_n is still SLS at 0.0085 lb/cu in. The material for t_e is ESA at 0.029 lb/cu in.

The ablator equation for Case II is then

$$W_t \text{ Nose} = 1.05 \times 0.19\, R_B^2\, t_n\, \rho_n = 0.017\, t_n\, R_B^2$$

$$W_t \text{ Cone} = 1.05 \left[\pi \left(R_B + R_x\right) \frac{R_B - R_x}{\cos 20}\, t_e\, \rho_e \right]$$

$$= 1.05 \left[\pi\, 1.171\, R_B \times 0.882\, R_B \times t_e\, \rho_e \right]$$

$$= 1.05 \left[0.094\, t_e\, R_B^2 \right] = 0.0985\, t_e\, R_B^2$$

$$\text{Total } W_t = \left(0.017\, t_n + 0.0985\, t_e\right) R_B^2$$

Values for t_n and t_e come from figures D15 and D16.

For expanded aeroshells, the weight of the ablator on the extension must be added to the above. Thus, the general equation is:

$$W_{\text{Total Ablator}} = W_{\text{15 ft A/S Ablator}} + W_{\text{Extension Ablator}}$$

The thicknesses required are based on the data for edge thickness for 15-ft (fig. D16). A check was made for 30-ft true diameter, and the difference between 15 and 30 ft was negligible and did not warrant developing thicknesses for diameters between 15 and 30 ft.

APPENDIX D

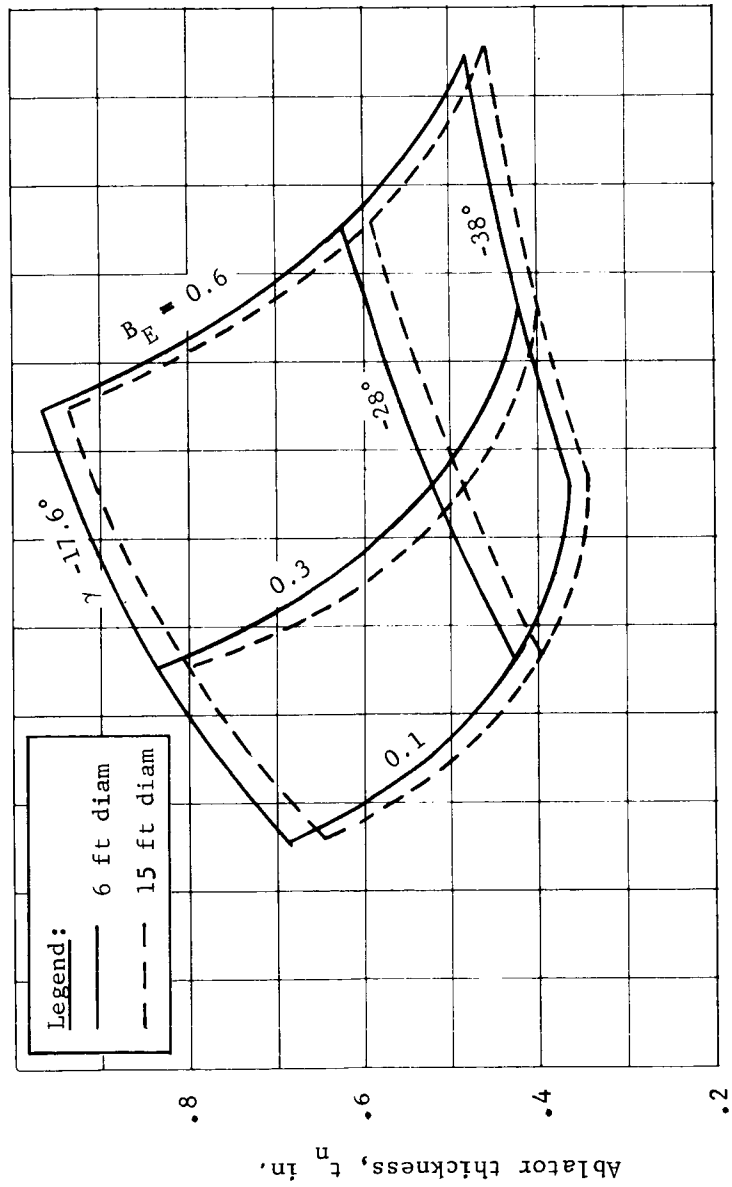

Figure D15.- Direct Entry Nose Ablator Thickness

APPENDIX D

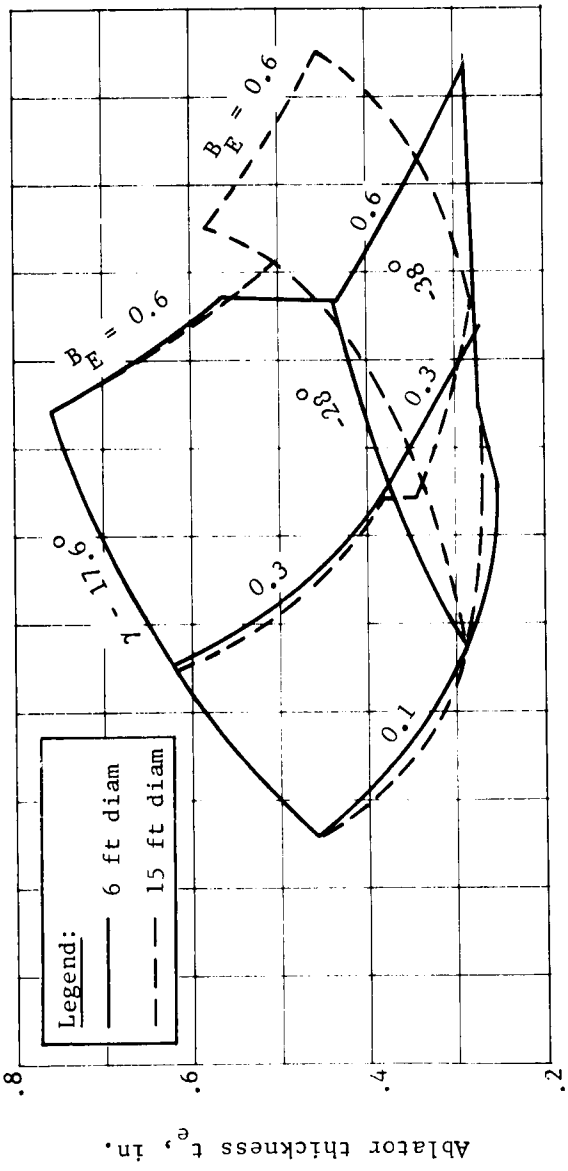

Figure D16.- Direct Entry Edge Ablator Thickness

Thus, the ablator weight for extensions are as follows:

1) Flaps Case I,

$$W_{ABL} = 0.009\ t_{e_{15\ ft}} \times \text{Flap Area, sq in.}$$

2) Flaps Case II,

$$W_{ABL} = 0.0304\ t_{e_{15\ ft}} \times \text{Flap Area, sq in.}$$

For airbag extension, the ESA-type material must be used all over and is less efficient than the SLS. Thus, where the basic material for 15 ft is SLS, the thickness must be increased 25% taking this percentage into account:

1) Airmat extension Case I,

$$W_{ABL} = 0.038\ t_{e_{15\ ft}} \times \text{Airmat Area, sq in.}$$

2) Airmat extension Case II,

$$W_{ABL} = 0.0304\ t_{e_{15\ ft}} \times \text{Airmat Area, sq in.}$$

The paint and miscellaneous equation is the same as for the orbital case.

Aerodecelerator weight, expended, $W_{A/D-E}$, parachutes. - These data come from figure D17, which is for a chute operating below a q of 12 -- a minimum material weight. Thus, the final equations are

$$W_{A/D-E} = 0.0191\ (D_{A/D})^2 \quad \text{for } q \leq 12$$

$$W_{A/D-E} = 0.0191\ (D_{A/D})^2\ \frac{q}{12} \quad \text{for } q > 12$$

Aerodecelerator weight, expended, $W_{A/D-E}$, ballute. - Attached tucked-back with 10% burble fence:

$$W_{A/D-E} = \text{Weight Cloth } (W_C) + \text{Weight Installation } (W_I)$$

$$W_C = 1.76(10^{-5})\ qR^4$$

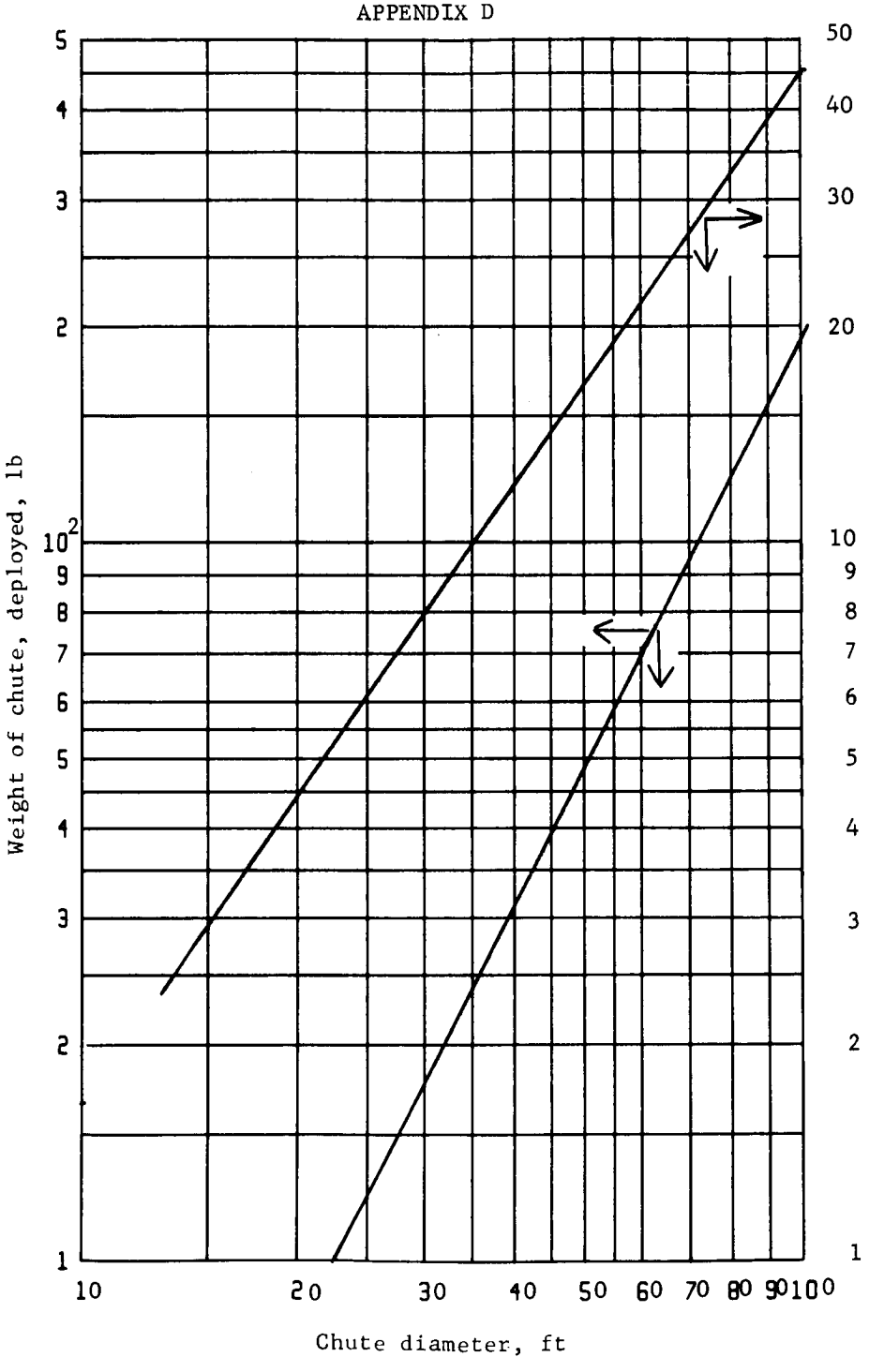

Figure D17.- Parachute Weight Versus Chute Diameter

when

$$R \geq 6.15 + 1/2 \sqrt{151 + 51\ 200/q}$$

otherwise,

$$W_C = 0.225\ R^2 + 2.17\ (10^{-4})\ qR^3$$

$$W_I = 0.00377\ q\ R^2 + 5\ D_{A/S}$$

where R = ballute expanded radius in feet.

These data are based on a JPL study, and for this program, it is assumed that all of W_I will be jettisoned with the ballute.

Backface shield weight, W_{BF}. - For the orbital case, backface heating is assumed to be handled by insulation on individual critical areas. This will be handled in the thermal control equation. Therefore, for orbital entry,

$$W_{BF} = 0$$

For direct entry, an ablator-coated heat shield is considered. This shield will be released when the parachute is released.

The ablator will be supported on 0.020-in. stiffened magnesium sheet (or equivalent weight), and will be 1/8-in. SLS type ablator material. A Teflon rf transparent window that weighs 5 lb will also be required.

Shield Area (15 ft) = 15 diam cir area × 1.03 dev factor

= 182.5 sq ft or 26 300 sq in.

Weight, 15-ft base = ρ × area × 0.020 × 1.5 (non OPS and STR factor)

= 0.068 × 26 300 × 0.020 × 1.5 = 53

Ablator = 1.05 × 26 300 × 0.125 × 0.0085 = 29.4

Total 15-ft Shield = 53 + 29.4 = 82.4

$$\text{Parameter} = \frac{82.4}{225} = 0.36$$

$$W_{BF} = 5 + 0.36\ D_{A/S}^{\ 2} \text{ max.} = 15 \text{ ft}$$

APPENDIX D

Attitude control system weight, expended, W_{ACS-E}. - The weight of the ACS is based on data developed during Phase B. The total impulse for Phase B was divided into two categories that depended on the vehicle thrust magnitude and on the inertia of the vehicle as follows:

	Impulse, lb-sec	
	f I	f thrust
Separation (reduce tipoff)	79.5	
Coast (small limit cycle)	56.8	
Maneuver	39.0	
Deorbit roll		121.7
Coast	48.6	
Maneuver	39.7	
Coast	8.4	
Rate damping in atmosphere	278.0	
Vernier roll control	____	240.0
	550.0	36.17

Because the first coast is a small percentage of the total, it was ignored for basic equations. If a long coast is selected for this program, it will be corrected for the Phase II.

From the above:

1) 60% of impulse is a function of I;
2) 40% of impulse is a function of W;
3) Phase B design entry weight was 4720;
4) Phase B $D_{A/S}$ was 19 ft;
5) Phase B ACS propellant weight was 10 lb.

For inertia-dependent impulse, ACS weight will vary as

$$W_{ACS} \approx \frac{I}{L} \approx \frac{W D_{A/S}}{L}$$

where L = length of the thrust nozzle arm. Thus, $L \approx D_{A/S}$. Then:

APPENDIX D

$$W_{ACS} \approx \frac{W\ D_{A/S}^2}{D} \approx W\ D_{A/S}$$

thus

$$W_{ACS\text{-}E} = \frac{0.6 \times 10 \times W_E\ D_{A/S}}{4\ 720 \times 19} + \frac{0.4 \times 10 \times W_E}{4\ 720}$$

$$= 0.00007\ W_E\ D_{A/S} + 0.00085\ W_E$$

Weight of science in the aeroshell, $W_{S\text{-}A/S}$. - Using the entry science list in the proposal, which it is assumed includes the weight of electronics and cabling for these instruments, the following list of minimum science instruments on the aeroshell was selected:

Stagnation pressure	3.0
Base pressure	2.0
Supersonic probe	3.0
Mounting and structure beefup	5.0
	13.0

$$W_{S\text{-}A/S} = K = 13$$

Vernier propellant weight, expended, $W_{VP\text{-}E}$. - The weight of vernier propellant expended is an output of the basic machine program.

Lander structure weight, W_{LS}. - This weight is based on the equation in figure D4 plus the equation for landing gear (fig. D18 as combined in fig. D19). These are based on g-loadings for orbital entry.

Therefore, for orbital entry

$$W_{LS} = 20 + 1.10\ (W_L)^{0.7}$$

For direct entry, the g-loadings average 40 g rather than 20 g. Therefore, that part of the equation that applies to the basic structure should be modified as follows:

$$W = 0.74\ (2\ W_L)^{0.7} = 1.21\ (W_L)^{0.7}$$

APPENDIX D

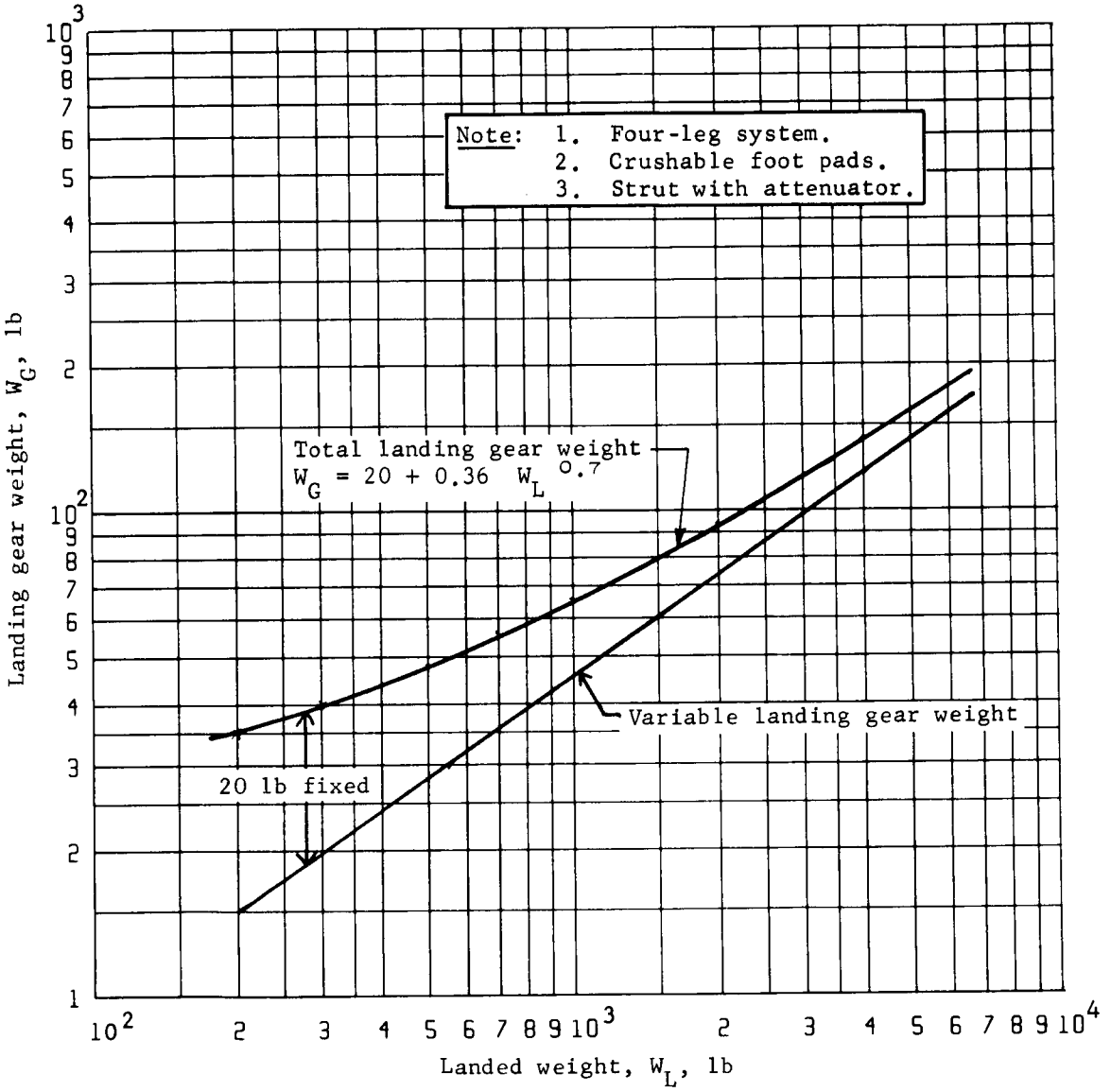

Figure D18.- Landing Gear Weight Versus Landed Weight

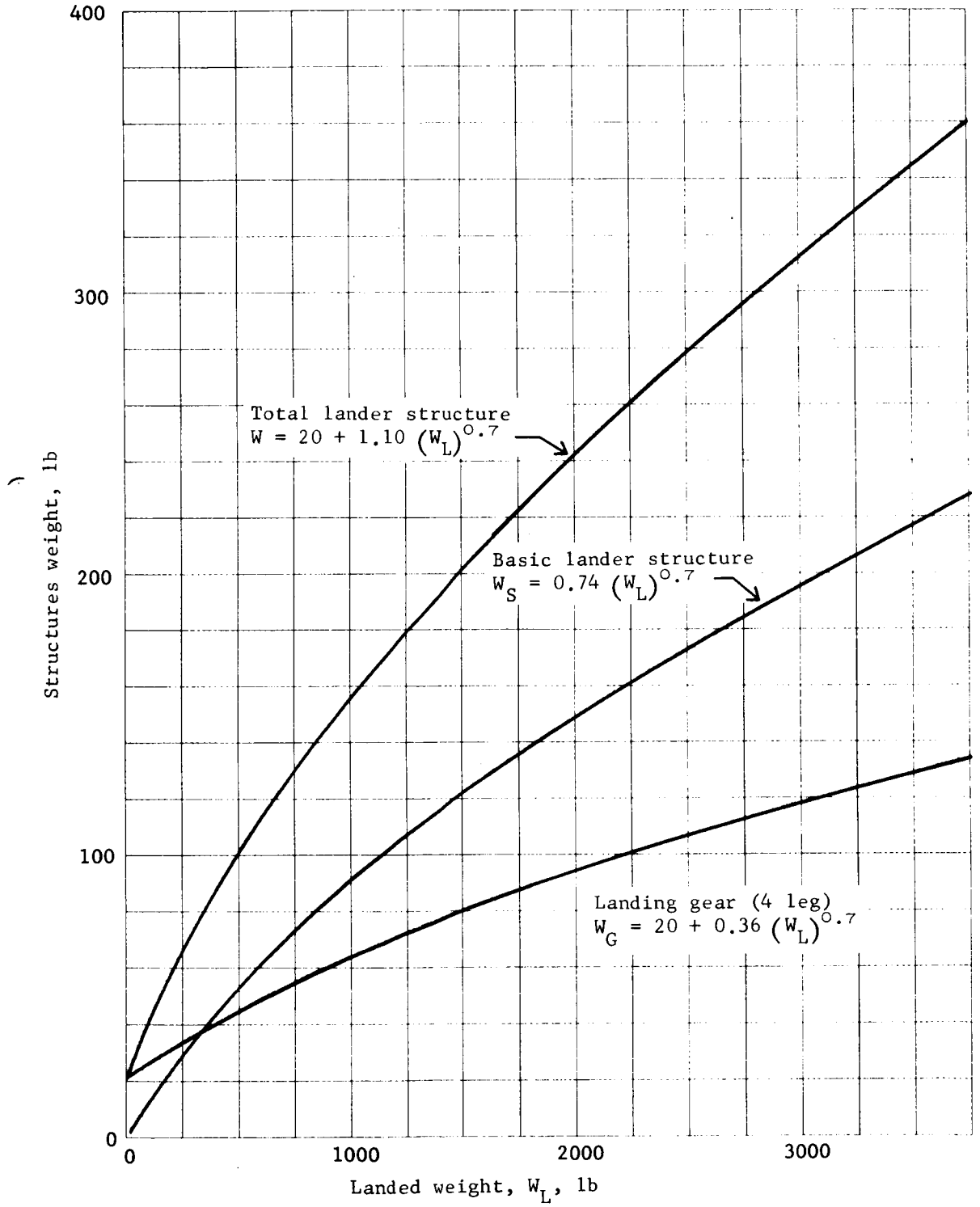

Figure D19.- Total Lander Structure Weight Versus Lander Weight

Therefore, for direct entry,

$$W_{LS} = 20 + 1.57 \left(W_L\right)^{0.7}$$

Aerodecelerator weight, fixed, $W_{A/D-F}$. - For the parachute from figure D17, this weight includes mortar, container, crush material to absorb shock, and tie-down fittings.

$$W_{A/D-F} = 0.055 \left(D_{A/D}\right)^{1.45}$$

For ballutes, the conservative approach is to assume all the ballute mechanism and container is jettisoned.

Vernier propellant weight, fixed, W_{VP-F}. - Total vernier propulsion weight comes from propulsion curves based on propellant weight as developed by machine program.

$$W_{VP-F} = W_{VP} - W_P$$

W_{VP} is total propulsion system.

Attitude control system weight, fixed, W_{ACS-F}. - This weight is based on the same base data as W_{ACS-E} and the following weight information from Phase B:

1)	Fixed weight values, etc.	23.5
2)	Impulse-dependent weight	32.0
		55.5

$$W_{ACS-F} = 23.5 + \frac{0.6 \times 32 \times W_E \, D_{A/S}}{4720 \times 19} + \frac{0.4 \times 32 \, W_E}{4720}$$

$$W_{ACS-F} = 23.5 + 0.00022 \, W_E \, D_{A/S} + 0.0027 \, W_E$$

Telecommunication cabling weight, W_{TE}. - The telemetry cabling is a function of the size of the vehicle, therefore, f $D_{A/S}$. Based on Phase B information, this results in

$$W_{TE} = 2.0 \, D_{A/S} \text{ max.} = 15 \text{ ft}$$

APPENDIX D

The weight of the telecommunication components comes from W_{LE} and is a function of system type.

Thermal control weight, W_{TH}. - For orbital entry, this weight is based on Phase B data, where 13 lb of equipment was fixed components and 36 lb was a function of the vehicle size including the material to protect backface hot spots. Thus, for orbital entry

$$W_{TH} = 13 + 0.1 \left(D_{A/S}\right)^2$$

$$D_{A/S} \text{ max.} = 15 \text{ ft}$$

For direct entry, a backface heat shield will be used; therefore, the equation is modified to

$$W_{TH} = 13 + 0.02 \left(D_{A/S}\right)^2$$

$$D_{A/S} \text{ max.} = 15 \text{ ft}$$

Pyrotechnic control weight, W_{PY}. - From figure D20, assuming

60 bridgewires 12/20 sec (a typical lander quantity)	23 lb
Supports	2 lb
	25 lb
Pyrotechnic wire based on Phase B	
Vernier bus and entry science	37.1

$$\frac{37.1}{19} = 2.0 \text{ lb/ft diam}$$

Therefore:

$$W_{PY} = 25 + 2.0\ D_{A/S}$$

$$D_{A/S} \text{ max.} = 15 \text{ ft}$$

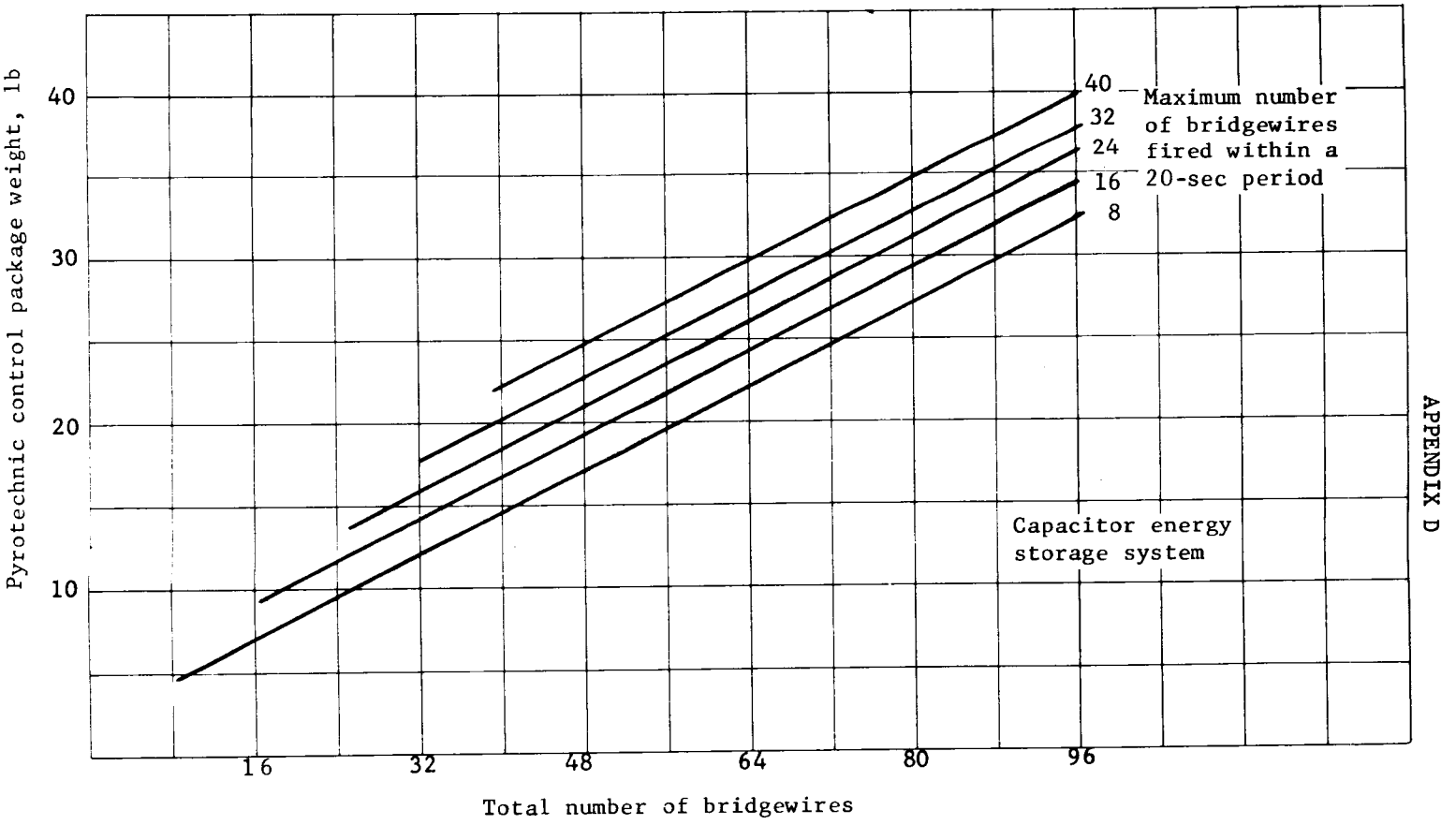

Figure D20.- Pyrotechnic Control Weight Versus Bridgewires

APPENDIX D

Aerodecelerator weight, $W_{A/D}$, revised data. - The data shown for aerodecelerator in the earlier part of this appendix section were used for the machine program. After completion of that effort, the Langley equation for parachute cloth weight became available and was found to give higher weights for parachutes larger than 50 ft diameter. Because Martin Marietta did not have sufficient data to confirm the data in this size range, it was decided to use the Langley equation for the point design work to follow. These data are plotted in figure D21.

A detailed study of five-point design parachutes showed that the noncloth weight associated with the parachute, including mortar, risers, bag, crushable shock attenuator, and attachment fittings, could be plotted as a function of the cloth weight as shown in figure D22.

Also, because the fixed parachute weight became so large for large parachutes, it was decided to jettison this material when the parachute was jettisoned for all of the point design configurations.

Point Designs

Tables D1 thru D3 give detailed weight breakdowns for the three major point designs -- configurations 1A, 1B, and 2A.

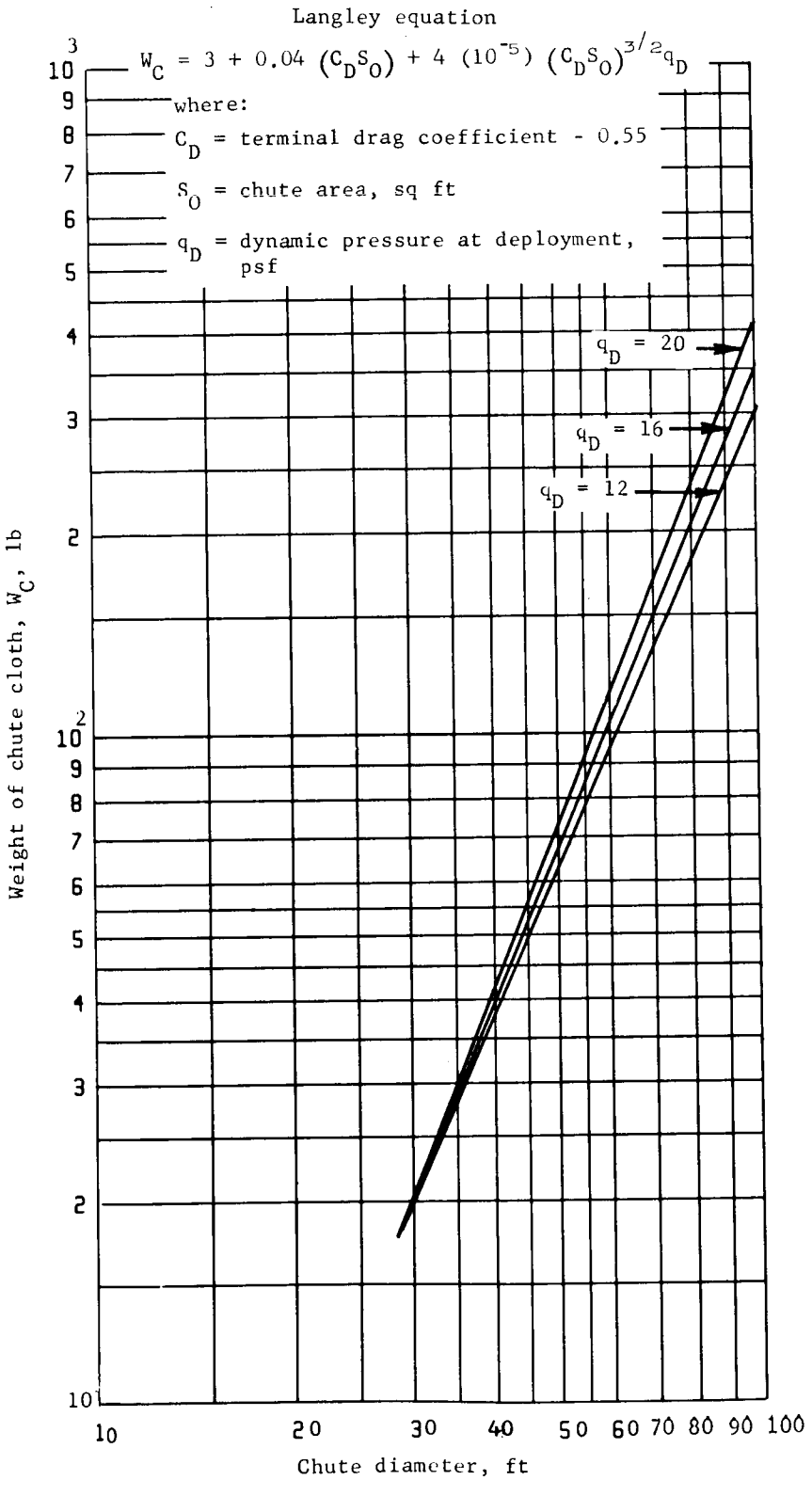

Figure D21.- Parachute Cloth Weight

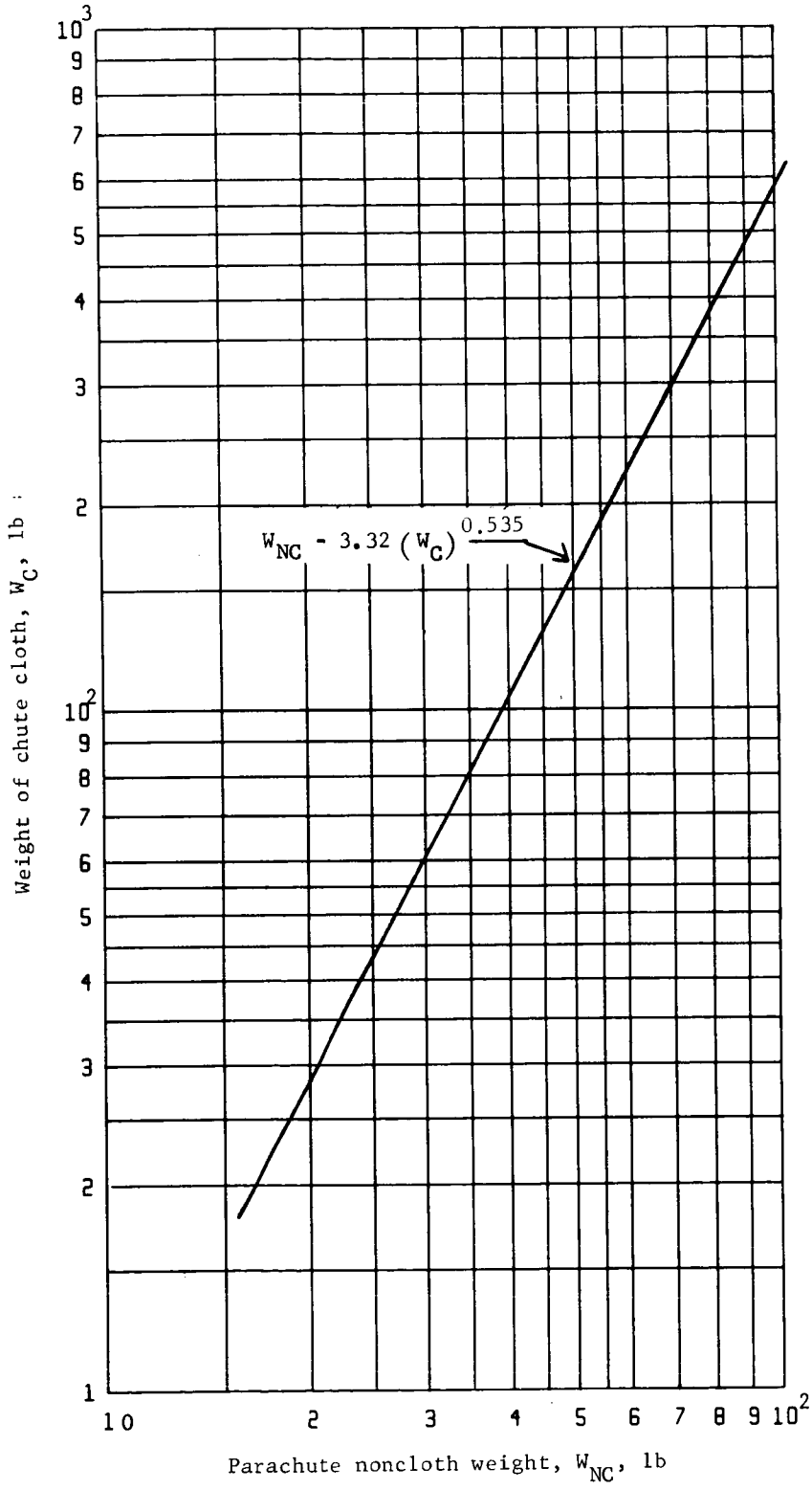

Figure D22.- Parachute Noncloth Weight

APPENDIX D

TABLE D1.- DETAILED SEQUENTIAL WEIGHT STATEMENT, CONFIGURATION 1A

Orbital entry 570 lb landed equipment 8.5-ft diameter aeroshell Monopropellant deorbit and vernier Maximum entry γ = -18°		Deorbit ΔV 120 mps Nominal science Isotope thermal heaters
Total flight capsule		(1723.0)
Canister		165.0
Aft section - body	(102.0)	
Interface frame	14.0	
Structure	53.0	
Longerons	18.0	
Vents	3.0	
Aeroshell separation bolts	5.0	
Insulation	4.0	
Miscellaneous	5.0	
Forward section - lid	(45.0)	
Structure	39.0	
Insulation	3.0	
Miscellaneous	3.0	
Electrical in canister	(18.0)	
Status voltage regulator	3.5	
Power management control	3.0	
Separation disconnect	2.0	
Packaging and mount	4.0	
Cabling	5.5	
Separation weight		(1558.0)
Deorbit structure		30.0
Deorbit propulsion		61.0
Engine (1) 510 lb thrust	15.1	
Engine mounts	4.5	
Fuel tanks	4.8	
Gas tank	3.0	
Tank support	12.2	
Plumbing and valves	13.0	
Residuals		
Fuel	4.1	
Gas	2.2	
Electrical cabling	2.1	
Deorbit propellant		81.5
ACS propellant		2.5

TABLE D1.- DETAILED SEQUENTIAL WEIGHT STATEMENT, CONFIGURATION 1A - Continued

Entry weight (B_E = 0.466)		(1383.0)
Aeroshell		126.5
Skin and stringers, Payload frame, Aft frame, Nose cap	72.0	
Ablator	44.5	
Miscellaneous	5.0	
Separation bolts	5.0	
Science in aeroshell		18.0
ACS propellant		1.5
Decelerator load		(1237.0)
Chute weight (65 ft)		169.0
Verniered weight		(1068.0)
Vernier propellant		108.0
ACS propellant		1.0
Landed weight		(959.0)
Propulsion system		113.7
Engines (3) thrust = 510 lb max./engine	45.3	
Engine mount	13.5	
Fuel tank	5.8	
Gas tank	4.1	
Tank supports	14.2	
Plumbing and valves	18.3	
Residuals		
Fuel	5.5	
Gas	3.0	
Electrical	4.0	
Useful landed weight		(845.3)
Structure		156.0
Truss	92.0	
Landing legs	64.0	

TABLE D1.- DETAILED SEQUENTIAL WEIGHT STATEMENT, CONFIGURATION 1A - Continued

ACS		32.6
Thrusters	6.4	
Fuel tank	.6	
Gas tank and gas	1.4	
Valves and plumbing	13.0	
Electrical Cable	2.5	
Supports	8.7	
Power system		211.0
Batteries		
Silver-zinc 76 A-h	60.0*	
Ni-Cd 17 A-h	62.0*	
Solar Panels 44 sq ft	48.0*	
Power control	33.0*	
Cabling	4.0*	
Supports	4.0*	
Guidance and control		131.0
Inertial measurement unit	22.0*	
Altitude marking radar	12.0*	
Touchdown and landing radar	33.0*	
Digital computer	32.0*	
Phase II computer	3.0*	
Input-output	10.0*	
Cabling	6.0*	
Packaging and supports	13.0*	
Telecommunication		(93.4)
Telemetry	(50.9)	
Encoder	10.0*	
Storage	4.0*	
Sterilization monitor (battery)	4.0*	
Status monitor	6.7*	
Transducer power supply	.7*	
Signal conditioner	1.5*	
Package	6.0*	
Supports	1.0*	
Cabling	17.0	
Relay link	(13.9)	
Telemetry	4.5*	
Beacon receiver	1.9*	
Antenna	4.6*	
Cable	1.0*	
Supports	1.9*	

TABLE D1.- DETAILED SEQUENTIAL WEIGHT STATEMENT, CONFIGURATION 1A - Concluded

Direct link	(28.6)	
MFSK modulator	1.0*	
Modulator exciter	3.0*	
TWTA and power supply	7.8*	
Command receiver	5.0*	
Command detect	4.0*	
Package	3.6*	
Diplexer	1.3*	
Antenna	.6*	
Cabling	1.0*	
Supports	1.3*	
Thermal Control		87.0
Insulation, Heaters radioisotope	47.0*	
Structure skin	20.0*	
Entry thermal	20.0	
Pyrotechnic control		49.5
Control package	30.5	
Cabling	17.0	
Supports	2.0	
Science		84.8
Entry	(18.9)	
Ballistic phase in lander	3.1*	
Terminal descent and landing phase	15.8*	
Landed	(41.7)	
Surface meteorology	12.7*	
Surface imaging	16.5*	
Surface characteristics	12.5*	
Data automation system	(24.2)	
DAS package	12.0*	
Tape recorder	11.0*	
Supports and cabling	1.2*	

*Landed equipment weight, W_{LE} = 570.2.

APPENDIX D

TABLE D2.- DETAILED SEQUENTIAL WEIGHT STATEMENT, CONFIGURATION 1B

Orbital entry 627 lb landed equipment 10.5-ft diameter aeroshell Monopropellant deorbit and vernier Maximum entry γ = -18°		Deorbit ΔV 120 mps Nominal science Isotope thermal heaters
Total flight capsule		(1982.0)
Canister		219.0
Aft section - body	(139.0)	
Interface frame	14.0	
Structure	77.0	
Longerons	22.0	
Vents	5.0	
Insulation	11.0	
Aeroshell separation bolts	5.0	
Miscellaneous	5.0	
Forward section - lid	(62.0)	
Structure	49.0	
Insulation	9.0	
Miscellaneous	4.0	
Electrical in canister	(18.0)	
Status voltage regulator	3.5	
Power management control	3.0	
Separation disconnect	2.0	
Packaging and mount	4.0	
Cabling	5.5	
Margin		22.0
Separation weight		(1741.0)
Deorbit structure		31.0
Deorbit propulsion		65.8
Engine (1) 635-lb thrust	17.9	
Engine mounts	5.2	
Fuel tanks	5.0	
Gas tank	3.2	
Tank support	12.6	
Plumbing and valves	13.0	
Residuals		
Fuel	4.4	
Gas	2.4	
Electrical cabling	2.1	
Margin		10.0

TABLE D2.- DETAILED SEQUENTIAL WEIGHT STATEMENT, CONFIGURATION 1B - Continued

Deorbit propellant		89.0
ACS propellant		4.0
Entry weight (B_E = 0.336)		(1541.2)
Aeroshell		169.0
Skin and stringers, Payload frame, Aft frame, Nose cap	102.0	
Ablator	56.0	
Miscellaneous	6.0	
Separation bolts	5.0	
Science in aeroshell		18.0
ACS propellant		1.5
Margin		18.0
Weight on chute		(1307.7)
Chute weight (48 ft)		90.0
Margin		9.0
Verniered weight		(1208.7)
Vernier propellant		113.0
ACS propellant		1.0
Landed weight		(1094.7)
Propulsion system		124.8
Engines (3) 635 lb thrust/engine	53.7	
Engine mount	15.6	
Fuel tank	5.9	
Gas tank	4.1	
Tank Supports	14.6	
Plumbing and valves	18.3	
Residuals		
Fuel	5.5	
Gas	3.0	
Electrical	4.0	

TABLE D2.- DETAILED SEQUENTIAL WEIGHT STATEMENT, CONFIGURATION 1B - Continued

Useful landed weight		(969.9)
Structure		168.0
Truss	99.0	
Landing legs	69.0	
ACS		33.2
Thrusters	6.4	
Fuel tank	.8	
Gas tank and gas	1.8	
Valves and plumbing	13.0	
Electrical cable	2.5	
Supports	8.7	
Power system		211.0
Batteries		
Silver-zinc 76 A-h	60.0*	
Ni-Cd 17 A-h	62.0*	
Solar panels 44 sq ft	48.0*	
Power control	33.0*	
Cabling	4.0*	
Supports	4.0*	
Guidance and control		131.0
Inertial measurement unit	22.0*	
Altitude marking radar	12.0*	
Touchdown and landing radar	33.0*	
Digital computer	32.0*	
Phase II sequencer	3.0*	
Input-output	10.0*	
Cabling	6.0*	
Packaging and supports	15.0*	
Telecommunication		97.4
Telemetry	(54.9)	
Encoder	10.0*	
Storage	4.0*	
Sterilization monitor (battery)	4.0*	
Status monitor	6.7*	
Transducer power supply	.7*	
Signal conditioner	1.5*	
Package	6.0*	
Supports	1.0*	
Cabling	21.0	

TABLE D2.- DETAILED SEQUENTIAL WEIGHT STATEMENT, CONFIGURATION 1B - Concluded

Relay link	(13.9)	
Telemetry	4.5*	
Beacon receiver	1.9*	
Antenna	4.6*	
Antenna cable	1.0*	
Supports	1.9*	
Direct link	(28.6)	
MFSK modulator	1.0*	
Modulator exciter	3.0*	
TWTA and power supply	7.8*	
Command receiver	5.0*	
Command detect	4.0*	
Package	3.6*	
Diplexer	1.3*	
Antenna	.6*	
Cabling	1.0*	
Supports	1.3*	
Thermal control		91.0
Insulation, Heaters radioisotope	47.0*	
Structure skin	20.0*	
Entry thermal	24.0	
Pyrotechnic control		53.5
Control package	30.5	
Cabling	21.0	
Supports	2.0	
Science		84.8
Entry	(18.9)	
Ballistic phase in lander	3.1*	
Terminal descent and landing phase	15.8*	
Landed	(14.7)	
Surface meteorology	12.7*	
Surface imaging	16.5*	
Surface characteristics	12.5*	
Data automation system	(24.2)	
DAS package	12.0*	
Tape recorder	11.0*	
Supports and cable	1.2*	
Margin on landed equipment		57.0*
Margin on lander		43.0

*Weight of landed equipment, W_{LE} = 627.2.

APPENDIX D

TABLE D3.- DETAILED SEQUENTIAL WEIGHT STATEMENT, CONFIGURATION 2A

Direct entry 570 lb landed equipment	Deflection ΔV 75 mps	
10 3/4-ft diameter aeroshell	Nominal science	
Monopropellant deorbit and vernier	Isotope thermal heaters	
Maximum entry γ = -24°		
Total flight capsule		(2077.0)
Canister		244.0
Aft section - body	(142.0)	
Interface frame	14.0	
Structure shell	80.0	
Longerons	22.0	
Vents	5.0	
Insulation	11.0	
Aeroshell separation bolts	5.0	
Miscellaneous	5.0	
Forward section - lid	(64.0)	
Structure shell	51.0	
Insulation	9.0	
Miscellaneous	4.0	
Electrical in canister	(18.0)	
Status voltage regulator	3.5	
Power management control	3.0	
Separation disconnect	2.0	
Packaging and mount	4.0	
Cabling	5.5	
Separated capsule weight		(1853.0)
Deflection module structure		33.0
Deflection propulsion		57.6
Engine (1) 540-lb thrust	15.7	
Engine mounts	4.8	
Fuel tanks	3.9	
Gas tank	2.5	
Tank support	11.0	
Plumbing and valves	13.0	
Residuals		
Fuel	3.0	
Gas	1.6	
Electrical cabling	2.1	
Deflection propellant		61.0
ACS propellant		1.8

TABLE D3.- DETAILED SEQUENTIAL WEIGHT STATEMENT, CONFIGURATION 2A - Continued

Entry weight (B_E = 0.35)		(1699.6)
Aeroshell		257.0
Skin and stringers, Payload frame, Aft frame, Nose cap	163.0	
Ablator	83.0	
Miscellaneous	6.0	
Separation bolts	5.0	
Science in aeroshell		18.0
ACS propellant		1.5
Decelerator load		(1423.1)
Chute weight (71 ft) q = 20		228.0
Backface		47.0
Verniered weight		(1148.1)
Vernier propellant		116.0
ACS propellant		.8
Landed weight		(1031.3)
Propulsion system		117.6
Engines (3) 540 thrust/engine	47.1	
Engine mount	14.4	
Fuel tank	5.9	
Gas tank	4.2	
Tank supports	14.8	
Plumbing and valves	18.3	
Residuals		
Fuel	5.8	
Gas	3.1	
Electrical	4.0	
Useful landed weight		(913.7)
Structure		222.0
Truss	154.0	
Landing legs	68.0	

TABLE D3.- DETAILED SEQUENTIAL WEIGHT STATEMENT, CONFIGURATION 2A - Continued

ACS		32.0
Thrusters	6.4	
Fuel tank	.6	
Gas tanks and gas	1.2	
Valves and plumbing	13.0	
Electrical cable	2.5	
Supports	8.3	
Power system		211.0
Batteries		
Silver-zinc 76 A-h	60.0*	
Ni-Cd 17 A-h	62.0*	
Solar panels 44 sq ft	48.0*	
Power control	33.0*	
Cabling	4.0*	
Supports	4.0*	
Guidance and control		131.0
Inertial measurement unit	22.0*	
Altitude marking radar	12.0*	
Touchdown and landing radar	33.0*	
Digital computer	32.0*	
Phase II sequencer	3.0*	
Input-output	10.0*	
Cabling	6.0*	
Package and supports	13.0*	
Telecommunication		97.4
Telemetry	(54.9)	
Encoder	10.0*	
Storage	4.0*	
Sterilization monitor/battery	4.0*	
Status monitor	6.7*	
Transducer power supply	.7*	
Signal conditioner	1.5*	
Package	6.0*	
Supports	1.0*	
Cabling	21.0	
Relay link	(13.9)	
Telemetry	4.5*	
Beacon receiver	1.9*	
Antenna	4.6*	
Antenna cable	1.0*	
Supports	1.9*	

TABLE D3.- DETAILED SEQUENTIAL WEIGHT STATEMENT, CONFIGURATION 2A - Concluded

Direct link	(28.6)	
MFSK modulator	1.0*	
Modulator exciter	3.0*	
TWTA and power supply	7.8*	
Command receiver	5.0*	
Command and detect	4.0*	
Package	3.6*	
Diplexer	1.3*	
Antenna	.6*	
Cabling	1.0*	
Supports	1.3*	
Thermal control		82.0
Insulation, Heaters radioisotope	47.0*	
Structure skin	20.0*	
Entry thermal	15.0	
Pyrotechnic control		53.5
Control package	30.5	
Cabling	21.0	
Supports	2.0	
Science		84.8
Entry	(18.9)	
Ballistic phase in lander	3.1*	
Terminal descent and landing phase	15.8*	
Landed	(41.7)	
Surface meteorology	12.7*	
Surface imaging	16.5*	
Surface characteristics	12.5*	
Data automation system	(24.2)	
DAS package	12.0*	
Tape recorder	11.0*	
Supports and cable	1.2*	

*Landed equipment weight, W_{LE} = 570.2.

This page intentionally left blank.

APPENDIX D

2. THERMAL CONTROL PARAMETRIC STUDIES

The objective of the parametric studies is to develop data and procedures that could be used to estimate the thermal control system weight over a wide range of all parameters. Three compatible thermal control systems are required for the flight capsule. These are cruise mode, descent mode, and Mars surface. Primary emphasis was placed on the Mars surface thermal control because a large number of parameters are involved and because many thermal control systems and components could be considered.

The Mars surface parametric data include the following:

1) A definition of all the important parameters that affect the thermal control system weight;

2) An analysis of each of the parameters to establish nominal values and maximum expected ranges of each;

3) A procedure to estimate thermal control system weights based on data generated by a large number of computer runs;

4) Examples of the results of the procedure developed.

The data for the cruise mode and descent modes are based on Martin Marietta Corporation's Voyager Phase B studies and full-scale testing we have performed.

Mars Surface Thermal Control

Thermal control parameters. - All of the parameters that have a significant effect on the thermal control system are listed in table D4 along with a nominal value and expected range of each.

Surface environment: Four surface environments were defined -- cold extreme, intermediate, clear day, and hot extreme. The parameters for each of these environments are listed in table D5.

The cold extreme environment represents the condition resulting in maximum heat loss from the landed equipment compartment. Under conditions of no solar flux, the environmental temperature is assumed to be -190°F, the sublimation temperature of carbon dioxide at 20 mb pressure. In addition, a continuous wind velocity of 74 fps results in a high convection coefficient between the vehicle and the atmosphere. Gas conductivity within vented insulations is assumed equal to that of pure nitrogen.

APPENDIX D

TABLE D4.- THERMAL CONTROL PARAMETERS

Parameter	Range		
Life	2 days to years		
Size (volume of survivable equipment)	10 to 100 ft^3		
Environment (see table D5)	Clear day, cold and hot extreme, intermediate		
	Nominal	Range	
Insulation performance			
Conductivity, Btu/hr-ft-°F	0.0125	0.007	0.025
Density, lb/ft^3	1	0.5	4
Thermal control energy source specific weights			
Batteries, lb/Btu	Function of output (fig. D28)		
Chemical, lb/Btu	Function of output and type (figs D29 & D31)		
Radioisotope, lb-hr/Btu	0.044	0.035	0.088
Solar cell with phase change, lb-day/Btu[a]	0.022	0.01	0.04
Solar cell with battery, lb-day/Btu[a]	0.050	0.03	0.08
Capillary pumped loop for RTG, lb-hr/Btu	0.01 (+ 5 lb)	0.005 (+ 2 lb)	0.02 (+ 6 lb)
Energy storage, phase change material, lb/Btu	0.0125	0.01	0.015
Energy rejection device, temperature-controlled heat pipe, $lb/W_{(Rej)}$	0.17 (+ 5 lb)	0.10 (+ 3 lb)	0.25 (+ 7 lb)
Equipment power dissipation			
Average, W	60	15	130
Daytime peak, W-h	300	25	750
Penetration losses (40 to -190°F), W	15	5	60

[a]Based on a clear day environment. For the intermediate environment, add 0.01 to the nominal and minimum and 0.015 to the maximum. These systems are not applicable in the cold extreme environment.

TABLE D5.- THERMAL ENVIRONMENTS

Environmental parameter	Cold extreme	Intermediate	Clear day	Hot extreme
(1) Solar flux at Mars, Btu/hr-ft^2	----	160	180	232
(2) Solar transmissivity of atmosphere	0	.5	1.0	1.0
(3) Solar absorptivity (α) of Martian surface	----	.80	.80	.95
(4) Emissivity (ϵ) of Martian surface	.85	.92	.92	.85
(5) Martian surface thermal inertia, $\sqrt{k\rho c}$, Btu/ft^2-°F-hr$^{\frac{1}{2}}$	----	.97	.97	.97
(6) Martian surface temperature, °F	-190	Calculated using parameters (1) to (5)		
(7) Wind velocity, fps (continuous at 1 m elevation and 20 mb)	74	100	0	0
(8) Atmospheric pressure, mb	20	10	10	5
(9) Atmospheric temperature, °F	-190	Estimated based on parameter (6)		
(10) Atmospheric composition, %	100 N_2	----	----	100 CO_2

APPENDIX D

An intermediate environment represents conditions at the Mars aphelion solar flux of 160 Btu/hr ft^2. In addition, a cloud cover is assumed to reduce the atmospheric transmissivity to 50%. A surface α/ϵ of 0.80/0.92 and a ground thermal inertia ($\sqrt{k\rho c}$) of 0.97 Btu/ft^2°F $hr^{\frac{1}{2}}$ is assumed. These parameters are used to calculate the transient ground surface temperature at selected latitudes and subsolar points. A wind velocity of 100 fps provides a high convection coefficient between the vehicle and the atmosphere.

The clear day environment represents clear day conditions at the 1973 landing conditions. The solar flux is 180 Btu/hr-ft^2 and the atmosphere is assumed to be 100% transparent. A zero wind velocity is assumed.

The hot extreme environment represents conditions of maximum solar flux, 100% atmospheric transmissivity, zero wind velocity, and a Mars surface α/ϵ = 0.95/0.85. The gas conductivity in vented insulation is assumed to be equal to that of pure carbon dioxide.

Changes in the atmospheric temperature in the vicinity of the planet surface over short time periods are related empirically to the corresponding ground temperatures as follows:

$$T_{a_2} - T_{a_1} = C \left[\left(T_{g_2} + T_{g_1} \right) \Big/ 2 - T_{a_1} \right]$$

where

T_{a_1} = air temperature at beginning of time period

T_{a_2} = air temperature at end of time period

T_{g_1} = ground temperature at beginning of time period

T_{g_2} = ground temperature at end of time period.

C = 0.4 for one-hour time periods

This relation was used to generate the transient air temperature curves shown for three environments in figures D23, D24, and D25. The ground and air temperatures for the cold extreme environment are assumed to be constant at -190°F.

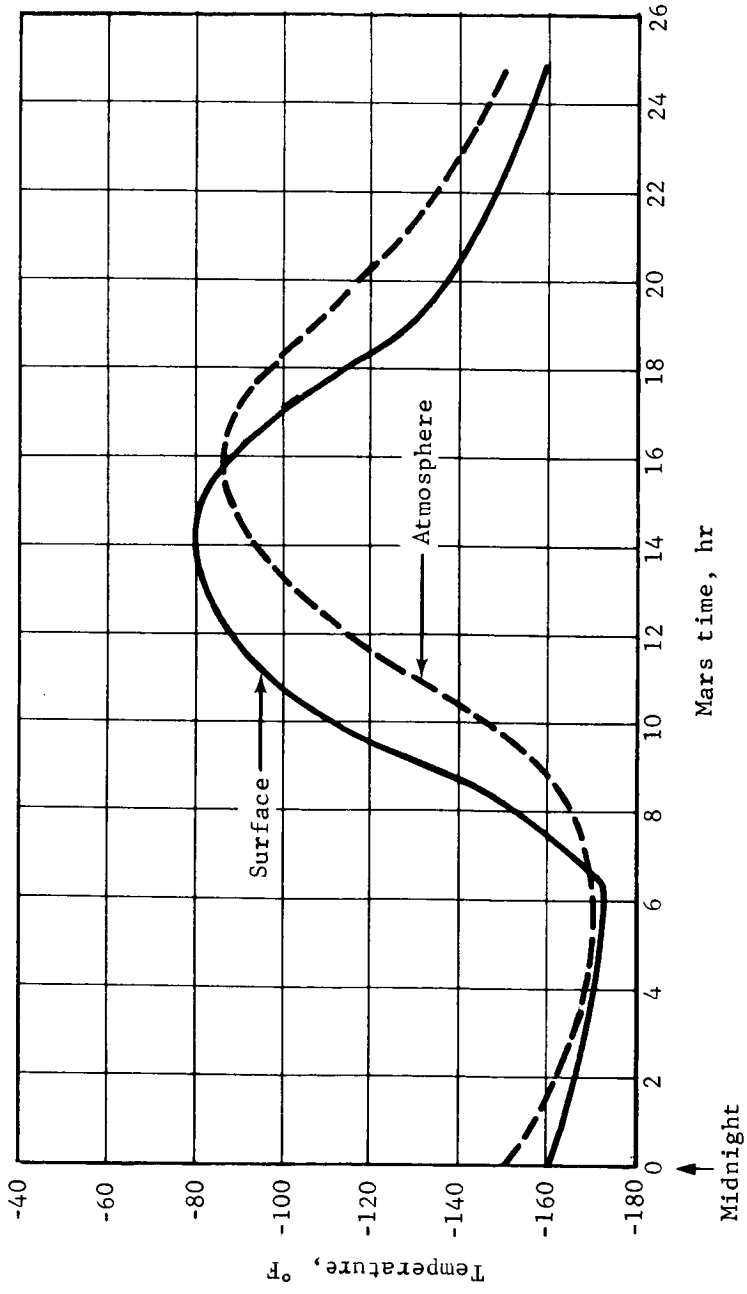

Figure D23.- Mars Surface and Atmospheric Temperatures, Intermediate Environment

APPENDIX D

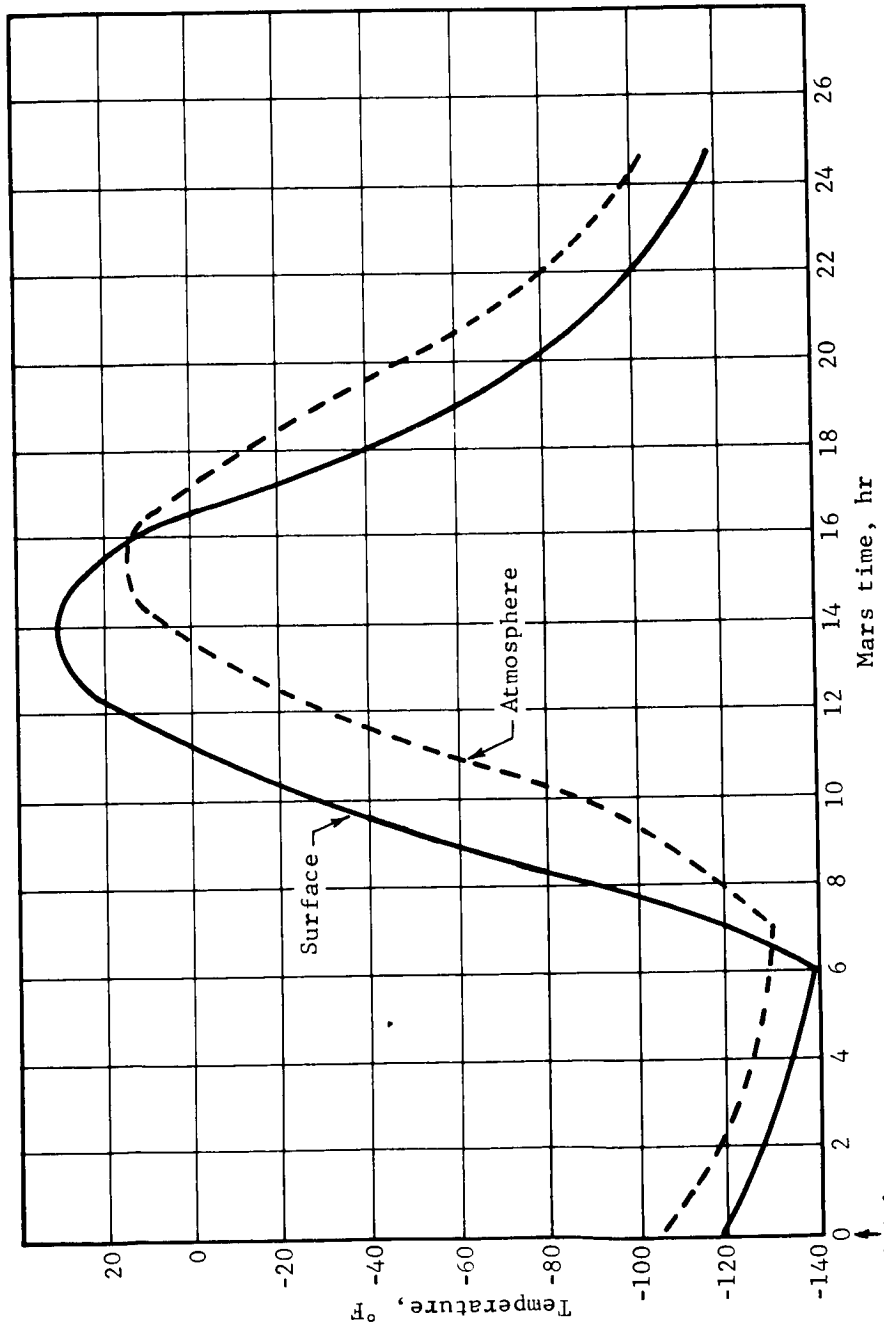

Figure D24.- Mars Surface and Atmospheric Temperatures, Clear Day Environment

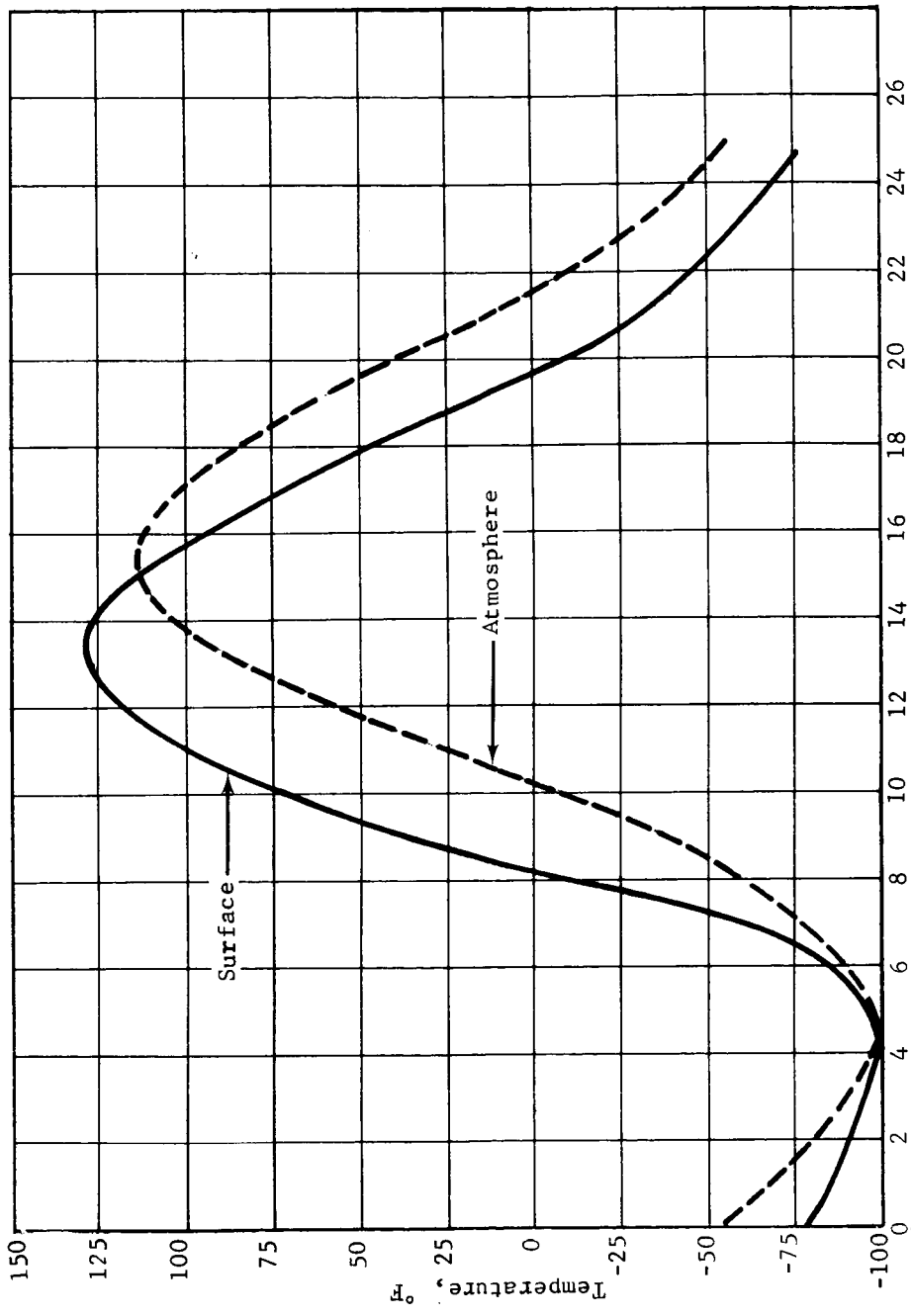

Figure D25.- Mars Surface and Atmospheric Temperatures, Hot Day Environment

APPENDIX D

Insulation performance: A large number of possible insulations might be used. The possible candidates include fibrous types, foams, multilayer, and combinations of these materials. Thermal performance of these materials in the Mars environment is not available at this time. Also, compatibility of these materials with the natural and induced environments of the mission has not been established. A contract to acquire the necessary data for candidate materials is expected to be let by JPL in June 1968.

A particular insulation system design was analyzed to establish conductivity for our point designs. It consists of gold film radiation shields separated by 1-in. layers of low density (0.53 lb/cu ft) AA fiberglas. This insulation is installed between aluminum walls separated by epoxy-fiberglas standoffs at 1-ft intervals.

The following analysis was performed to estimate the performance of the insulation in the Mars environment, including effects of attachments. Test data were used for the fiberglas; the effects of gas conduction, radiation, and solid conduction were separated. We then analytically included the effects of the radiation shields and attachments.

The thermal conductivity of fiberglas insulation was based on the following experimental data (ref. D1) for 0.53 lb/cu ft fiberglas in air at 10 mm Hg pressure between oxidized copper plates at 50°F and 100°F:

Mechanism	Conductivity, Btu in./hr ft^2°F
Radiation	0.045
Solid conduction	0.013
Gas conduction	0.182
	0.240

The effective emittance for the radiation flux between two copper plates at 50°F and 100°F through 1 in. of fiberglas is

$$[0.045/(0.1714)(5.6^2 + 5.1^2)(5.6 + 5.1)]\ 10^2 = 0.043$$

APPENDIX D

The effective emittance ϵg through 1 in. of fiberglas alone is determined from the relation

$$\frac{1}{\frac{2}{\epsilon(\text{Cu-glass})} + \frac{1}{\epsilon g}} = 0.043$$

where

$$\epsilon(\text{Cu-glass}) = \frac{1}{\frac{1}{\epsilon(\text{Cu})} + \frac{1}{\epsilon(\text{glass})} - 1}$$

$$\epsilon(\text{Cu}) = 0.6, \ \epsilon(\text{glass}) = 0.8.$$

Then

$$\epsilon(\text{Cu-glass}) = 0.52 \text{ and } \epsilon g = 0.0515.$$

The effective emittance for radiant flux between two gold shields separated by 0.53 lb/cu ft fiberglas is

$$\overline{\epsilon}(\text{Au}) = \frac{1}{\frac{2}{\epsilon(\text{Au-glass})} + \frac{1}{\epsilon g}}$$

where

$$\epsilon(\text{Au-glass}) = \frac{1}{\frac{1}{\epsilon(\text{Au})} + \frac{1}{\epsilon(\text{glass})} - 1}$$

$$\epsilon(\text{Au}) = 0.05 \text{ and } \epsilon(\text{glass}) = 0.08.$$

Then $\epsilon(\text{Au-glass}) = 0.0465$ and $\overline{\epsilon}(\text{Au}) = 0.0166$. The effective emittance for four 1-in. sandwiches in series is $\epsilon = 0.0166/4 = 0.00415$. The effective emittance for 4 in. of this insulation installed between aluminum walls is

$$\overline{\epsilon}(A\ell) = \frac{1}{\frac{2}{\epsilon(\text{Au-}A\ell)} + \frac{1}{0.00415}}$$

where

$$\epsilon(\text{Au-A}\ell) = \frac{1}{\frac{1}{\epsilon(\text{Au})} + \frac{1}{\epsilon(\text{A}\ell)} - 1}$$

$$\epsilon(\text{Au}) = 0.05,\ \epsilon(\text{A}\ell) = 0.20.$$

Then

$$\epsilon(\text{Au-A}\ell) = 0.0416 \text{ and } \overline{\epsilon}(\text{A}\ell) = 0.0035$$

The contribution of gas conduction through the insulation was determined from the thermal conductivity of the atmosphere at the average insulation temperature. Nitrogen was selected as representative of the maximum gas conductivity and carbon dioxide was selected as representative of the minimum gas conductivity. The thermal conductivity for each of these two gases is shown in figure D26 as a function of temperature.

For solid conduction paths the thermal conduction through the standoff and support structure was based on 2 ft of epoxy-fiberglas, 1/8-in. wide and 4-in. deep for each square foot of surface area. The effective transfer coefficient k/x for this penetration is

$$(0.07)(2)(1/8)/(4) = 0.0044 \text{ Btu/hr ft}^2\text{°R}.$$

The thermal conductivity for the AA fiberglas is 0.013 Btu in./hr ft^2°F. The effective transfer coefficient, k/x, for a 4-in. layer is 0.013/4 = 0.0032 Btu/hr ft^2°R.

The effective transfer coefficient for both the standoff structure and the fiberglas insulation is then 0.0076 Btu/hr ft^2°R.

The overall effective conductivity of the installed insulation was determined at three temperature levels for both nitrogen and carbon dioxide gases. The calculations are summarized in table D6 and the conductivities are plotted as a function of average insulation temperature in figure D27. Since gas conduction is the major mode of heat transfer, there is a significant difference in insulation performance if the Mars atmosphere is CO_2 and if the atmosphere is N_2. Therefore, in analyzing the cold extreme environment the N_2 conductions must be used; conversely, the CO_2 conduction must be used when analyzing the hot extreme. The conductivity range of 0.007 to 0.025, given in table D4, is expected to cover the range from an insulation containing CO_2 at low temperature to one containing N_2 at high temperatures.

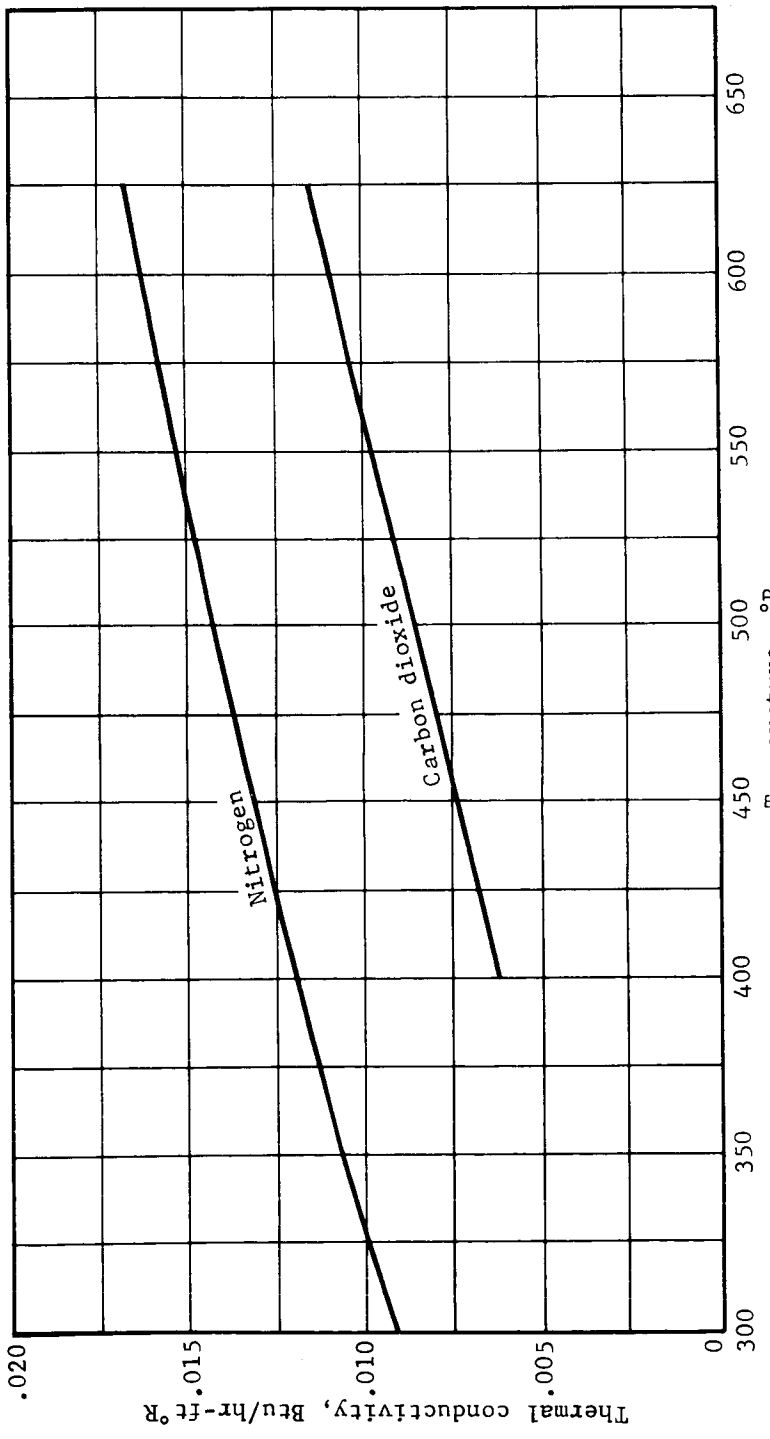

Figure D26.- Gas Thermal Conductivity as a Function of Temperature

APPENDIX D

TABLE D6.- EFFECTIVE CONDUCTIVITY AS A FUNCTION OF TEMPERATURE

$T_1 = 700°R$ $T_2 = 560°R$ $T_{av} = 630°R$	
Nitrogen gas	Conductivity Btu/hr ft°R
Radiation (0.0035/3) (0.1714) $(7^2 + 5.6^2)$ (7 + 5.6) 10^{-2}	0.0020
Gas conduction (from fig. D26)	0.0170
Solid conduction	0.0025
Total	0.0215
Carbon dioxide gas	
Radiation	0.0020
Gas conduction (from fig. D26)	0.0120
Solid conduction	0.0025
Total	0.0165
$T_1 = 560°R$ $T_2 = 510°R$ $T_{av} = 535°R$	
Nitrogen gas	
Radiation (0.0035/3) (0.1714) $(5.6^2 + 5.1^2)$ (5.6 + 5.1) 10^{-2}	0.0012
Gas conduction (from fig. D26)	0.0150
Solid conduction	0.0025
Total	0.0187
Carbon dioxide gas	
Radiation	0.0012
Gas conduction (from fig. D26)	0.0095
Solid conduction	0.0025
Total	0.0132
$T_1 = 530°R$ $T_2 = 300°R$ $T_{av} = 415°R$	
Nitrogen gas	
Radiation (0.0035/3) (0.1714) $(5.3^2 + 3^2)$ (5.3 + 3) 10^{-2}	0.0006
Gas conduction (from fig. D26)	0.0125
Solid conduction	0.0025
Total	0.0156
Carbon dioxide gas	
Radiation	0.0006
Gas conduction (from fig. D26)	0.0065
Solid conduction	0.0025
Total	0.0096

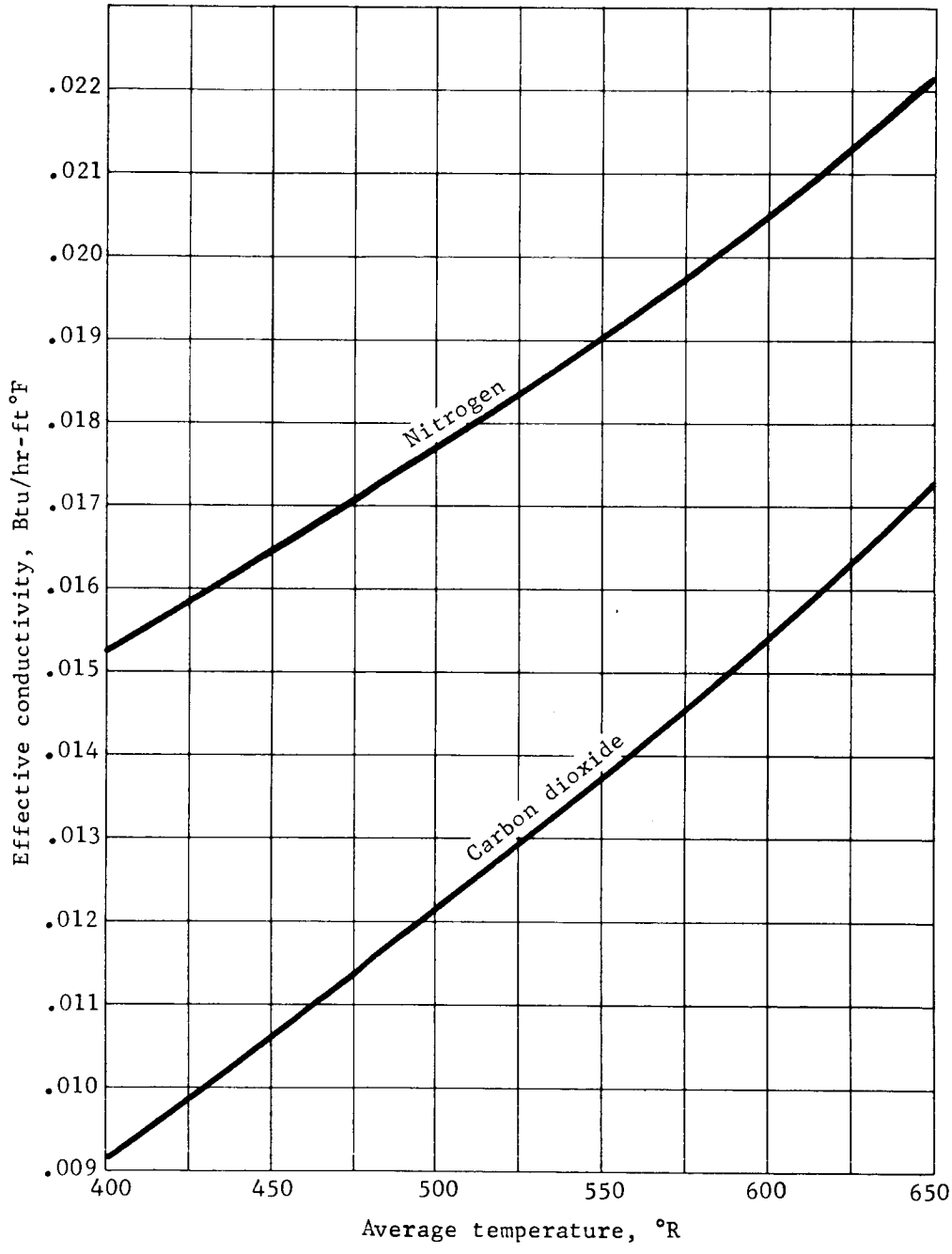

Figure D27.- Insulation Effective Conductivity

APPENDIX D

Energy sources. - Many energy sources were considered in our parametric studies including consumable types such as batteries and chemical and nonconsumable types such as radioisotopes and solar collector systems. Each of these approaches is discussed in the following paragraphs.

Consumable energy source, batteries: Figure D28 shows the sterilizable silver-zinc battery specific weight in lb/Btu as a function of total battery energy required in the system. The derivation of this curve is given in Section 8 of this appendix.

Consumable energy source, chemical: The most important requirements for chemical energy sources are: the products must be contained (i.e., in the solid or liquid phase) to prevent landing site contamination; they should be as simple as possible; and they should have a minimum specific weight (lb/Btu).

Many chemical reactions could be considered. Two of the more promising reactions are shown in figures D29 and D30 along with implementation concepts.

The concept shown in figure D29 consists of solid fuel slugs, consisting of CuO and Aℓ in a conduction plate, which are fired sequentially by a hot wire by demand from a thermostat. The conduction plate could be copper or beryllium. In preliminary feasibility tests conducted by R. Riebling of JPL a 0.5-in. copper plate was used with 0.75-in.-diameter fuel slugs. The specific weight of this design is estimated to be 0.003 lb/Btu. If a beryllium conduction plate were used the specific weight would be approximately 0.001 lb/Btu. A reasonable range of performance for this system is 0.001 to 0.004 lb/Btu. The primary advantage of this approach is that it is simple and has built-in redundancy. However, its specific weight is relatively high.

The concept shown in figure D30 consists of a reactor containing lithium powder into which CLF_3 is injected through a thermostatically controlled valve. Although this system is more complex than the solid reactant concept, it has a much lower specific weight as shown in figure D31. The assumptions used are as follows:

1) 100 percent excess lithium, 6000 Btu/lb of propellant;
2) Fixed hardware weight (reactor, lines, valves, etc.), 10 lb;
3) $C\ell F_3$ tankage calculated as a function of amount required using a titanium tank.

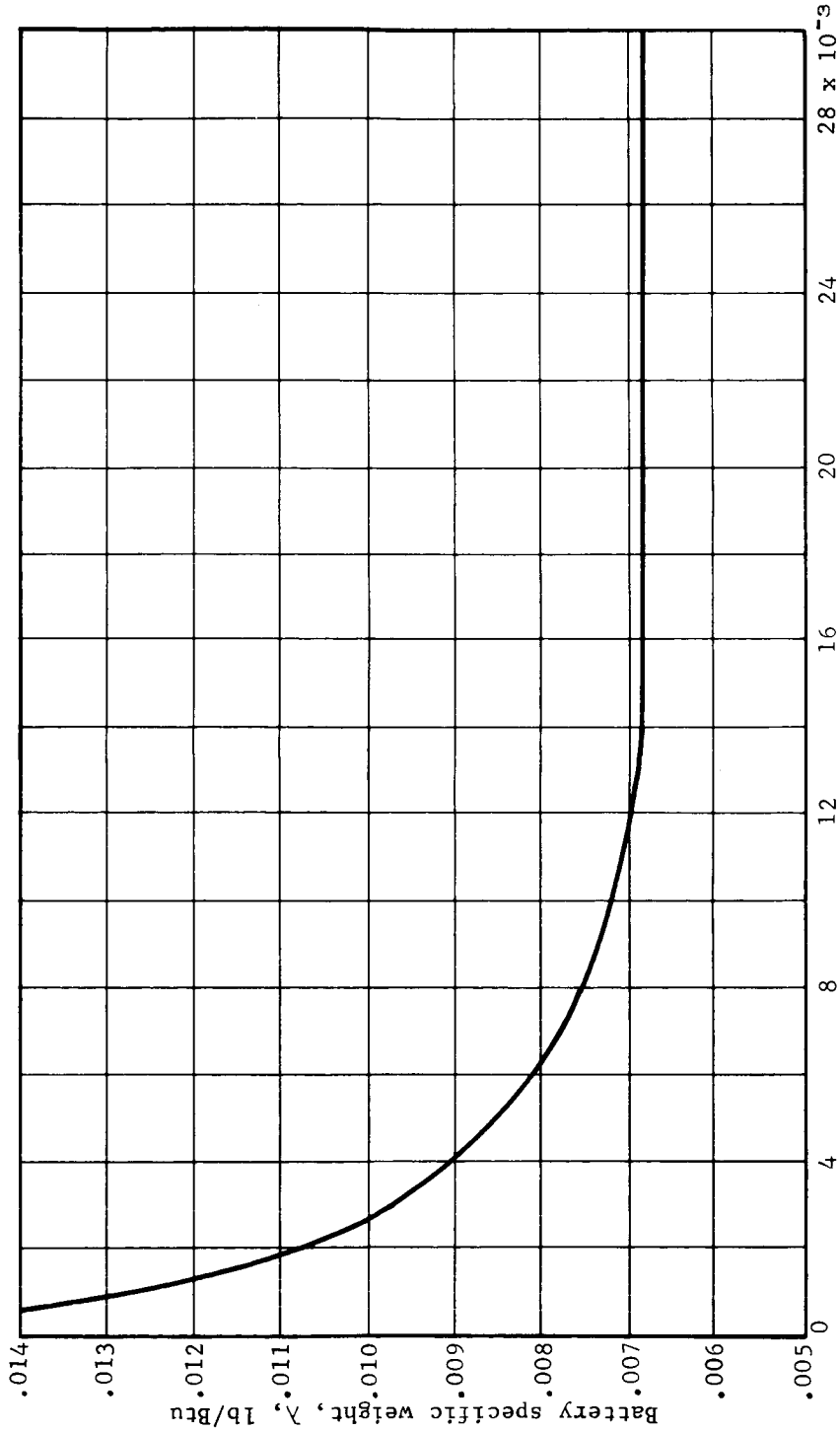

Figure D28.- Battery Specific Weight versus Size, Sterilized Silver-Zinc

Example

$3CuO + 2A\ell \rightarrow 3Cu + A\ell_2 O_3$

Theoretical heat release 1627 Btu/lb

Mechanization concept

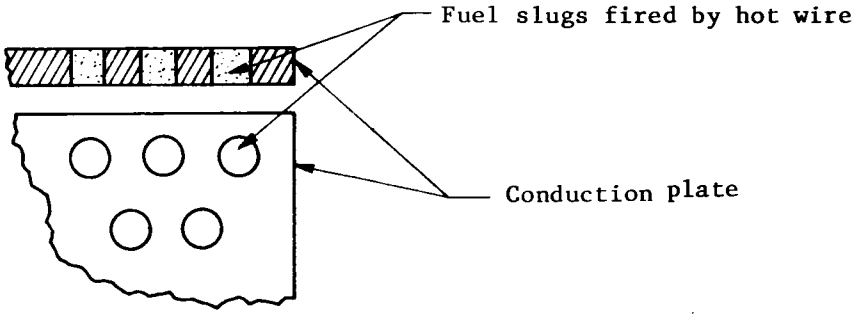

Estimated system specific weight - 0.003 lb/Btu

Preliminary feasibility tests being conducted by R. Riebling of JPL.

Figure D29.- Chemical Energy Source Concept, Solid Reactants - Solid Products

Example

$C\ell F_3 + 4Li \rightarrow LiC\ell + 3LiF$

Theoretical heat release 7400 Btu/lb

Mechanization concept

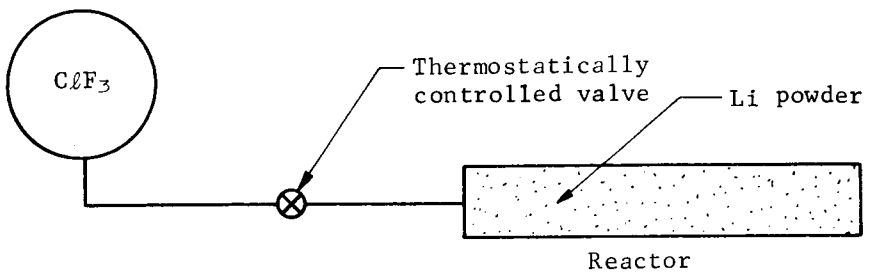

Estimated system specific weight - Shown on fig. D31 as a function of output.

Feasibility tests planned to start about July 1, 1968, by R. Riebling of JPL.

Figure D30.- Chemical Energy Source Concept, Liquid/Solid Reactants - Solid Products

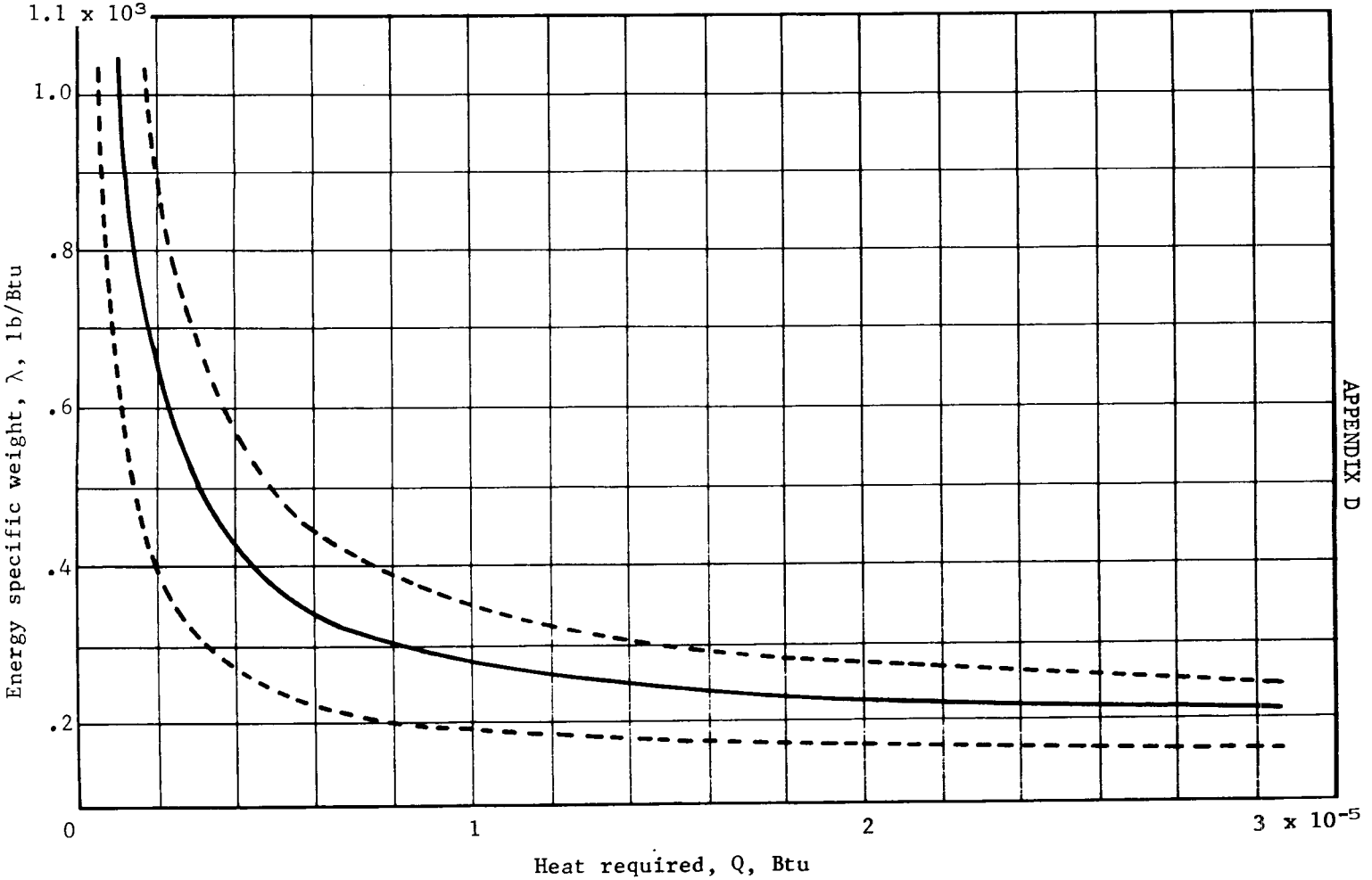

Figure D31.- Liquid-Solid Chemical Heater, $C\ell F_3$ + Li

APPENDIX D

Nonconsumable energy source, radioisotope heaters: A four-month study was recently completed by Atomics International for Bendix on a 25 to 30 W Pu^{238} heater for the ALSEP program. The study results which are shown in table D7 include the ablator and structure required for intact entry in the event of an abort. An installation concept is shown in figure D32 along with an installed weight estimate, which shows that a nominal specific weight of 0.044 lb-hr/Btu is considered reasonable.

Nonconsumable energy source, solar cells with phase change storage: Solar cells are estimated to produce 30 W-h/(lb/day) at a maximum Mars distance from the sun of 1.67 AU with a clear atmosphere (see section 8 of this appendix). Solar cell specific weight is 0.01 lb-day/Btu for the clear day environment and 0.02 for the intermediate environment. Many phase change materials could be considered (see ref. D2), most of which have a heat of fusion of about 100 Btu/lb. For example, hexadecane ($C_{16}H_{34}$) has a heat fusion of 102 Btu/lb and a melting point of 64°F. However, the packaging typically consists of an aluminum container with honeycomb to increase the conductivity and would weigh about 20 percent of the material weight. Therefore, the installed phase change would have a performance of 80 Btu/lb or a specific weight of 0.0125 lb/Btu. Assuming that all of the energy collected by the solar cells must be stored in the phase change material, the system specific weight is 0.01 + 0.0125 or 0.022 lb-day/Btu for a clear day environment and 0.032 lb-day/Btu for an intermediate (50 percent solar) environment.

Nonconsumable energy source, solar cell with battery storage: For long cycle life a nickle-cadmium battery with an output of 25.6 Btu/lb is used. Assuming all the energy collected by the solar cells must be stored in the batteries the system specific weight is 0.01 + 1/25.6 = 0.05 lb-day/Btu.

Nonconsumable energy source, capillary pumped fluid loop for RTG: An attractive approach for thermal control of landers that have RTGs (radioisotope thermoelectric generators) for electrical power is to use the waste heat from the RTGs. A concept for controlling the flow of heat from the RTGs is shown in figure D33. It consists of a capillary pump, condenser duct, and temperature control valve. The feasibility of this device was demonstrated in the testing reported in reference D3. The primary reason this approach appears more attractive than a more conventional heat pipe is that a heat pipe performance is very sensitive to an adverse gravity head but the capillary pumped loop is not. A weight estimate was made of the hardware required and is shown in figure D33.

APPENDIX D

TABLE D7.- 25 TO 30 W ISOTOPE HEATER SUMMARY

Materials		
Fuel		$Pu^{238}O_2$
Structure		Ta-10 W
Fuel liner		TA-10 W
Clad		Hastelloy X
Ablator		80 $A\ell F_3$-20 W
Dimensions		
Fuel volume, cu in. (50% void)		.935
Structure and liner thickness, in.		.150
Clad thickness, in.		.030
Minimum ablator thickness, in.		.600
Capsule diameter, in.		1.57
Ablator diameter, in.		2.77
Weight, lb		
Fuel		.170 (for 30 W)
Structure and liner		.564
Clad		.065
	Total	.80
Ablator		1.84
	Total	2.64

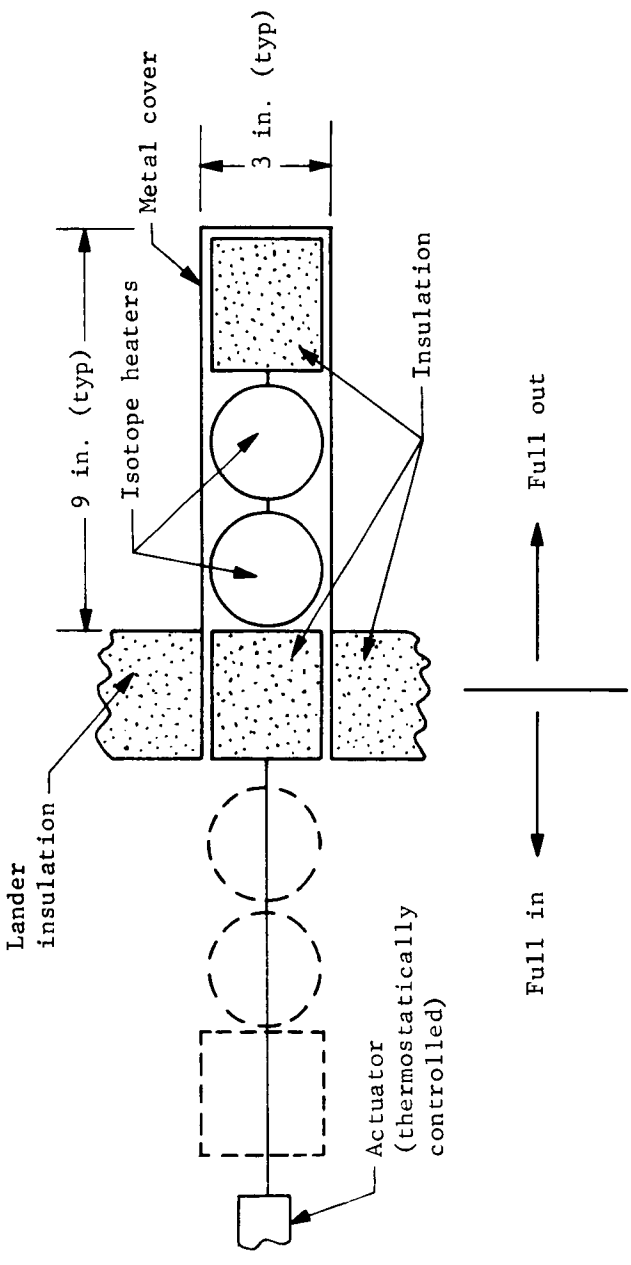

Figure D32.- Isotope Heater Control Concept

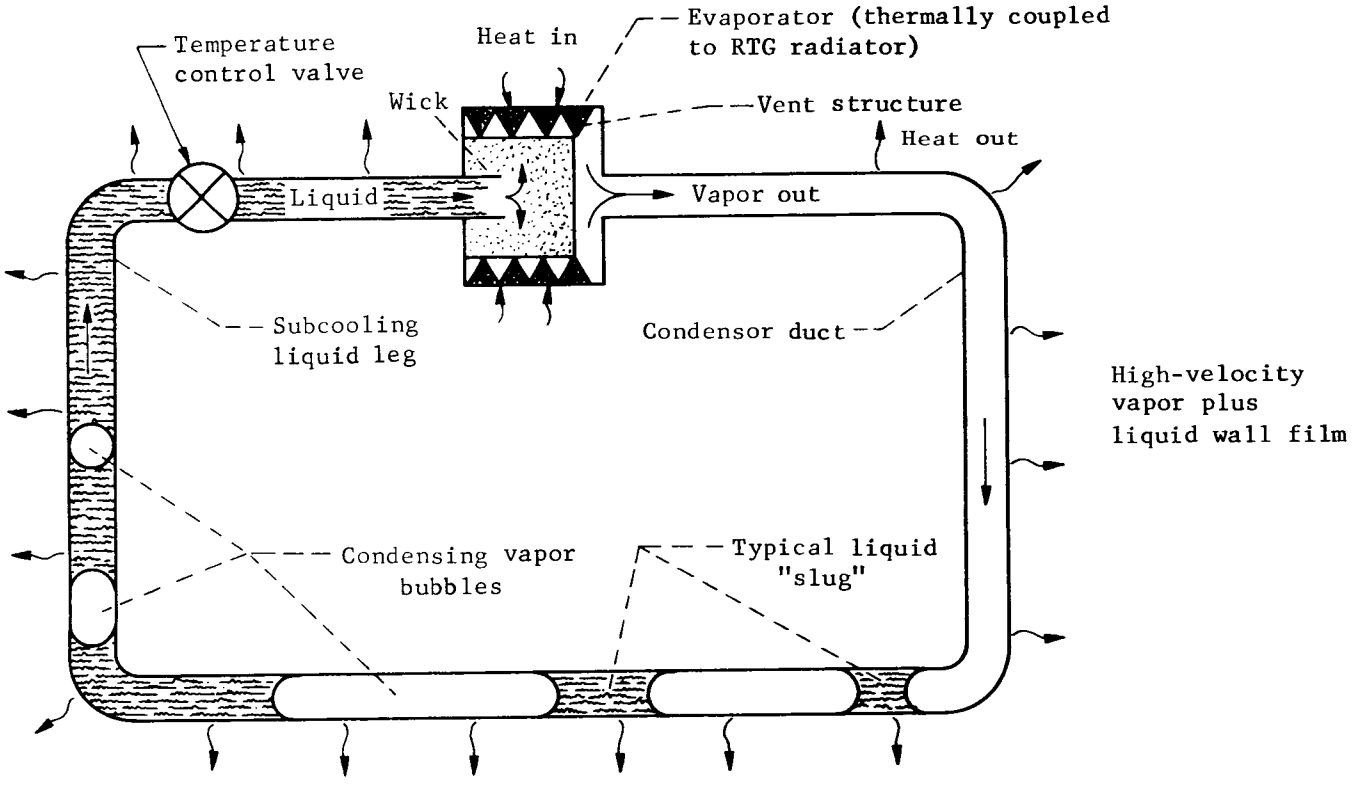

Estimated system specific weight - 0.01 lb/Btu + 3 lb (ref. D3)

Figure D33.- Capillary Pumped Fluid Loop

APPENDIX D

Energy rejection device: In some thermal control designs it may be necessary to reject heat from the sytem through a control device. A concept that could be used is shown in figure D34. It consists of two vertical radiators on opposite sides of the lander to ensure that the radiator in operation does not have direct solar exposure. The radiators are sized so that all the heat could be rejected from a single radiator. This is an important feature since it is difficult to ensure a low α/ϵ coating in the dust and erosion environment of Mars. The heat pipe evaporator is attached to the distribution plate. The condenser tubes are attached to the radiators. The radiator was sized assuming a radiator temperature of 80°F (540°R) and an emissivity of 0.8 which is capable of rejecting 35 W/ft^2. It was estimated that the radiator including the condenser tubes would weigh 2 lb/ft^2. Since two radiators are used the radiator system would weigh 4/35 = 0.11 lb/W. The evaporator is also expected to weigh 2 lb/ft^2 and have an average input of 30 W/ft^2, which results in 2/30 = 0.06 lb/W. The valve fittings, etc., were estimated to weigh 5 lb. The total estimated system weight is 5 + 0.17P, where P is the maximum heat rejected in watts.

Procedure for estimating thermal control system weights. -

Heat requirements: The total weight of the thermal control subsystem is a function of the environment, vehicle size and shape, surface radiation properties, insulation conductivity density and thickness, and the internal temperature requirements. For such energy sources as a battery, chemical heater, or solar collector system, the weight is a function of the total heat loss; for a radioisotope heater energy source the system weight is a function of the peak rate of heat loss.

Because of the large number of combinations among these variables, a parametric correlation was made of the daily heat requirement and the peak heat rate for a flat octagon, having a width-to-height ratio of 4.5, as a function of insulation thickness. Thermal insulation conductivities of 0.007, 0.0125, and 0.025 Btu/hr ft°F were treated as parameters under each of the four environments defined in table D5. The insulation density was fixed at 1 lb/cu ft. The heat loss to the environment was based on maintaining the internal temperature at 40°F (minimum allowable equipment temperature) for all environments except the hot extreme. For the hot extreme environment, the internal temperature was maintained at 100°F. Analyses on various sizes of vehicles under similar conditions indicated that within the size limits under consideration, the heat loss was proportional to the surface area.

APPENDIX D

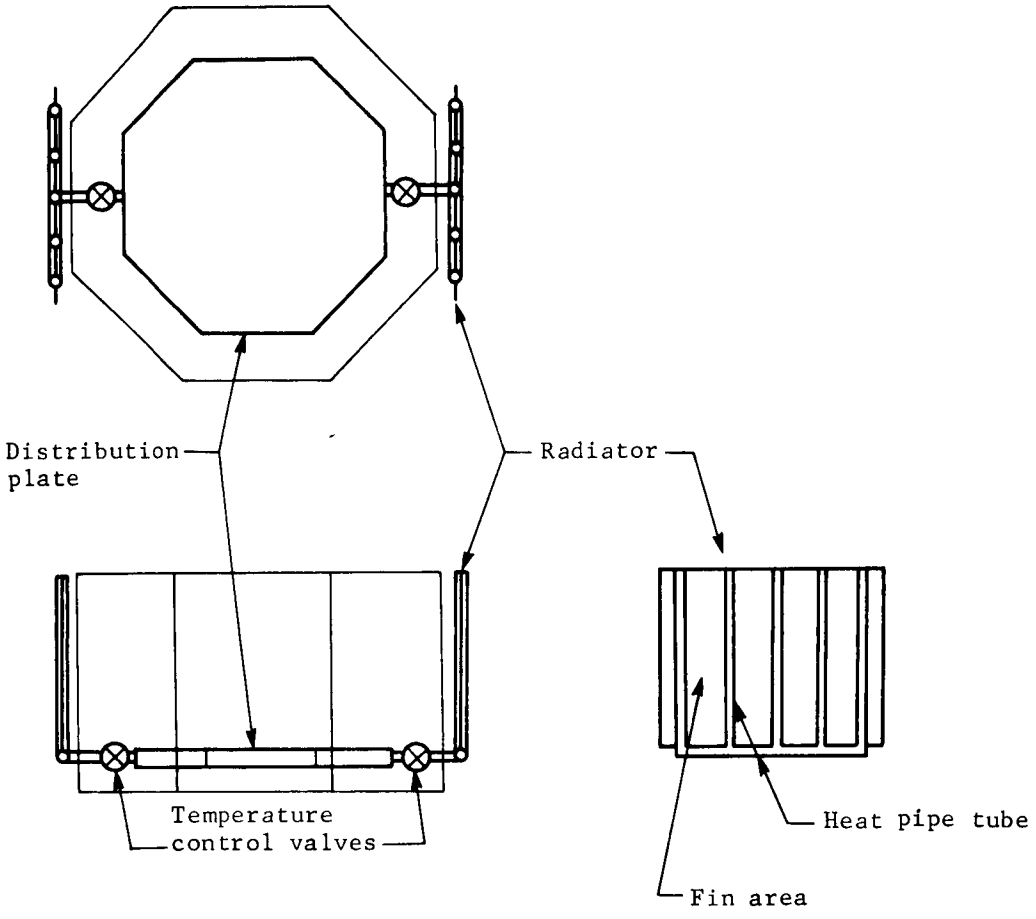

Weight estimate:

$$W_R = 5. + 0.17\ P_{E(max.)}$$

where:

W_R = weight, lb

$P_{E(max.)}$ = maximum equipment power, W

Figure D34.- Temperature Control Heat Pipe Concept

APPENDIX D

The heat required to maintain the desired internal temperature was determined by a transient thermal analysis over a sufficient number of daily cycles to establish a cyclic temperature response. The daily heat requirement was determined over one complete cycle. The peak heat rate was determined over a half-hour period just before dawn. The results of these analyses are plotted in figures D35 thru D42.

Procedure for estimating subsystem weights: Thermal control of the landed equipment compartment is accomplished by insulating the external surfaces to provide isolation from the environment, and then adding energy sources and controls to maintain the internal temperature within the desired range. The total thermal control subsystem weight is essentially the sum of these two major components.

A procedure for estimating the subsystem weight is outlined below based on the assumption that the average environmental temperature is below the desired range of internal temperatures:

1) Optimize the insulation and energy source weights for the coldest environment anticipated;

2) Determine if the system that has been optimized for the coldest anticipated environment will overheat in the hottest anticipated environment;

3) If the system does overheat in the hottest environment, one of the following modifications must be made,

   a) Reduce the insulation to increase the heat loss in the hottest environment and add energy source capacity to maintain the desired internal temperature under the coldest environment,

   b) For short life landers, add phase change material to absorb excess heat within the desired temperature range,

   c) If options a) and b) result in an unacceptable weight penalty, add a temperature controlled heat pipe to increase the rate of heat rejection in the hottest environment.

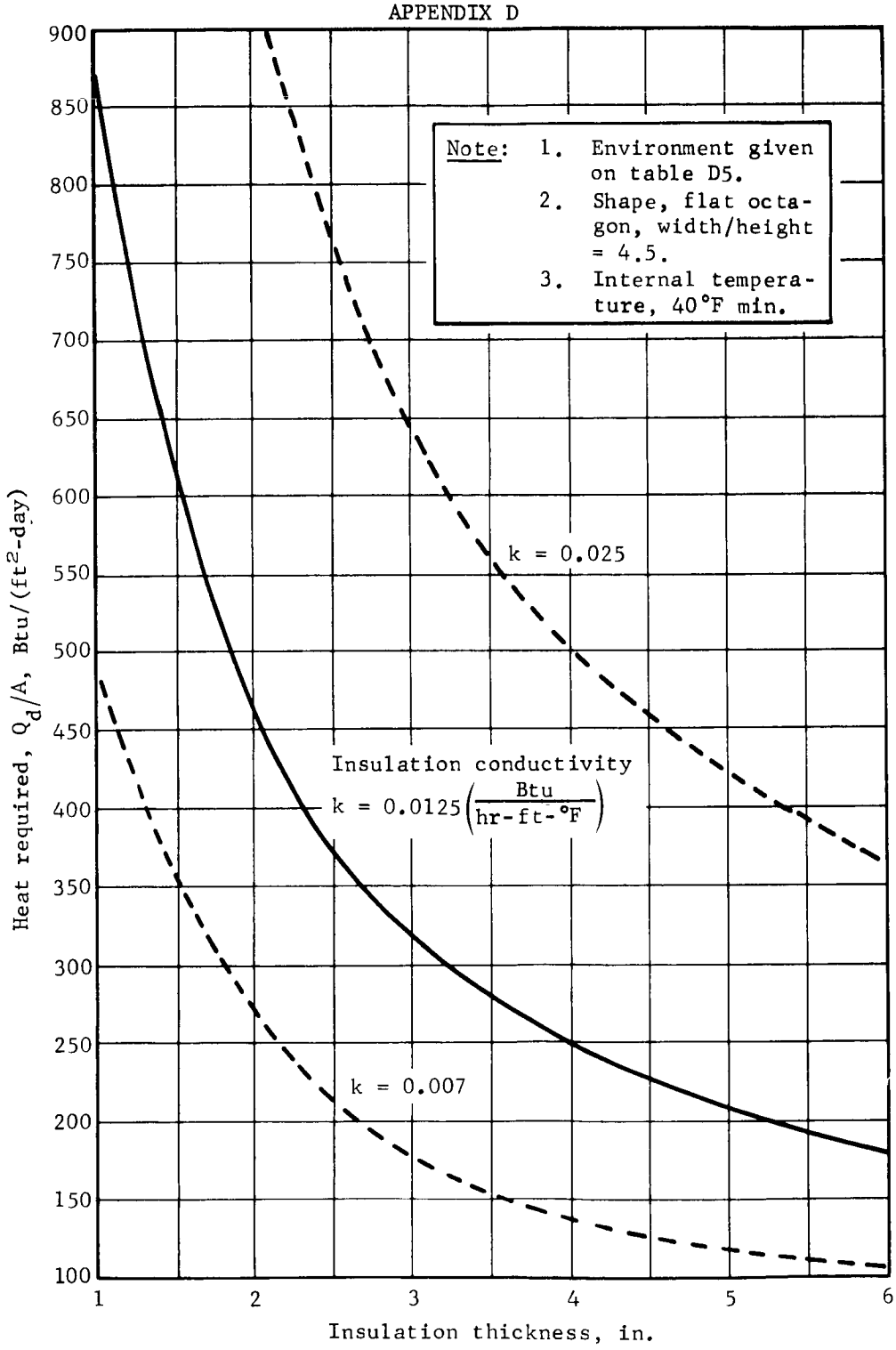

Figure D35.- Heat Required, Cold Extreme Environment

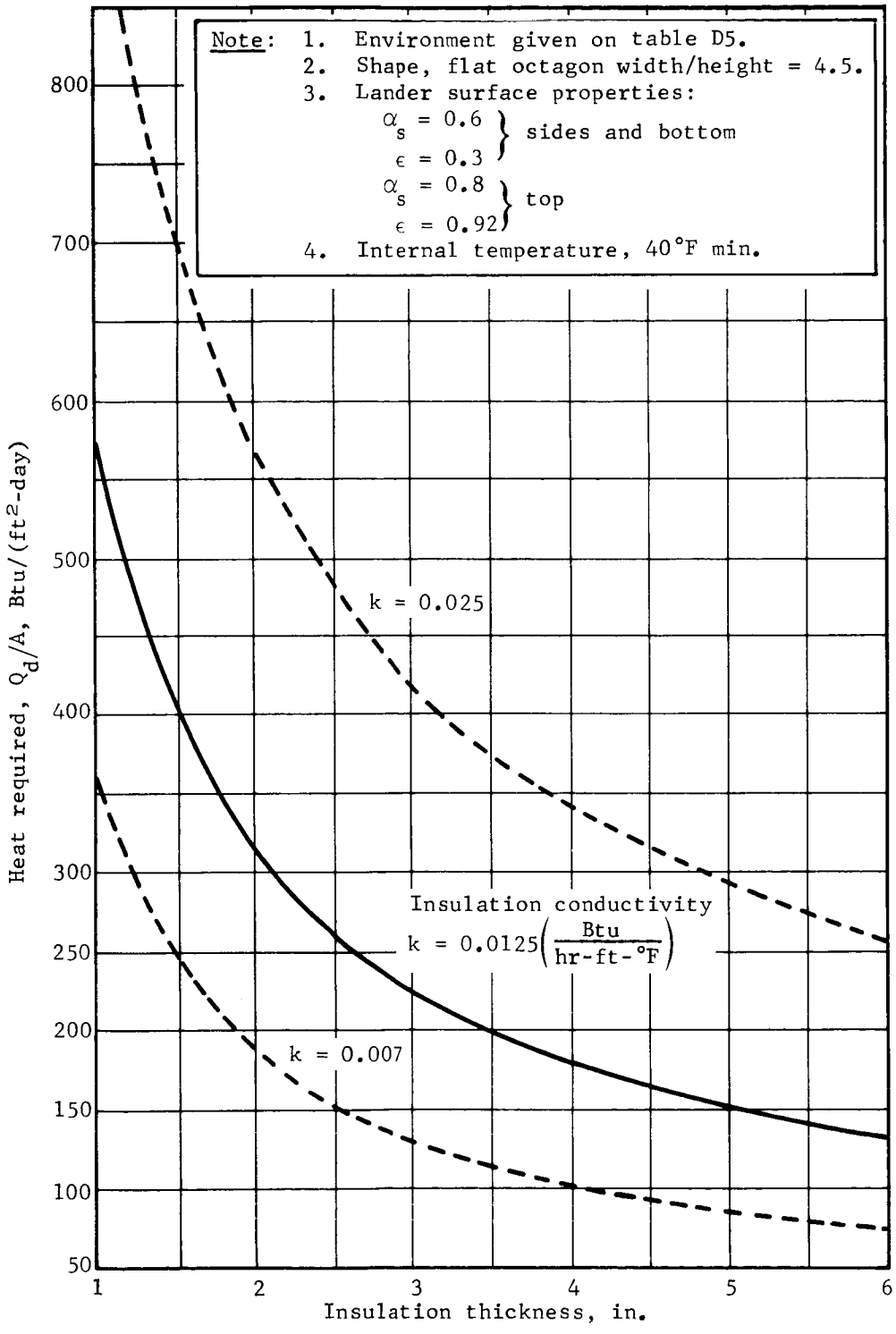

Figure D36.- Heat Required, Intermediate Environment

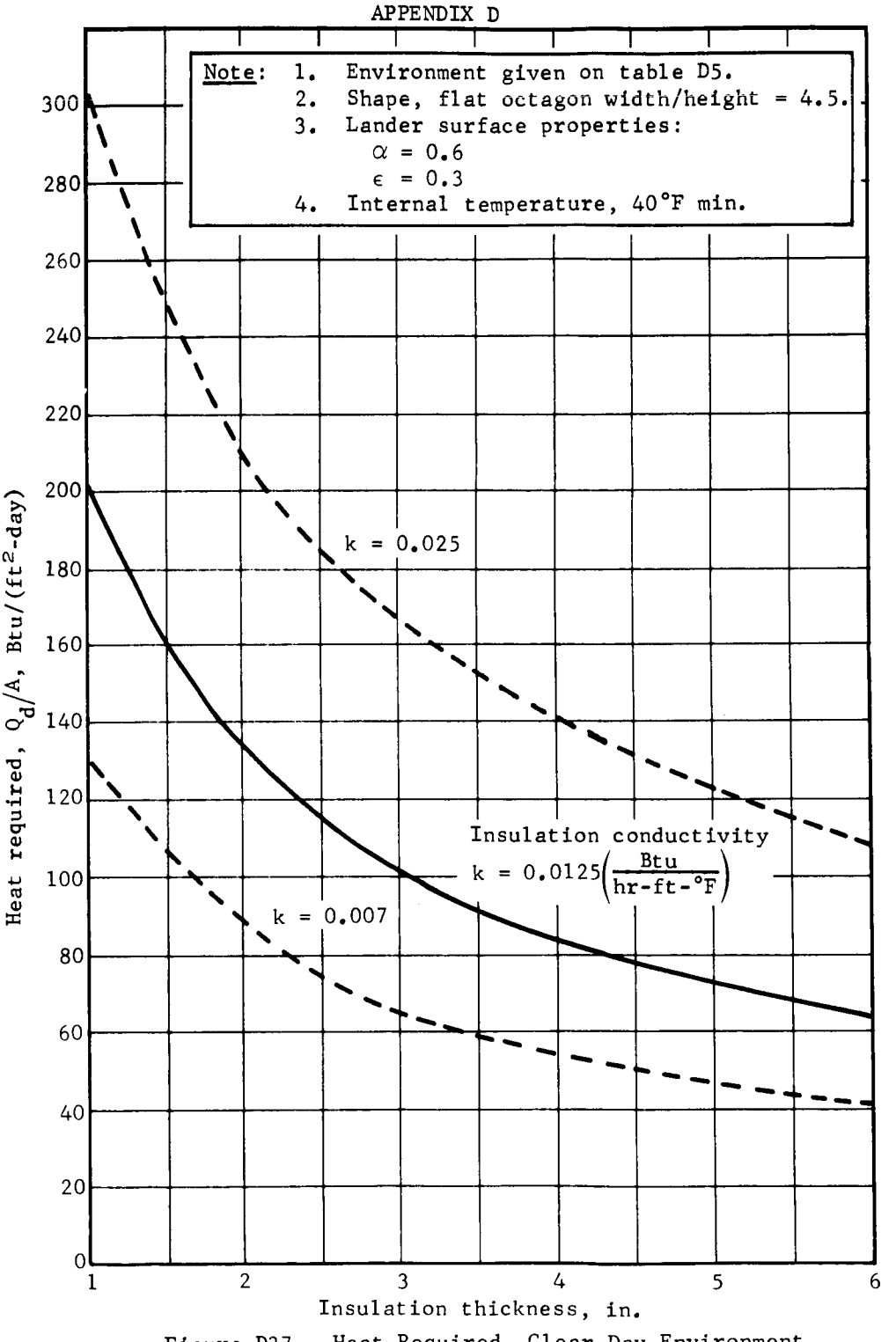

Figure D37.- Heat Required, Clear Day Environment

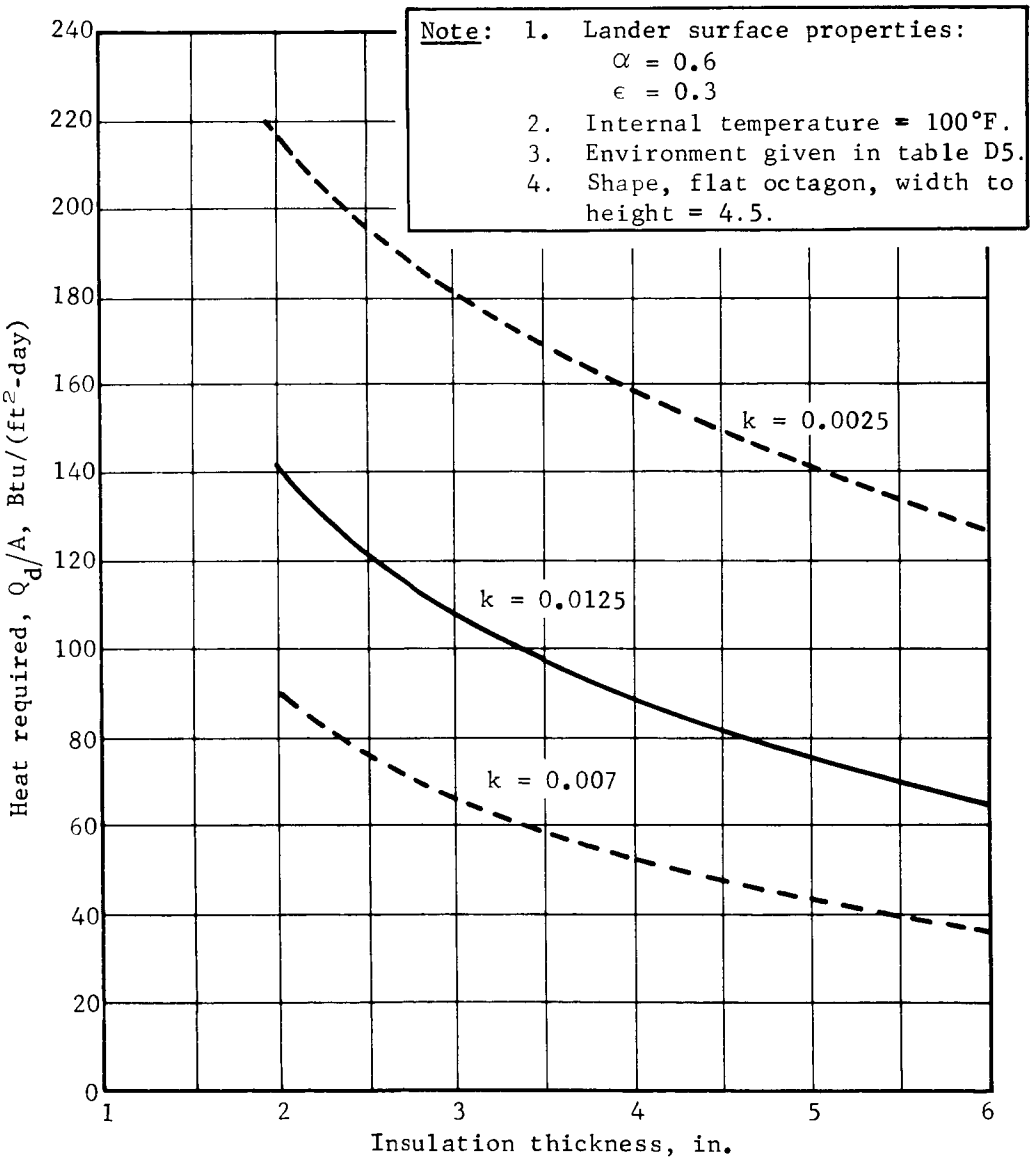

Figure D38.- Heat Required, Hot Environment (α = 0.6, ϵ = 0.3)

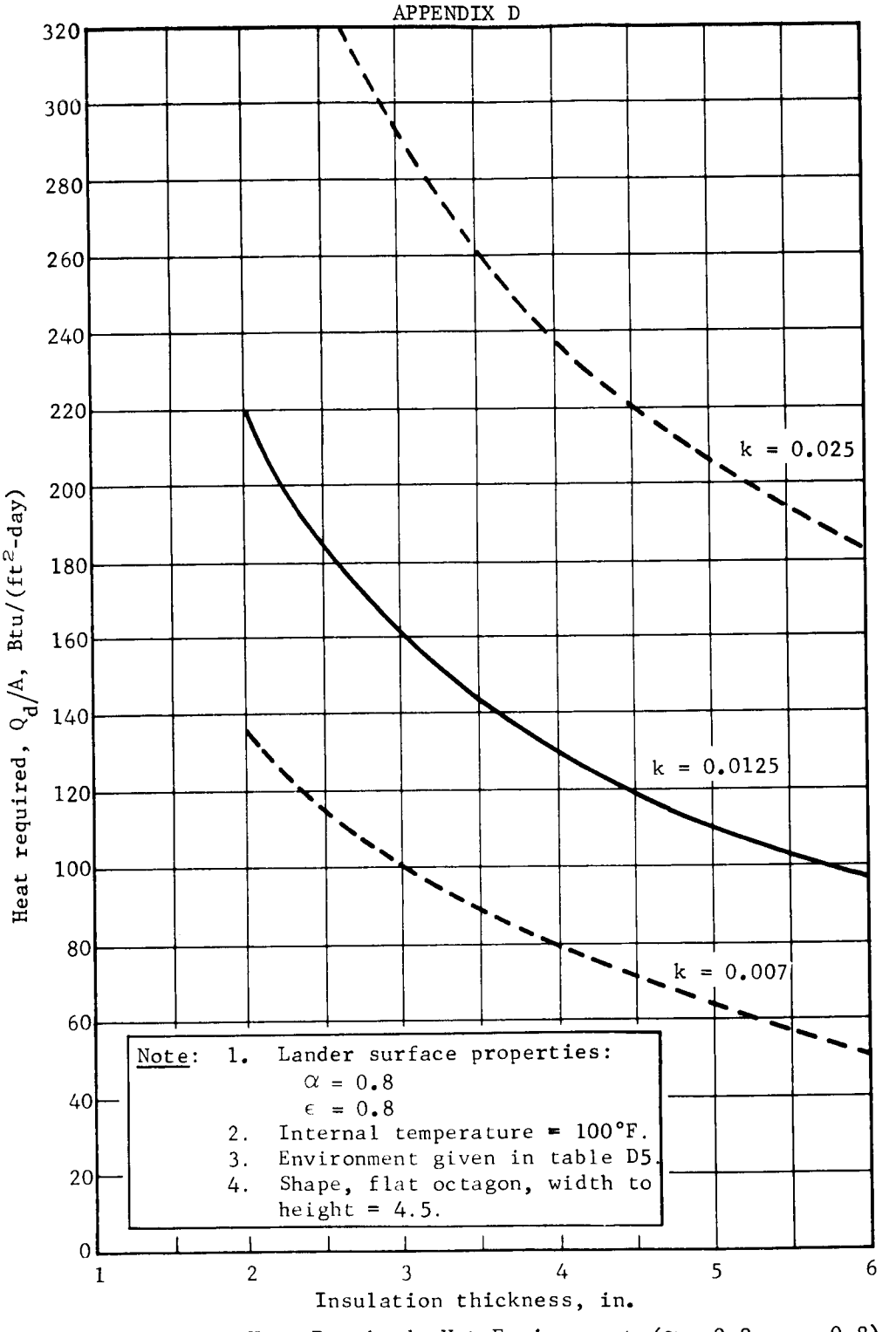

Figure D39.- Heat Required, Hot Environment (α = 0.8, ϵ = 0.8)

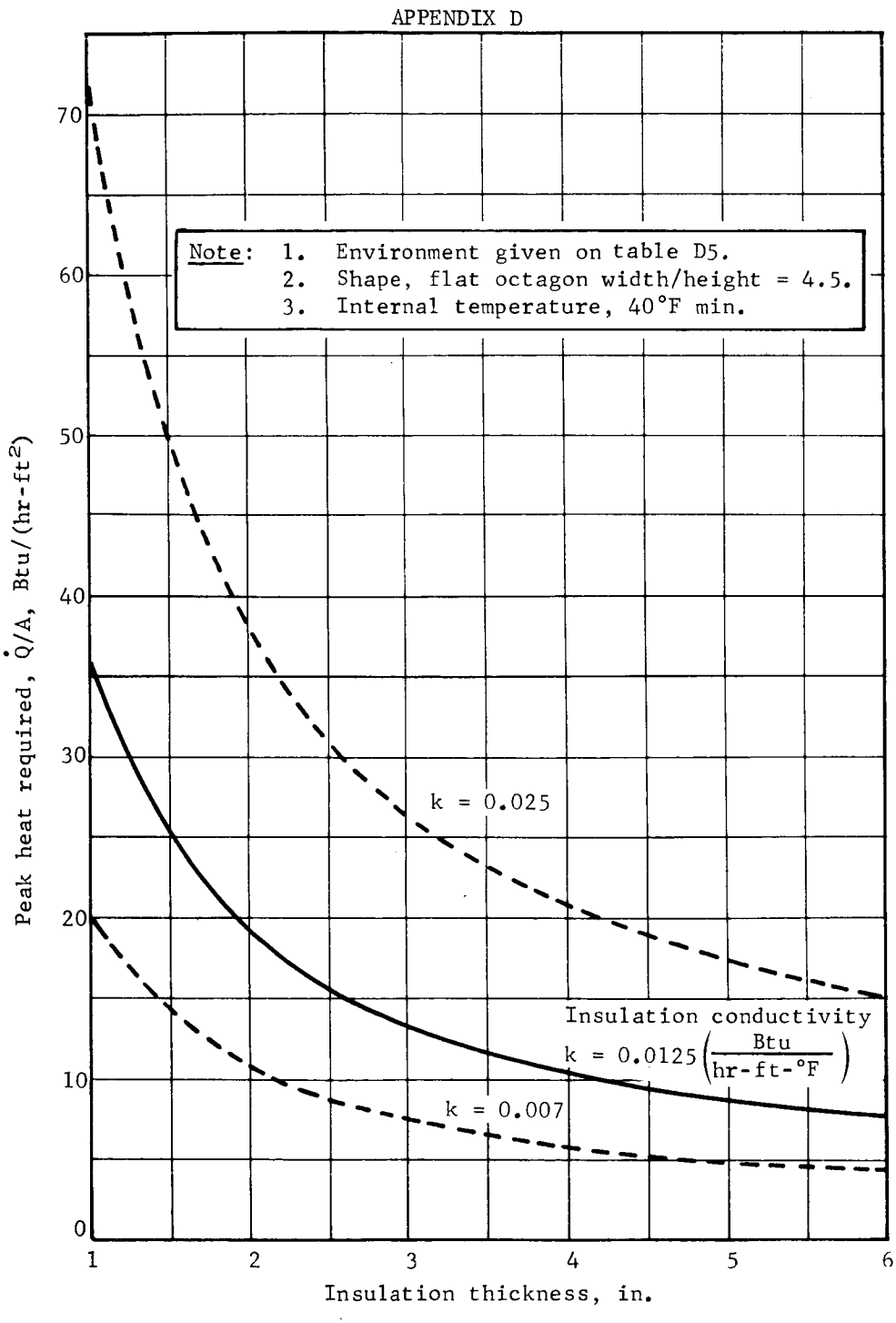

Figure D40.- Peak Heat Required, Cold Extreme Environment

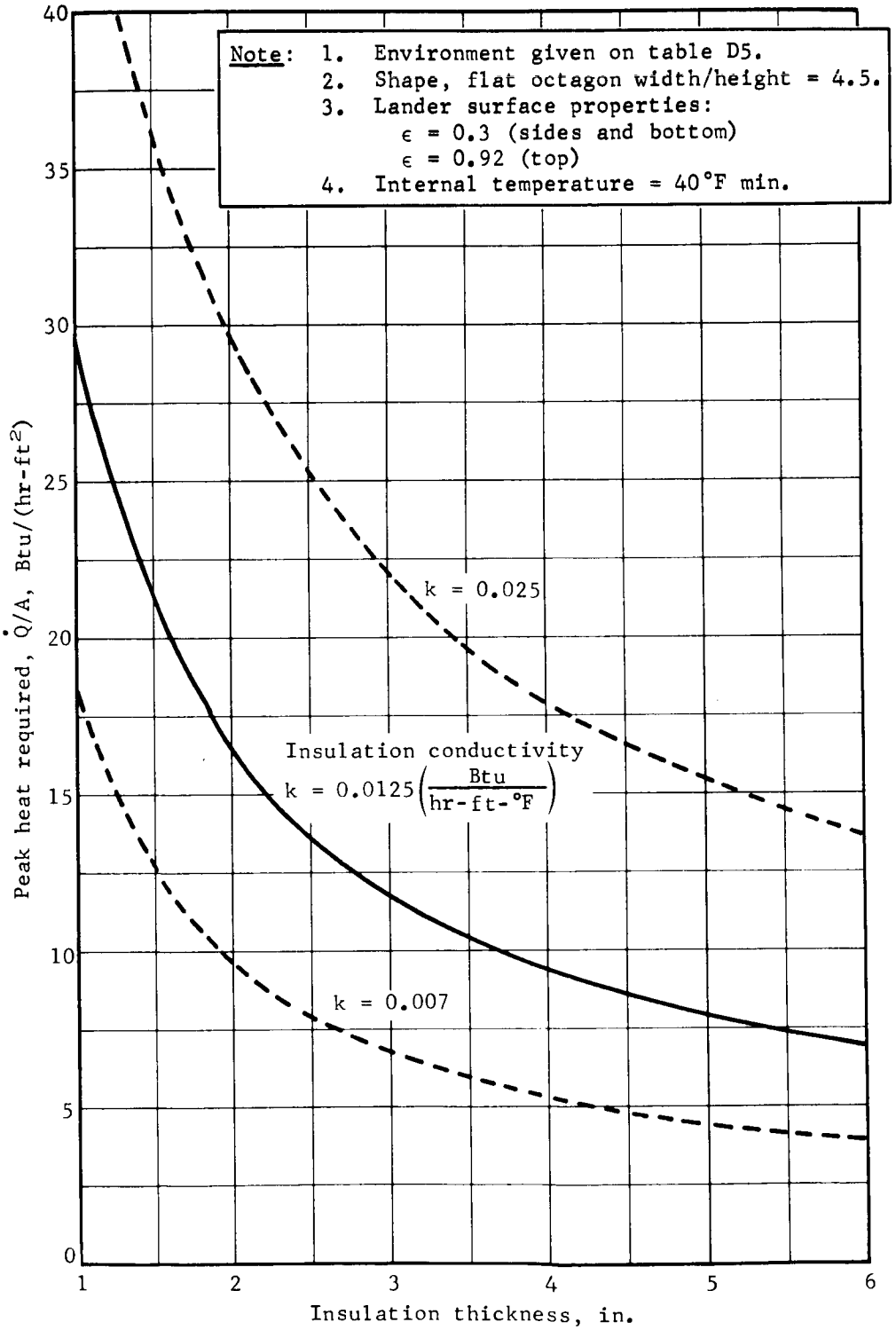

Figure D41.- Peak Heat Required, Intermediate Environment

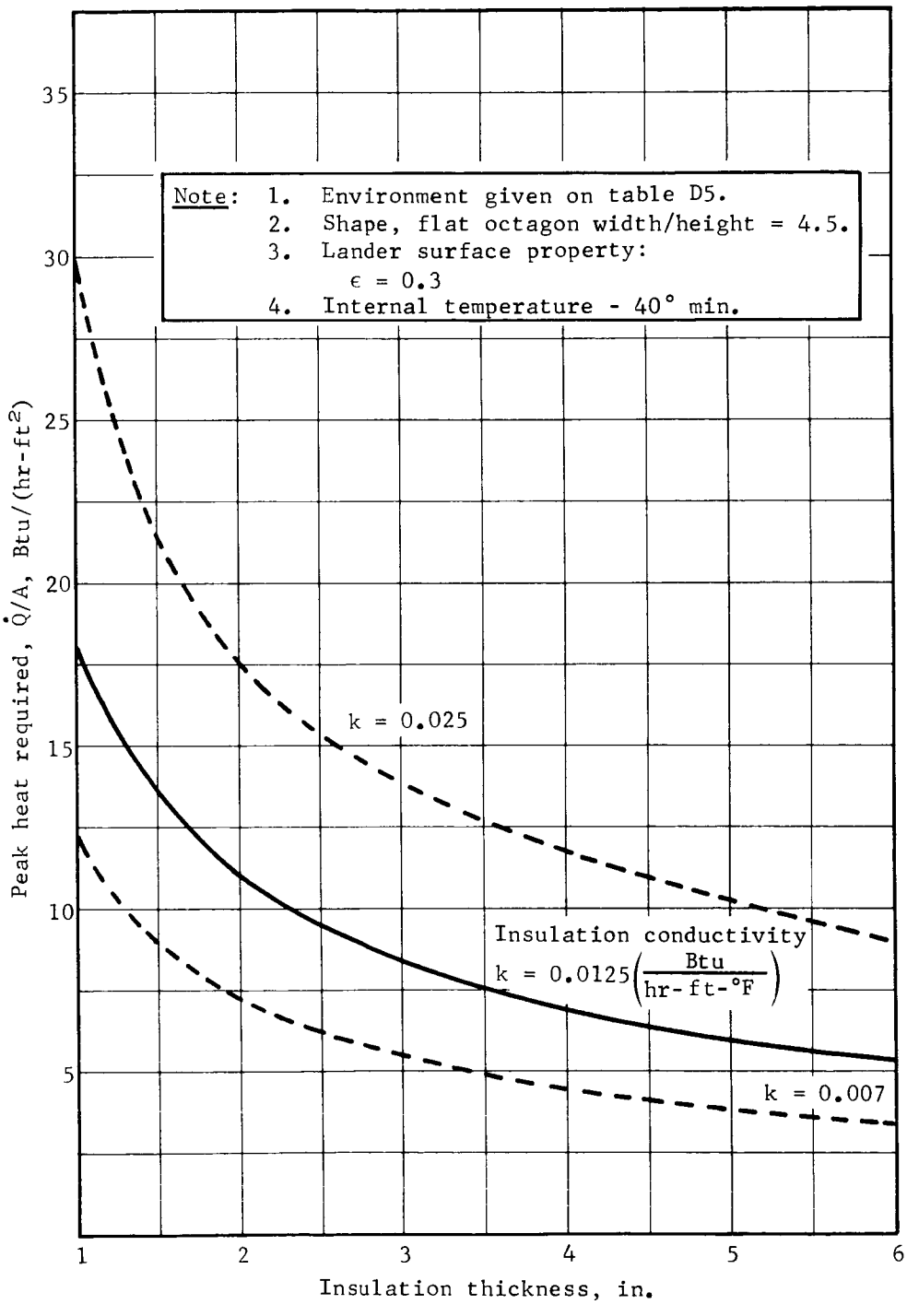

Figure D42.- Peak Heat Required, Clear Day Environment

APPENDIX D

A procedure for determining the weight of a thermal control subsystem using consumable energy sources is outlined below:

1) Determine the total heat required as a function of insulation thickness up to a maximum of 6 in.,

$$Q = \overbrace{A\,\theta\,\left(Q_d/A\right)}^{\text{(Heat Rejected)}} - \overbrace{(24.6\theta)(3.41)\,\left(P_e - CP_p\right)}^{\text{(Net Equipment Heat)}}$$

where

Q = total heat required, Btu

A = lander area inside insulation, ft^2

θ = life time, Mars days

Q_d/A = daily heat requirement per unit area, Btu/ft^2 day obtained from correlations in figures D35 thru D38 for the selected environment, insulation thickness and thermal conductivity. (A high conductivity based on 100% nitrogen atmosphere is recommended)

P_e = average equipment power, W

P_p = penetration loss for extreme cold environment, W

C = 1.0 for extreme cold environment

= 0.76 for the intermediate environment

= 0.48 for the clear day environment (not applicable for the extreme hot environment;

2) Determine the consumable energy source weight as a function of insulation thickness,

$$W_E = Q\lambda$$

where

W_E = weight of energy source, lb

Q = total heat required, Btu from Step 1)

λ = specific weight of energy source, lb/Btu from table D4 for selected energy source;

3) Determine the insulation weight as a function of insulation thickness,

$$W_I = \left(W_I/A\right)A$$

where

W_I = weight of insulation, lb

W_I/A = weight of insulation per unit inside area, lb/ft^2 from figure D43, for selected lander size, insulation density and thickness;

4) Determine total weight as a function of insulation thickness,

$$W_T = W_E + W_I, \text{ lb};$$

5) Select as optimum, the insulation thickness $\left(I_{opt}\right)$ corresponding to the minimum total weight. The weight penalty required to increase the insulation thickness so that no energy source is required (i.e., equipment heat alone is sufficient) should be calculated. If the weight penalty is acceptable the system without an energy source should be selected since it would be simpler;

6) Using the equation in step 1), determine if the internal temperature of the selected system exceeds 100°F in the hottest environment anticipated,

   a) If the extreme hot environment is selected, Q_d/A is determined directly from either figure D38 or D39 for optimum insulation thickness and the minimum insulation conductivity. A conductivity based on a pure carbon dioxide atmosphere is recommended,

   b) If an environment other than the hot extreme is selected, the $\left(Q_d/A\right)$ as determined from figure D36 or D37 must be modified to correct from an internal temperature of 40°F to one of 100°F by the factor $(\Delta t + 60)/\Delta t$ where

$$\Delta t = \left(\frac{\left(Q_d/A\right)}{24.624}\right)\left(\frac{I_{opt}}{12}\right)\Big/ k, \ ^\circ F;$$

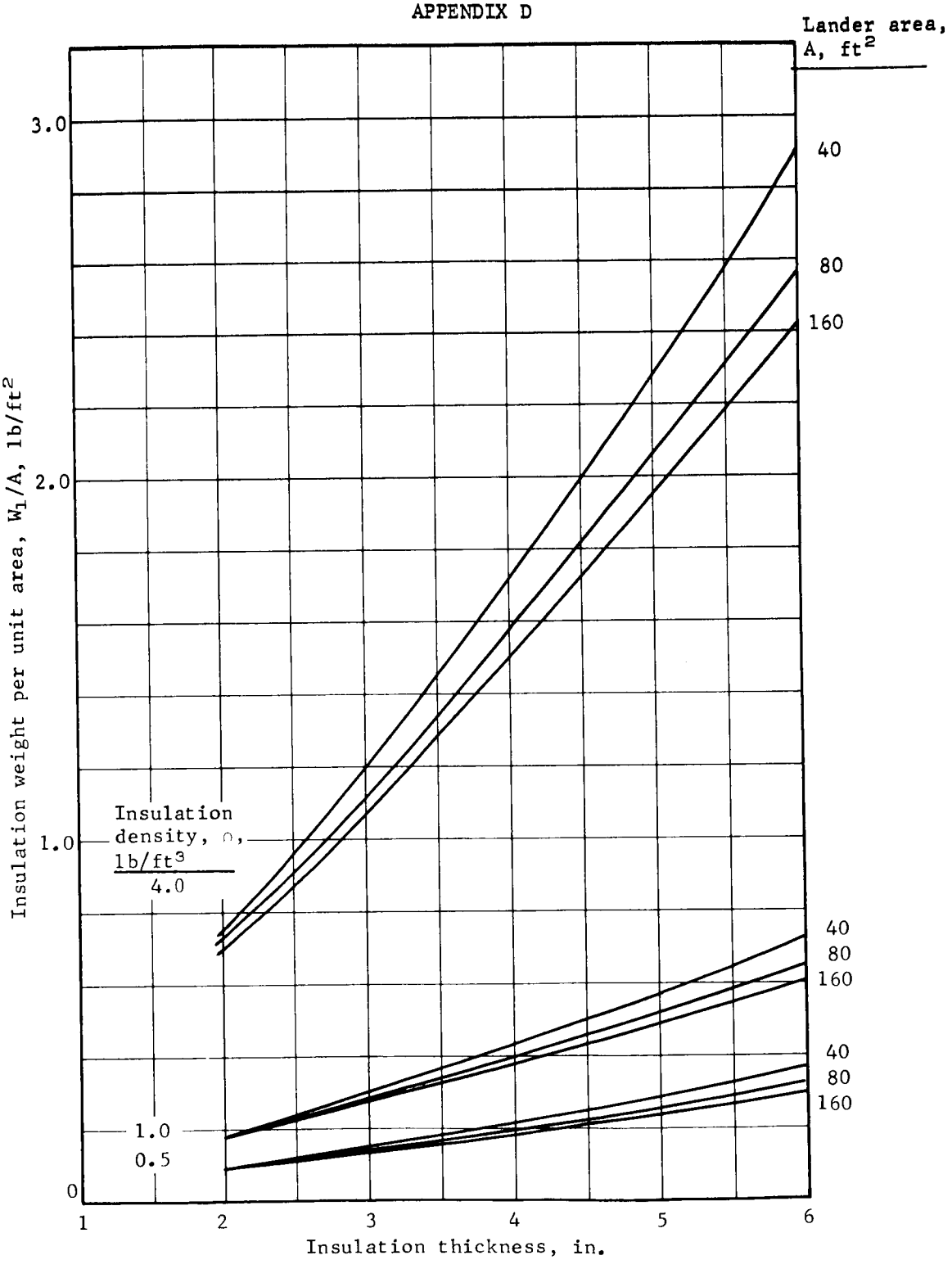

Figure D43.- Insulation Weight versus Thickness

7) If $\left(Q_d/A\right)A$ is greater than $(24.6)(3.41)\left(P_e-CP_P\right)$, general overheating will not occur. However, temporary overheating may occur during daytime peak power periods. For the range of peak power values in table D4, the maximum internal temperature can be controlled by adding phase change material having a latent heat of 80 Btu/lb in the amount of P(peak)(3.41/80) lb. This weight is added to the subsystem weight determined in Step 4). If the phase change material weight is unacceptable, a temperature controlled heat pipe rejection device should be considered;

8) If $\left(Q_d/A\right)A$ is less than $(24.6)(3.41)\left(P_e-CP_P\right)$ the internal temperature will exceed 100°F and the rate of heat loss must be increased by one of the following methods,

   a) Reduce insulation thickness until $\left(Q_d/A\right)A = (24.6)(3.41)\left(P_e-CP_P\right)$ and determine W_T at the reduced insulation thickness from Step 5); then add the phase change material weight of P (peak) (3.41/80) as in Step 7),

   b) For short-life missions of a few days, add phase change material to absorb excess heat. The weight of this additional phase change material is $\left[(24.6)(3.41)\left(P_e-CP_p\right) - \left(Q_d/A\right)A\right](\theta/80)$,

   c) If acceptable weights cannot be obtained with the relative simplicity of methods a) or b), a temperature controlled heat pipe and radiator system shown in figure D34 can be added. The estimated weight of this heat rejection system is

$$W_R = 5.0 + 0.17\ P_E\ (\max)$$

   where P_E (max) is the maximum equipment power, W. This weight is added to the subsystem weight determined in Step 5) to determine the total weight.

Subsystem weights using solar cells or solar collectors that store solar energy in batteries or phase change materials for use during nonday-light periods can be estimated according to the above procedure by basing the energy requirements on one daily cycle.

APPENDIX D

The weight of a system using isotope heaters or RTG waste heat depends on the maximum heat rate required and assumes the use of a temperature control device (see figs, D32 and D33).

The maximum heat rate required is determined from the equation

$$\dot{Q} = A\,(\dot{Q}/A)\ \max - 3.41\left(P_e\ (\min) - CP_p\right)$$

where

$\dot{Q}$ = maximum heat rate required, Btu/hr

A = lander area inside insulation, ft^2

P_e (min) = minimum equipment power, W

P_p = penetration loss for extreme cold environment, W

C = 1.0 for extreme cold environment

= 0.91 for intermediate environments

= 0.74 for clear day environment (not applicable for extreme hot environment)

$(\dot{Q}/A)$ max = maximum heat rate per unit inside area, Btu/hr ft^2 (from figs. D40, D41, and D42) for the selected environment, insulation thickness and conductivity. A high conductivity based on a 100% nitrogen atmosphere is recommended.

The procedure for determining the subsystem weight based on the maximum heat rate required is analogous to the procedure based on the total heat required. An example of the application of this procedure to configuration 1A is presented below. This configuration uses isotope heaters and the extreme cold and hot environments are used for the limiting heat requirements.

A = 38.51 ft^2	P_e (min) = 10 W
k(cold) = 0.0133 Btu/hr ft°R	P_e (max) = 35 W
k(hot) = 0.0120 Btu/hr ft°R	P_e (peak) = 144 W-h
ρ = 1.0 lb/ft^3	$P_p = (0.263/3.41)\ (\dot{Q}/A)\ A$ W
λ = 0.044 lb hr/Btu	C = 0.217 for hot environment

Using the equation $\dot{Q} = A(\dot{Q}/A)\ \max - 3.41\ (P_e - CP_p)$ for required heat input as a function of insulation thickness and $(\dot{Q}/A)$ max values from figure D40, the following tabulation is determined.

APPENDIX D

Insulation, in.	$(\dot{Q}/A)_{max}$, (Btu/hr ft^2)	$A(\dot{Q}/A)_{max}$, Btu/hr	CP_p, W	$3.41(P_e - CP_p)$, Btu/hr	$\dot{Q}$, Btu/hr
2.0	20.0	770.	59.	169.	939.
2.5	16.3	629.	48.	131.	760.
3.0	13.9	536.	41.	107.	643.
3.5	12.2	470.	36.	90.	560.
4.0	10.9	420.	32.	77.	497.
4.5	9.9	382.	30.	67.	449.
5.0	9.1	351.	27.	58.	409.

Then using the equations $W_E = \lambda\dot{Q}$, $W_I = (W_I/A)A$ and $W_{pc} = P$ (peak) 3.41/80, and the W_I/A values from figure D43, the following weights tabulation is determined.

Insulation, in.	W_E, lb	W_I/A, lb/ft^2	W_I, lb	W_{pc}, lb	W_T, lb
2.0	41.3	0.190	7.3	6.1	54.7
2.5	33.5	0.244	9.4	6.1	49.0
3.0	28.3	0.302	11.6	6.1	46.0
3.5	24.6	0.363	14.0	6.1	44.7
4.0	21.9	0.428	16.5	6.1	44.5
4.5	19.7	0.496	19.1	6.1	44.9
5.0	18.0	0.568	21.9	6.1	46.0

Therefore, the minimum weight is obtained with about 3.8 in. of insulation, although anywhere between 3 and 5 in. would be acceptable. With the hot environment and 5 in. of insulation, the heat that must be disipated is (24.6) (3.41) $\left[P_e(max) - CP_p\right]$ or 2446 Btu/day. With Q_d/A from figure D38 of 73 Btu/day ft^2, the minimum heat dissipated at 100°F is 2811 Btu/day so there are no hot environment limitations.

The actual point design calculations for configuration 1A produced a thermal control subsystem weight of 46.8 lb with 3.0 in. of insulation. This minimum-acceptable thickness was selected for structural reasons.

APPENDIX D

Examples: There is an enormous number of combinations of parameters and thermal control system options that could be considered; however, the procedure developed above will be an important aid in that it can be used to quickly estimate the thermal control system weight for any combination of parameters and thermal control options. Figures D44 thru D50 show examples that were calculated using the procedure developed. It is important to note the following:

1) The results are valid only for the nominal conditions given in the figures;
2) Where overheating occurred the solution was to reduce the insulation thickness only;
3) All points are based on optimized insulation thickness except where it was necessary to reduce the insulation thickness to prevent overheating;
4) The clear day environment (table D5) was used in these examples to check for overheating;
5) The insulation thickness was limited to a maximum of 6 in.

Cruise and Descent Modes

Cruise and descent modes are discussed in the following paragraphs.

Cruise. - The following assumptions are used as a basis for our weight estimates:

1) Cruise mode thermal control for a capsule without RTGs consists of multilayer insulation on the outside of the sterilization canister and thermostatically controlled heaters powered from the orbiter solar cells;
2) A 50 percent margin over test data was used for the multilayer insulation performance to account for material and installation variability;
3) Biovent and other penetration losses are assumed to be proportional to the capsule area;
4) RTGs can be cooled passively during the cruise mode. This concept was proved in full-scale tests conducted by Martin Marietta and reported in reference D4. RTGs with 13 600 W thermal output were tested in a capsule with an area of 750 ft^2.

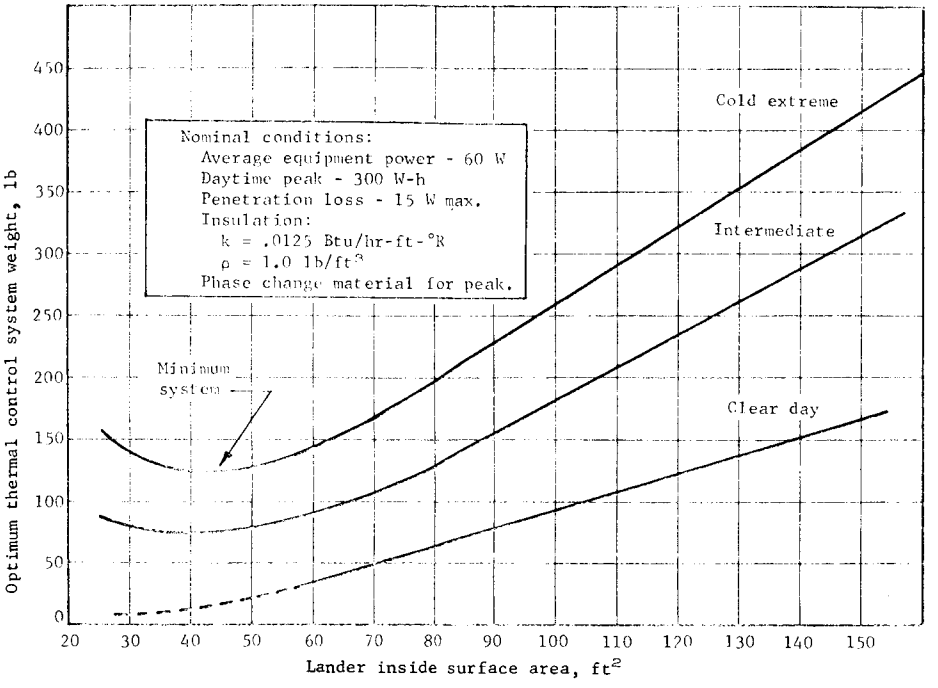

Figure D44. - Thermal Control System Weight versus Lander Size (2-Day Life), Battery Heat Source

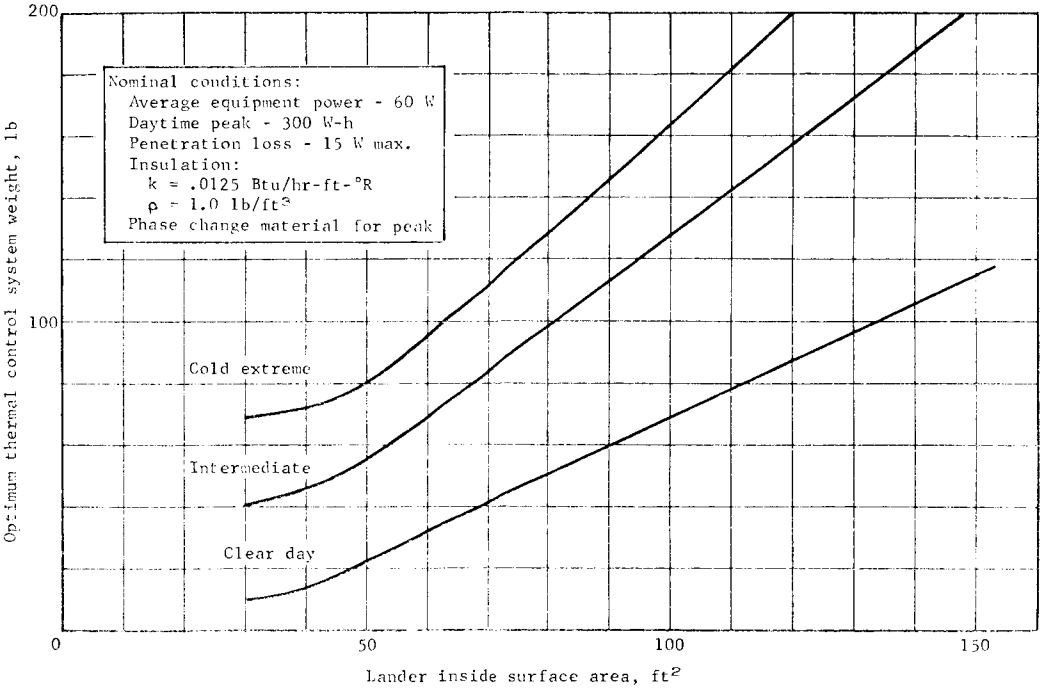

Figure D45.- Thermal Control System Weight versus Lander Size (2-Day Life), Solid Chemical Energy Source

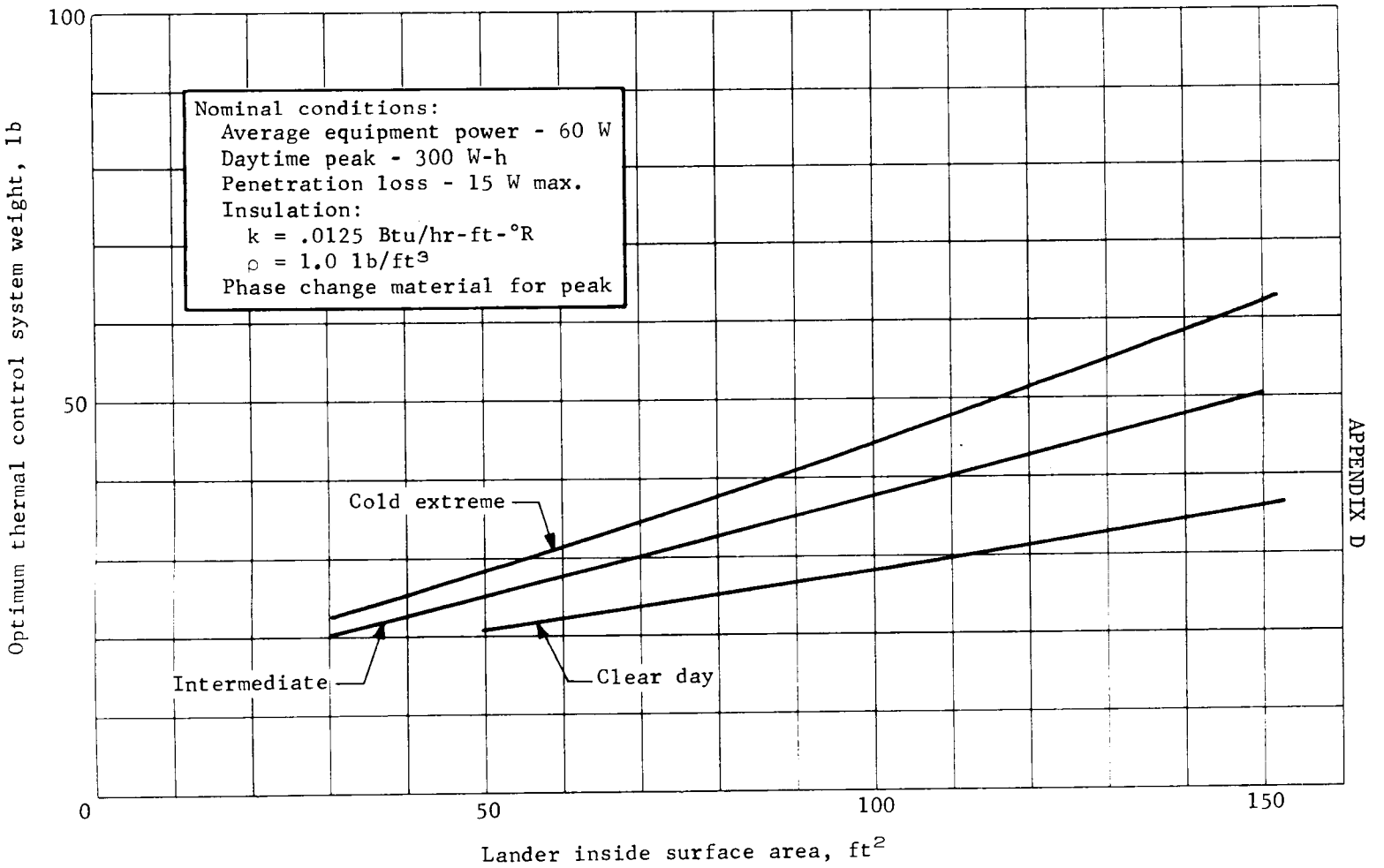

Figure D46.- Thermal Control System Weight versus Lander Size (2-Day Life), Liquid Chemical Energy Source

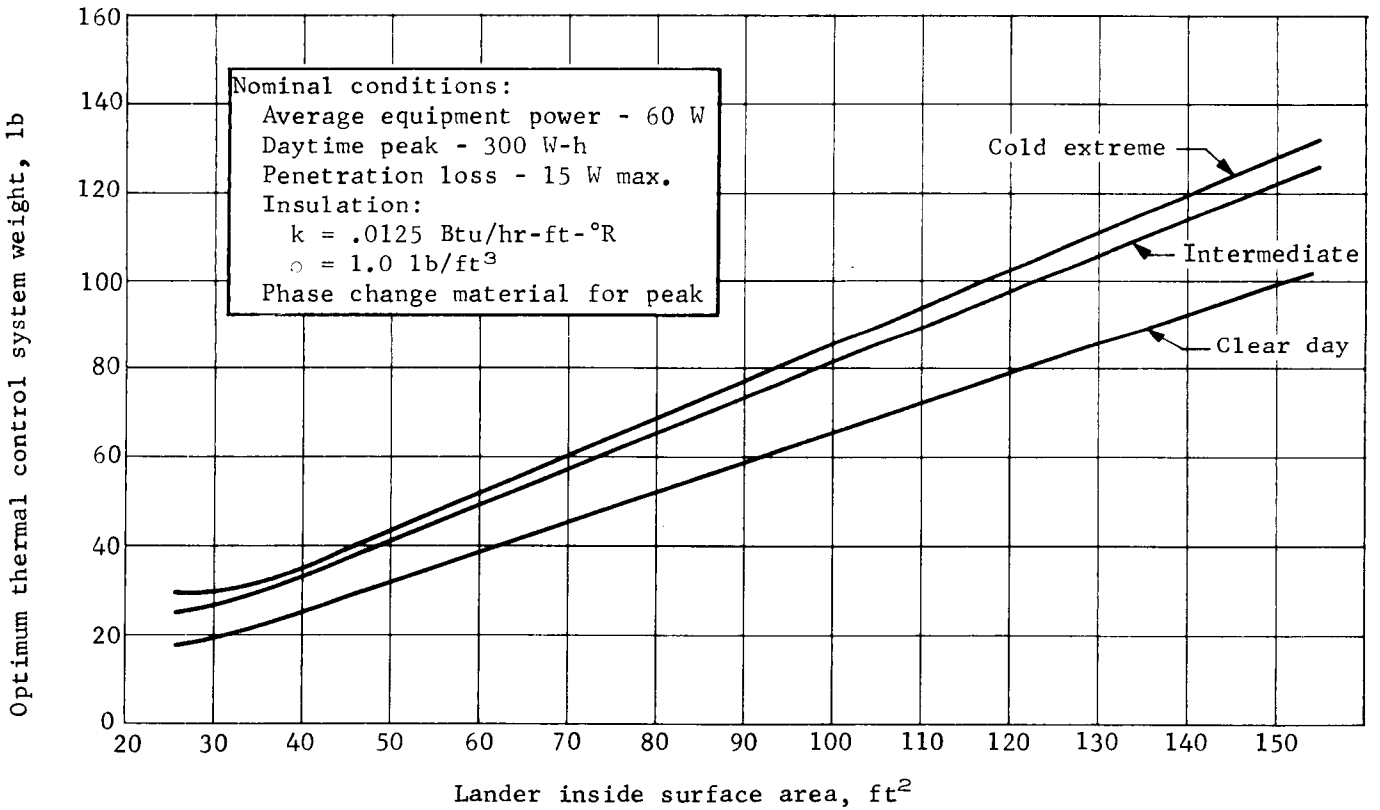

Figure D47. - Thermal Control System Weight versus Lander Size, Radioisotope Heat Source

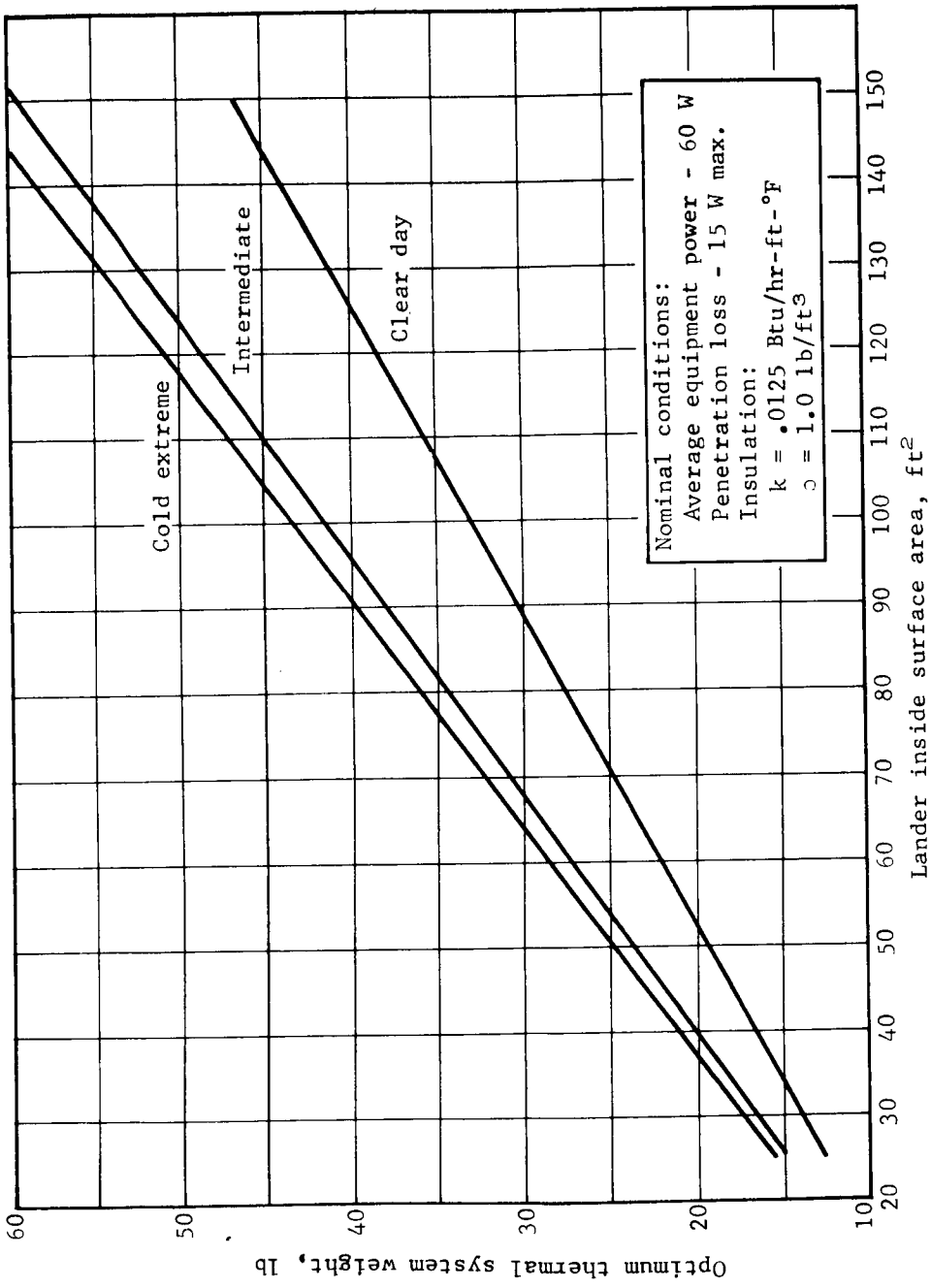

Figure D48. - Thermal Control System Weight versus Lander Size, Heat from RTG by Capillary Pumped Loop

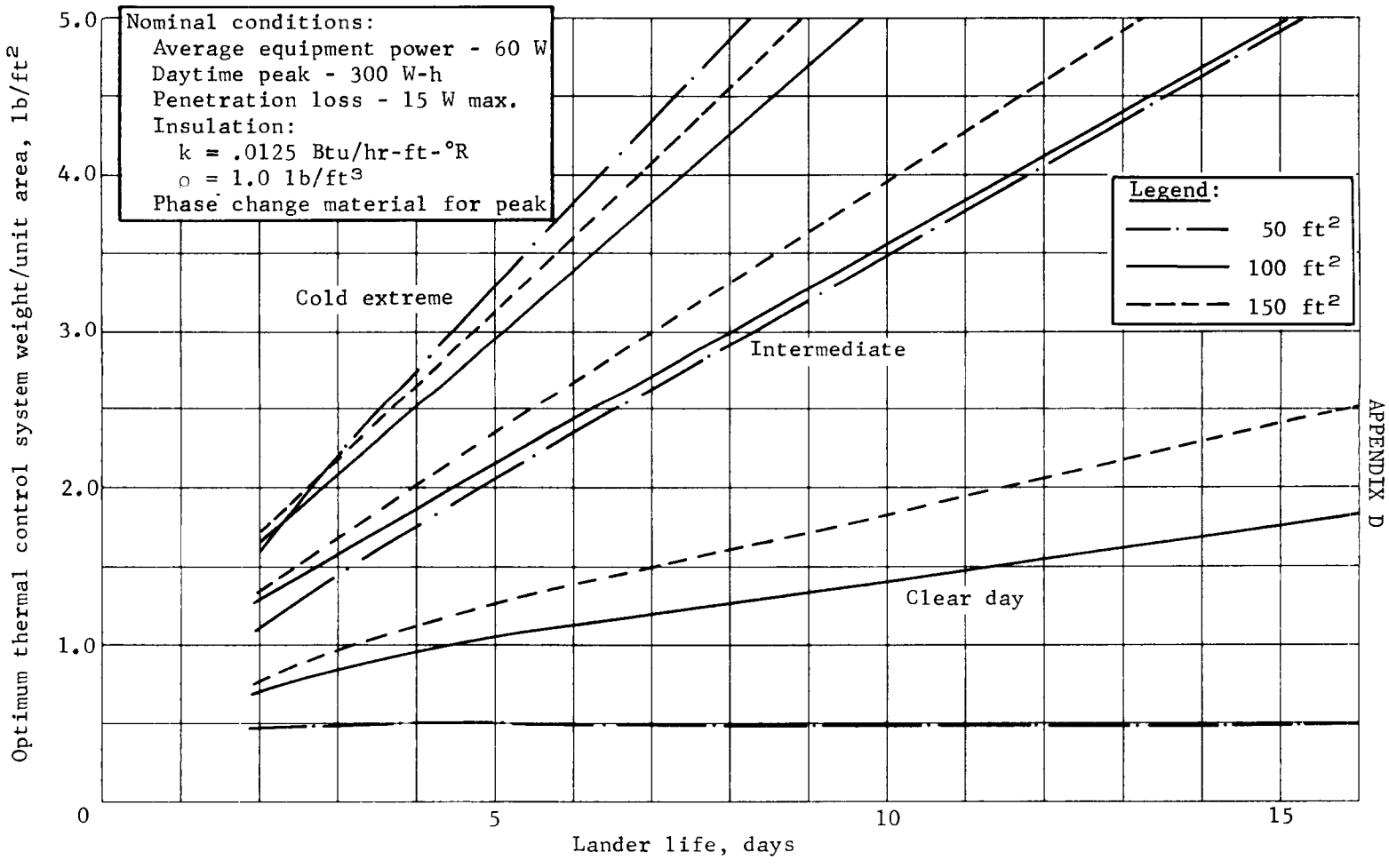

Figure D49.- Thermal Control System Weight versus Lander Life, Solid Chemical Energy Source

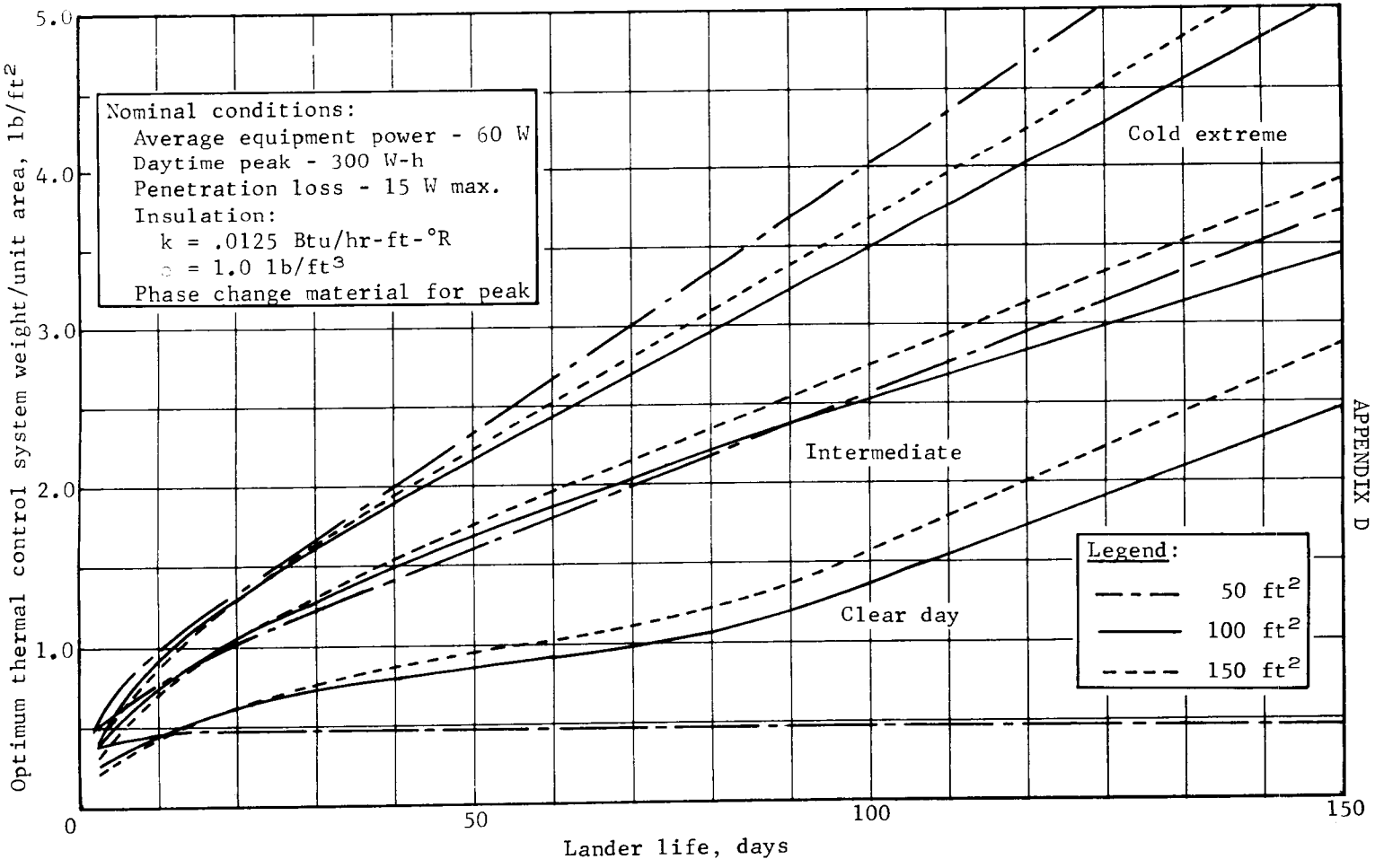

Figure D50.- Thermal Control System Weight versus Lander Life, Liquid Chemical Energy Source

APPENDIX D

Multilayer insulation: The most critical component in the cruise and descent mode design is the multilayer insulation. Full-scale tests of a cruise mode insulation system were conducted by Martin Marietta Corporation (ref. D4). This insulation consisted of 10 layers of ¼-mil Mylar aluminized on both sides with two layers of silk mesh between each shield. The following performance was achieved.

$$q/A = 0.40 \text{ Btu/(hr-ft}^2\text{) at } 55°\text{F}$$

$$\text{Weight } W/A = 0.078 \text{ lb/ft}^2 \text{ (with 2-mil Kapton cover)}$$

In addition, an R&D program was conducted by General Electric on contract to JPL to develop an insulation for this application (see ref. D5). The insulation system developed consists of 22 layers of ¼-mil crinkled Mylar gold plated on one side with a 2-mil Kapton cover. A large number of tests were conducted including ETO and heat sterilization, small-scale thermal tests, including the effects of joints and attachments, shock, vibration and launch depressurization. In addition, full-scale thermal tests were conducted that resulted in performance essentially the same as the Martin Marietta tests.

The penetration losses during the Martin Marietta full-scale tests were 25 percent of the insulation loss. Less penetration loss would be expected in this vehicle because conservatively large biovents (4-1 ft diam) were used in the 750 ft^2 capsule and most of the penetration losses were through these vents. Using these factors and a 50 percent margin for insulation material and installation variability, the heater power required from the orbitor is 0.22 W/ft^2.

Capsule with isotope heaters: In some system designs isotope heaters are used for the lander thermal control. This heat is available for cruise mode thermal control and will reduce the amount of insulation required. In the insulations described above, the cover and attachments weighted 0.02 lb/ft^2 and the shields (and separators) weighed 0.06 lb/ft^2. The insulation weight required for the isotope cases can be approximated as follows:

$$(W/A) = \frac{0.4}{(Q'/A)} \times 0.06 + 0.02$$

where

$$Q' = Q_{IH} - Q_{PL} + Q_{EH}$$

Q_{IH} = output of isotope heaters, Btu/hr

Q_{PL} = penetration losses, Btu/hr

Q_{EH} = electrical heater power, Btu/hr

In the full scale tests conducted by Martin Marietta on a 750 ft^2 capsule the penetration losses were 25-W (85 Btu/hr). Assuming the penetration losses are proportional to the capsule area Q_{PL} can be estimated as follows

$$Q_{PL} = \frac{A}{750} \times 85 \text{ Btu/hr}$$

The electrical heaters (thermostatically controlled) are used to control the capsule temperature which would vary as a result of heat loss unpredictability (primarily through the multilayer insulation). Installed insulation repeatability was not determined in either the General Electric or Martin Marietta tests described above. However, we estimate that the repeatability should be about $\pm$25%. Therefore, Q_{EH} should be equal to 0.25 Q_{IH}.

Capsule with RTGs: Based on assumption 4) above, the only weight that must be added to a capsule with RTGs is for a thermal coating on both the inside and outside of the sterilization canister. Detailed analysis and test results for this approach are presented in references D4 and D6 for a 20-ft-diameter capsule which had a total RTG thermal output up to 13 600 W (500 W electrical). Assuming that the capsule and RTG designs are geometrically similar to those in the references given above, the maximum RTG output allowable would be approximately $(D/20)^2$ (13 600) W thermal and $(D/20)^2$ (500) W electrical.

Descent. - The following assumptions were used as a basis for the weight estimates for the out-of-orbit cases:

1) A passive thermal control system similar to that developed in our Voyager Phase B studies (ref. D6) will be used;

2) The weight estimate is based on the detail weights calculated during our Voyager Phase B studies and are assumed to be proportional to the square of the capsule diameter (i.e., geometric similarity is assumed) except as indicated below.

Voyager Phase B Weights	Weight, lb
1. Engine insulation[a]	10
2. Coatings (on aeroshell)	9
3. Equipment multilayer insulation	7
4. Entry base heating insulation	28
5. Standoffs[a]	2
6. Heaters[a]	1
[a]Independent of capsule size.	

The estimated weights are:

$$\text{Landed equipment weight} = 13 + 35\,(D/19)^2 = 13 + 0.1D^2$$

$$\text{Aeroshell weight} = 9\,(D/19)^2 = 0.025D^2$$

For direct entry cases the same assumptions are made except that a separate entry base heating shield is added to the design. The weight equation for the landed equipment for this case is the same as above except that the entry base heating insulation is not needed since a separate base heating shield is used

$$W = 13 + 7\,(D/19)^2 = 13 + 0.02D^2$$

APPENDIX D

This page intentionally left blank.

APPENDIX D

3. PROPULSION PARAMETRIC DATA AND SUBSYSTEM STUDIES

This section presents the parametric data and analyses performed on the propulsion subsystem in the course of the Mars Mission Mode contract.

These data include propulsion subsystem weight as a function of velocity increment, a comparison of monopropellant and solid deorbit systems, a comparison of blowdown and regulated pressurization systems, and a comparison of monopropellant and nitrogen attitude control systems.

Parametric Data

During Part I of the Mars Mission Mode Study, propulsion subsystem parametric data were generated for the capsule weights and velocity increments considered in the study. Bipropellant, monopropellant, and solid systems were sized for the deorbit, deflection, and retro functions, while bipropellant and monopropellant systems were considered for the landing function. The constraints used in deriving the parametric data are shown in table D8. In figure D51, the solid motor weight for the deorbit, deflection, or retro maneuvers is plotted as a function of total impulse. The range of total impulse covers the range of weight and velocity increment for the deorbit, deflection, and retro maneuvers. Two values of specific impulse were used to allow comparison of aluminized and nonaluminized propellant.

Figure D52 presents propulsion subsystem weight versus total impulse for bipropellant and monopropellant deorbit and direct entry systems. The ranges of ΔV and capsule weight are the same as those used in deriving the solid motor data. Figure D53 is an amplification of the near-origin section of figure D52. The equations used to determine engine weights for the systems presented in figures D53 and D53 were derived from vendor data and are listed below. For monopropellant engines, the following weight equations were used:

1) Conventional engine weight = 0.02875 (thrust) + 14.875;

2) Advanced engine weight = 0.02225 (thrust) + 3.725.

TABLE D8.- CONSTRAINTS

Function	Deorbit and deflection	Retro	Landing	Two-burn retro
Initial weight, lb	500 to 10 000	400 to 8000	300 to 6000	1500 to 6000
Velocity increment	50 to 610 mps	150 to 610 mps	600 to 850 fps	910 to 1530 mps
Initial thrust to weight (Earth)	.05 to 1.5	----	----	25
Blowdown ratio	3:1	3:1	3:1	----
Burntime limits, sec	10 to 180	----	----	----
Bipropellant systems				
I_{sp}, lb_f/lb_m-sec	300	300	285	----
Area ratio	20:1	20:1	20:1	----
Chamber pressure (max.), psia	300	300	300	----
Type of chamber	Ablative	Ablative	Ablative	----
Monopropellant systems				
I_{sp}, lb_f/lb_m-sec	230	230	225	----
Area ratio	20:1	20:1	20:1	----
Chamber pressure, psia	300	300	300	----
Solid motors				
I_{sp}, lb_f-sec/lb_m	250 and 280	250 and 280	----	287.5
Mass fraction	.88	.88	----	----

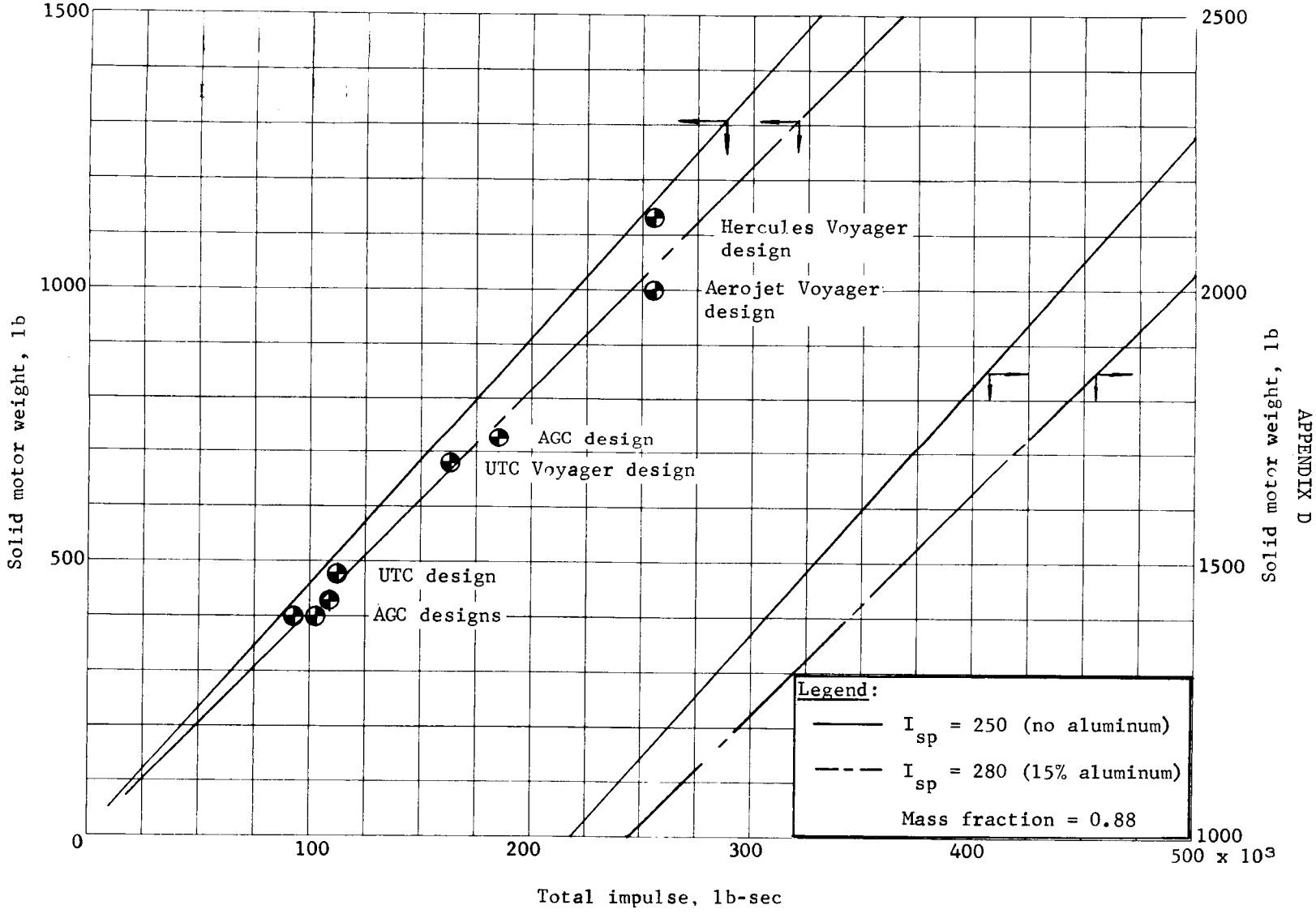

Figure D51.- Solid Motor Weight versus Total Impulse

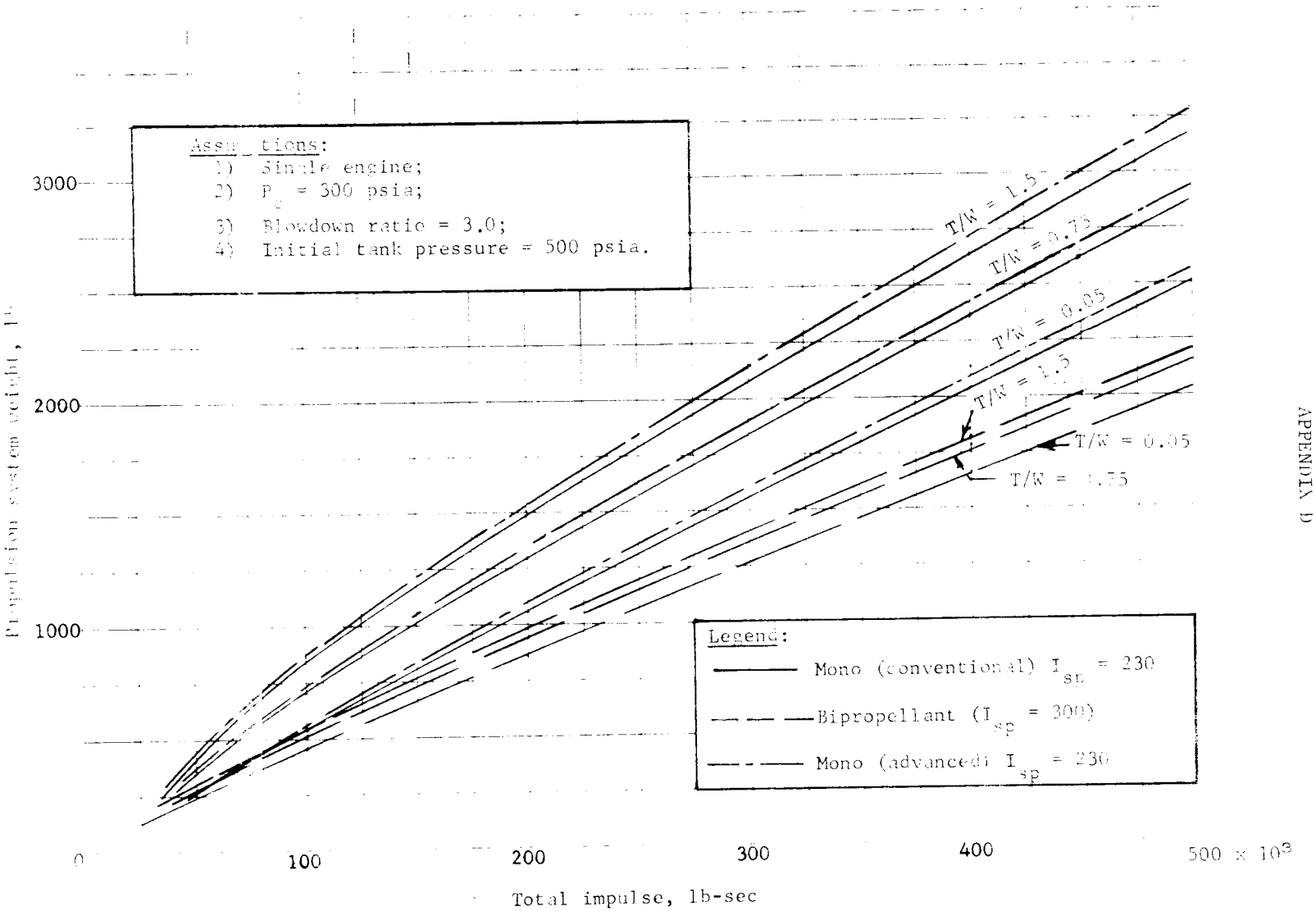

Figure D52.- Deorbit or Deflection Propulsion System Weight versus Total Impulse

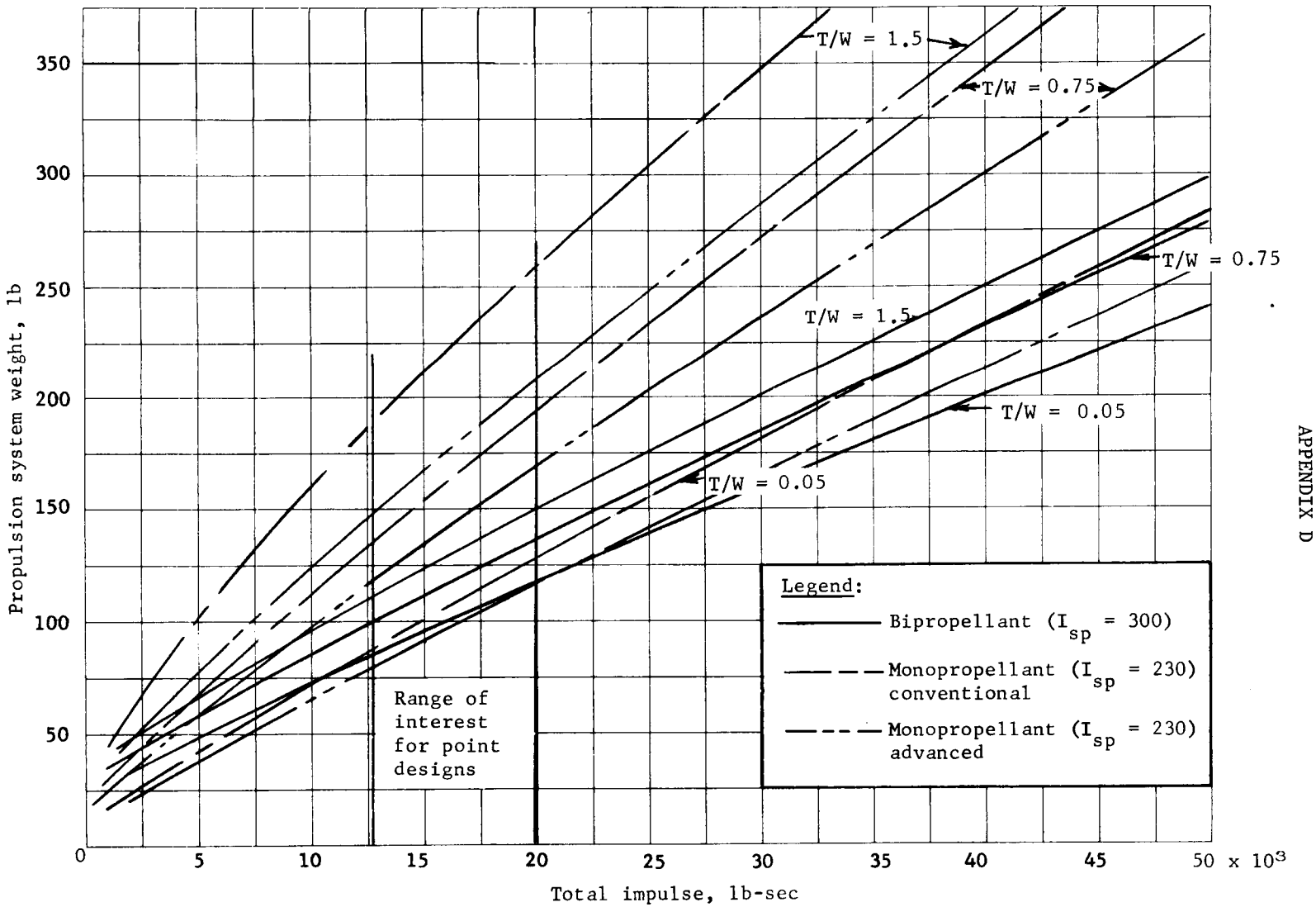

Figure D53.- Deorbit or Deflection Propulsion System Weight versus Total Impulse

APPENDIX D

These relations are based on Rocket Research and TRW data. Figure D54 shows engine weight as a function of thrust for ablative bipropellant engines and a burning time of 100 sec. Figure D55 shows how to adjust figure D54 weights as a function of burntime and the ratio of thrust to chamber pressure. All burntimes in figures D54 and D55 are useful burntimes; a factor of three margin was used between burning time and engine life.

In addition to the rubber engine weights used to calculate figures D52 thru D54, propulsion system weights were determined based on existing engines.

Figure D56 presents propulsion subsystem weight versus total impulse for systems using the Lunar Orbiter and Mariner '69 engines. These systems are most applicable to deflection or low ΔV, low weight deorbit, and retro maneuvers.

Figure D57 presents propulsion system weight versus total impulse for systems using the Lunar Module ascent and descent engines. These data are constrained by the 10-sec minimum burntime limit required by the guidance system and are, therefore, applicable only to missions having high energy requirements.

Figures D58 and D59 present propulsion subsystem weight not including engine and engine support weight versus propellant weight for monopropellant and bipropellant landing and retro systems, respectively. These data are applicable to weights ranging from 300 to 6000 lb and velocity increments of 600 to 850 fps and retro weights ranging from 400 to 8000 lb and velocity increments of 500 to 2000 fps. The deletion of engine weight from these curves permits flexibility in the thrust-to-weight ratio and the number of engines used on a given configuration. By using these equations or curves, the engine weight can be determined. Engine support weight can then be calculated from the following equation:

$$W_{\text{eng supports}} = 0.07\ (\text{thrust})^{2/3}$$

With $W_{\text{eng supports}}$ always ≥ 2.0.

Attitude control system (ACS) parametric data were also generated during Part I. Figure D60 presents attitude control system weight as a function of required ACS total impulse. These data have been generated for the 500- to 10 000-lb range of capsule weight.

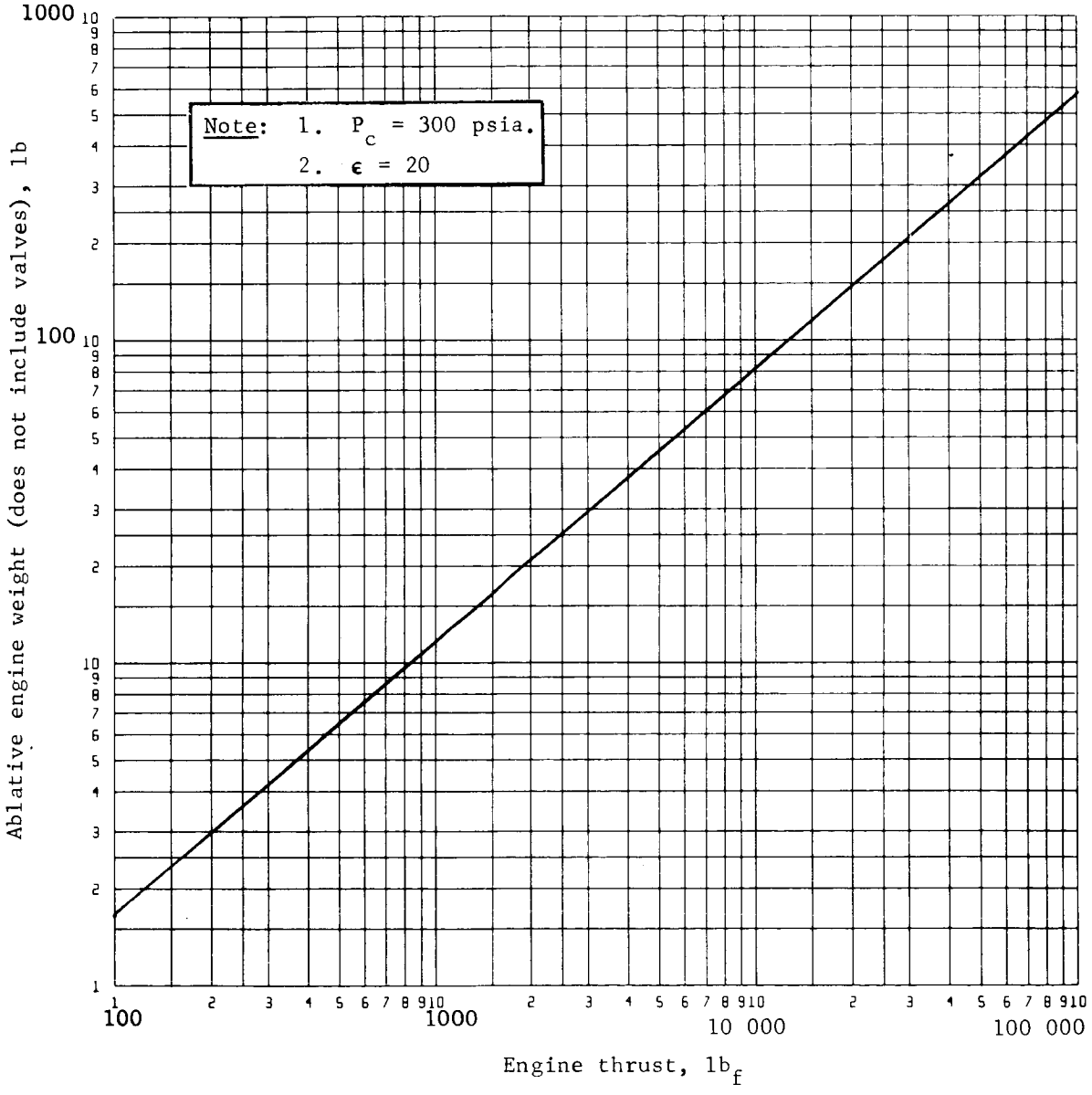

Figure D54.- Engine Weight as a Function of Thrust for Ablative Bipropellant Engine, Burntime = 100 sec

APPENDIX D

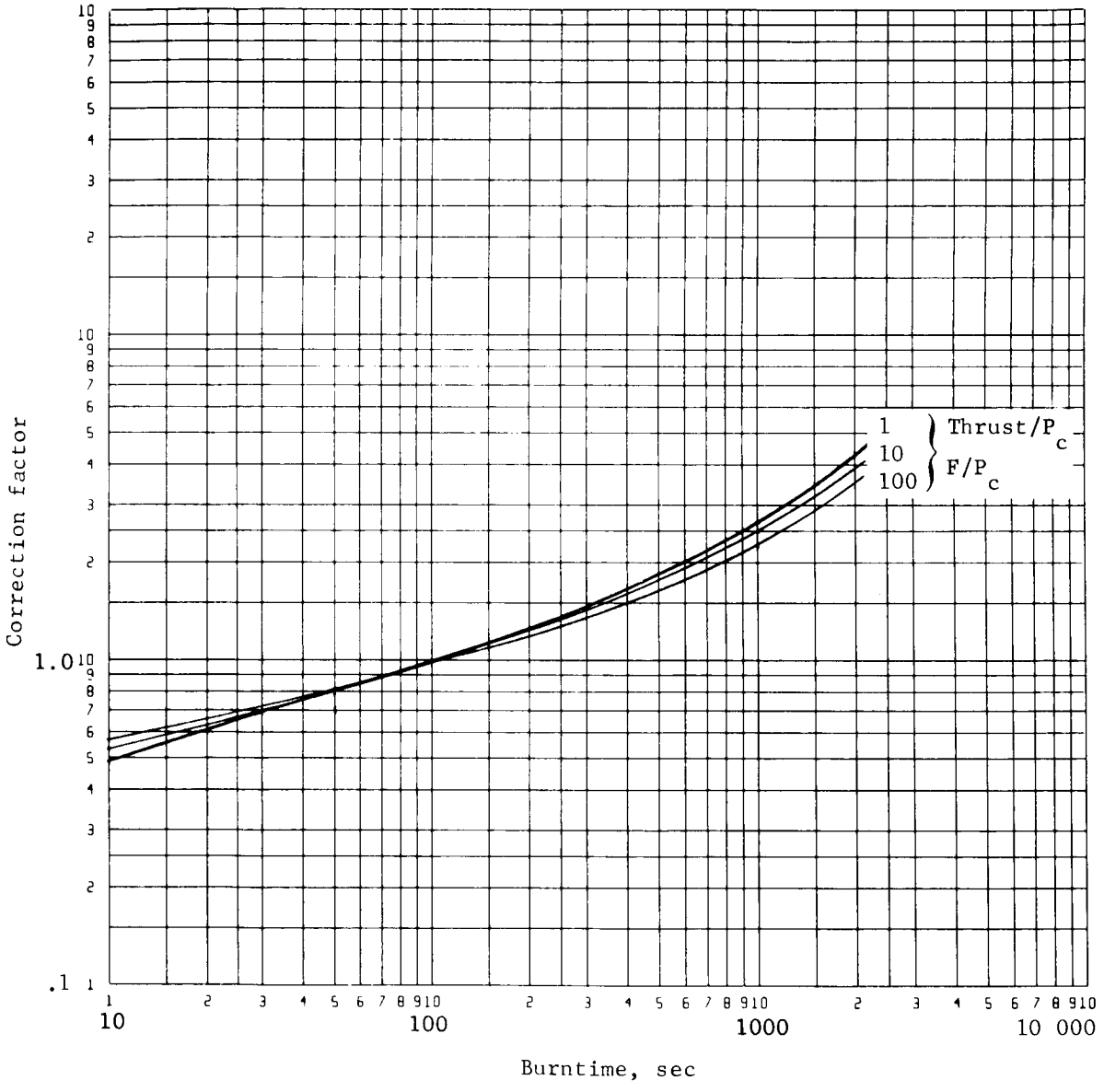

Figure D55.- Correction Factors for Adjusting Figure D54 Weights as a Function of Burntime and Thrust-to-Chamber Pressure Ratio

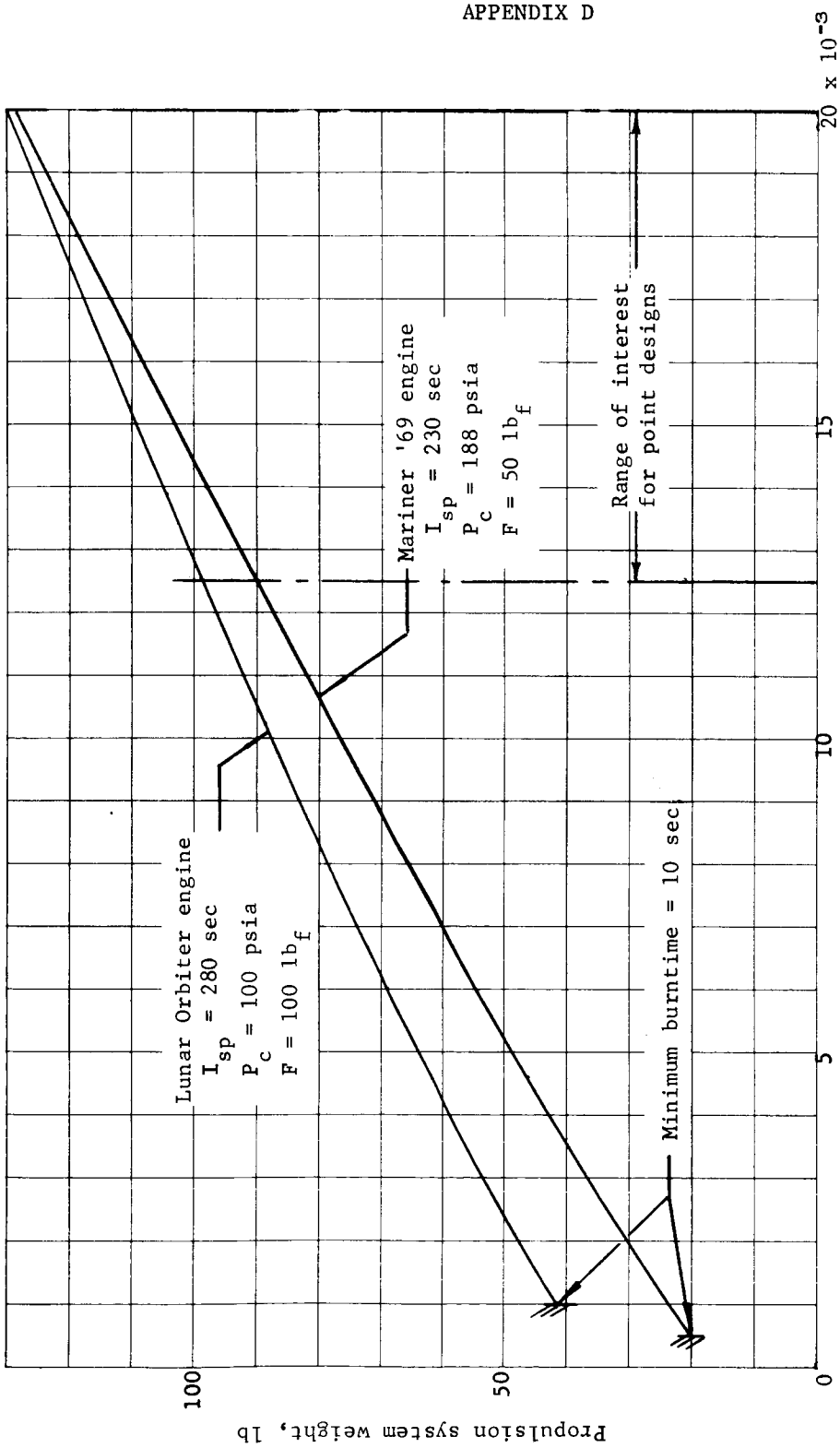

Figure D56.- Deorbit or Deflection Propulsion System Weight versus Total Impulse

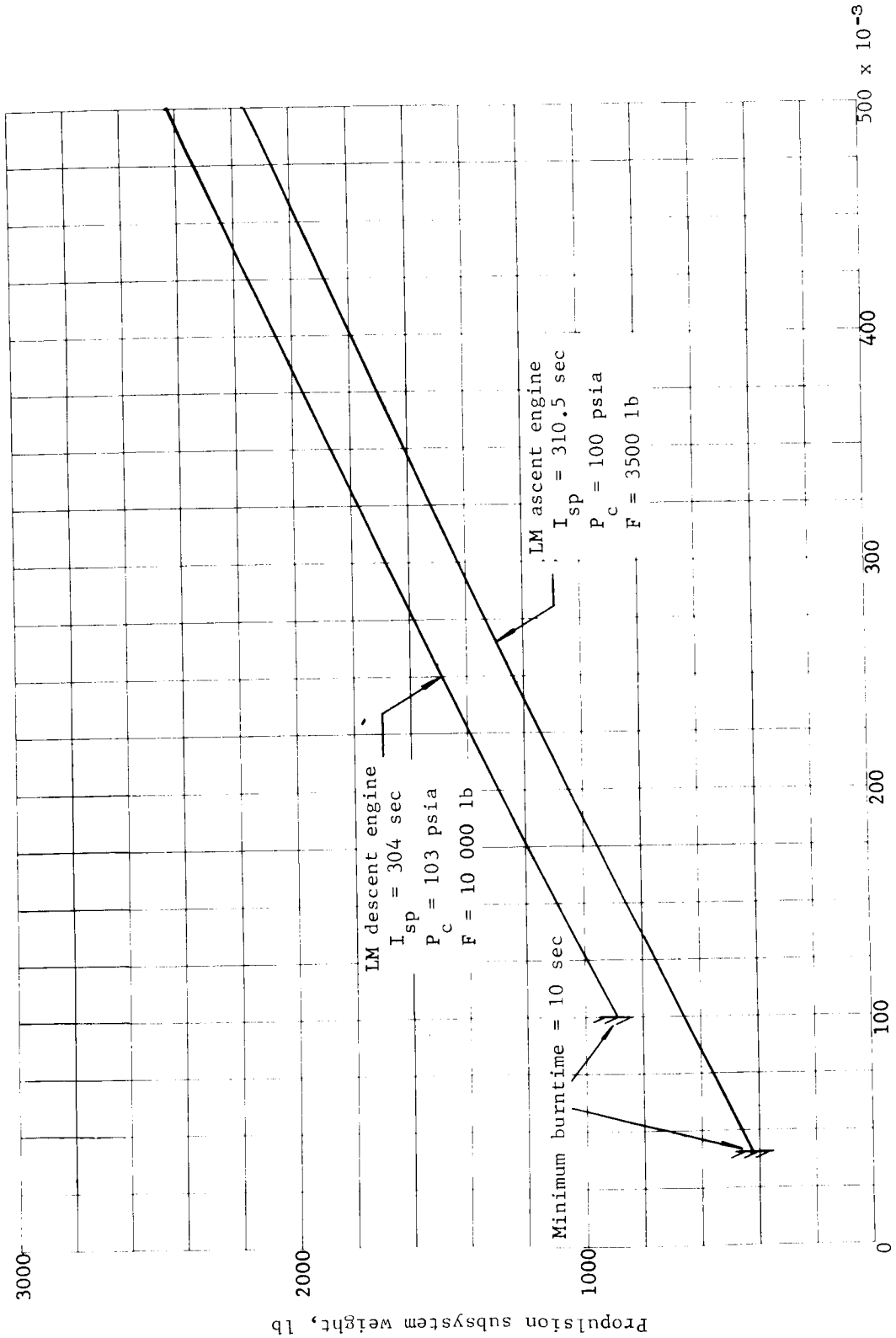

Figure D57.- Deorbit or Deflection Propulsion Subsystem Weight versus Total Impulse

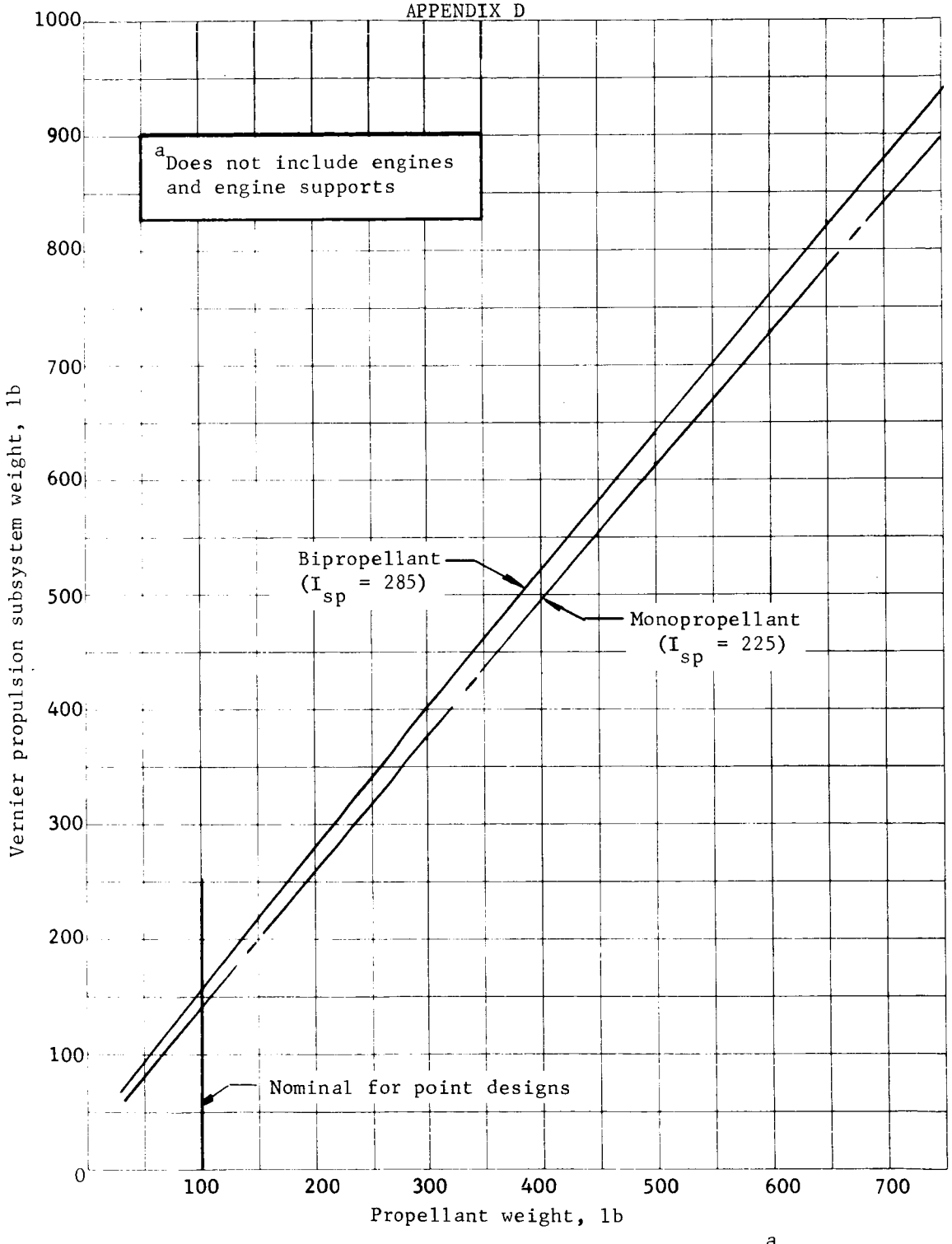

Figure D58.- Vernier Propulsion Subsystem Weight[a] versus Propellant Weight

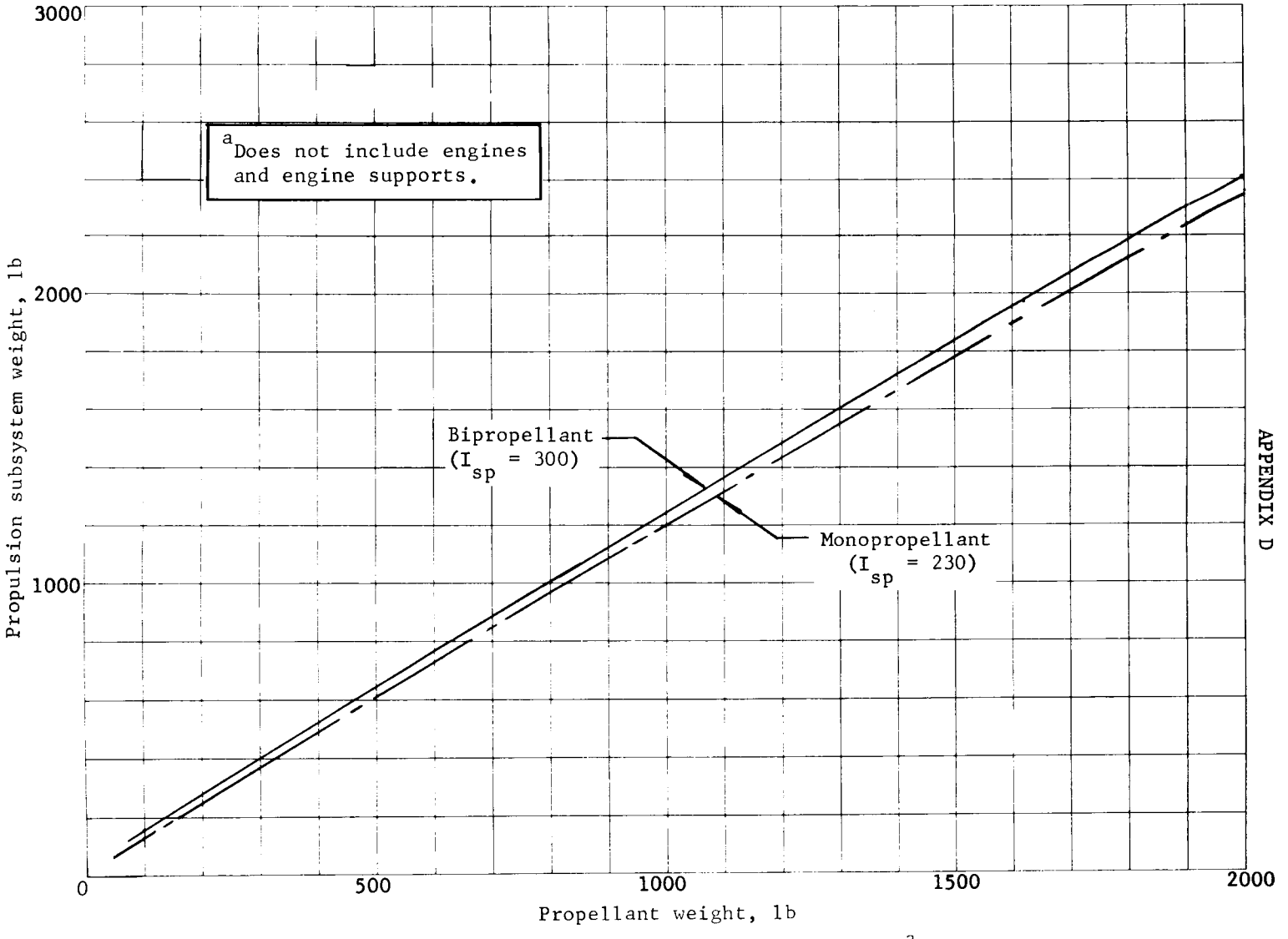

Figure D59.- Retro Propulsion Subsystem Weight[a] versus Propellant Weight

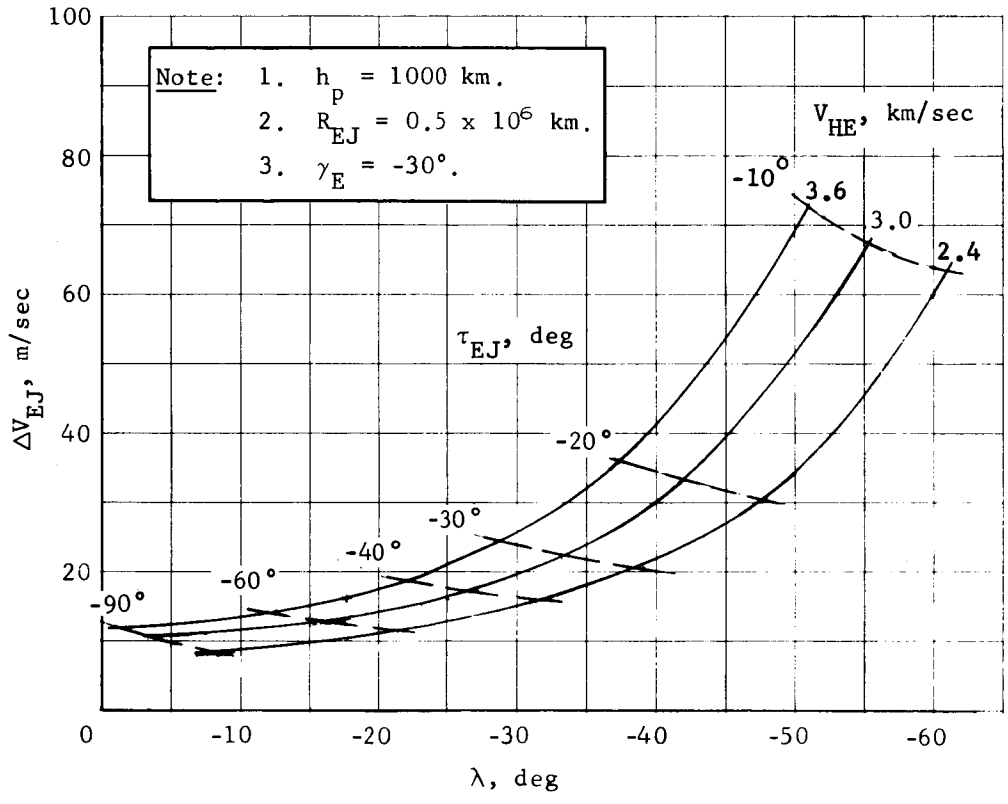

Figure A88.- Ejection ΔV Requirements

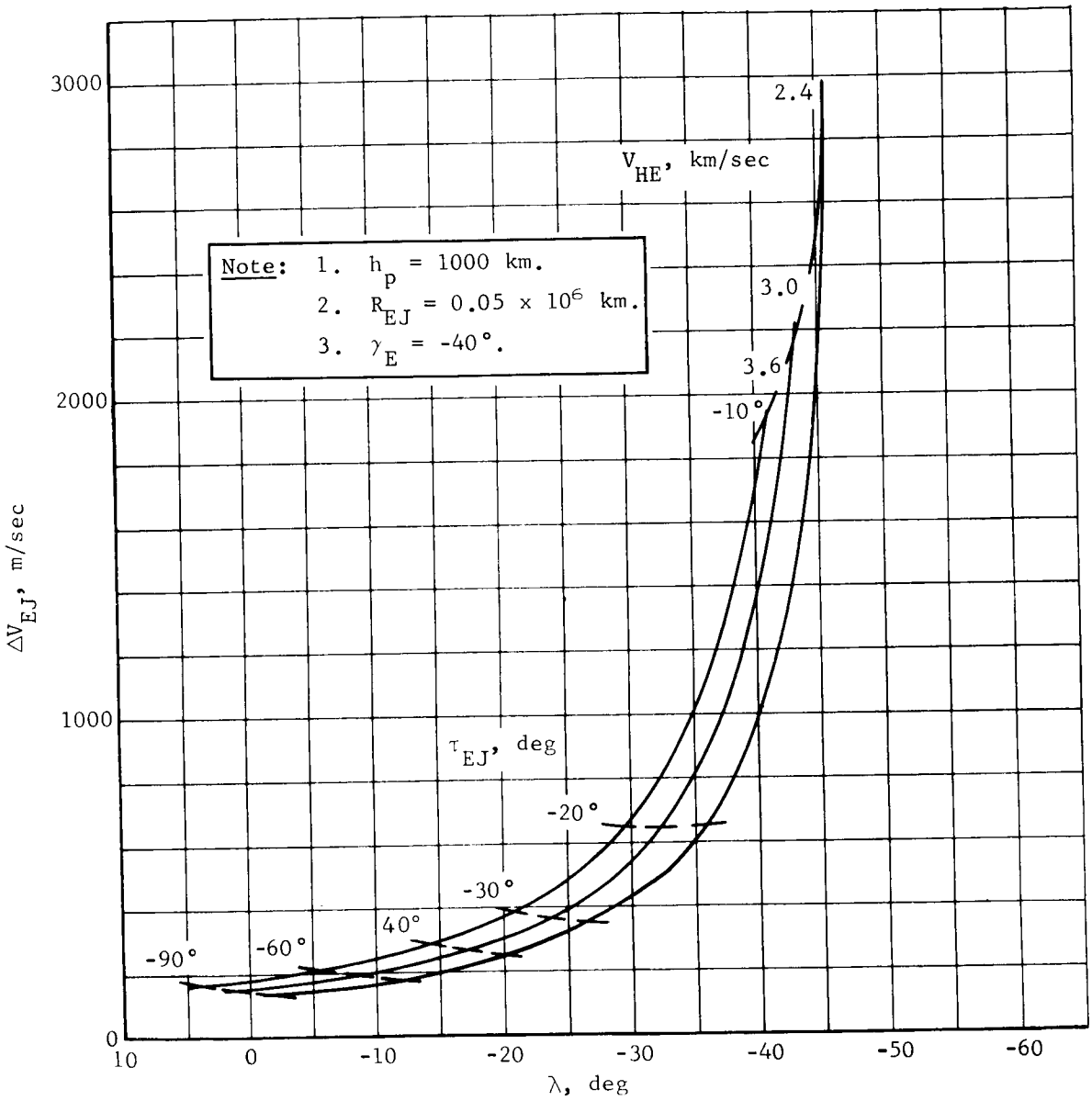

Figure A89.- Ejection ΔV Requirements

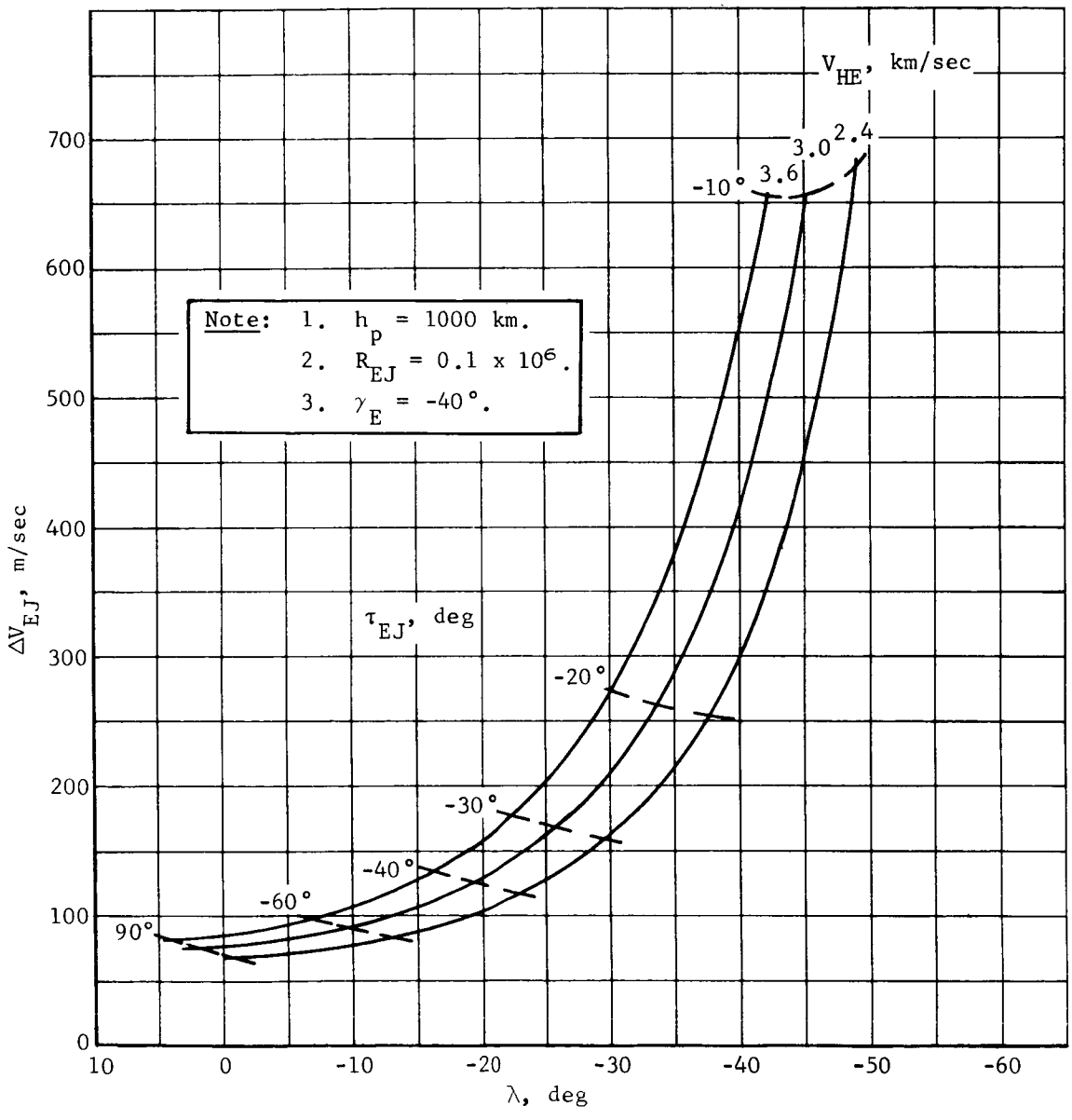

Figure A90.- Ejection ΔV Requirements

APPENDIX A

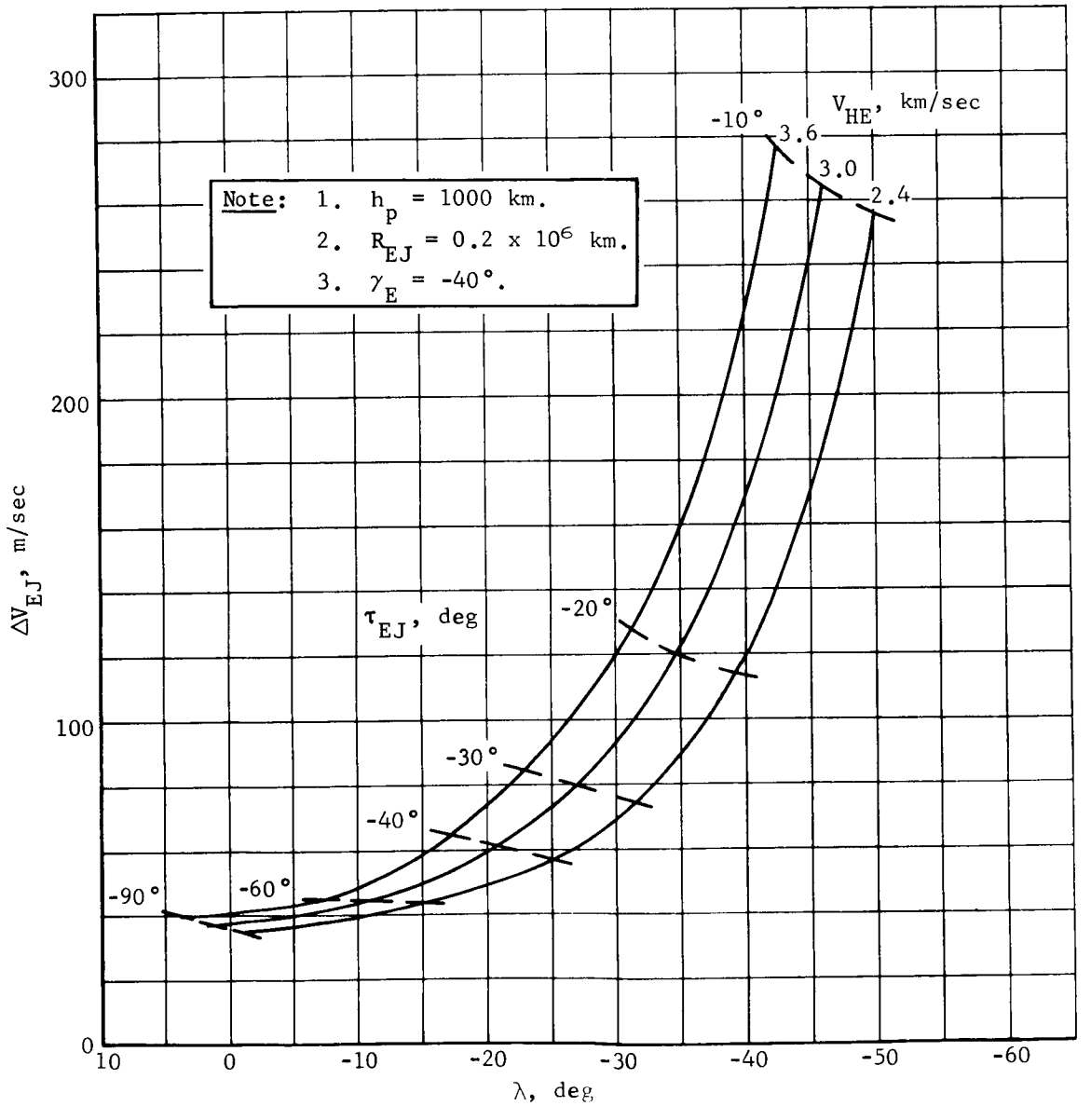

Figure A91.- Ejection ΔV Requirements

b) Solid rocket motor

1 motor,

I_{sp} = 280 sec (aluminized propellant),

Mass fraction = 0.85;

2) Deflection - same as deorbit;

3) Vernier, monopropellant,

a) 3 engines,

b) $T/W_{initial}$ (Mars) = 3.3,

c) Blowdown pressurization (BDR = 3.0),

d) $I_{sp_{av}}$ = 225 sec,

e) ϵ = 20:1,

f) Initial tank pressure = 500 psia,

g) P_c = 300 psia,

h) $T/W_{initial}$ (Mars) = 0.8.

Table D9 presents a weight comparison of the two configurations with solid and monopropellant deorbit or deflection systems. These data indicate that a gain in landed equipment weight of 48.5 and 41.5 lb is achievable by using a solid motor for the deorbit or deflection functions.

The data in table D9 account for growth in the delivery elements that are produced by the increase in entry weight for the solid systems. Changes in aeroshell, parachute, vernier propulsion subsystem, and landing structure are shown in the table. Entry ballistic coefficient $\left(B_e\right)$ was held constant to maintain the same descent trajectory when comparing the configurations.

TABLE D9.- WEIGHT STATEMENTS

Item	Weight, lb			
	Configuration 1, monopropellant deorbit	Configuration 1, SRM deorbit	Configuration 1, monopropellant deflection	Configuration 2, SRM deflection
Capsule system	1668.0	1668.0	1963.0	1963.0
Adapter and canister	152.0	172.0	202.0	222.0
Separated weight	1516.0	1496.0	1761.0	1741.0
Deorbit or deflection propellant module	176.0	86.0	151.0	63.0
Entry weight	1340.0 (B_e = 0.445)	1410.0 (B_e = 0.445)	1610.0 (B_e = 0.351)	1678.0 (B_e = 0.351)
Aeroshell	137.0 (D = 8.5 ft)	142.0 (D = 8.7 ft)	250.0 (D = 10.5 ft)	259.0 (D = 10.7 ft)
Backface heat shield	----	----	45.0	45.0
Parachute	105.0 (D = 64 ft)	111.0 (D = 66.5 ft)	155.0 (D = 70 ft)	161.0 (D = 72 ft)
Verniered weight	1098.0	1157.0	1160.0	1213.0
Vernier propellant	100.0	106.0	105.0	111.0
ACS propellant	2.0	2.0	2.0	2.0
Landed weight	996.0	1049.0	1053.0	1100.0
Nonusable landed weight	400.0	405.5	462.0	467.5
Propulsion	(100.0)	(104.5)	(101.0)	(105.5)
ACS	(34.0)	(34.0)	(30.0)	(30.0)
Telecommunications	(17.0)	(17.0)	(17.0)	(17.0)
Thermal control	(20.0)	(20.0)	(15.0)	(15.0)
Pyrotechnics	(49.0)	(49.0)	(49.0)	(49.0)
Structure	(180.0)	(181.0)	(250.0)	(251.0)
Available for landed equipment	596.0	644.5	591.0	632.5

APPENDIX D

Comparison of Regulated and Blowdown Pressurization

An analysis was performed to determine the mode of pressurization for an out-of-orbit Mars soft lander. The results of this analysis indicate that from a weight and reliability standpoint, a blowdown system is preferred when compared to a regulated system.

The following configuration was considered in this study:

1) Initial capsule weight = 1500 lb;
2) Deorbit weight = 1365 lb;
3) Deorbit velocity increment = 300 mps;
4) Vernier weight = 1040 lb;
5) Vernier velocity increment = 724 fps;
6) Monopropellant (N_2H_4) propulsion subsystem;
7) Gaseous nitrogen pressurization;
8) One engine for deorbit, three engines for vernier;
9) Landing engine used as the deorbit engine.

This configuration is representative of those considered in the Mars Mission Modes Study. The net landed useful payload is approximately 500 lb. The deorbit and vernier velocity are taken from the mission modes data and represent the maximum for each phase of the mission.

To determine the engine size for the vernier system, the thrust-to-weight ratio (T/W) as a function of blowdown ratio must be derived. Figure D62 presents the relationship of T/W and vernier initial altitude for a constant thrust descent (regulated system) where initial altitude is defined as the point at which the lander is released from the parachute. Figure D63 shows the percentage of initial thrust remaining at the end of blowdown versus blowdown ratio.

To determine the initial T/W required for the blowdown systems, the T/W was adjusted to compensate for the average thrust during blowdown.

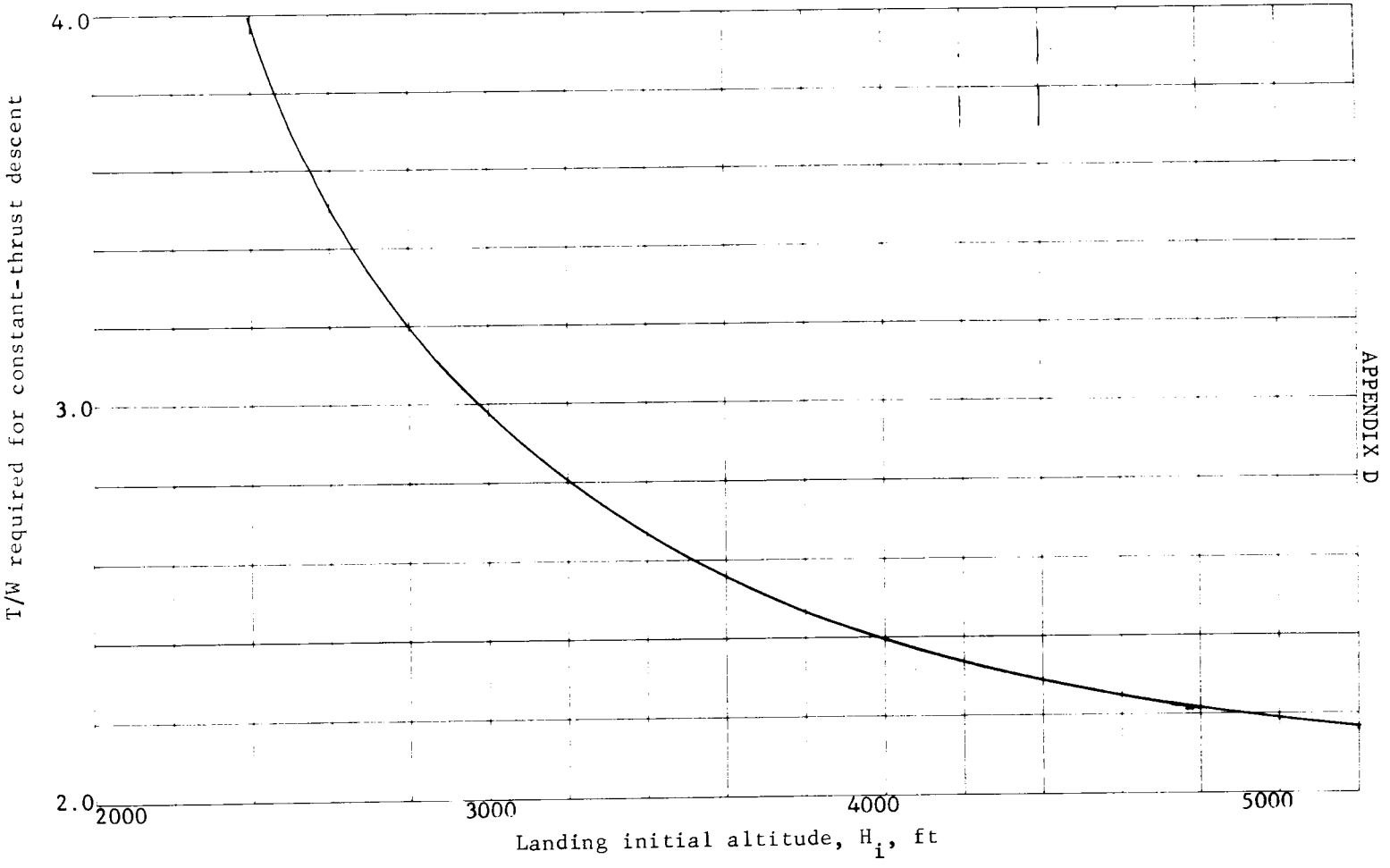

Figure D62.- T/W Required versus Initial Altitude

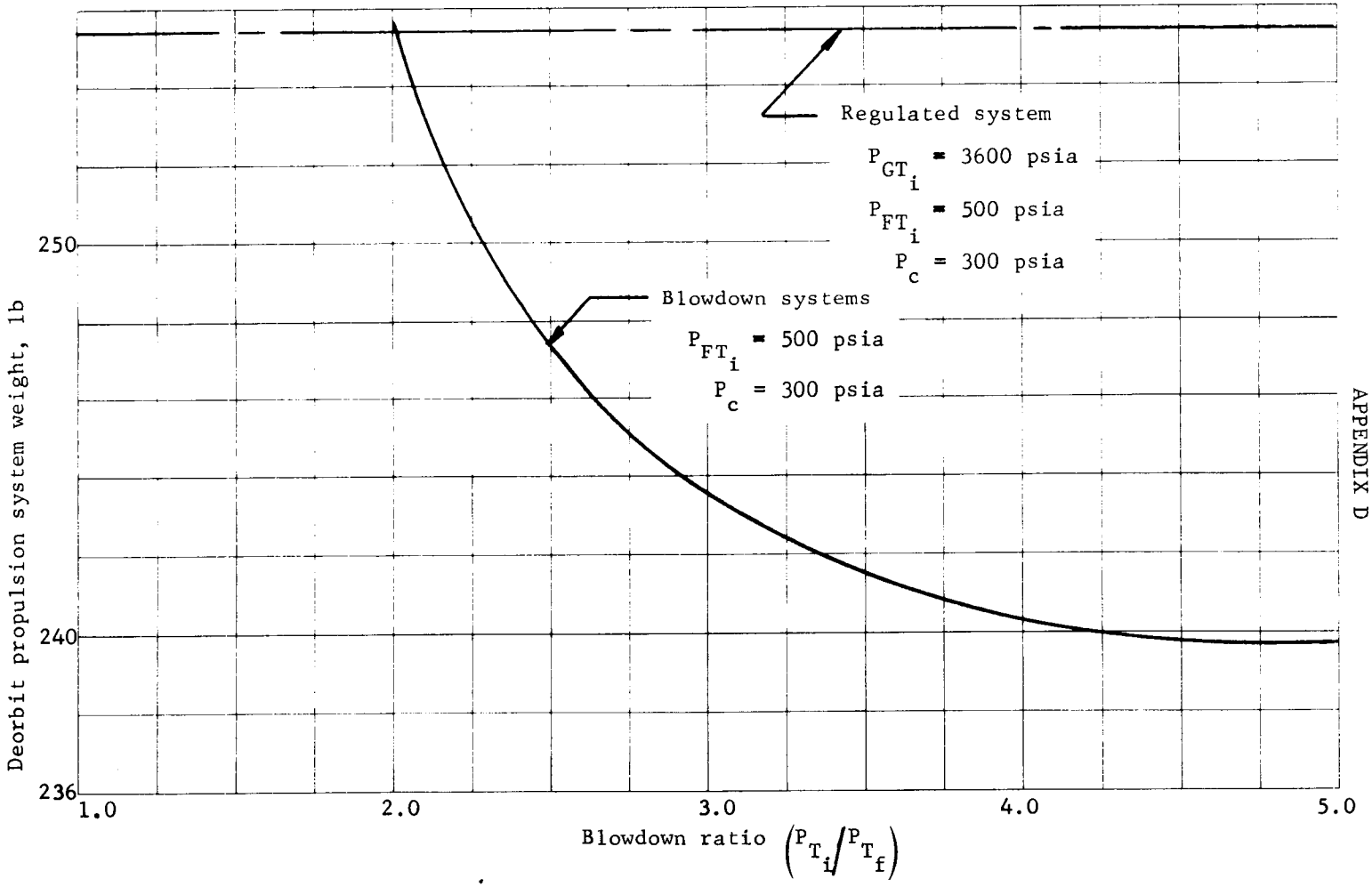

Figure D63.- Deorbit Propulsion System Weight versus Blowdown Ratio

APPENDIX D

The thrust to weight versus blowdown ratio data are presented in figure D64. Figure D64 was used to determine the maximum vernier engine thrust for the various blowdown ratios. The same thrust was then used to provide the deorbit impulse, thereby maintaining the concept of similar engines for deorbit and landing.

Figure D65 presents deorbit propulsion subsystem weight versus blowdown ratio. These data indicate that blowdown systems are lighter than the regulated system. This penalty is produced by the additional components and pressurant required for the regulated system.

Figure D66 presents the same data for the vernier propulsion subsystem. These data indicate that a blowdown ratio 3 is optimum, although the weight differentials are small. This curve reflects the effect of engine weight on total systems weight. Figure D67 is a summation of figures D65 and D66.

Point designs having the characteristics tabulated below were analyzed to show the origin of these weight differences:

Regulated system	
Pressurant tank pressure, psia	3600
Propellant tank pressure, psia	500
Chamber pressure, psia	300
I_{sp}, deorbit, sec	230
I_{sp}, vernier, sec	225
Blowdown system	
Pressurant tank initial pressure, psia	500
Propellant tank initial pressure, psia	500
Chamber pressure, psia	300
I_{sp}, deorbit, sec	228
I_{sp}, vernier, sec	225
Blowdown ratio	3:1
General	
Deorbit velocity increment, mps	300
Vernier velocity increment, fps	724

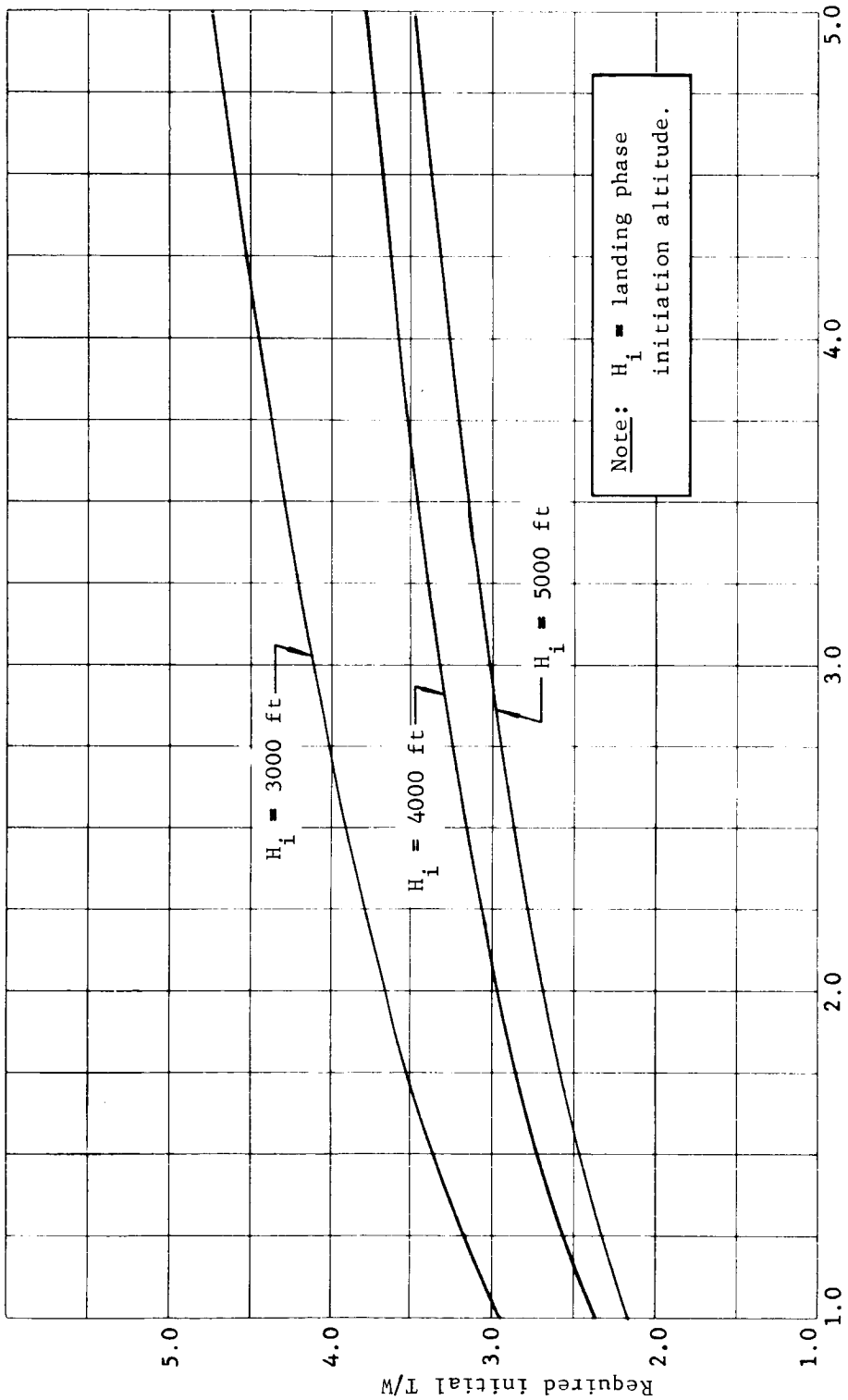

Figure D64.- Required T/W versus Blowdown Ratio

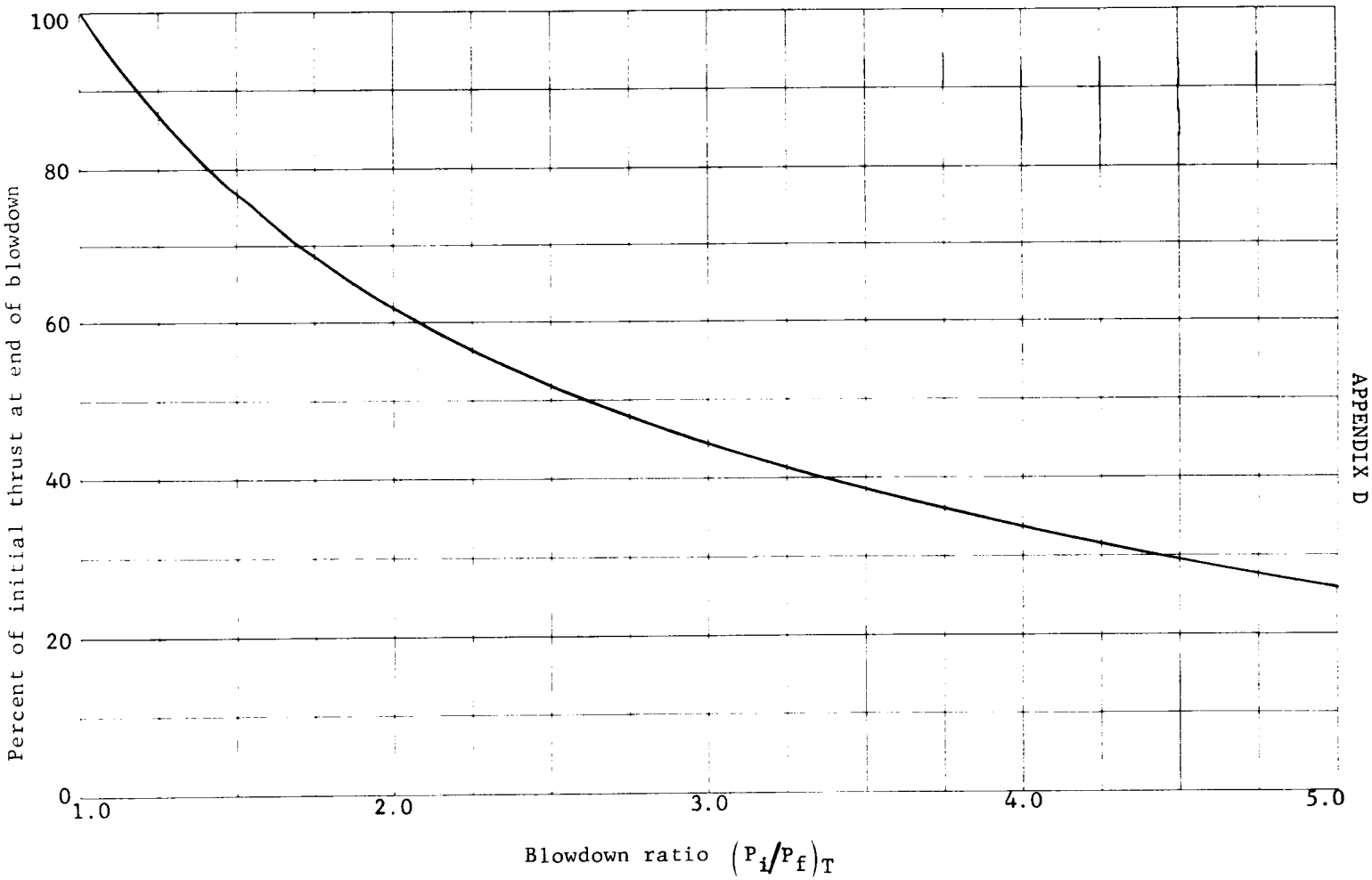

Figure D65.- Percent of Initial Thrust at End of Blowdown versus Blowdown Ratio

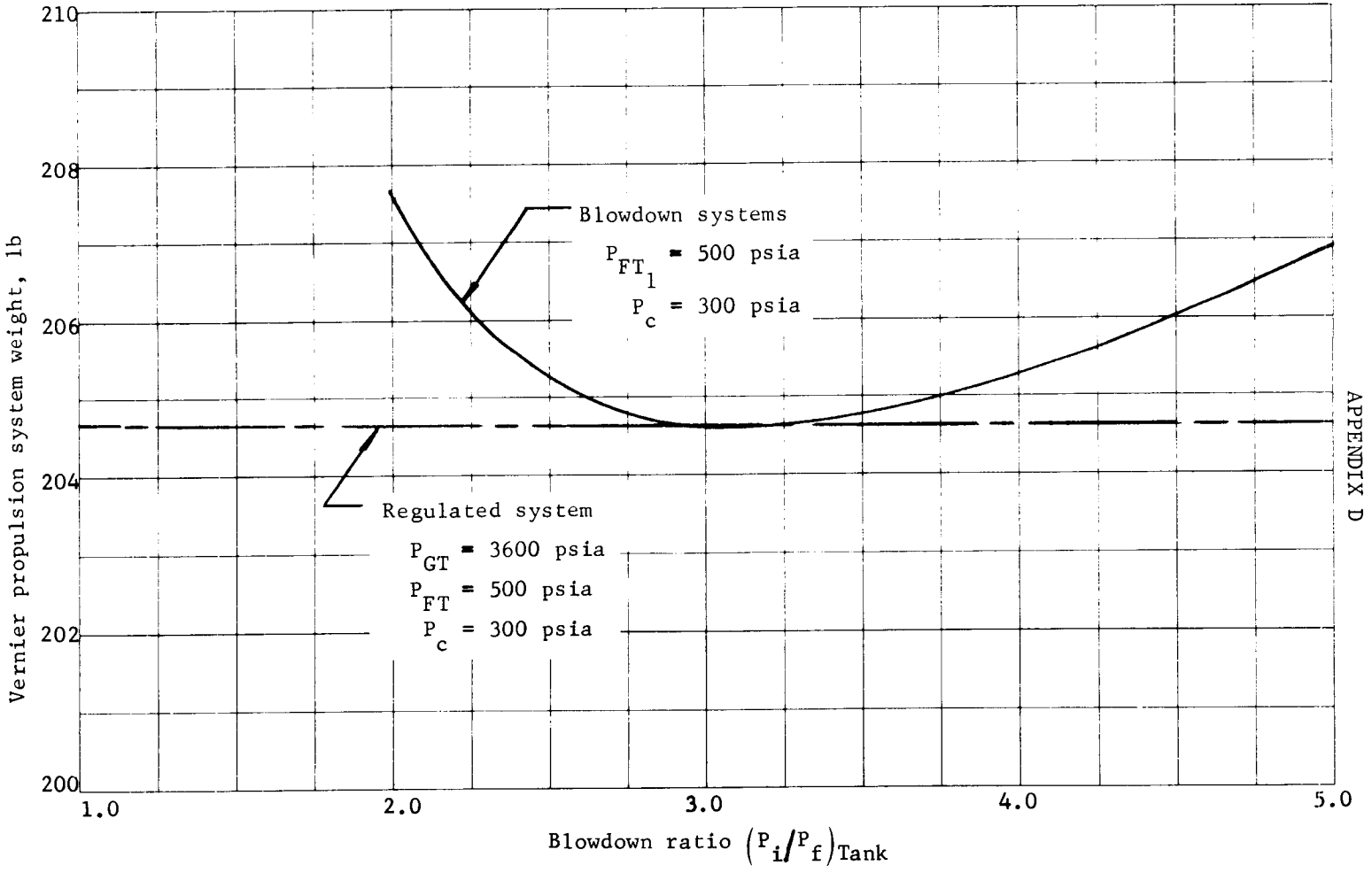

Figure D66.- Vernier Propulsion System Weight versus Blowdown Ratio

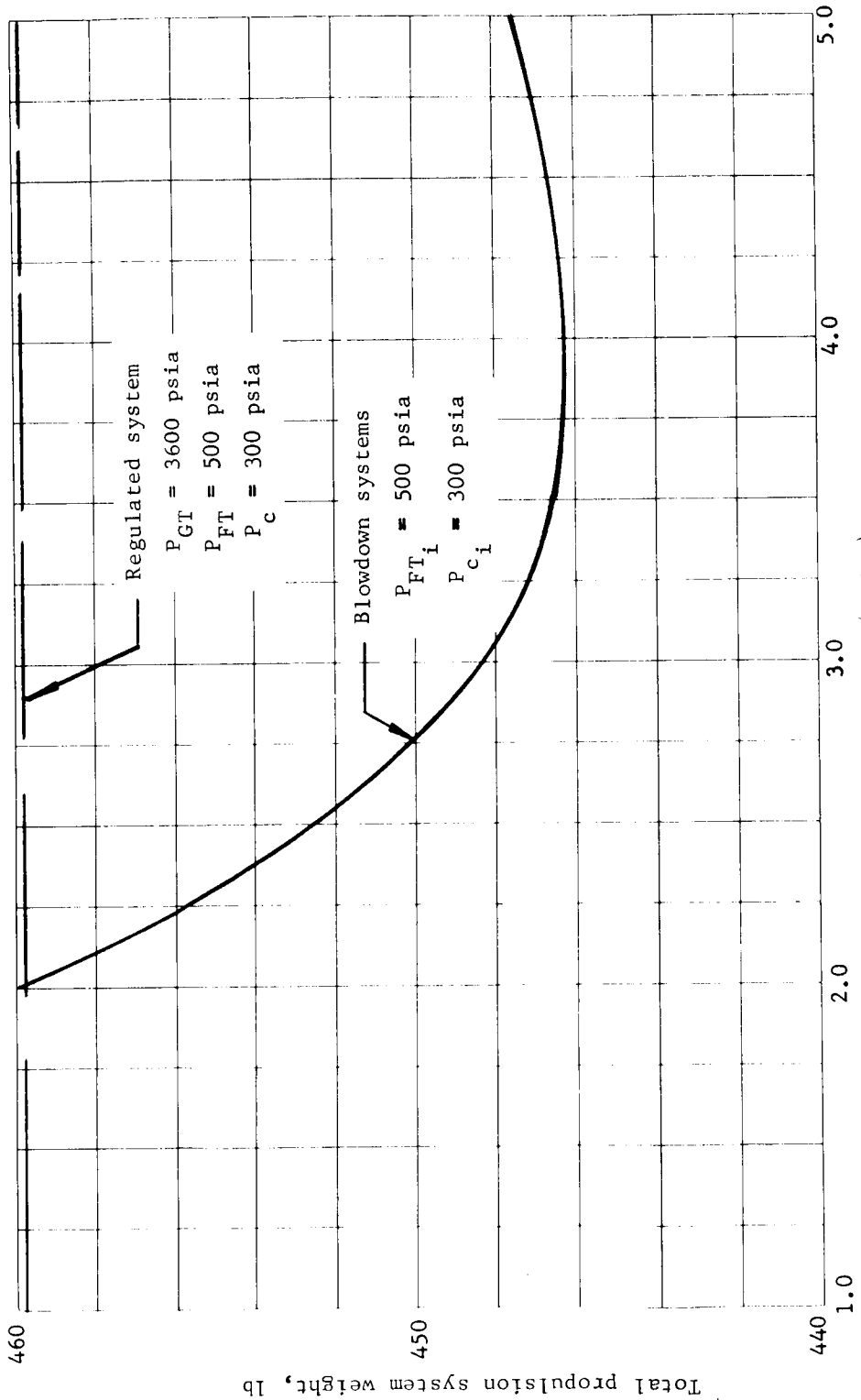

Figure D67.- Total Propulsion System Weight versus Blowdown Ratio

APPENDIX D

The weights for these systems are shown in table D10, which shows that the weight advantage of the blowdown system comes from the more efficient use of pressurizing gas and reduced number of components. These savings essentially compensate for the larger and heavier engine required for the blowdown systems.

The blowdown system has an undeniable reliability advantage that results from the reduced number of active components. Our estimate of this reliability advantage is shown in figure D68. The failure rate data are based on the assumption that 25% of the regulator failures cannot be prevented by redundancy, i.e., contamination failures and cross talk.

This study shows both a reliability and a weight advantage for the blowdown system; the system is therefore preferred.

TABLE D10.- REGULATED AND 3:1 BLOWDOWN SYSTEM WEIGHTS

Item	Regulated		3:1 Blowdown	
Deorbit				
Propellant		178.5		180.0
Usable	170.0		171.4	
Trapped	8.5		8.6	
Propellant tanks		7.8		7.8
Pressurant (GN_2)		10.2		4.6
Pressurant tanks		13.2		6.0
Engine (1)		12.6		15.7
Components, lines		16.3		13.0
Engine mount, supports		16.8		16.3
Total wet weight		255.4		243.6
Vernier				
Propellant		103.9		104.8
Usable	99.0		99.8	
Trapped	4.9		5.0	
Propellant tanks		5.4		5.4
Pressurant		5.9		2.7
Pressurant tanks		7.7		3.5
Engines (3)		37.8		47.1
Components, lines		21.6		18.3
Engine mounts, supports		22.2		22.8
Total wet weight		204.5		204.6
Total deorbit and vernier system weight		459.9		448.2

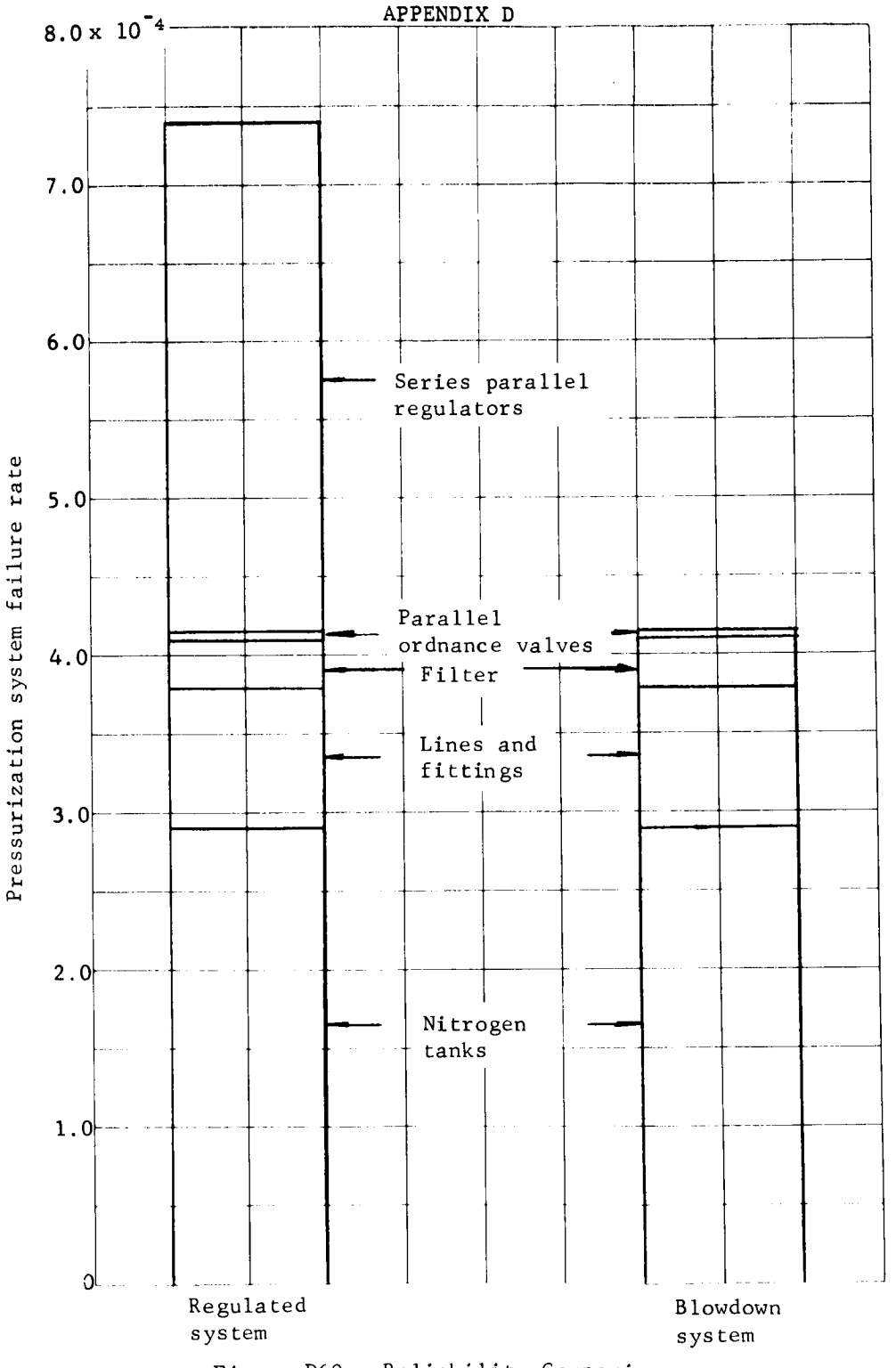

Figure D68.- Reliability Comparison

APPENDIX D

Comparison of Hydrazine and Nitrogen Attitude Control Subsystems

The purpose of this study is to compare monopropellant hydrazine and cold gas (N_2) attitude control systems for the Mars Mission Modes point designs. The characteristics of the two systems compared are tabulated below:

Item	N_2H_4 system	N_2 system
I_{sp} (pulse mode), sec	150	50
P_c (maximum), psia	200	200
Fuel tank pressure (maximum), psia	360	----
N_2 tank pressure (maximum), psia	361	3600
Pressurization	1.5:1 blowdown	Regulation
Thrust, lb		
Pitch, yaw	2.4	2.4
Roll	3.2	3.2

To determine the ACS weight, the following propellant utilization schedule was used. This schedule is representative of the propellant required for the out of orbit mission mode.

Item	Total impulse required (lb-sec)	$(I_{sp} = 150)$ $N_2H_4{}_{req}$	$(I_{sp} = 50)$ $N_2{}_{req}$
Separate from capsule	2.5	0.02	0.05
Coast, 30 minutes	11.9	0.08	0.24
Maneuver for deorbit thrust	4.6	0.03	0.09
Deorbit thrust attitude hold	176.0	1.17	3.52
Coast, 8 hr	10.8	0.07	0.22
Maneuver for entry	4.2	0.03	0.08
Coast, 4 minutes	1.8	0.01	0.04
Rate damping at entry	91.5	0.61	1.83
Landing phase roll hold	63.6	0.42	1.27
Total required	367.0	2.45	7.35
Contingency (100%)	367.0	2.45	7.35
Total loaded	734.0	4.9	14.7

APPENDIX D

From the preceding duty cycle, the weights for the N_2H_4 and N_2 attitude control systems have been calculated:

Item		Weight N_2H_4		Weight N_2
Propellant (including residual)		5.1		15.6
Propellant tanks		.6		20.6
Pressurant		.4		----
Pressurization tanks		1.0		----
Thrusters		6.4		4.0
Components, lines		19.4		12.3
Ordnance valves	8.0		5.6	
Filters	1.0		.4	
Hand valves	1.5		.5	
Disconnects	1.5		.3	
Pipe cutters	1.6		----	
Instrumentation	3.6		3.0	
Lines	2.0		2.5	
Propellant control device	.2		----	
Supports		8.7		12.4
Tanks	2.7		6.4	
Thrusters	6.0		6.0	
Total		41.6		64.9

The weight data indicate that the N_2H_4 system has a weight advantage of 23.3 lb when compared to the N_2 system.

A comparison of the reliability values of the two systems considered in this study is presented below:

System	Reliability
N_2H_4	0.9967
N_2	0.9981

These data indicate that the nitrogen system has a reliability advantage.

APPENDIX D

The thrust levels required for the ACS $\left(2.4,\ 3.2\ lb_f\right)$ do not represent significant development risk for either the N_2H_4 or N_2 systems in that considerable development work has been done in this thrust range.

The parametric data derived in Part I indicate that for the N_2 system to be competitive from a weight standpoint, gas regulation is required. The regulator represents a significant failure source as evidenced by past programs.

The N_2H_4 system has been selected for the Part II point designs primarily due to its weight advantage and elimination of gas regulation.

APPENDIX D

This page intentionally left blank.

APPENDIX D

4. GUIDANCE AND CONTROL

Planetary Approach Guidance

Problem definition and approach. - As a spacecraft approaches Mars the trajectory will be known to within a covariance matrix, P_o, which is the result of errors in deep space network (DSN) tracking, planet ephemeris, and physical constants of the equations of motion. These errors will result in entry condition errors for a capsule separated from the spacecraft and placed on an entry trajectory. Also, they will result in orbit ephemeris errors when the orbiter part of the spacecraft is placed into orbit about the planet. Through the use of onboard measurements, the navigation errors of the spacecraft can be reduced. With improved navigation, the velocity correction required to place the capsule on the entry trajectory can be modified to reduce the entry condition errors. Similarly, the orbit insertion maneuver for the orbiter can be used to correct the trajectory for that case.

For the case of the capsule entry condition, maneuver execution errors in applying the deflection impulse result in an entry angle error of about 1/2° (1σ). A position error of 25 km normal to the approach velocity and in the trajectory plane will also produce an entry angle error of 1/2°. For this reason 25 km was chosen as a design goal for evaluating approach navigation results.

The types of measurements that can be considered for onboard mechanization are active ranging, celestial angles, and inertial angular velocity.

Active ranging has been considered briefly for both direct radar measurements from the spacecraft or differential ranging using an earth transmitter and receivers on the spacecraft receiving the direct earth signal and the bounce from Mars. Either of these approaches was quickly eliminated due to size, weight, and power penalties. Measuring the inertial angular velocity requires extremely accurate gyros mounted on a planet tracker. Because the spacecraft approaches the planet on a hyperbolic trajectory that is nearly a straight line, at the ranges of interest (600 000 km to 50 000 km) the angular velocity of the orbit is very small so that poor signal-to-noise characteristics are obtained (ref. D7).

Celestial techniques consist of measurement of line of sight (LOS) directions to the sun, stars, the planets, and planet moons.

APPENDIX D

Planet moon ephemeris accuracy is questionable. Sun, star, and planet LOS measurements are state-of-the-art techniques used on most spacecraft, although usually for attitude control. The simplest ranging technique is to measure the planet subtended angle (or disc angle). Therefore, the system considered for further study consisted of a sun tracker, a star tracker, and a Mars tracker measuring the LOS directions to those bodies and a disc angle measurement, considered to be a second function of the Mars tracker. The geometry of this system is defined in reference D8 and has previously been studied in reference D9. The simplified geometry of the measurements is shown in figure D69.

The primary purpose of this study was to define the required measurement accuracy and to assess the feasibility of obtaining instruments that could perform adequately. Consequently, several simplifying assumptions were made to focus attention on the sensor requirements and to simplify the analysis and simulation problems. The primary assumptions and ground rules are as follows:

1) The spacecraft approach orbit was assumed to be a two-body hyperbola with final hyperbolic velocity of 3 km/sec and periapsis altitude of 1000 km;

2) Measurements were to be made between 600 000 km and 50 000 km from the planet;

3) DSN tracking would provide an initial trajectory estimate with the associated covariance matrix. For this study, a spherical position error of 150 km (1σ) and a spherical velocity error of 0.02 m/sec (1σ) were assumed as the initial errors;

4) DSN measurements and onboard measurements would not be processed jointly in the same statistical process;

5) The sensor errors could be represented by Gaussian white noise of specified mean and variance;

6) A Kalman filter would be used for estimating the position, velocity, and sensor biases from the onboard measurements.

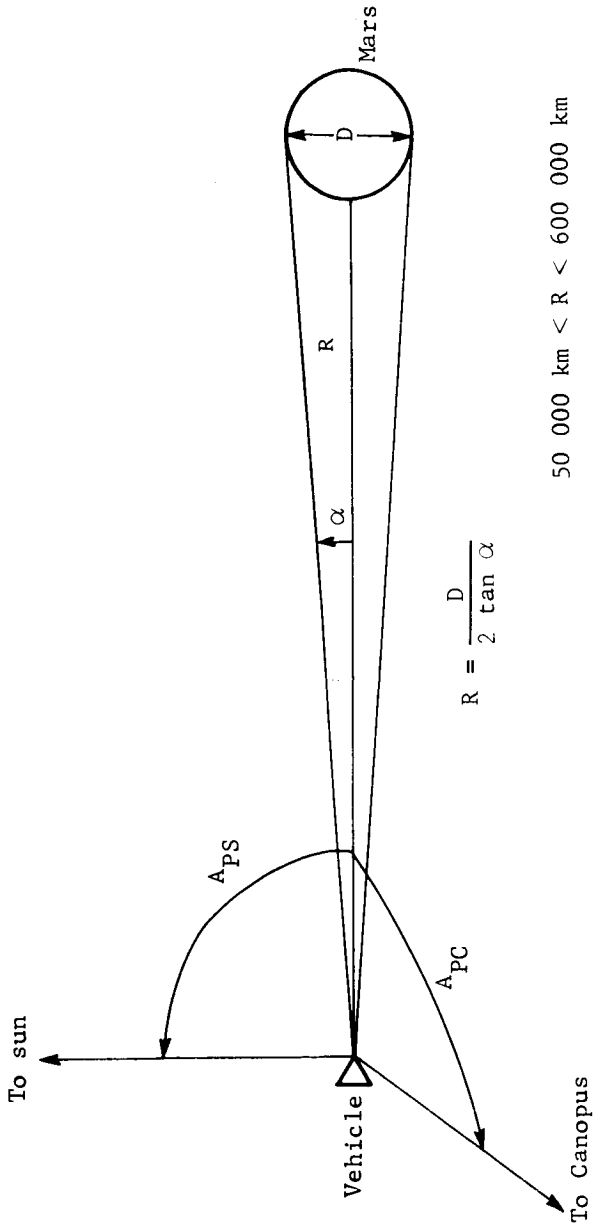

Figure D69.- Planetary Approach Measurement (Geometry)

APPENDIX D

Assumption 1) was made for computational simplicity and is equivalent to assuming that perturbations about the actual orbit can be described by perturbations in the hyperbolic orbit. The range defined in Assumption 2) is limited by spacecraft ΔV requirement on the small end and the planet sphere of influence on the large end. In Assumption 3), the intent was to show that the onboard measurements could improve the navigation accuracy for pessimistic estimates of DSN accuracy. Assumptions 4), 5), and 6) simplify the analysis problem considerably. The resulting data on sensor accuracy requirements are then specified so that the sensors will definitely cause the navigation accuracy to improve whether DSN tracking data are combined with the measurements or not. Since the onboard measurements are essentially position measurements and velocity must be implied, the DSN measurements at interplanetary distances are velocity measurements, combined processing is complementary and should yield better navigation accuracy than either set of measurements processed alone.

Mathematical formulation. - The variables to be estimated will be called the state vector, X, which consists of three position deviations from a nominal trajectory, three velocity deviations from nominal, and three measurement angle biases. Deviations from a nominal trajectory are used so that the well-developed techniques of sensitivity analysis and linear estimation theory can be used. The measurement vector, Y, also consists of three deviations from nominal in the angles A_{PC}, A_{PS}, and α shown in figure D69. The measurement vector is related to the state vector by a matrix of partial derivatives obtained from the geometry of the problem (ref. D8). For this study,

$$Y = HX + \eta \tag{D1a}$$

$$H = \left[\begin{array}{c|c|c} H_p & 0 & I \end{array}\right] \tag{D1b}$$

where

η = measurement noise with zero mean

0 = the 3 x 3 zero matrix

I = the 3 x 3 identity matrix

APPENDIX D

$$H_p = \begin{bmatrix} \frac{C_{11}}{R} & \frac{C_{12}}{R} & \frac{C_{13}}{R} \\ \frac{C_{21}}{R} & \frac{C_{22}}{R} & \frac{C_{23}}{R} \\ \frac{C_{31}}{f} & \frac{C_{32}}{f} & \frac{C_{33}}{f} \end{bmatrix} \tag{D1c}$$

where

R = range from planet

$$f = \frac{R^2}{D}\sqrt{1 - (D/4R)^2} \tag{D1d}$$

where

D = planet diameter

C_{ii} = direction cosines dependent on measurement geometry.

In these equations, as shown, the three measurements Y are not a function of velocity (hence the zero matrix) and directly contain the measurement bias states (hence the identity matrix). The useful data in the measurement Y is position data as defined by the matrix transformation H_p. Notice that the measurement sensitivity for the sun-planet and star-planet angles are directly proportional to range, R, whereas the disc angle measurement sensitivity is proportional to R^2. Thus, as the range decreases, the measurement quality improves for fixed sensor accuracy.

The state, X, is a physical vector that can be calculated from the perturbed equations of motion. For this study, the matrizant, Φ, of reference D10 was used to propagate trajectory deviations from one measurement time (t_k) to the next $(t_k + 1)$. That is,

$$X_{k+1} = \Phi\left(t_{k+1}, t_k\right) X_k + \epsilon_k \tag{D2}$$

ϵ_k is an error source to represent inexact knowledge of the equations of motion. The recursive Kalman filter is mechanized by the equations,

APPENDIX D

$$\hat{X}_{k+1} = \Phi \hat{X}_k + K \left(Y_{k+1} - H \Phi \hat{X}_k \right) \tag{D3a}$$

where

$$K = P'_k H^T \left(H P'_k H^T + R \right)^{-1} \tag{D3b}$$

$$P'_k = \Phi P_k \Phi^T + Q \tag{D3c}$$

$$P_{k+1} = P'_k - K H P'_k \tag{D3d}$$

In these equations, K is the optimum gain matrix that makes $\hat{X}$ a minimum variance estimator of the state, X. The covariance matrix of error in the estimate is P. The symbol R is the covariance matrix of the sensor noise, η. Q is the covariance matrix of the dynamic equation error, ϵ.

A digital simulation program containing all the preceding equations was constructed for the IBM 1130. The simulation also contains supplemental calculations to define the measurement matrix H in terms of arbitrary angles for the three celestial bodies used plus equations to compute the nominal orbit position velocity and time. This simulation used a random number generator to produce Gaussian noise of specified mean and variance for use in the measurement equation (D1a). An actual perturbed trajectory (non-zero X) could be simulated through use of the state transition matrix Φ. Thus, absolute convergence of the estimated state $\hat{X}$ to the actual state X could be checked as well as the filter internally generated covariance P. Under stable filter operation the square root of the diagonal elements of P form an upper bound for the actual deviation,

$$\Delta X = \left| \hat{X} - X \right| \tag{D4}$$

Simulation results. - Many preliminary computer runs were made to check the simulation and define which parameters were not significant contributers to the overall conclusions. These runs are not presented here; however, the basic conclusions made are as follows:

1) The dynamic model noise, ϵ, with covariance, Q, has no appreciable effect on the results because the time available for measurements is not long enough to produce data saturation and filter divergence. For this reason the runs presented have $Q = 0$;

2) The convergence time of the filter covariance is decreased as the time between measurements is descreased and a larger number of measurements is obtained. Measurement intervals shorter than 0.1 hr were not tried since computer run time becomes long. Measurement intervals of 15 minutes produce good results within the available time of 24 hr;

3) Ranges larger than 300 000 km yield poor results for the range of sensor accuracies studied due to the sensitivity effect described previously;

4) The convergence time is insensitive to the choice of the position terms of the initial covariance matrix, P_o. Very large values of P_o are reduced to reasonable values after one measurement. This statement is not true, however, for the velocity terms of P_o because the measurements do not directly define velocity.

Table D11 summarizes the most useful results obtained. Each of the 12 cases shown is plotted in figures D70 thru D82, as indicated in the table.

Cases 1 thru 4 of the table show the sensitivity of the navigation process to the disc angle accuracy. Downrange position (X) is affected strongly while inplane normal (Y), and crossrange (Z), are not affected appreciably. Comparing Cases 3 and 4 shows that a disc angle error of 90 arc-sec is only slightly better than no disc measurement at all. In these runs, the sun was assumed to be near the trajectory plane and Canopus about 60° below the plane. As shown in Case 8, a sun sensor accuracy degradation affects in-plane errors X and Y. Case 9 shows that the Canopus error affects only the cross plane error Z. The planet line-of-sight angle affects both the angles A_{PC} and A_{PS} shown in figure D69. Thus, as Case 10 shows, all three positions errors are affected by this measurement accuracy. The effects of biases in the measurements are shown in Cases 5, 6, 11, and 12. In these cases, the Kalman filter is mechanized to estimate the biases and remove them from the measurements. As seen, the convergence is not as good; however, these runs were taken with a fixed number of measurements. Taking more frequent measurements will probably reduce the effect of biases further.

TABLE D11.- PLANETARY APPROACH GUIDANCE, SUMMARY OF RESULTS[a]

Case	Sensor accuracy[b], arc-sec (1σ)				Accuracy, km			Bias	Figure
	Sun	Star	Planet	Disc	Position X	Error[c] Y	(1σ) Z		
1	20	20	16	5	7	2.1	2.1	No	D70, D71
2	20	20	16	30	38	3.1	2.1	No	D72
3	20	20	16	90	71	4.8	2.1	No	D73
4	20	20	16	None	73	5.2	2.1	No	D74
5	20	20	16	None	128	14.5	5.5	Small[d]	D75
6	20	20	16	None	136	15.9	5.7	Large[d]	D76
[e]7	20	20	16	None	95	6.2	1.9	None	D77
8	120	20	16	None	150	15.4	2.1	None	D78
9	20	120	16	None	86	5.6	12.5	None	D79
10	20	20	120	None	150	15.5	12.6	None	D80
11	20	20	120	None	153	36.6	33.0	Large	D81
12	20	20	120	90	119	35.2	33.0	Large	D82

[a]All results taken after 20 hr of measurements at 15-minute intervals starting at a range of 300 000 km.

[b]Sensor accuracy represents random error on sun LOS, star LOS, planet LOS, and planet disc angle, respectively, no biases included.

[c]X is direction along velocity vector, Y in trajectory plane normal to X, and Z is normal to plane.

[d]Small bias represents 20, 20, 16, 5 arc-sec bias added to the four measurements. Large bias represents 20, 20, 200, 50 arc-sec.

[e]Case 7 is identical to Case 4 except arbitrary star directions were assumed, rather than sun-Canopus.

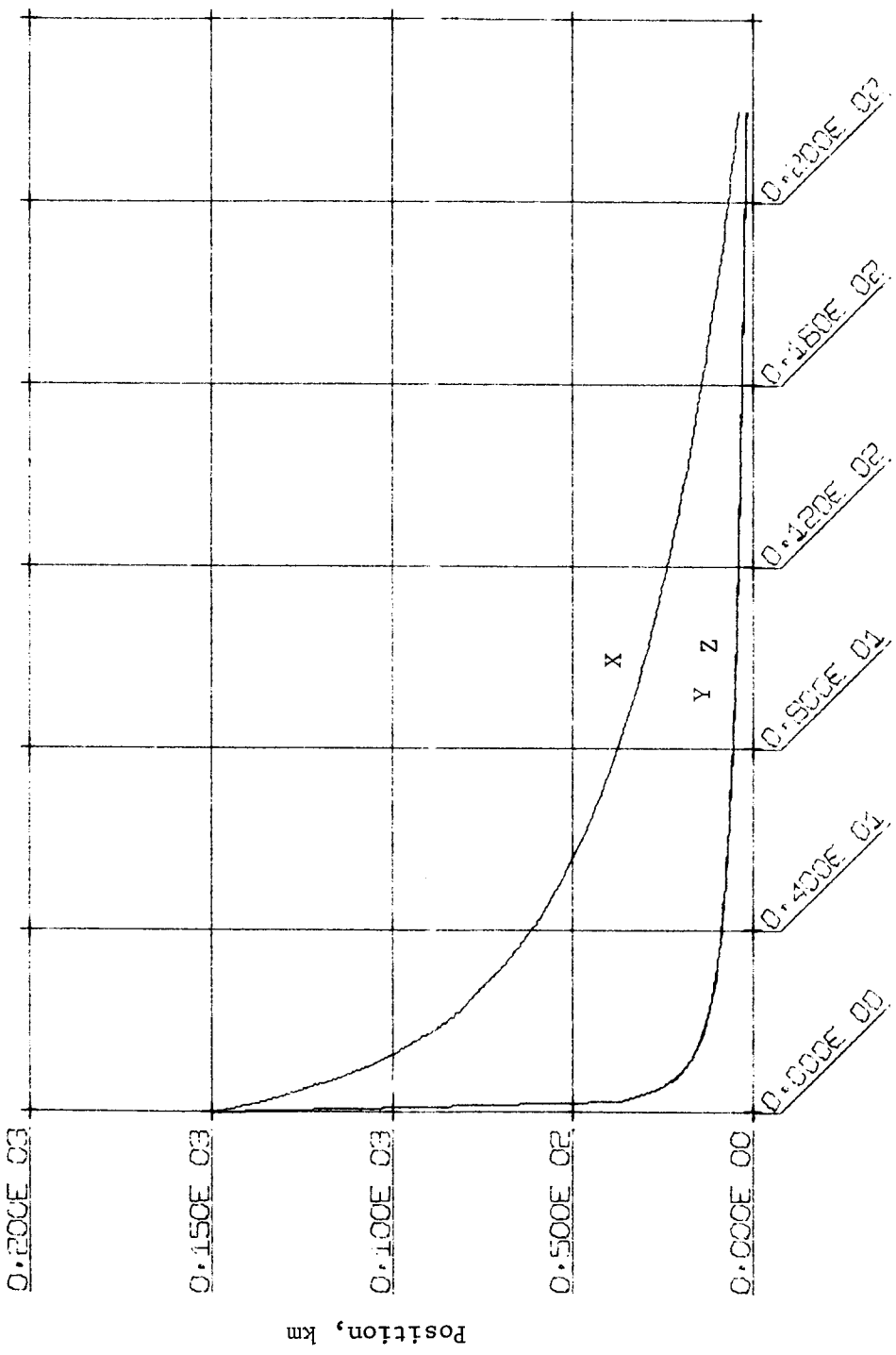

Figure D70.- Position Error, 1 Sigma, Sensors 20, 20, 16, 5 arc-sec, Case 1

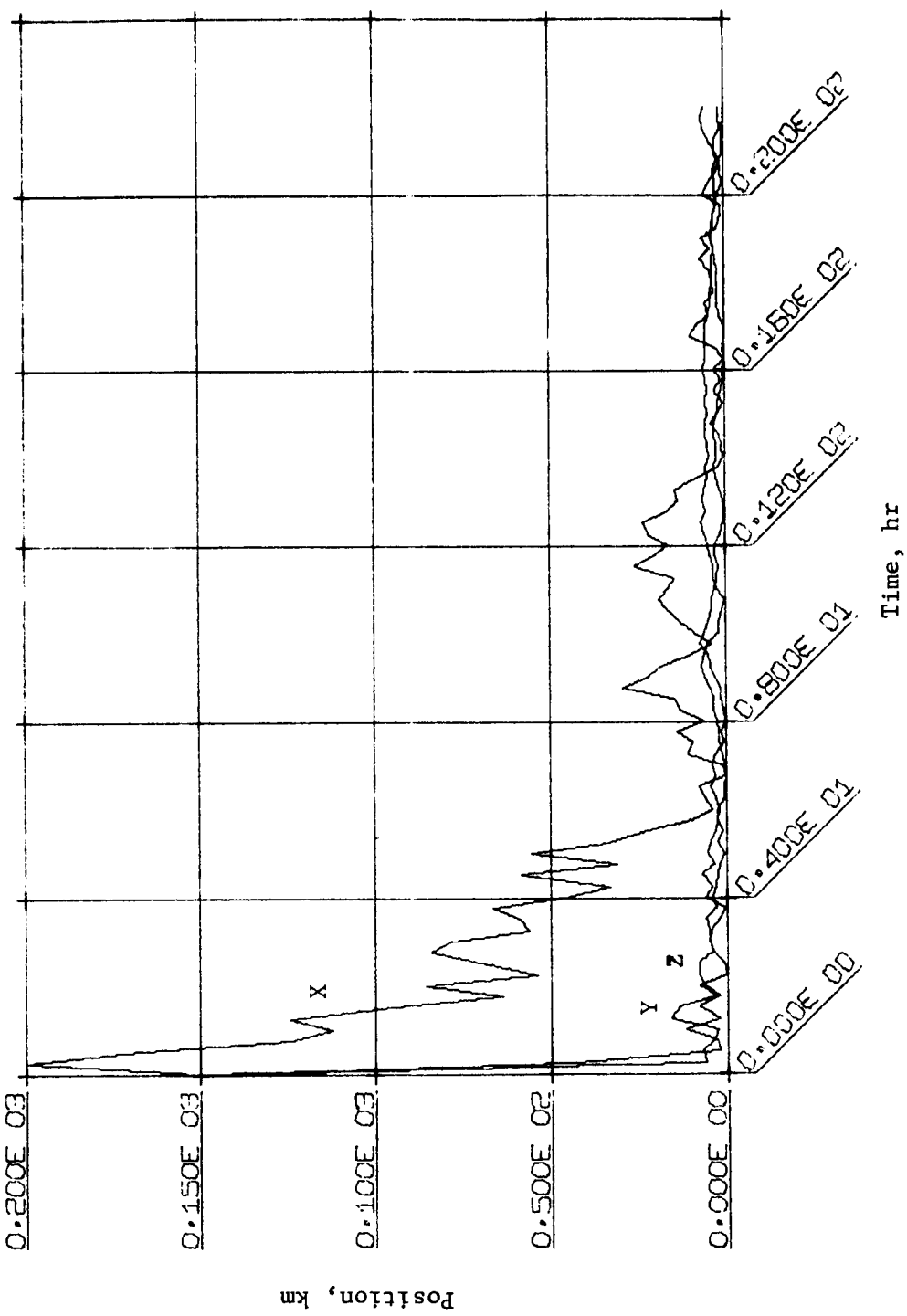

Figure D71.- Position Error, Actual Deviation, Sensors 20, 20, 16, 5 arc-sec, Case 1

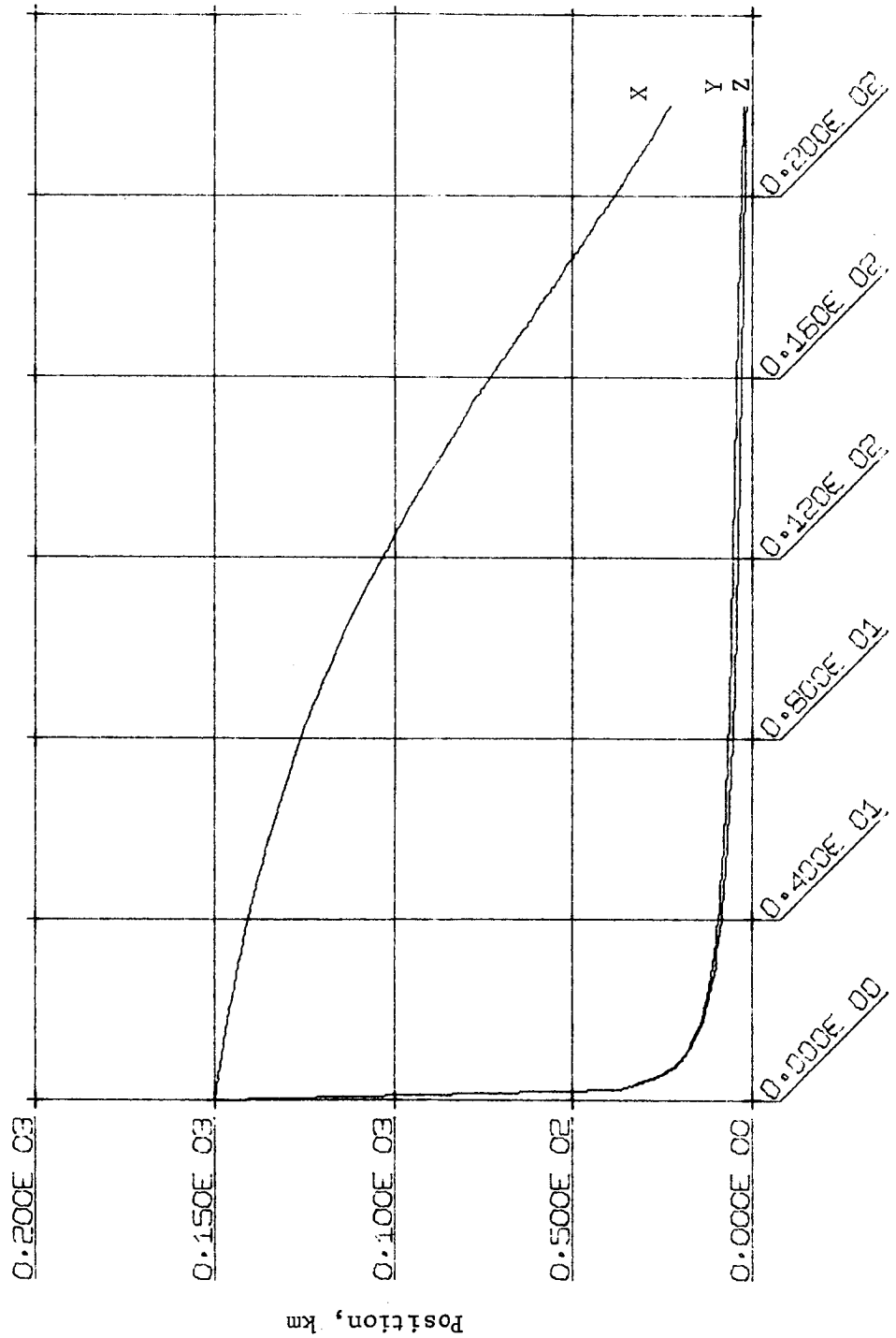

Figure D72.- Position Error, 1 Sigma, Sensors 20, 20, 16, 30 arc-sec, Case 2

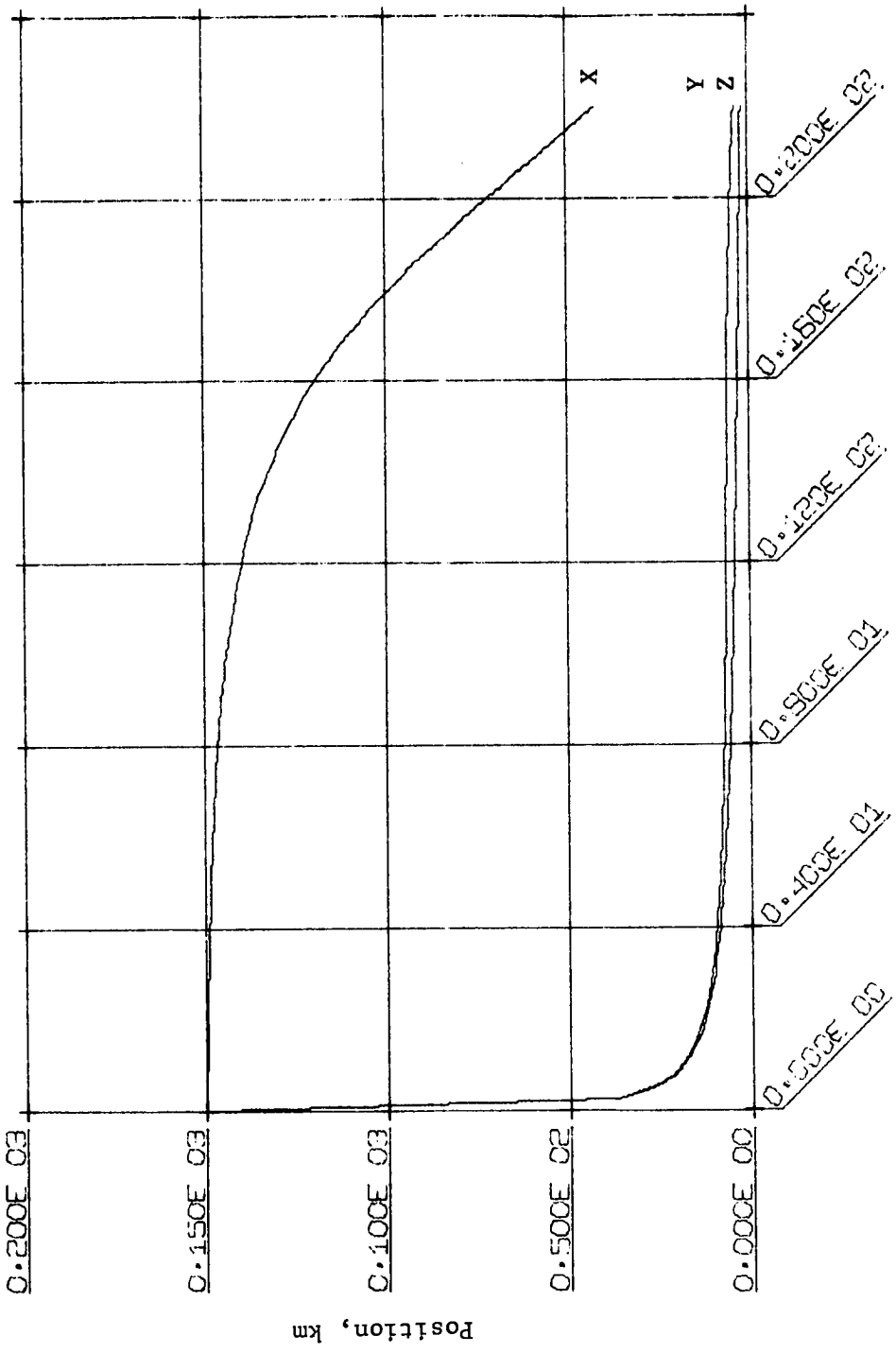

Figure D73.- Position Error, 1 Sigma, Sensors 20, 20, 16, 90 arc-sec, Case 3

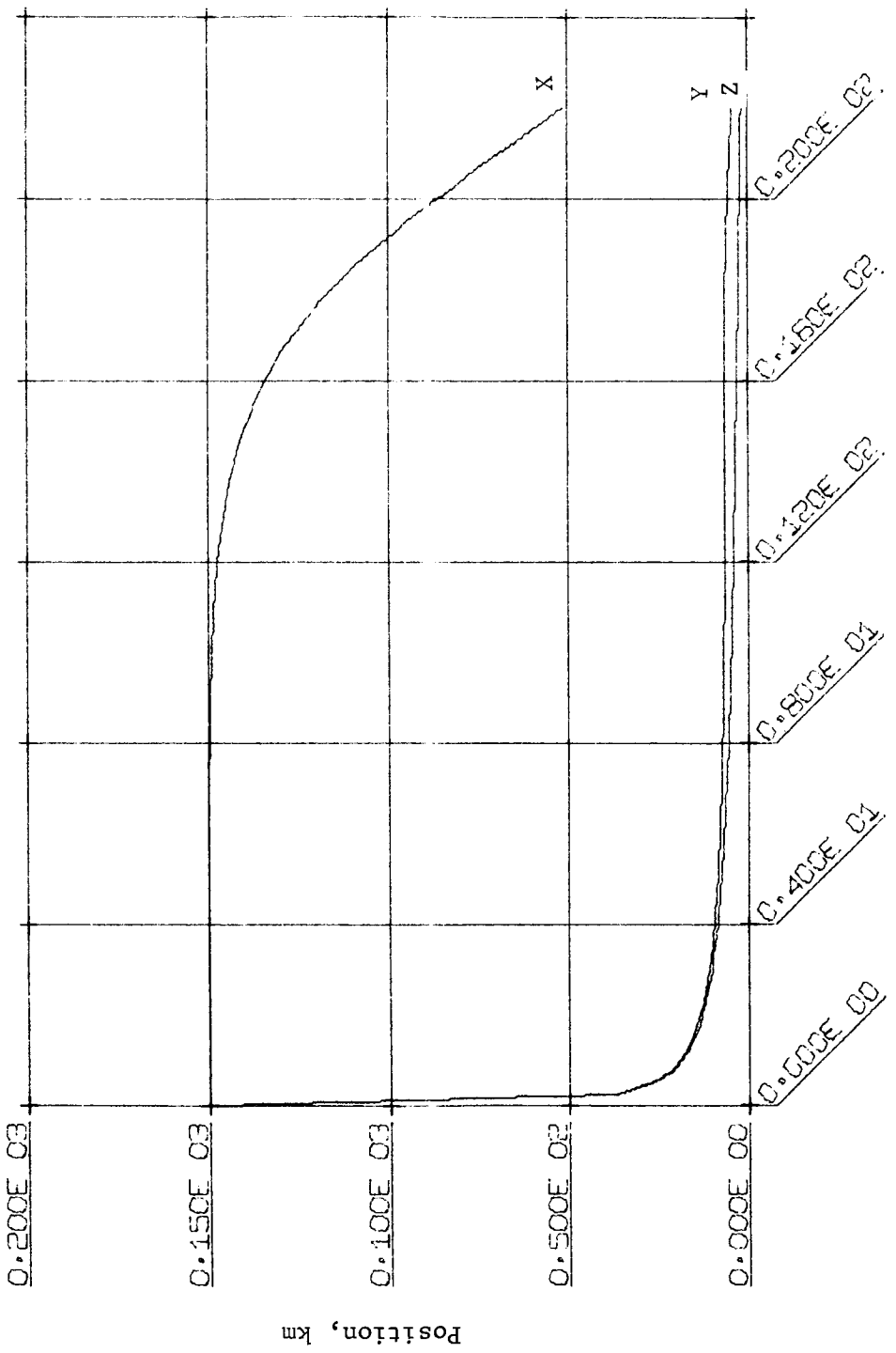

Figure D74.- Position Error, 1 Sigma, Sensors 20, 20, 16 arc-sec
Case 4

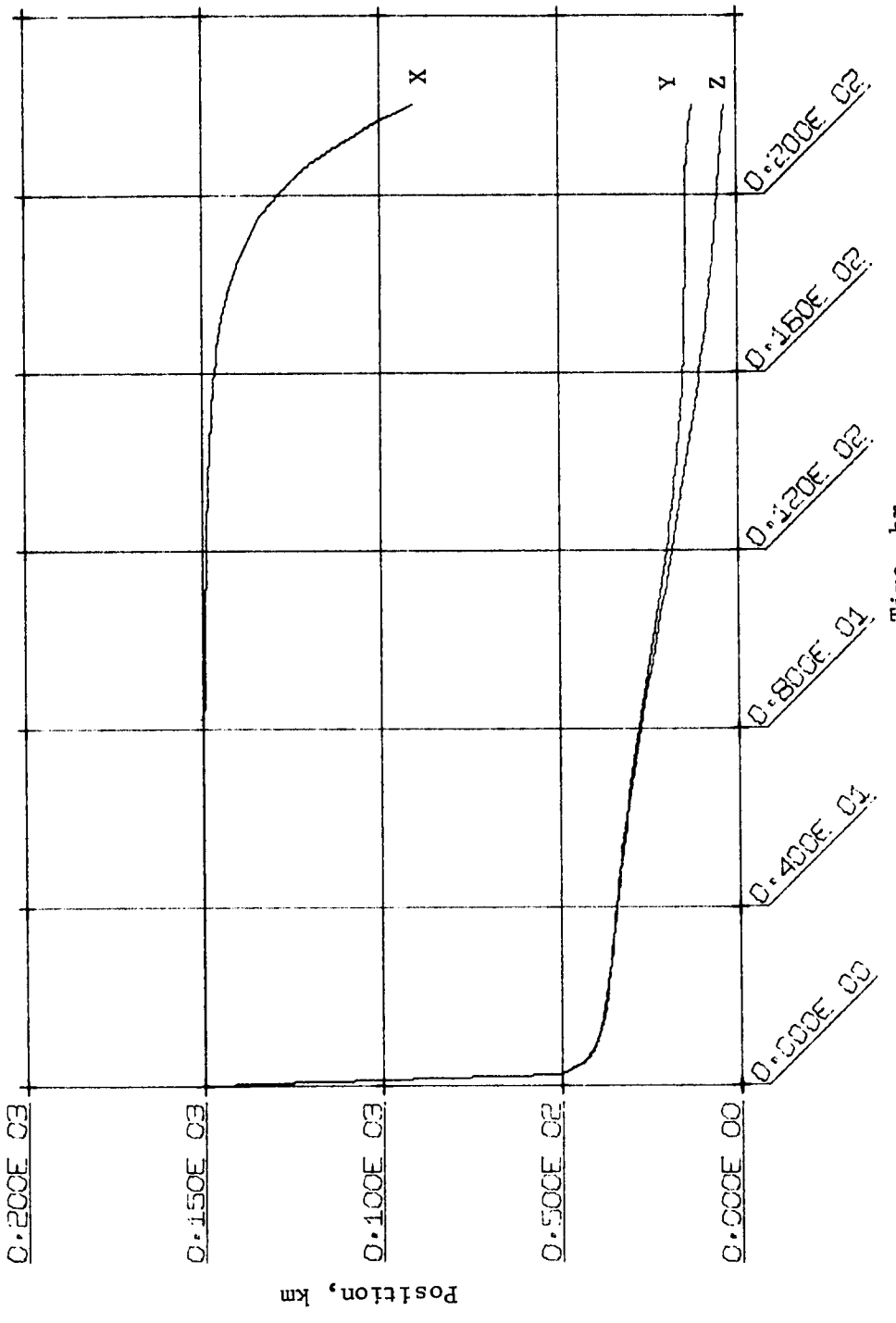

Figure D75.- Position Error, 1 Sigma, Sensors 20, 20, 16 arc-sec, Small Bias, Case 5

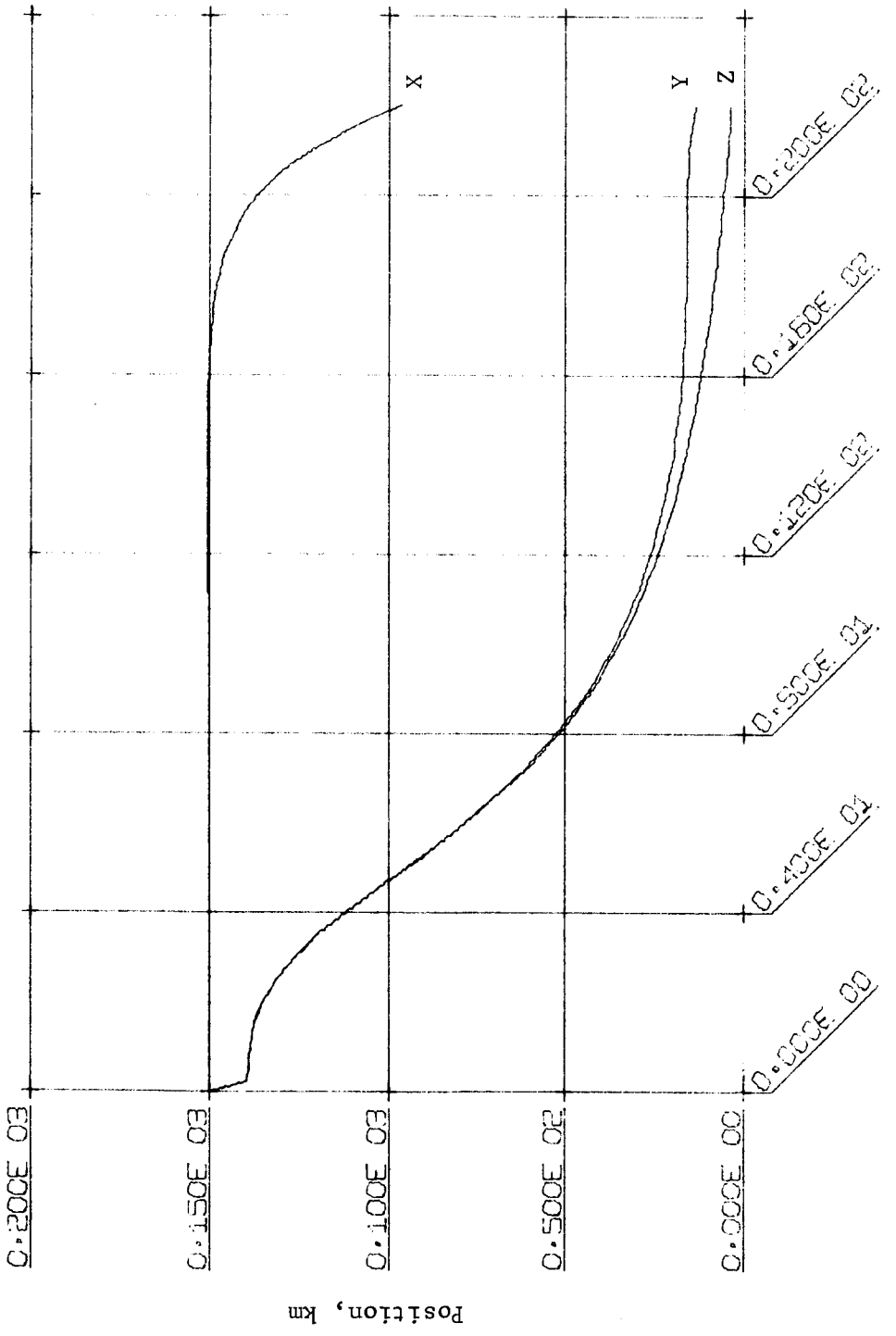

Figure D76.- Position Error, 1 Sigma, Sensors 20, 20, 16 arc-sec, Large Bias, Case 6

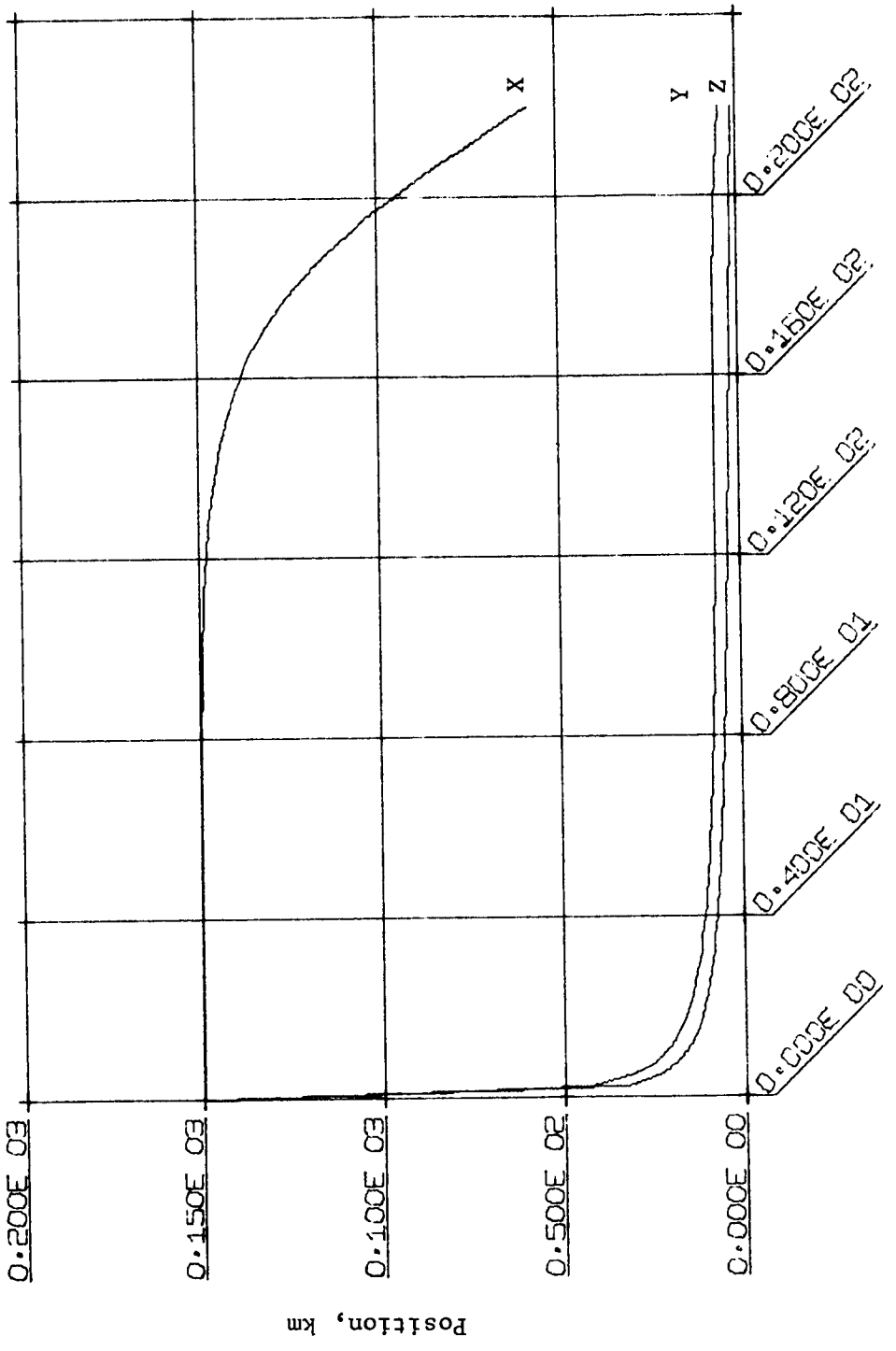

Figure D77.- Position Error, 1 Sigma, Sensors 20, 20, 16 arc-sec, Case 7

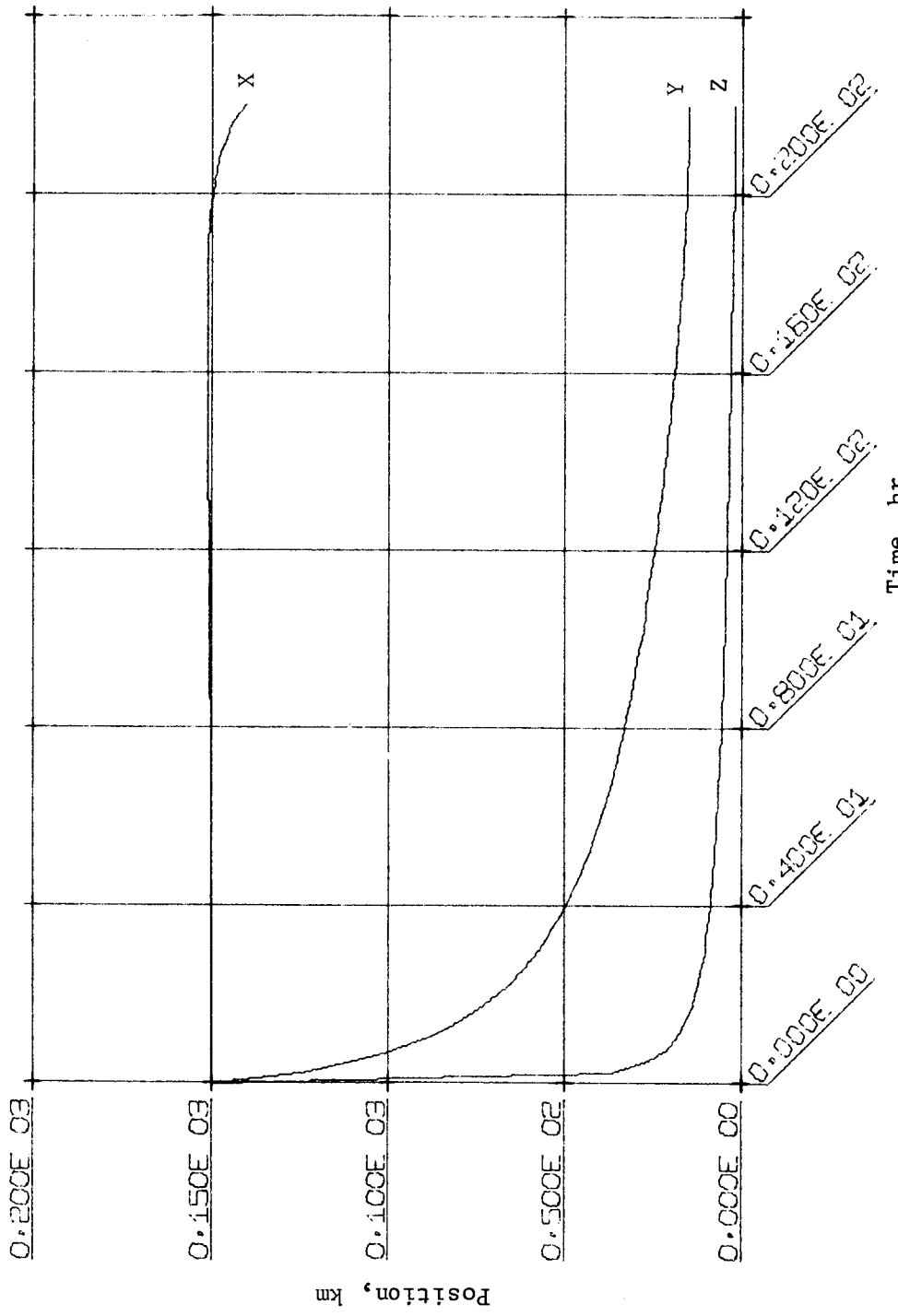

Figure D78.- Position Error, 1 Sigma, Sensors 120, 20, 16 arc-sec, Case 8

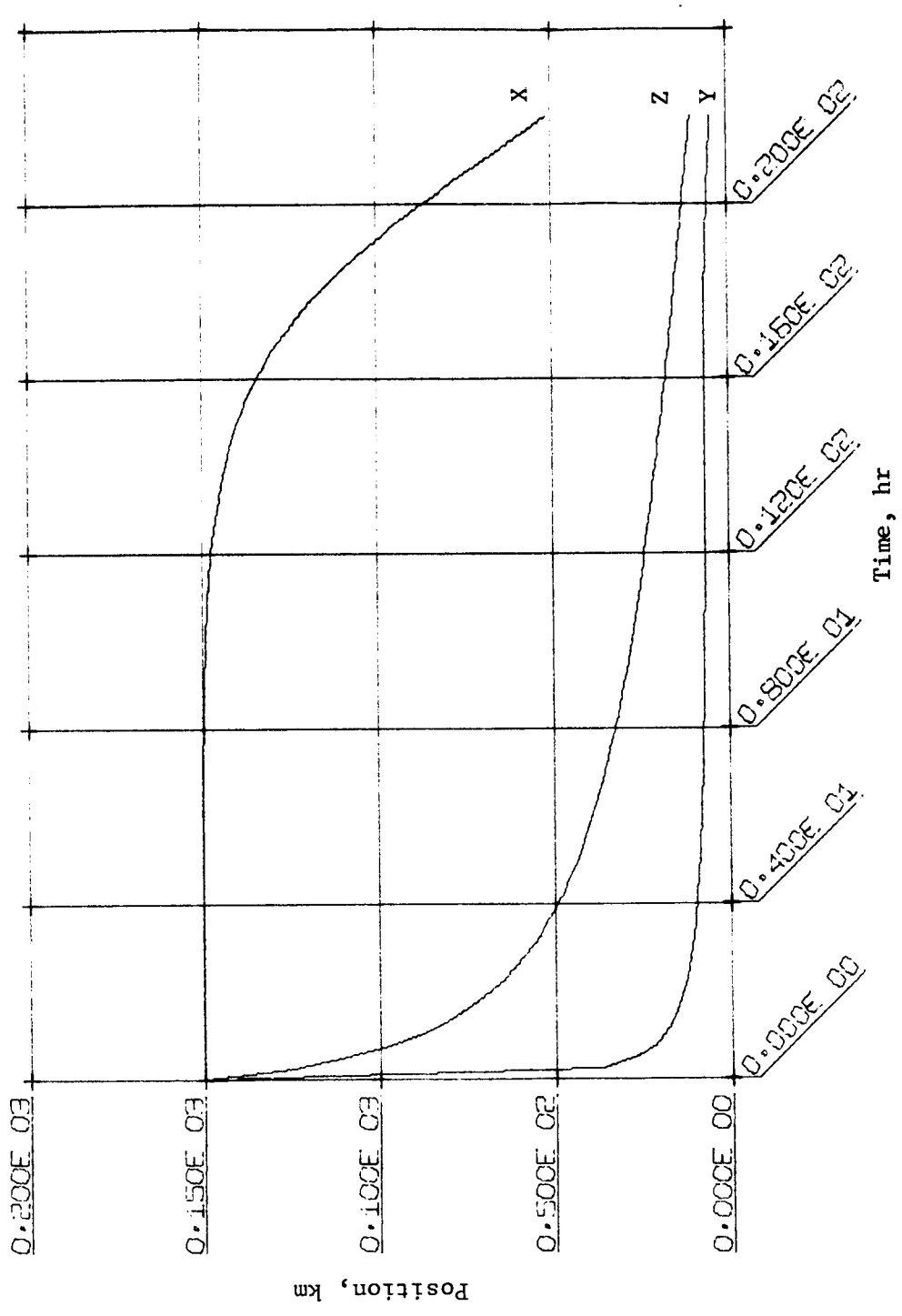

Figure D79.- Position Error, 1 Sigma, Sensors 20, 120, 16 arc-sec, Case 9

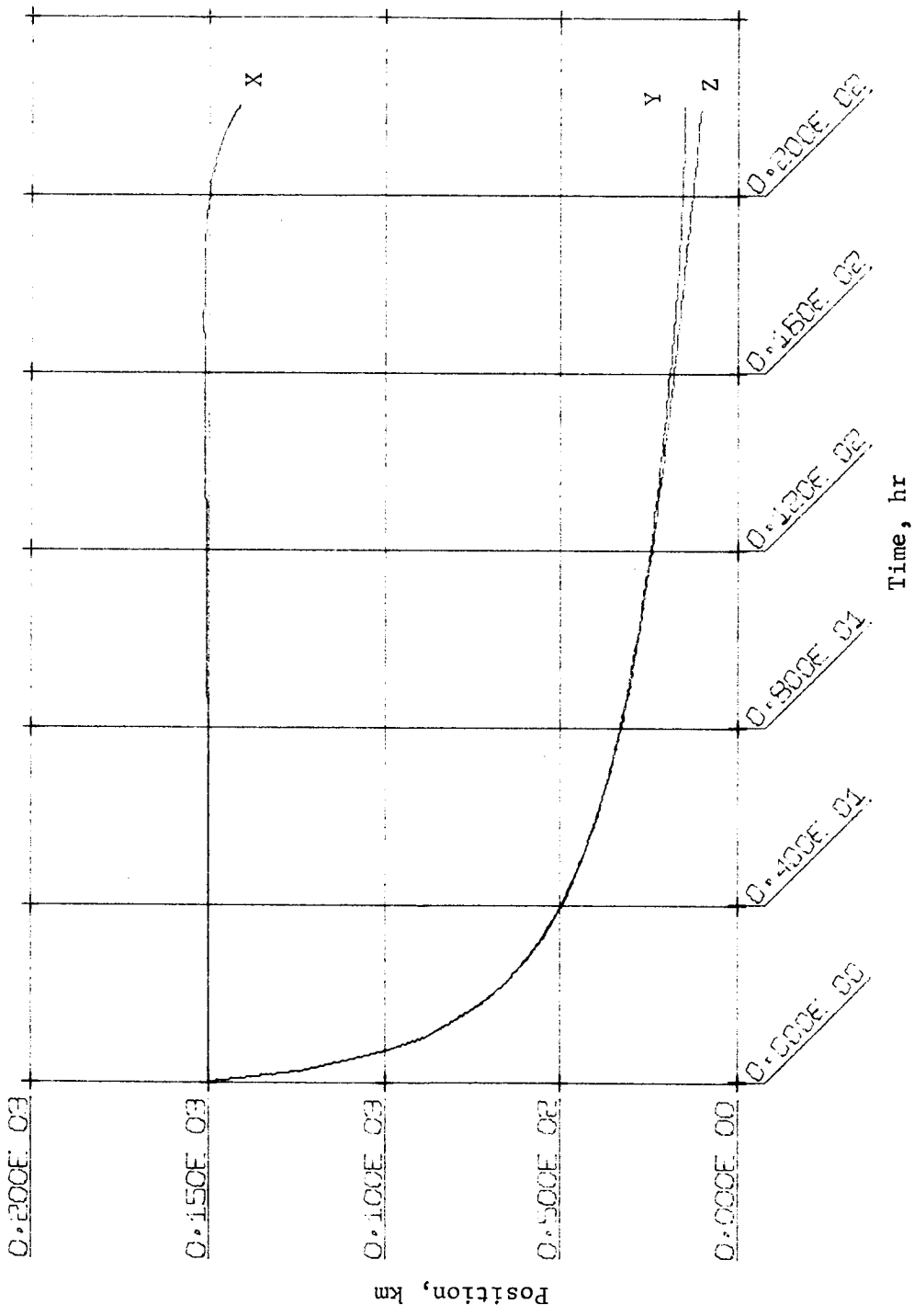

Figure D80.- Position Error, 1 Sigma, Sensors 20, 20, 120 arc-sec, Case 10

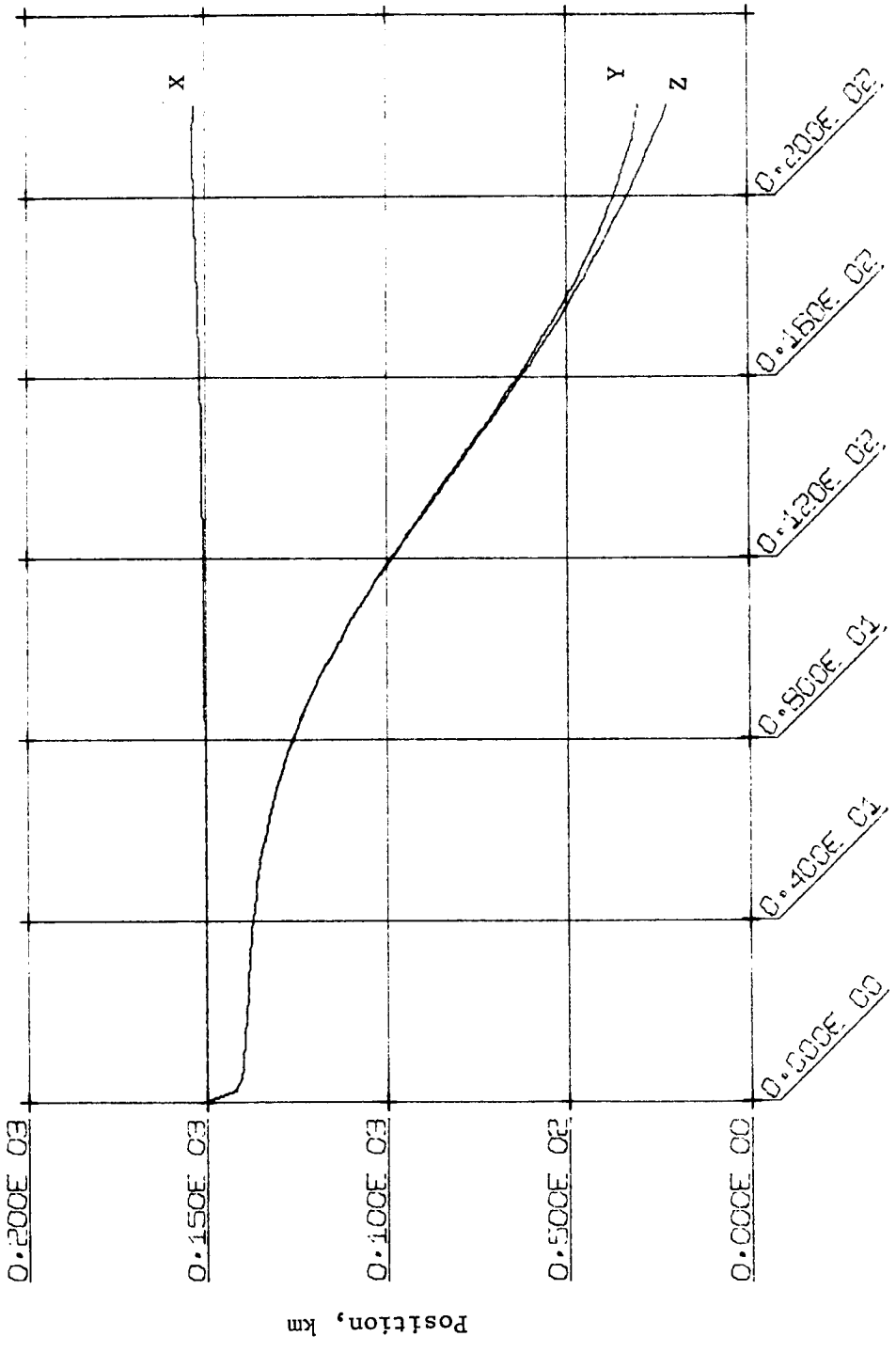

Figure D81.- Position Error, 1 Sigma, 20, 20, 120 arc-sec, Large Bias, Case 11

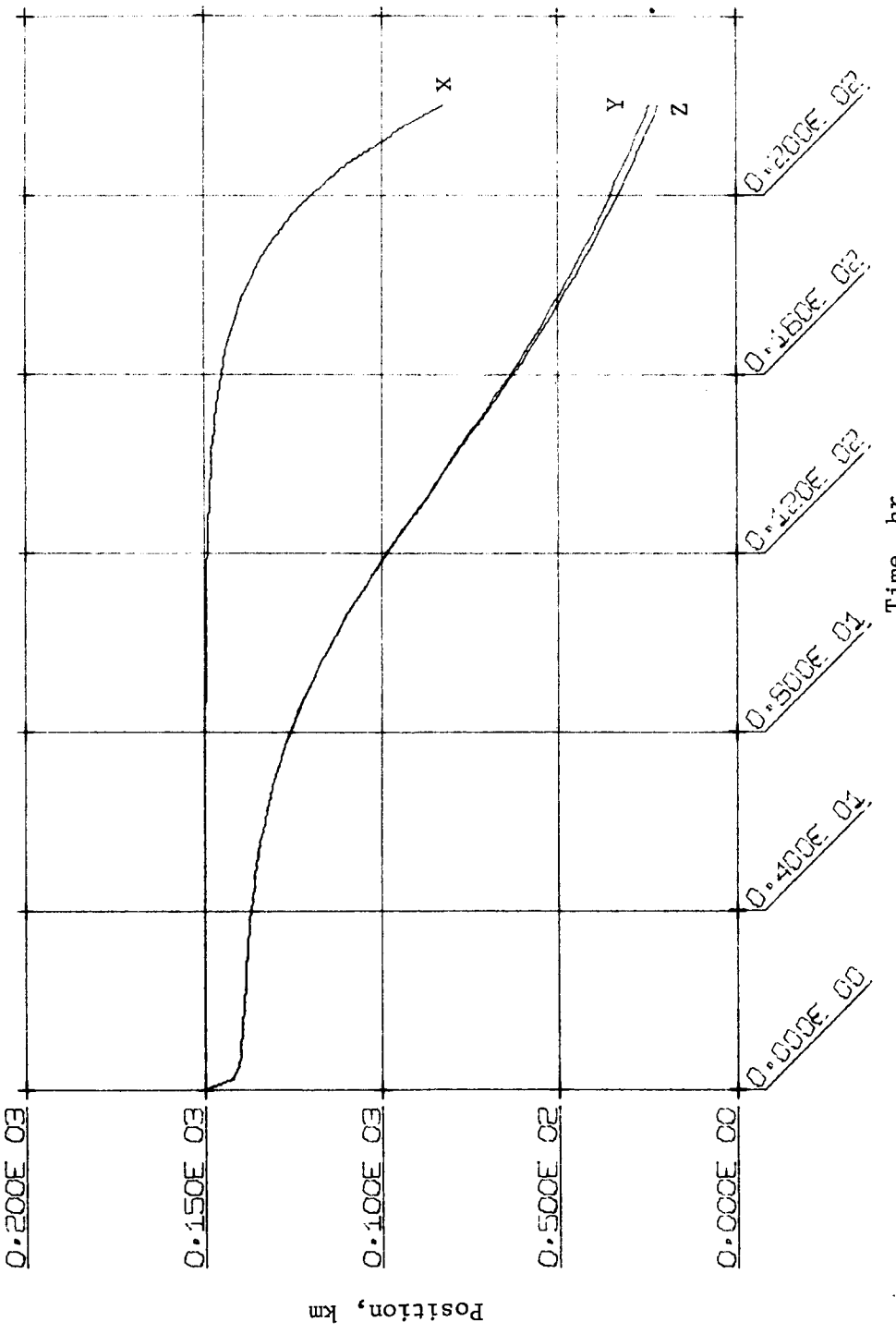

Figure D82.- Position Error, 1 Sigma, Sensors 20, 20, 120, 90 arc-sec, Large Bias, Case 12

APPENDIX D

The figures corresponding to the cases in the table are all plots of the Kalman filter generated covariance matrix, P, except for figure D71. Figure D71 is a plot of the absolute value of the estimated state minus the actual state, equation (4). As can be seen, the curves of figure D70 bound those of figure D71. This is generally true if the filter is well designed.

Interpreting these results in terms of the capsule entry is simplified because the entry angle error is sensitive only to the Y direction error. The X direction error produces only a time of arrival error at the arbitrarily specified entry altitude. The Z direction error produces negligible error in the entry angle. Scanning the results of table D11 shows that the Y direction error is less than 25 km for all cases except the large bias, Cases 11 and 12. This is true even though some cases do not mechanize the disc angle measurement. The large bias Case 11 is small enough to believe that a slightly more frequent measurement interval would reduce the error below 25 km.

The use of planetary approach guidance to improve the orbiter ephemeris accuracy was not considered in this study. It is obvious, however, that some improvement could be achieved over the case with DSN tracking alone. For the orbit injection case, the disc angle error is probably more important.

Sensor survey. - Three basic sensor types are considered in this survey:

1) A sun sensor providing two-axis pointing to the sun;

2) A star sensor (Canopus) providing two-axis pointing;

3) A planet sensor providing two-axis line of sight to the planet. This sensor could also measure the planet subtense angle for range determination.

The technology for both sun and star sensors is well developed and the choice of a specific sensor is dictated by a tradeoff of mission requirements, weight, and cost. Planet sensors are not as well developed, nor the target characteristics as well known, as the other two types.

Sun sensors operate on a relatively large and intense target. The angular accuracy of the sensor is limited by its ability to locate the center of the solar disc. Three techniques are considered here that yield different accuracies at related cost and weight.

APPENDIX D

The simplest sun sensors consist of radiation balance detectors in a bridge configuration. The coarse and fine "Eyes" built by Ball Brothers are representative of this type. This type of sensor exhibits good accuracy at null with a relatively narrow range of linearity. Typical specifications include:

Fine Eye FE-5

Field of view (FOV)	±15°
Linear range	±1°
Accuracy	1'
Size	.875 in. diam x .95 in. long
Weight	9.5 gr ea

The next type of sensor is the digital readout unit characterized by the Adcole Digital Solar Aspect Sensors. These have good linearity over wide angles and have accuracies similar to the radiation balance units. Vernier techniques are available to give better accuracy at the cost of increased weight and complexity. Typical specifications include:

Grey Code Processor

FOV	Up to 128° cone
Resolution	1/2° to 1°
Sensor weight	4 oz
Power	2 W
Electronics size	7-3/4x3x4 in.

Vernier (V Brush) Processor

FOV	128° cone
Resolution	1′
Power	1 W
Weight (est)	1 lb

The third sensor type is the high precision sensor used for an attitude reference by an astronomical satellite. These are relatively complex and heavy, but are highly accurate. The Honeywell Fine Sun sensor is of this type and uses a pair of critical angle prisms in a radiation balance circuit to track

the edge of the solar disk. Operation of this sensor is extremely sensitive to apparent solar diameter and is not suitable for use over variable ranges. Specifications include:

AOSO Fine Sun Sensor (nonimaging)

Accuracy	
Basic	1.7"
Stability	0.1" (short term)
FOV	80' to 2.5°
Scan	±20' each axis

Star sensors may be characterized as one of two basic types -- boresighted or gimbaled. The boresighted units can be used to provide an attitude reference as in the Surveyor or Mariner Canopus sensors. The gimbaled sensors are more generally used with navigation computers. The gimbaled units are much more complex and heavier than the boresighted sensors, but can be used over a wide angular range. Of the three sensors, star trackers have the best inherent accuracy due to the effective "point source" nature of a star. Accuracy is quite typically in the order of 5 to 15 sec (1σ) for precision types. Typical specifications for star sensors are:

Canopus MM '69

Tracking accuracy	
Short term	0.002°
Long term	0.05°
Weight	8.0 lb
Power	5.5 W + 6.5 W shutter
Size	11.5x5x4.3 + 12.25x7.2x5.3 in.

The projected accuracy for the Polaris tracker is 30 sec.

Planet sensors are at the earliest stage of development. Electro Optical Systems has built a planet sensor for JPL that operates in the visible light spectrum and uses data processing to determine line of sight. This sensor has the following characteristics:

FOV	10° x 10°
Alignment	±2 sec/4 days or ±4 sec/9 days
Planet diam (apparent)	0.035 to 1°
Gibbons Phase Angle	0 to 30°
Size	11x10x7 in.
Weight	14.5 lb
Accuracy	150 sec

The least developed aspect of the planet sensor is the capability to measure range to the planet. Over the range involved, power required for direct radar ranging is prohibitive, calling for several kilowatts of peak power for a pulse-type system of 20 to 50 W for a high duty cycle (ICW) system. It would also require very large antennas to achieve sufficient gain due to low frequencies needed to overcome the space loss. In addition, there may be considerable Doppler shift from closing velocity that could require wider bandwidths than desired to enhance the signal-to-noise ratio at the receiver.

The implementation of a disk angle measurement capability in the planet sensor may be a possible method of determining range. Present implementation of the planet tracker described above gives planet angle to 2% (about 96 arc-sec at 300 000 km) of apparent disk.

For this application, although an extensive trade study was not done, it appears that use of a boresighted planet tracker, a boresighted Canopus tracker, and a wide angle (Adcole type) sun sensor may be feasible. The planet disc measurement may be difficult to improve, but as shown previously, is not necessary for entry flight angle corrections.

Conclusion. - The following guidance approach is recommended. The sun-Canopus and planet tracker should be mounted on the orbiter. In a direct approach mode, measurements could begin as far out as 600 000 km for the purpose of partially removing sensor bias. However, the most useful data occurs within 300 000 km as the error sensitivity becomes smaller. These measurements would be processed in conjunction with DSN tracking on Earth to define the actual approach trajectory to within the accuracy described above. Allowing 3 hr for communication link and ground data processing, 20 hr of useful data can be obtained from 300 000 km to 50 000 km. The capsule deflection impulse could be applied at

50 000 km with the required velocity based on the improved trajectory estimate. Use of a longer link time than 3 hr causes the measurements to be required at greater ranges, resulting in less accuracy.

An alternative mechanization to place the sensors on the capsule has several disadvantages:

1) A duplication of the sun-Canopus sensor function already on the orbiter is required;

2) The capsule would have to be separated from the orbiter at about 300 000 km to allow adequate error convergence time;

3) If the capsule were separated closer in, say 50 000 km, only about 4 hr remains to entry, so onboard data processing is required;

4) The sensor data may not be available for the orbiter in applying the orbit insertion maneuver.

In conclusion, it appears that significant improvement is possible in the capsule entry angle over what can presently be achieved with DSN tracking alone. The sensor accuracy required is 1 to 2 arc-min on the sun, Canopus, and planet tracker. The disc angle measurement is not required. Bias up to 2 arc-min in the measurements can be tolerated by proper mechanization of the recursive data processing. Sun and star trackers of this quality are currently available. The planet tracker originally considered for Mariner '69 is in the accuracy range required and should be considered as a potential spacecraft sensor for direct mode missions.

Vernier Phase Parametric Data

Parametric data have been generated for the vernier phase ignition altitude and propellant consumption as a function of thrust-to-weight ratio, horizontal velocity, and vertical velocity. A summary of these data has been used in the capsule efficiency trade studies.

APPENDIX D

The data are plotted in figures D83 thru D87. The data were developed through a three-degree-of-freedom simulation of the following descent contour:

1) Ignite engines at 20% throttle and descend for 3 sec;
2) Descend at 90% throttle until a velocity of 10 fps is reached;
3) Descend at 10 fps for 5 sec;
4) Cut off and fall 10 ft;
5) Gravity turn steering is used throughout the descent.

The altitude plotted is the altitude at which the parachute is released. An attitude maneuver of 3 sec is allowed to place the thrust vector along the velocity vector. The vehicle is assumed to have constant thrust but the thrust/weight ratio can be interpreted as average for a blowdown thrust system.

F_{norm} is a normalized propellant factor. To obtain weight of propellant in earth pounds use

$$W_{prop} = \frac{\left(F_{norm}\right)\ (Wt)}{I_{sp}}$$

where

Wt = verniered weight, earth lb

I_{sp} = propellant specific impulse.

These numbers do not include impulse for random steering effects but that requirement is under 5%.

Vernier Phase Control System Analysis

The vernier phase guidance and control system has been analyzed through the use of analog and digital simulations with supporting linear stability analysis. Most of the applicable analysis is presented in reference D11. This section is a summary of the results of these and subsequent studies.

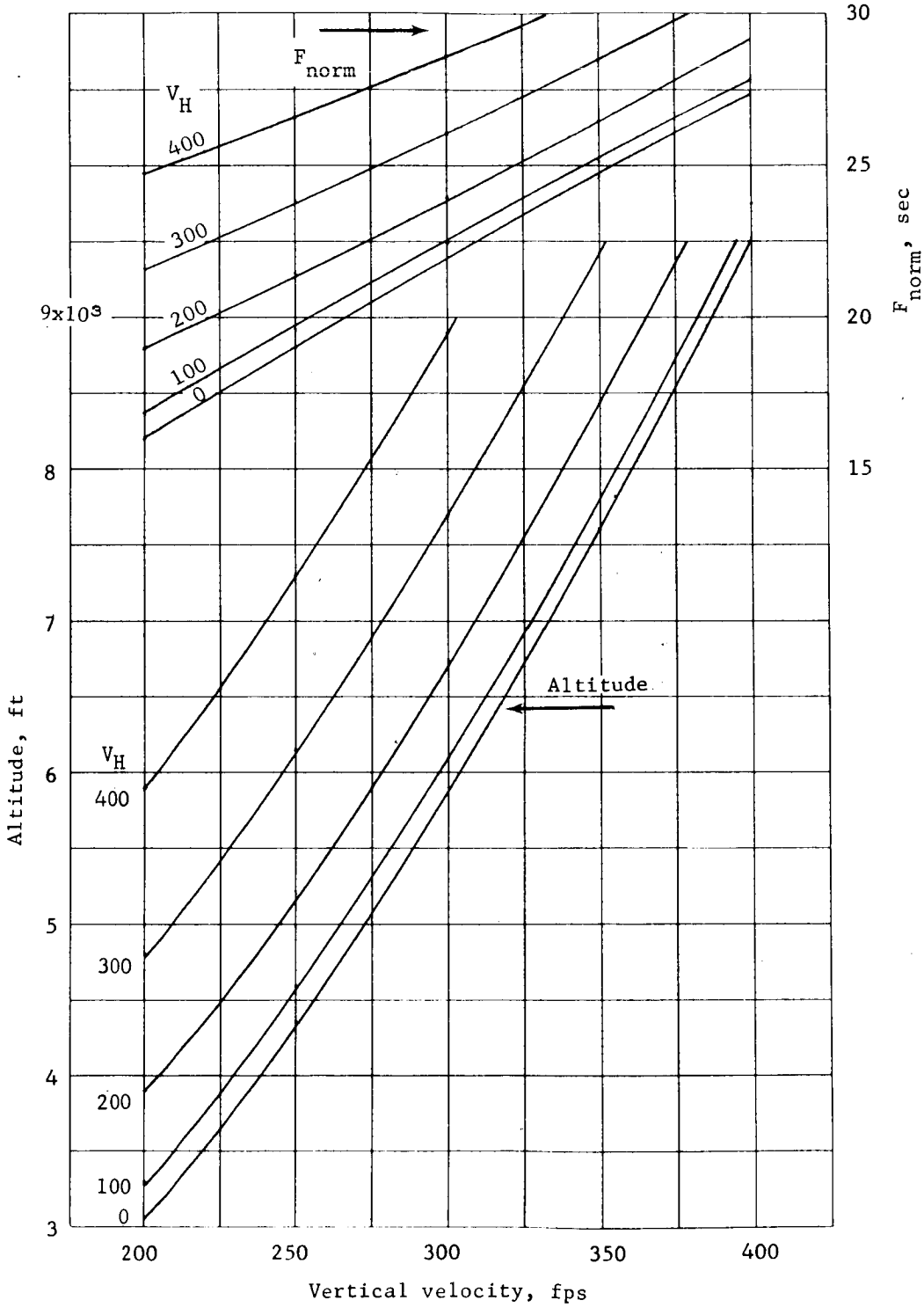

Figure D83.- Vernier Phase Initiation Attitude and Propellant Consumption, Thrust/Weight = 2.0

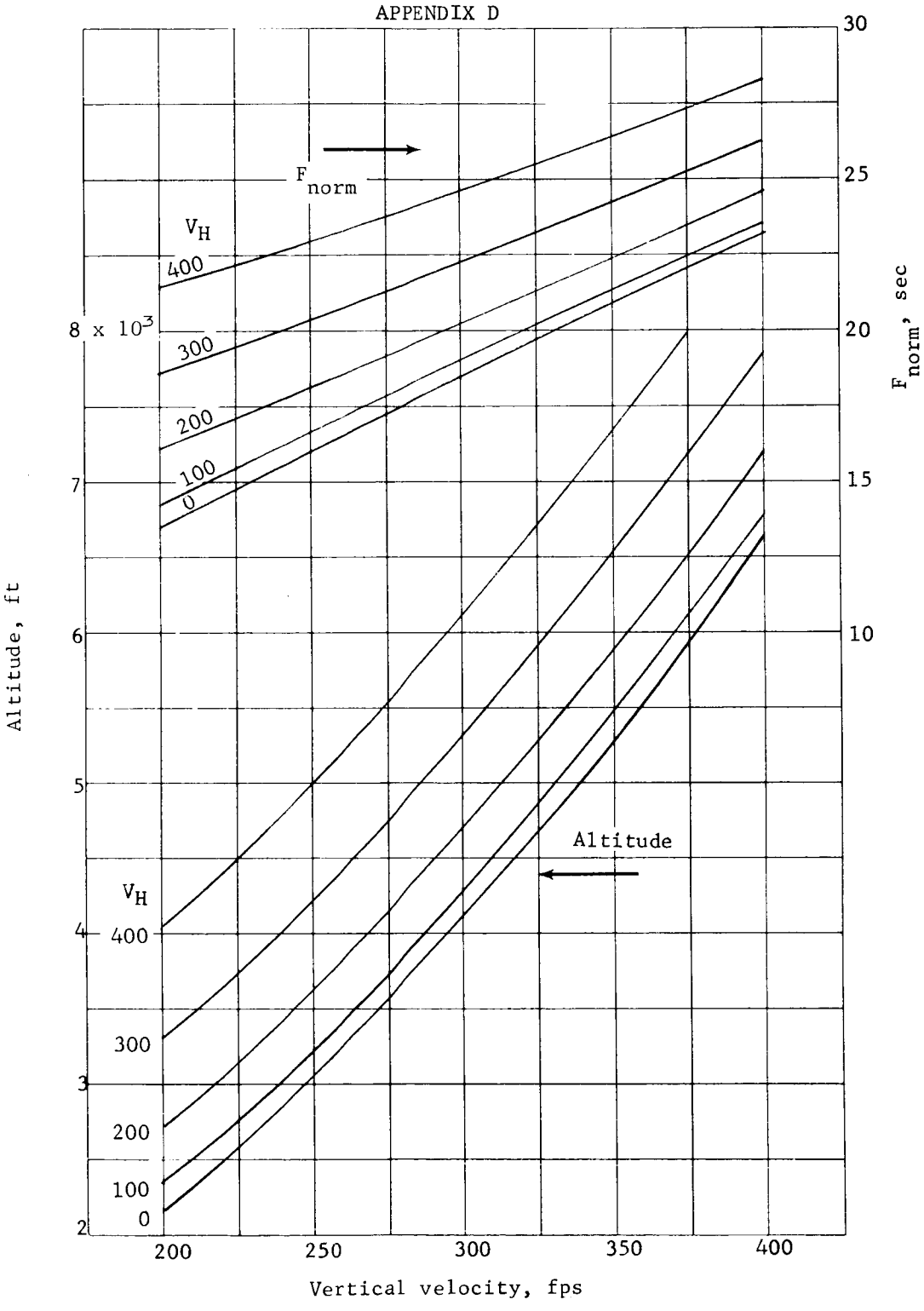

Figure D84.- Vernier Phase Initiation Altitude and Propellant Consumption, Thrust/Weight = 2.5

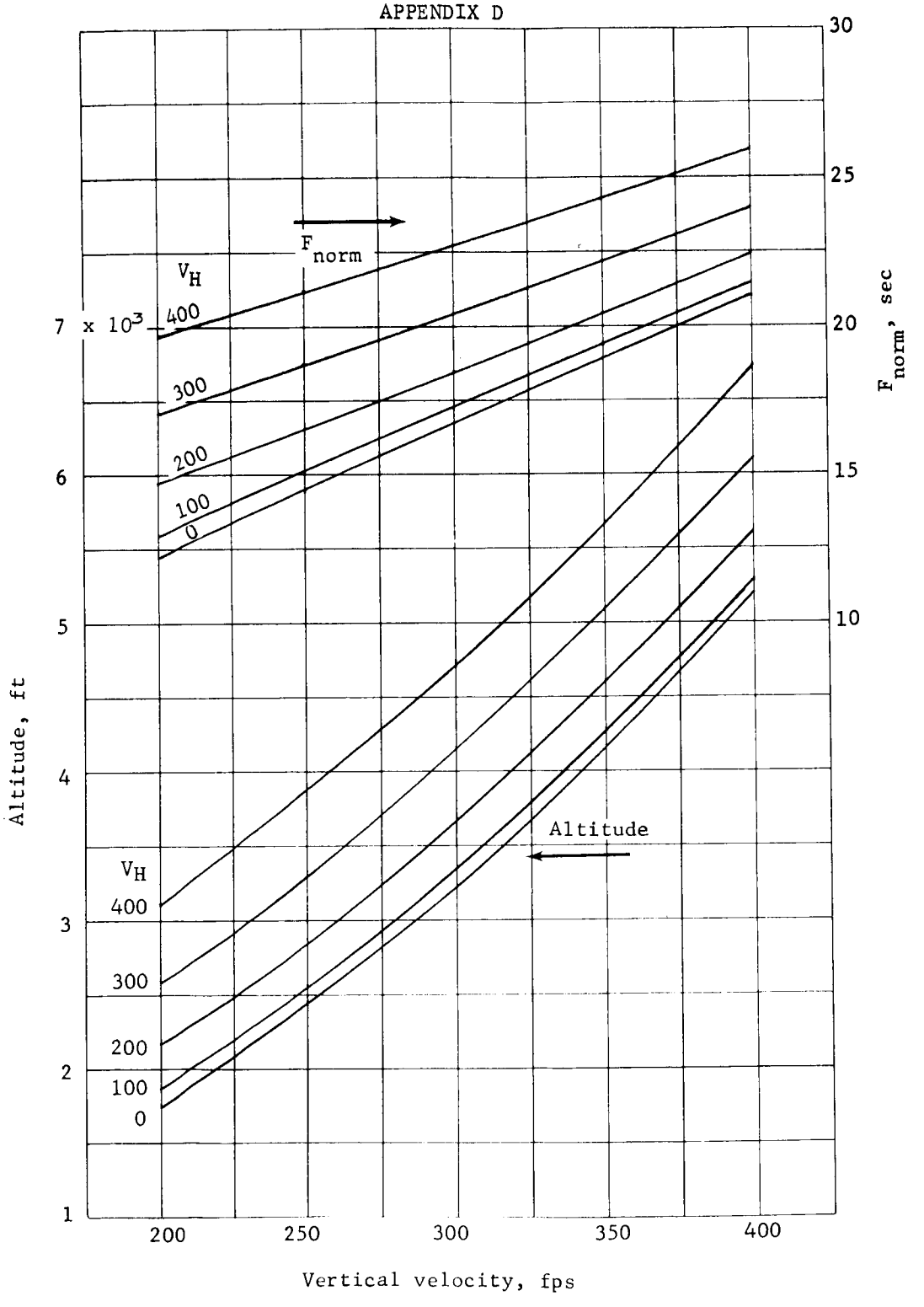

Figure D85.- Vernier Phase Initiation Altitude and Propellant Consumption, Thrust/Weight = 3.0

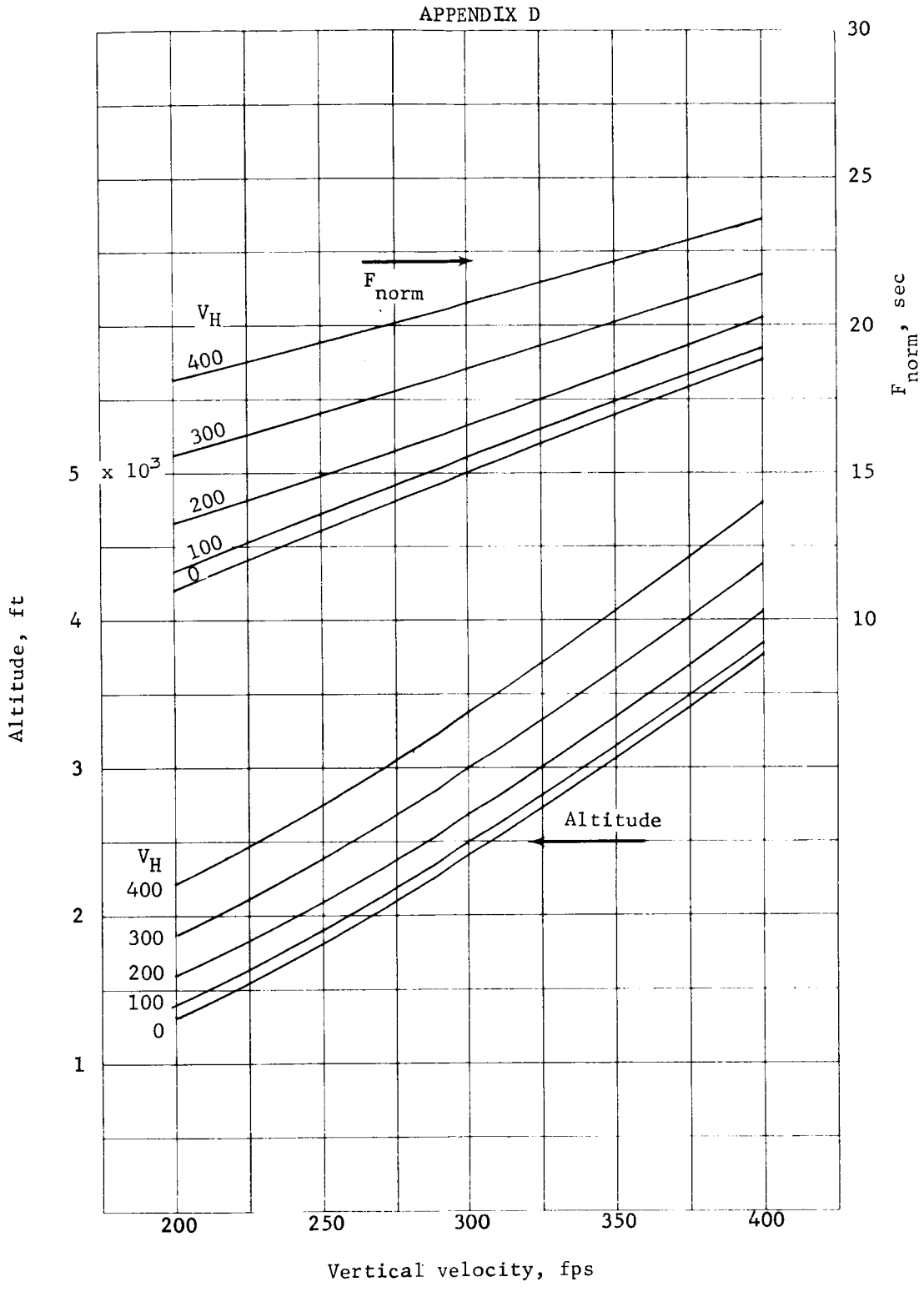

Figure D86.- Vernier Phase Initiation Altitude and Propellant Consumption, Thrust/Weight = 4.0

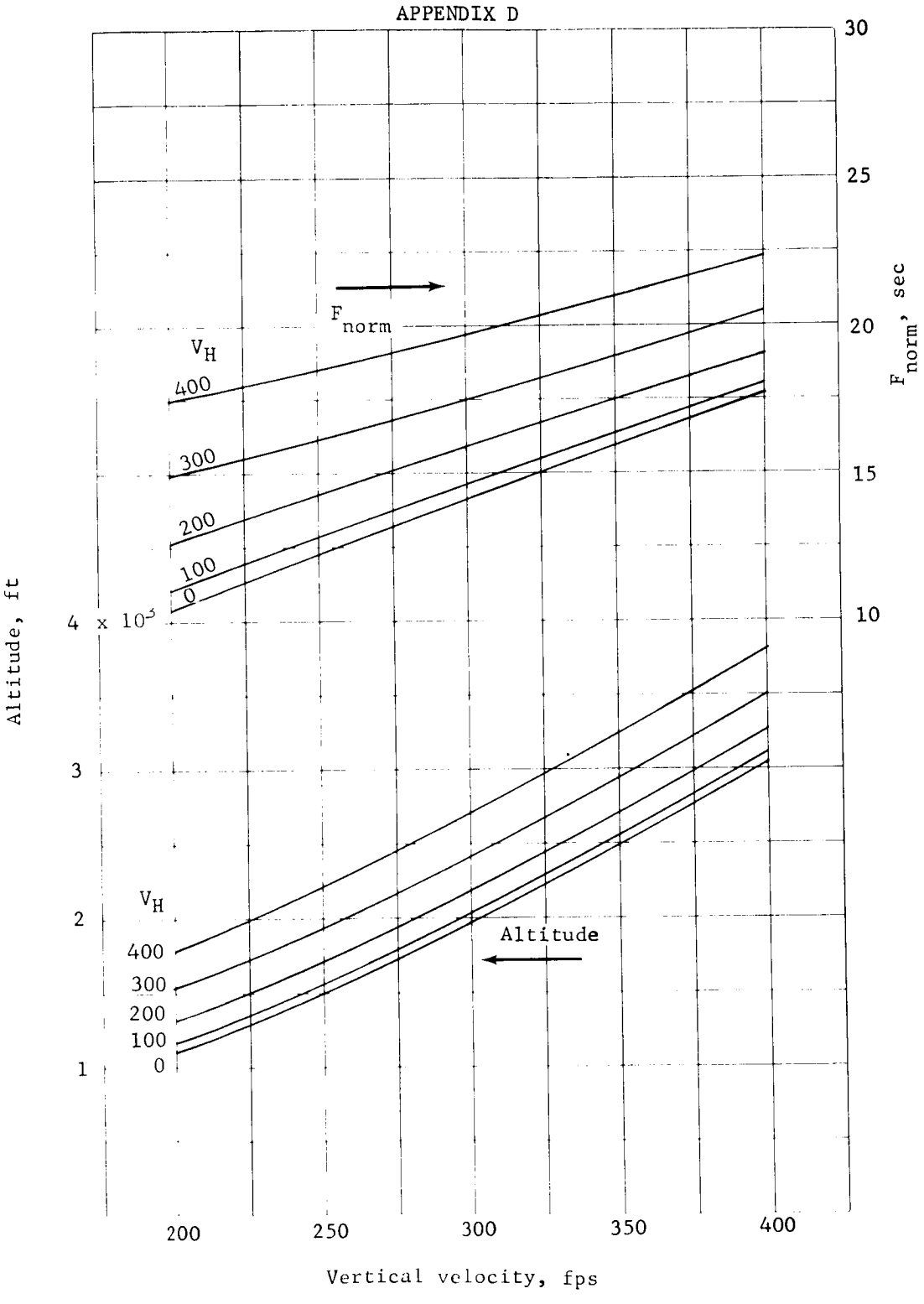

Figure D87.- Vernier Phase Initiation Altitude and Propellant Consumption, Thrust/Weight = 5.0

APPENDIX D

The descent contour used for velocity control is a preprogramed function of range as described previously in this appendix. The acceleration command is generated by comparing measured total velocity, V, from the radar, with the desired velocity, V_d. That is:

$$V_d = f(R)$$

$$V_e = V - V_d$$

$$A_c = K_v V_e$$

where

R = range

f (R) = descent contour

V_e = velocity error

A_c = acceleration command

K_v = gain.

Gravity turn steering is used throughout the vernier phase according to the steering laws:

$$q_c = K_\alpha \frac{w}{u}$$

$$r_c = K_\beta \frac{v}{u}$$

where

q_c = pitch rate command

r_c = yaw rate command

u, v, w = radar body axis velocity components along roll, pitch, yaw, respectively

K_α, K_β = control gains.

APPENDIX D

Figure D88 is a block diagram showing the control system loops. The radar measurements of range and velocity are inherently noisy and as shown, the data must be filtered. In the attitude (pitch or yaw) channels, this filtering causes poor stability unless compensation techniques are used. The q/s feed-paths shown near the radar filter provide this compensation (ref. D11). Proportional plus integral feedback is used to reduce steady-state steering biases. In the velocity control channel, the stability problem is not as difficult so special compensation is not required. The throttle limiter is used to prevent the velocity control channel from saturating the engine thrust and preventing attitude control. For a 5:1 throttle ratio this limiter is set at 90% maximum and 30% minimum limits.

The signals from the pitch, yaw, and velocity channels must be mixed to provide the throttle command for each engine. For a three-engine configuration this mixing matrix is:

$$\begin{bmatrix} X_{c1} \\ X_{c2} \\ X_{c3} \end{bmatrix} = \begin{bmatrix} 1 & -2 & 0 \\ 1 & 1 & \sqrt{3} \\ 1 & 1 & -\sqrt{3} \end{bmatrix} \begin{bmatrix} X_v \\ X_p \\ X_y \end{bmatrix}$$

where

X_{c1}, X_{c2}, X_{c3} are the engine throttle command for each engine

X_v is the velocity channel throttle command

X_p is the pitch channel throttle command

X_y is the yaw channel throttle command.

This mixing matrix results in decoupled channels.

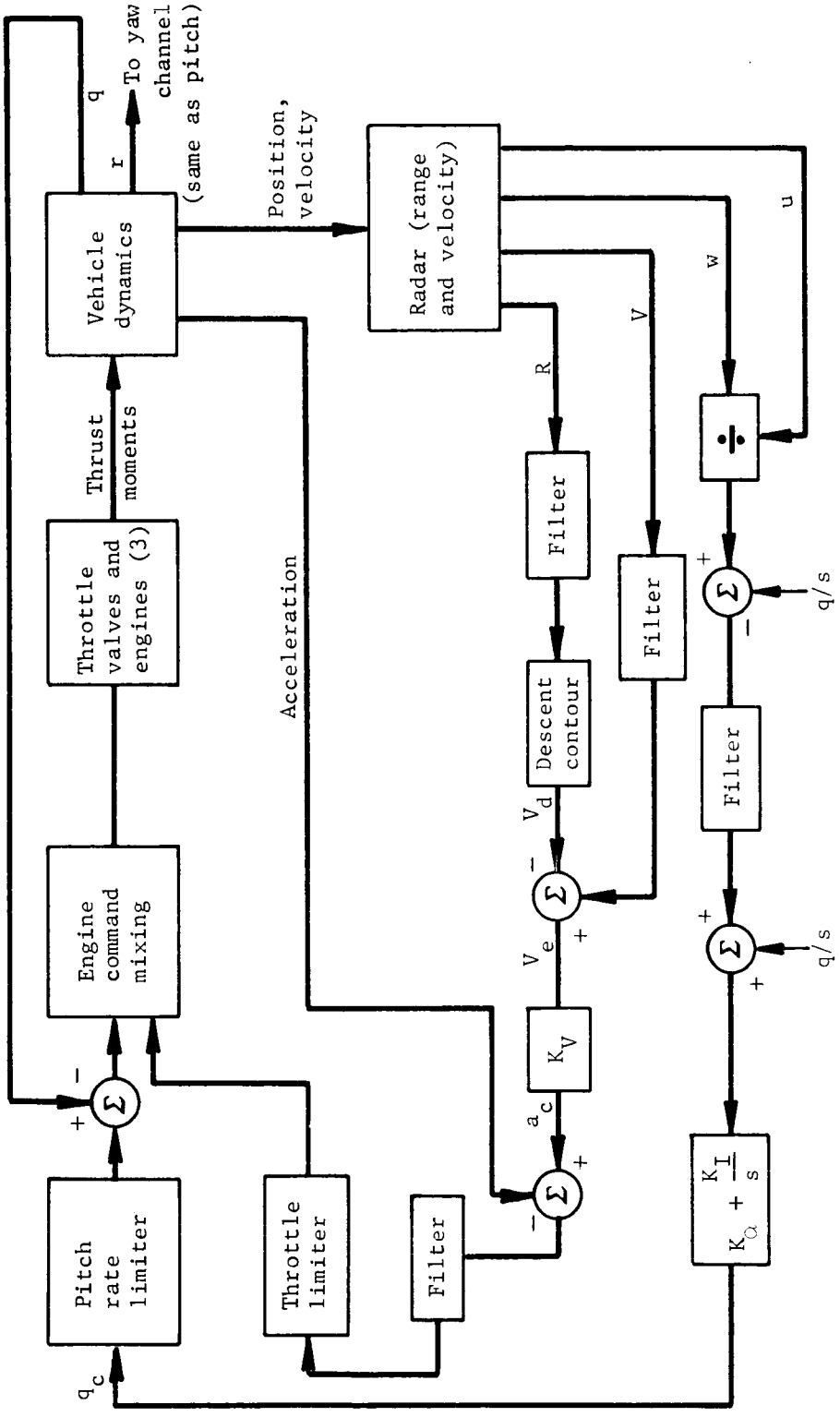

Figure D88.- Vernier Phase Control System

APPENDIX D

The valve-engine dynamic response is important to overall vehicle stability. The requirements for valve-engine response are derived primarily from the attitude channel stability requirements (ref. D11). For the engine combustion and propellant feed delay, a response of about 8 msec (0 to 63%) is expected according to analysis and test data correlation. With no degradation in stability, 15 msec can be tolerated. The valve dynamics are second-order for an electromechanical valve. Valve response of over 25 rad/sec with better than 0.5 damping ratio is required to produce good attitude channel stability. Figure D89 shows a root locus plot of the attitude channel with nominal system gains and dynamics. Figure D90 shows the velocity channel root locus.

The effect of radar noise on the control system transient behavior must be controlled by the filters shown in figure D88. Noise simulation has shown (ref. D11) that filters in the attitude loop with time constants of 0.5 sec or greater are required. The velocity loop filters should be 0.1 sec or greater. The root loci shown in the figures are based on these filter time constants. During the final constant velocity phase of the descent contour, the radar noise produces transient behavior as shown in table D12.

TABLE D12.- RADAR NOISE EFFECT ON VEHICLE RESPONSE

Vehicle variable	3 peak values
Attitude (q/s)	0.7 deg
Attitude rate (q)	0.7 deg/sec
Lateral velocity (W)	0.3 fps

Work is still continuing on the radar noise effects and control system noise sensitivity. This area of design analysis should receive considerable attention early in the program since it affects both radar and propulsion system design.

APPENDIX D

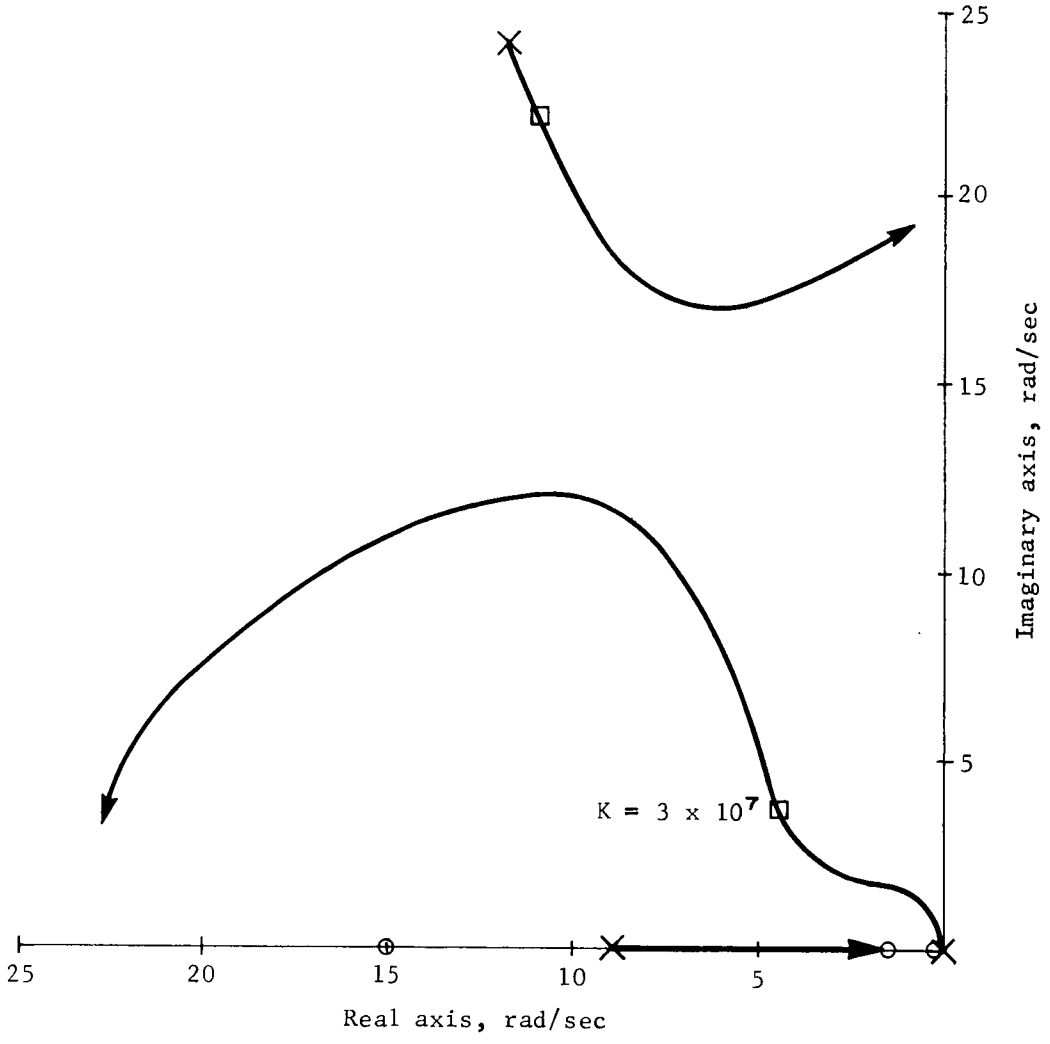

Figure D89.- Attitude Channel Root Locus, Nominal Case

APPENDIX D

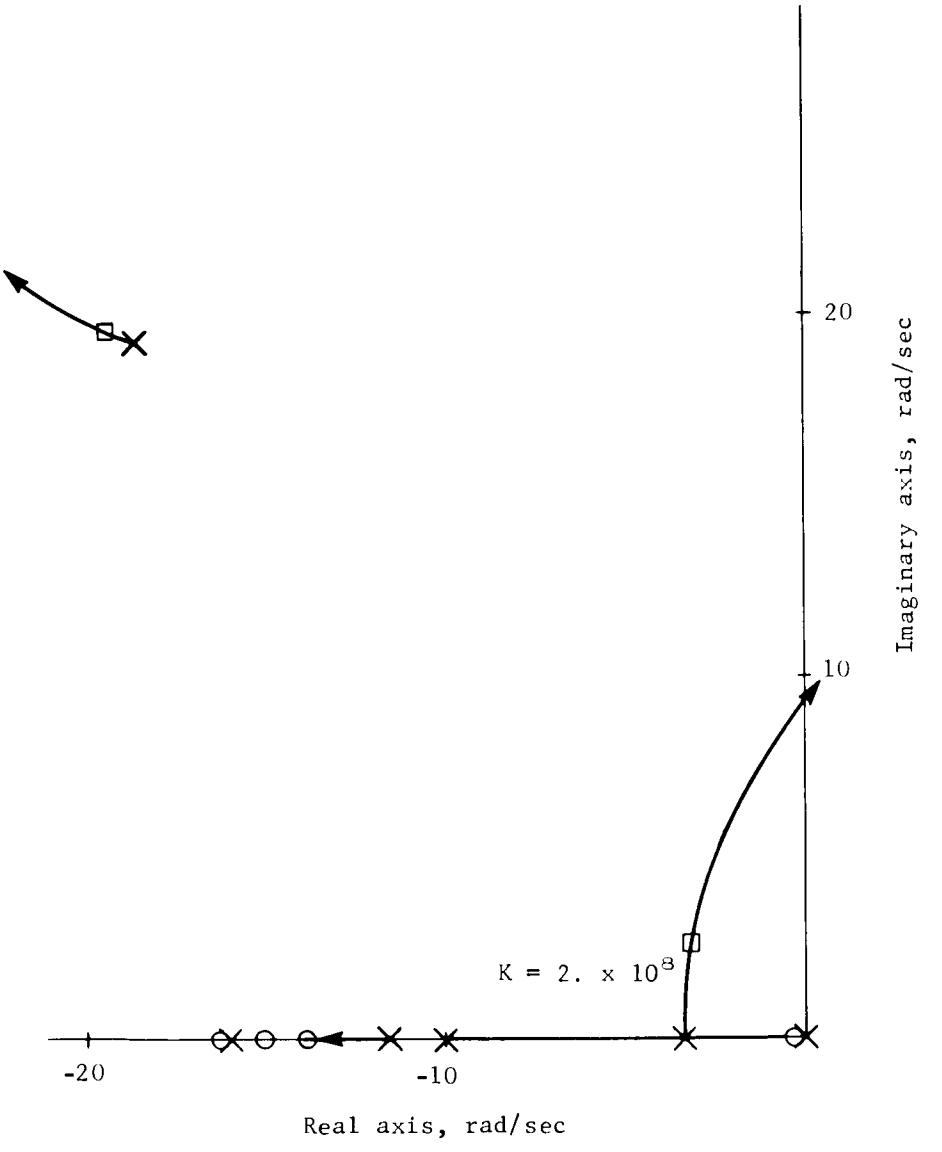

Figure D90.- Velocity Channel Root Locus, Nominal Case

APPENDIX D

5. DATA HANDLING AND STORAGE

A description of functions and defining characteristics for the science subsystem is given in Part II of this report. One of the most significant features of this conceptual design is the inclusion of a tape recorder for bulk storage of science data. The tradeoff involved is that of added cost for development of a sterilizable unit versus risking the loss of imaging data due to a landing when the real-time relay link would occur during darkness. This would be a serious loss because obtaining imagery of the Martian surface surrounding a lander carries the highest priority of all mission objectives.

This section of Appendix D gives essential details of the analysis leading to the conclusion that a tape recorder is required for the mission. The present tape recorder technology was reviewed and results of this review are included. This section is organized in three main topics: (1) a description of the provisions and procedures for data return from a two-day mission, considering both a synchronous and a 10-hr orbit; (2) a summary of constraints on the mission if the capability for storing imaging data is not included; and (3) a summary of the present technological status for developing a sterilizable tape recorder.

Data Return from Entry and Surface Science

Entry science. - Table D13 presents the entry science measurements and data they generate. Data collected during the entry phase of the mission are transmitted over the VHF relay link in both real time and delayed transmission. To prevent possible loss of data because of communications blackout at entry, data collected is delayed approximately 30 sec and interlaced with real-time data for transmission over the relay link.

Entry Science is categorized into two groups -- the high-altitude ballistic phase and the low-altitude terminal descent and landing phase. The type of instruments and their capabilities for entry science measurements are given in Part II. Table D13 gives data sampling rates for these instruments. Only the basic entry science instrument data have been tabulated; other engineering data will also be collected and transmitted to the spacecraft. Figure D91 is a block diagram of the entry science data handling and transmission system.

TABLE D13.- ENTRY SCIENCE DATA COLLECTION

Science instrument	Bits per sample	Sample per second	Total samples	Total bits	Remarks
Entry science - ballistic phase					
Stagnation pressure transducer 1	8	5	1250	10 000	Total samples and total bits
Stagnation pressure transducer 2	8	5	1250	10 000	are based on a nominal time
Accelerometer triad	24	5	1250	30 000	period of 250 sec from 800 000-
Total temperature transducer	8	5	1250	10 000	ft altitude to 20 000-ft
Open ion source mass spectrometer	900	1	20	18 000	altitude.
Entry science - terminal descent and landing phase					
Ambient pressure transducer	8	5	750	6000	Total samples and total bits
Ambient temperature transudcer	8	5	750	6000	are based on a nominal time
Hygrometer	8	5	750	6000	period of 150 sec from 20 000-
Double focusing mass spectrometer	1300	1/3 sec	50	65 000	ft altitude to landing.

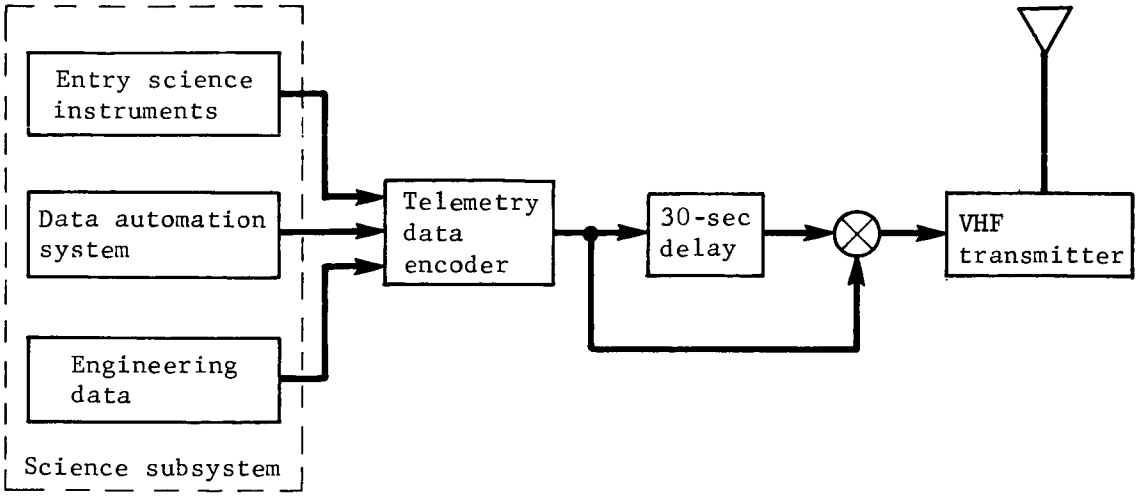

Figure D91.- Entry Science Data Handling and Transmission

Surface science-synchronous spacecraft orbit. - The requirements for surface science are defined in the Mars Mission Objectives. The surface instruments and their characteristics are given in Part II. Table D14 defines the data transmission rates. Relay link communication must be used to meet the goal of imagery data transmission. As noted from table D14 and figure D92, the first relay link communication opportunity is the first 6-minute period after landing, with a total of 1×10^6 bits transmitted. In the synchronous spacecraft mode subsequent relay data transmission opportunities occur every 24.6-hr period. Table D14 shows that in excess of 10^7 bits of imaging data are transmitted in the two-day mission.

TABLE D14.- RELAY LINK COMMUNICATION, SYNCHRONOUS ORBIT SPACECRAFT

Data transmission period	Data transmission duration minimum	Data transmission rate, bps	Data bits transmitted	Type of data
Entry	≈ 400 sec	1500	0.6×10^6	Entry science
Lander touchdown	6 min	3000	1.08	Imagery and meteorology
Touchdown + 24.6 hr	12 min	10 000	7.2	Image, meteorology, and alpha scatter
Touchdown + 49.2 hr	12 min	10 000	7.2	Imagery and meteorology

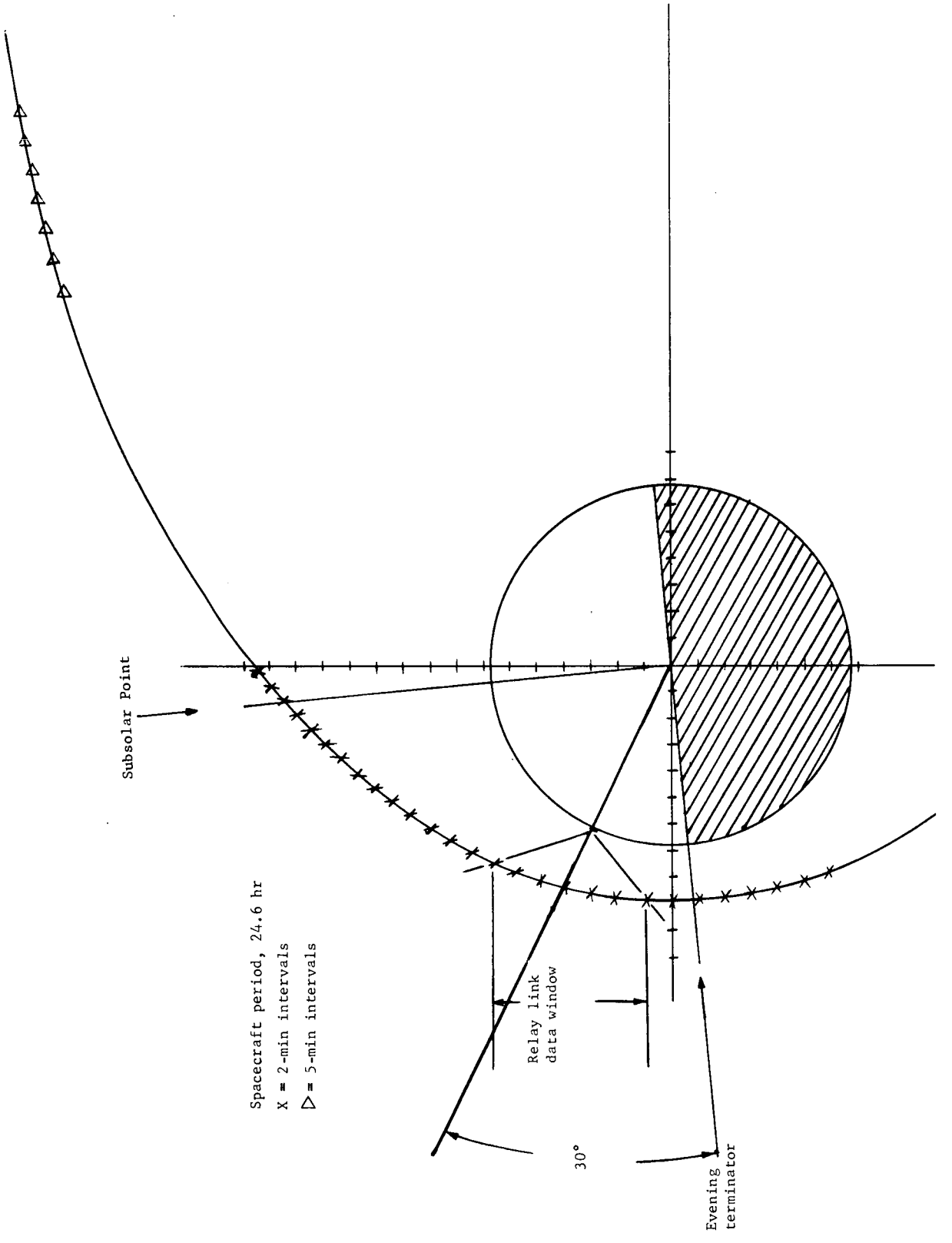

Figure D92.- Synchronous Spacecraft Orbit (1000 km x 33 070 km)

APPENDIX D

TABLE D15.- LANDED SCIENCE DATA COLLECTION, PHASE I

Landed science instrument	Landing, touch-down 0 to 6 min	First 24-hr period	Second 24-hr period
Facsimile camera			
Low resolution (0.1°) images	One 25° azimuth by 70° elevation scene. Total bits: 1.05×10^6	Three 25° azimuth by 70° elevation scenes. Total bits: 3.15×10^6	Two 25° azimuth by 70° elevation scenes. Total bits: 2.1×10^6
High resolution (0.01°) images	None	Two 5° azimuth by 5° elevation scenes. Total bits: 3.0×10^6	Three 5° azimuth by 5° elevation scenes. Total bits: 4.5×10^6
Meteorology package			
Pressure transducer	100 samples, 8 bit binary code. Total bits: 800	1 sample/hr; about 2000 bits/day.	1 sample/hr; about 2000 bits/day.
Temperature transducer	100 samples, 8 bit binary code. Total bits: 800	1 sample/hr; about 2000 bits/day.	1 sample/hr; about 2000 bits/day.
Hygrometer	100 samples, 8 bit binary code. Total bits: 800	1 sample/hr; about 2000 bits/day.	1 sample/hr; about 2000 bits/day.
Sonic anemometer Wind velocity	100 samples, 8 bit binary code. Total bits: 800	1 sample/hr; about 2000 bits/day.	1 sample/hr; about 2000 bits/day.
Wind direction	100 samples, 8 bit binary code. Total bits: 800	1 sample/hr; about 2000 bits/day.	1 sample/hr; about 2000 bits/day.
Alpha scatter spectrometer			
Alpha and proton mode	Instrument deployed to surface to start data collection. No data are transmitted at this time.	Composition data collected continuously over a 12-hr period. Total raw data collected are approximately 10^6 bits; compressed data transmitted are less than 100 000 bits.	None
Engineering data from science subsystem	10 000 bits	20 000 bits	20 000 bits
Summary of total bits	1.064×10^6 bits	6.28×10^6 bits	6.63×10^6 bits

TABLE D16.- RELAY LINK COMMUNICATION, NONSYNCHRONOUS ORBIT SPACECRAFT

Data transmission period	Data transmission duration minimum	Data transmission rate, bps	Data bits transmitted	Lander location at S/C periapsis	Type of data
Entry	≈ 400 sec	1500	0.6×10^6	----	Entry science
Lander touchdown	6 min	3000	1.08	30° from evening terminator	Imagery and meteorology
Touchdown + 31.3 hr (S/C orbit 3)	12 min	10 000	7.2	Dark side	Imagery, meteorology, and alpha scatter
Touchdown + 51.5 hr (S/C orbit 5)	12 min	10 000	7.2	Near evening terminator	Imagery and meteorology

Table D15 presents a breakdown of one possible way in which the surface science instruments may be programed for data collection and relay transmission as a function of the different data transmission opportunities. The quantity of data collected, as represented in table D15, is constrained by the bandwidth of the relay link for each transmission opportunity (see table D14).

Figure D92 is a presentation of the spacecraft in synchronous orbit around Mars. The planned surface lander touchdown point is 30° from the evening terminator. In this mode, the spacecraft passes within relay link communication range of the lander at the same time each day. All imaging data taken and transmitted in real time, therefore, will be obtained with the same sun angle. To provide time separation of viewing during the daylight period, a tape recorder is necessary. Additionally, the tape recorder would act as a backup if the landing on the surface is in an unfavorable imaging location, such as beyond the evening terminator.

Surface science, alternative (nonsynchronous) spacecraft.- Table D16 presents the relay link communications opportunities for landed science in the case of the alternative 1000 km x 15 000 km spacecraft orbit. This is a nonsynchronous orbit; the spacecraft period is 10.2 hr. Because of this, the lander position on the planet with respect to the spacecraft periapsis is different for each orbit. This is shown in figure D93. As noted in figure D93, spacecraft orbits when relay communication is possible (with the defined lander data rate and VHF transmitter power of 10 kbs and 30 W) are orbit 3 at approximately 31 hr and orbit 5 at approximately 51.5 hr. The location of the lander for orbits 3 and 5 when communication opportunities occur is unfavorable for real-time imaging and data transmission. A recorder is therefore necessary to permit imaging during daylight hours. This permits transmission of the data during the dark hours when the relay link to the spacecraft is available.

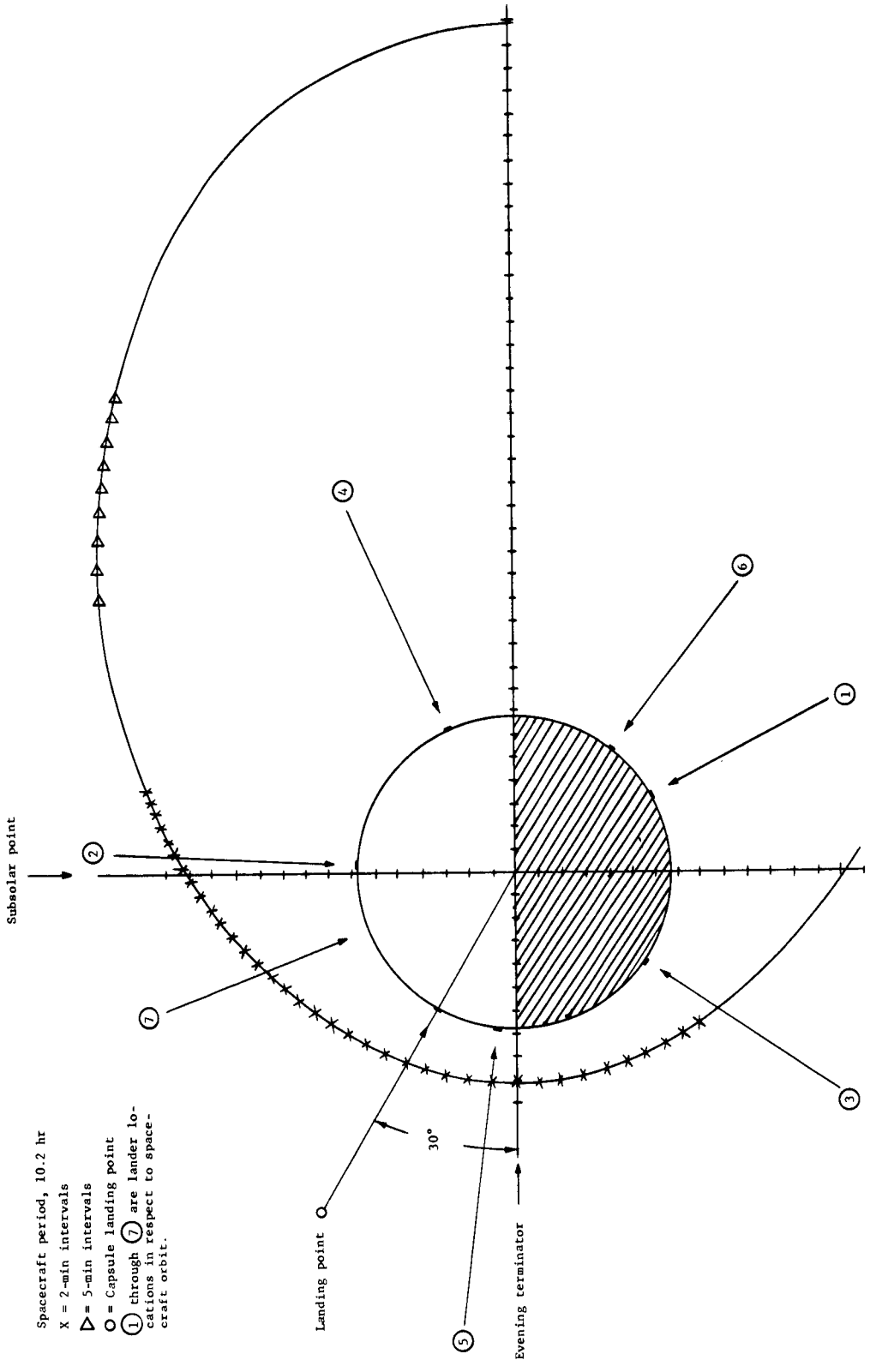

Figure D93.- Nonsynchronous Spacecraft Orbit (1000 km x 15 000 km)

APPENDIX D

Mission Constraint Without a Tape Recorder

The preceding discussion shows the need for a capability for bulk storage of imaging data for a Mars lander mission. This is especially true if the orbiting spacecraft on which relay communication depends is in a nonsynchronous orbit.

Without a tape recorder, the following constraints exist for the mission.

Synchronous orbit spacecraft case:

1) Imaging is limited to the same time each day -- the time when the relay link window occurs;

2) No imaging data will be obtainable if the actual landing site occurs very near or beyond the evening terminator.

The tape recorder provides an insurance factor for obtaining images, plus flexibility for obtaining images under different lighting conditions.

Nonsynchronous orbit spacecraft case:

1) Very low probability of obtaining image data (fig. D93);

2) Opportunities for obtaining images are far apart in time.

As noted in figure D93, the earliest opportunity to transmit image data to the spacecraft (after the initial touchdown period) is on the fifth spacecraft orbit after the initial touchdown period. Contact may be made with the spacecraft on the third spacecraft orbit; however, this is during the dark portion of the diurnal cycle when no imaging data can be taken. During the fifth spacecraft orbit the lander is very near the evening terminator and not in a good location for imaging.

Technology for Sterilizable Tape Recorders

The present technology for sterilizable tape recorders was surveyed. This section contains a review of some of the past programs or studies conducted on sterilizable tape recorders.

APPENDIX D

Table D17 presents some of the fundamental operation parameters for a tape recorder required for the science subsystem.

TABLE D17. TAPE RECORDER OPERATING PARAMETERS

Parameter	Surface laboratory recorder
Storage capacity	10^7 bits
Record rate	[a]10 000 to 20 000 bps
Playback rate	10 000 bps
Other requirements	Sterilizable (135°C)

[a]A fixed record rate within this range will be selected.

Historical review. - In 1963 a contract was awarded to Raymond Engineering Laboratory of Middletown, Connecticut by JPL (ref. D12) to define major problems associated with the complete sterilization (both dry heat and ethylene oxide) of a spacecraft magnetic tape recorder. The endless loop Mariner IV-type magnetic recorder was chosen as the basis for the work because it more closely approached actual flight hardware than any other unit under development at the time.

The initial phase of this effort was concerned with obtaining sterilizable components for the recorder. The individual components considered were magnetic tape, pressure and drive belts, record/playback motors, bearings and lubricants, record/reproduce heads, transport plate, preamplifier electronics modules, end-of-tape sensors, and covers and seals.

Each component developed for and used in the program survived the required sterilization (three 36-hr periods at 145°C) environment before transport assembly. However, the assembled transport, when exposed to the same treatment, was affected significantly by the creation and collection of deposits and debris resulting from numerous chemical interactions. Several transport bearings failed after only a few days of poststerilization operation.

After the failure with the Mariner IV endless loop magnetic tape transport, an investigation (ref. D13) was conducted to determine the effects of thermal sterilization on the 32 different materials used in the construction of this transport. Thermally induced changes in individual materials were considered as well as the mutual compatibility of the materials in the thermal environment.

APPENDIX D

Based on the criteria established, 25% of the products tested were rated compatible, and were recommended as satisfactory for use in a thermally sterilized tape recorder. Another 25% were found to be not compatible, and suitable sterilizable substitutes should be used. About 50% of the materials were considered marginal. Those rated marginal on the basis of percent weight loss can, in many instances, be rid of harmful outgassing materials by thermal-vacuum pretreatments, and thereby be rendered acceptable.

From the estimated quantities of each of the polymeric materials used in the tape recorder, and the total percent weight losses, it was determined that 3.5 to 4.0 g of volatile material was floating in the airtight transport housing after thermal sterilization. The volatile material was composed of water vapor and carbon dioxide, phenols, hydrocarbons, organic acids, esters, amines, and silicones. It was apparent that these chemicals acted deleteriously on both metallic and nonmetallic compoments of the tape transport, particularly in the sealed atmosphere during the elevated temperature cycle. This emphasized the importance of selecting fabrication materials with insignificant weight loss at sterilization temperatures. The necessity for careful and proper handling and cleaning techniques in the preparation of materials was also a conclusion.

As a result of this in-house work at JPL, a request for proposal (ref. D14) was submitted to industry for development of a sterilizable magnetic tape recorder. The RFP included a detailed performance specification (ref. D15) for a sterilizable magnetic tape recorder. This program was never funded.

Voyager Phase B tape recorder study. - During the Voyager Phase B program, a study of sterilizable tape recorders was performed. The information in the following paragraphs was taken from the report of this study (ref. D16).

The potential problem of sterilization reduces to one of obtaining a type of recording tape which does not "block" during prolonged exposure to the sterilization temperature of 135°C. "Blocking" is defined as that phenomenon which causes a roll of recording tape to fuse into a solid block, or "hockey puck," as a result of prolonged exposure to high temperature (ref. D17).

A survey of manufacturer's specifications for all other tape recorder components (e.g., motors, encoders, bearings, lubricants, magnetic heads, etc.) has shown that all can easily withstand prolonged exposure to the 135°C sterilization temperature. In fact,

many of these components can be operated safely at this temperature. Care must be taken during the design phase to assure that no deleterious chemical reactions will occur in the sealed atmosphere within the recorder case.

The only known high-temperature tape currently available is a metallized H-film (DuPont-Kapton) manufactured by Lash Laboratories and known as Pyrotrack. Sales literature available from the manufacturer refers to high packing densities and low head-wear; however, practically no test data are available to support these claims. Without operating experience a firm commitment to this tape is dangerous, however further investigation is warranted.

Under a NASA/GSFC support program (Mr. P. T. Cole), the Memorex Corporation (Dr. Peter Wyman), is now developing a high-reliability, long-life recording tape for aerospace applications. The current effort is essentially an iron-oxide coating, in a thermo-setting binder, on DuPont Kapton H-film. If this program is successful, the resulting tape will meet the Voyager sterilization requirements.

The only problem with sterilizable tape recorders is that of the tape at prolonged sterilization temperatures. Further effort should be devoted to obtaining and flight-qualifying such tape. Other problems, such as multispeed requirements, can be resolved during the design of the recorder. Further effort on the tape problem should include a test program on Lash Laboratories' Pyrotrack and on the tape currently being developed by the Memorex Corporation.

Industry contacts. - To support our present study and determine the latest tape recorder status throughout the industry, a number of industry contacts have been made by Martin Marietta Corporation. Status of various programs were received from the following companies.

Memorex Corporation, Santa Clara, California: Mr. E. Smith and Dr. Peter Wyman report that work has been completed for NASA/GSFC on high-temperature magnetic tape.

Reeves Soundcraft Corp., Danbury, Connecticut: Mr. William A. Morrison reports that no work is in progress at the present time. Reeves has a binder compatible with H-film tape and a patent has been issued on this concept.

APPENDIX D

Lash Laboratories, San Diego, California: Mr. I. J. Hutkin was contacted and reports that Lash has developed Pyrotrak tape, which is a metal-coated Kapton-base tape capable of operation up to 500°F. No new effort with a tape recorder manufacturer is in progress at the present time.

Raymond Engineering Laboratory (REL), Middletown, Connecticut: Messrs. Charles Halpin and Tom Sikora were the REL contacts. REL has provided satellite and space recorders for a number of programs including OSO, Apollo, and Mariner '64 and '67. REL also performed the sterilization tests on a modified Mariner IV tape recorder reported in reference D12. No new work toward sterilization is in progress at this time.

Lockheed Electronics Co., Metuchen, New Jersey: Mr. William Kyle reports that Lockheed Electronics provided the tape recorder for the Mariner '69 spacecraft. The recorder is a part of the data storage subsystem that is actually built by Texas Instruments. There is no sterilization requirement for this recorder.

Leach Corporation, Azuza, California: Messrs. E. D. Murray and J. F. Muench indicated that the Controls Division of Leach Corporation has provided over 260 tape recorders for satellites on NASA and USAF space programs. Leach gained experience in building recorders for unusual and harsh environments during the SNAPSHOT Program of the USAF/AEC. In this program Leach provided the Agena satellite tape recorder hardened for gamma and neutron radiation from the SNAP 10A nuclear reactor.

Leach responded to the JPL request for proposal (ref. D14) on a sterilizable unit. Their response (ref. D18), was prepared by Mr. Joel Slutsky, a recognized expert in the field and now manager of the Mechanical Design Department at Leach. The technical content of this document makes a significant contribution to the technology of sterilizable tape recorders. In summary, the proposal emphasized the problems concerning: chemical interaction resulting from outgassing, belt driven tension, bearings and lubricants, magnetic tape, capstan drive and assembly, the tape reel mechanism, and record and playback heads.

Conclusions. - The vendor survey results show that the state-of-the-art in sterilizable tape recorders has not changed in the past two years. Several programs and studies have been performed to identify the main technical problems and potential solutions to them. However, no concerted effort in terms of a funded program has been made to produce a sterilizable recorder.

APPENDIX D

Based on the information obtained from contacts with Lash Laboratories, Memorex Corporation, and Leach Corporation, it is the conclusion of Martin Marietta that a sterilizable tape recorder can be developed and procured for the '73 Mars mission. Furthermore, the total cost leading up to and including flight articles should be approximately $1 million.

The most important reason for this conclusion is that a required operating lifetime for the '73 lander recorder is only approximately 500 hr. This compares with operating lifetime up to 10 000 hr, which is more representative for space tape recorders. The short operating time will work to advantage in many ways in developing a sterilizable unit. For example, the problem of excessive head wear from a metal-coated tape would not be expected if only 500 hr of operation were required.

APPENDIX D

6. ENTRY SCIENCE ERROR ANALYSIS

To determine what instrumentation complement is necessary for a planetary lander to estimate the atmosphere requires a careful error analysis. This analysis should use reasonable estimates for instrumentation accuracy and should reflect the capabilities of the postflight data analysis techniques.

Several facts can be obtained from this analysis. These include the value of the measurement in estimating the atmosphere, the time during the flight when the measurement should be taken, and its relation to other measurements taken.

The atmosphere estimation task is dependent on the trajectory reconstruction task. Many of the measurements used to estimate the entry trajectory will also be used in the atmosphere estimation process (for example, onboard accelerometers and AMR); the trajectory reconstruction will be used to determine the altitude at which a measurement was taken, given the time it was taken. In fact, the results of the two analyses should be consistent. The Kalman-Bucy minimum variance filter is a technique applicable to simultaneously reconstructing the trajectory and estimating the atmosphere. This estimation scheme amounts to fitting solutions of the equation of motion to the data by linearizing the system equations and then applying the minimum variance linear filter theory.

The reentry model can be fitted into the general problem format wherein the dynamic system can be described by the following system of first order nonlinear differential equations:

$$\dot{X} = f\ (X,t) \tag{D5}$$

The vector X is an n-vector of state, and f is an n-vector of nonlinear functions. The variables being measured are related to the state via algebraic equations:

$$Y\ (t_i) = g\ (X\ (t_i),\ t_i) \tag{D6}$$

where Y is a p-vector of measurement variables. The calculated measurement Y, however, differs from the actual measurement Y_m, as follows:

$$Y_m\ (t_i) = Y\ (t_i) + q\ (t_i) = g\ (X\ (t_i),\ t_i) + q\ (t_i) \tag{D7}$$

where the vector $q\ (t_i)$ is assumed to be normally distributed white noise with zero mean with covariance matrix W.

APPENDIX D

The state vector X includes all variables to be estimated and, as a result of equation (D5), these variables must be solutions of differential equations. Six components of X will be the vehicle's position and velocity, and the differential equations which govern these variables are the kinematic and dynamic equations of motion. Other model parameters can be included in X so long as their governing differential equations can be defined. For example, parameters that are constant throughout the trajectory are governed by the differential equations that state that their time derivations are zero.

We can now state the problem as follows: given measurements $Y_m\left(t_i\right)$, $i = 1, \ldots, m$, determine the solution $X(t)$ to equation (D5) that causes the calculated variables in equation (D6) to agree with the actual measurement Y_m of equation (D7) in some statistical sense.

Before proceeding to the minimum variance estimate, we first must linearize equations (D5) and (D6). Applying a Taylor series expansion and truncating all terms higher than first order, we obtain

$$\dot{x}\ (t) = F\ (t)\ x\ (t) \tag{D8}$$

$$y_m\left(t_i\right) = G\left(t_i\right)\ x\left(t_i\right) + q\left(t_i\right) \tag{D9}$$

where

$$x\ (t) = X\ (t) - X_{ref}\ (t) \qquad y_m\ (t) = Y_m\ (t) - Y_{ref}\ (t) \tag{D10}$$

and

$$F\ (t) = (\partial f/\partial X)_{ref} \qquad G\ (t) = (\partial g/\partial X)_{ref} \tag{D11}$$

Note that the subscript "ref" refers to the reference trajectory about which the equations have been linearized. Equation (D8) has a solution

$$x\ (t) = \Phi\left(t, T_o\right)\ x\left(t_o\right) \tag{D12}$$

where Φ is the state transition matrix and has the property that $\Phi\ (t,t) = I$ for all values of t. Also, Φ satisfies the following matrix differential equation:

$$\dot{\Phi} = F\Phi$$

APPENDIX D

Discretizing equations (D9) and (D12) to times t_n and t_{n+1} yields

$$x\,(t_{n+1}) = \Phi\,(t_{n+1},\ t_n)\ x\,(t_n) \tag{D13}$$

$$y_m\,(t_{n+1}) = G\,(t_{n+1})\ x\,(t_{n+1}) + q\,(t_{n+1}) \tag{D14}$$

The minimum variance unbiased estimated $\hat{x}\,(t_{n+1}/t_{n+1})$ is

$$\hat{x}\,(t_{n+1}/t_{m+1}) = \Phi\,(t_{n+1},\ t_n)\ x\,(t_n) + K\,(t_{n+1})\left[Y_m(t_{n+1}) - Y(t_{n+1}/t_n)\right] \tag{D15}$$

where the optimal linear gain $K\,(t_{n+1})$ is

$$K\,(t_{n+1}) = P^-(t_{n+1})\ G^T\left[G\ P^-(t_{n+1})\ G^T + W\,(t_{n+1})\right]^{-1} \tag{D16}$$

The quantity $Y\,(t_{n+1}/t_n)$ is the best estimate of the measurement corresponding to $\hat{x}\,(t_{n+1}/t_n)$ via equation (D6). The covariance matrix of the state estimate is

$$P^+(t_{n+1}) = P^-(t_{n+1}) - K\,(t_{n+1})\ G\,(t_{n+1})\ P^-(t_{n+1}) \tag{D17}$$

The superscripts (+) and (-) indicate the value of P at time t_{n+1} just before and just after the measurement at t_{n+1} is processed. Between observations, the state and the covariance matrix are propagated by the following equations:

$$\hat{x}\,(t_{n+1}/t_n) = \Phi\,(t_{n+1},\ t_n)\ \hat{x}\,(t_n/t_n)$$

$$P^-(t_{n+1}) = \Phi\,(t_{n+1},\ t_n)\ P^+(t_n)\ \Phi^T(t_{n+1},\ t_n)$$

APPENDIX D

Application to the Entry Error Analysis Problem

This error analysis technique requires a reference trajectory. All matrices and derivatives are evaluated along this reference trajectory. Estimates must be made for the initial covariance matrix P and the error for each measurement, which is assumed to be available. The covariance matrix of the state vector is updated at each measurement time using equations (D16) and (D17).

The dynamic equations of motion that balance instantaneous forces and accelerations on a vehicle represented by a particle mass are:

$$\dot{u} = \frac{1}{m} F_{RV} + \frac{1}{r} (v^2 + w^2) - \mu/r^2 + \Delta\dot{u}_{ROT}$$

$$\dot{v} = \frac{1}{m} F_{ev} + \frac{1}{r} (v\, w \tan \varphi - u\, v)\, \varphi\, \Delta\dot{v}_{ROT}$$

$$\dot{w} = \frac{1}{m} F_{\varphi v} - \frac{1}{r} (v^2 \tan \varphi + uw) + \Delta\dot{w}_{ROT}$$

The kinematic equations for altitude, latitude, and longitude are:

$$\dot{h} = u$$

$$\dot{\varphi} = w/r$$

$$\dot{e} = v/r \cos \varphi$$

The external forces can be written

$$\begin{bmatrix} F_{RV} \\ F_{\theta V} \\ F_{\varphi V} \end{bmatrix} = q\ S\ A \begin{bmatrix} -C_D \\ C_Y \\ -C_L \end{bmatrix}$$

were A is a 3 x 3 matrix relating the stability axes with the axis system, which is a function of ψ_A, γ_A, σ, β.

APPENDIX D

The rotation terms are (using abbreviations s = sine and c = cosine):

$$\Delta\dot{u} = r\Omega^2 c^2\varphi + 2\Omega v c\varphi$$

$$\Delta\dot{v} = 2\Omega (w s\varphi - u c\varphi)$$

$$\Delta\dot{w} = -\Omega s\varphi [r c\varphi - 2 v]$$

The model atmospheres used in this analysis are of the VM type. These are defined by as adaibatic lapse rate up to the tropopause and a constant temperature above the tropopause. Five parameters are used to define such a model atmosphere. These five quantities are the surface pressure P_s, surface temperature T_s, tropopause temperature, T_u, tropopause altitude, h_T, and molecular weight, M_o. These five quantities determine the atmosphere by means of the of the barometric equation and perfect gas law. Below the tropopause the temperature is given by

$$T(h) = T_s + \left(\frac{T_u - T_s}{h_T}\right) h$$

The local pressure is given by

$$P(h) = P_s \left(\frac{T_s}{T(h)}\right)^{\frac{GM_o h_T}{R^* (T_u - T_s)}}$$

where $G = 3.75$ m/sec^2 and $R^* = 8.316963 \times 10^7$ erg/gram-mole deg. Above the tropopause, the temperature is constant. The local pressure is given by

$$P(h) = P_s \left(\frac{T_s}{T_u}\right)^{\frac{GM_o h_T}{R^* (T_u - T_s)}} \exp\left[-\frac{GM_o}{R^*}\left(\frac{h - h_T}{T_u}\right)\right]$$

The atmosphere density is obtained from the perfect gas law.

$$\rho = \frac{M_o}{R^*} \frac{P(h)}{T(h)}.$$

APPENDIX D

A computer program for the CDC 6400 has been written which solves these equations.

The state vector of quantities considered uncertain consists of the six trajectory defining quantites, u, v, w, h, φ, θ and three angles, σ, β, γ, which define the orientation of the vehicle with respect to the velocity oriented axis system. This state vector may be augmented to include the five defining parameters for the atmosphere, a bias on each of the accelerometers, correction terms in the aerodynamic model, and correction terms in the error models of the various sensor. The quantities measured are algebraic functions of the state vector and thus are not included as components in the state vector. If a computer er program using the minimum variance technique were developed to perform a trajectory reconstruction and atmosphere estimation, the quantities in the state vector would all be estimated. The measured angular rates are deterministically integrated to determine the vehicle orientation.

Quantities Measured

The measurements that were assumed to be available were:

1) Altitude from altitude measuring radar;
2) Accelerations from triad of accelerometers;
3) Stagnation pressure from pressure sensor;
4) Direct density measurement from high-altitude mass spectrometer;
5) Temperature measurement from high-altitude mass spectrometer;
6) Ambient pressure from low-speed pressure sensor.

The various measurements are functions of the components of the state vector.

Altitude

$$h_m = h$$

Stagnation Pressure

$$P_{ml} = \frac{1}{2} \rho \left(h, P_s, T_s, T_u, h_T, M_o\right) \cdot (u^2 + v^2 + w^2)$$

Accelerations

$$\begin{bmatrix} A_x \\ A_y \\ A_z \end{bmatrix} = \frac{qS}{m} \begin{bmatrix} c\alpha & 0 & s\alpha \\ 0 & 1 & 0 \\ -s\alpha & 0 & c\alpha \end{bmatrix} \begin{bmatrix} -C_D \\ C_Y \\ -C_L \end{bmatrix}$$

Density (from mass spectrometer)

$$\rho_m = \rho\left(h,\ P_s,\ T_s,\ T_u,\ h_T,\ M_o\right)$$

Temperature (from mass spectrometer)

$$T_{m1} = T_u$$

Pressure

$$P_{m2} = P\left(h,\ P_s,\ T_s,\ T_u,\ h_T,\ M_o\right)\left(1 + \frac{\gamma-1}{2} M^2\right)^{\gamma/\gamma-1}$$

Temperature

$$T_{m2} = T\left(h,\ T_s,\ T_u,\ h_T\right) \cdot \left(1 + \frac{\gamma-1}{2} M^2\right)$$

Initial conditions at 100 km for the entry trajectory were assumed for both a direct entry from the Earth-Mars transfer orbit and for an entry from a Martian planetary orbit (see table D18). Entry into both VM-5 and VM-8 atmospheres was considered. For the direct entry, a ballistic coefficient of 0.35 slug/ft^2 was used; for the entry from orbit, a ballistic coefficient of 0.45 slug/ft^2 was used.

APPENDIX D

TABLE D18.- STATE VECTOR COMPONENTS AND STANDARD DEVIATIONS AT 100 km

Parameter	Direct entry		Entry from orbit	
	Nominal	Standard deviation	Nominal	Standard deviation
Vertical velocity, m/sec	-2075.	15.	-1298.	22.8
Easterly velocity, m/sec	5166.	4.3	4143.	6.
Northerly velocity, m/sec	0.	1.	0.	1.
Altitude, km	100.	11.2	100.	38.7
Latitude, deg	0.	.182	0.	.206
Longitude, deg	0.	0.	0.	0.
Roll angle, deg	0.	.212	0.	.212
Sideship angle, deg	0.	.212	0.	.212
Angle of attack, deg	0.	.212	0.	.212
Atmosphere parameter	VM-5		VM-8	
Surface temperature, °K	275.	137.5	200.	100.
Tropopause temperature, °K	200.	100.	100.	50.
Surface pressure, mb	14.	7.	5.	2.5
Tropopause altitude, km	19.3	9.65	18.6	9.3
Molecular weight, kg/m^3	.0312	.0156	.044	.022

The standard deviation for each measurement was assumed to be a fraction of the expected measurement. However, to prevent the standard deviation on the accelerometer and dynamic pressure measurement from becoming too small, a constant 0.04 m/sec^2 and 0.1 mb was root sum squared with the standard deviation obtained by taking a fraction of the measurement to obtain the standard deviation processed by the computer program (table D19).

Several different instrumentation payloads were considered. The density and pressure of the less dense VM-8 atmosphere was more difficult to estimate at the higher altitudes (above 50 km) with only accelerometer and a stagnation pressure measurement. This is because of the low densities, and thus low accelerations and measured stagnation pressure above 50 km. However, the addition of a high altitude mass spectrometer clearly improves the estimate of these quantities at these altitude (fig. D94).

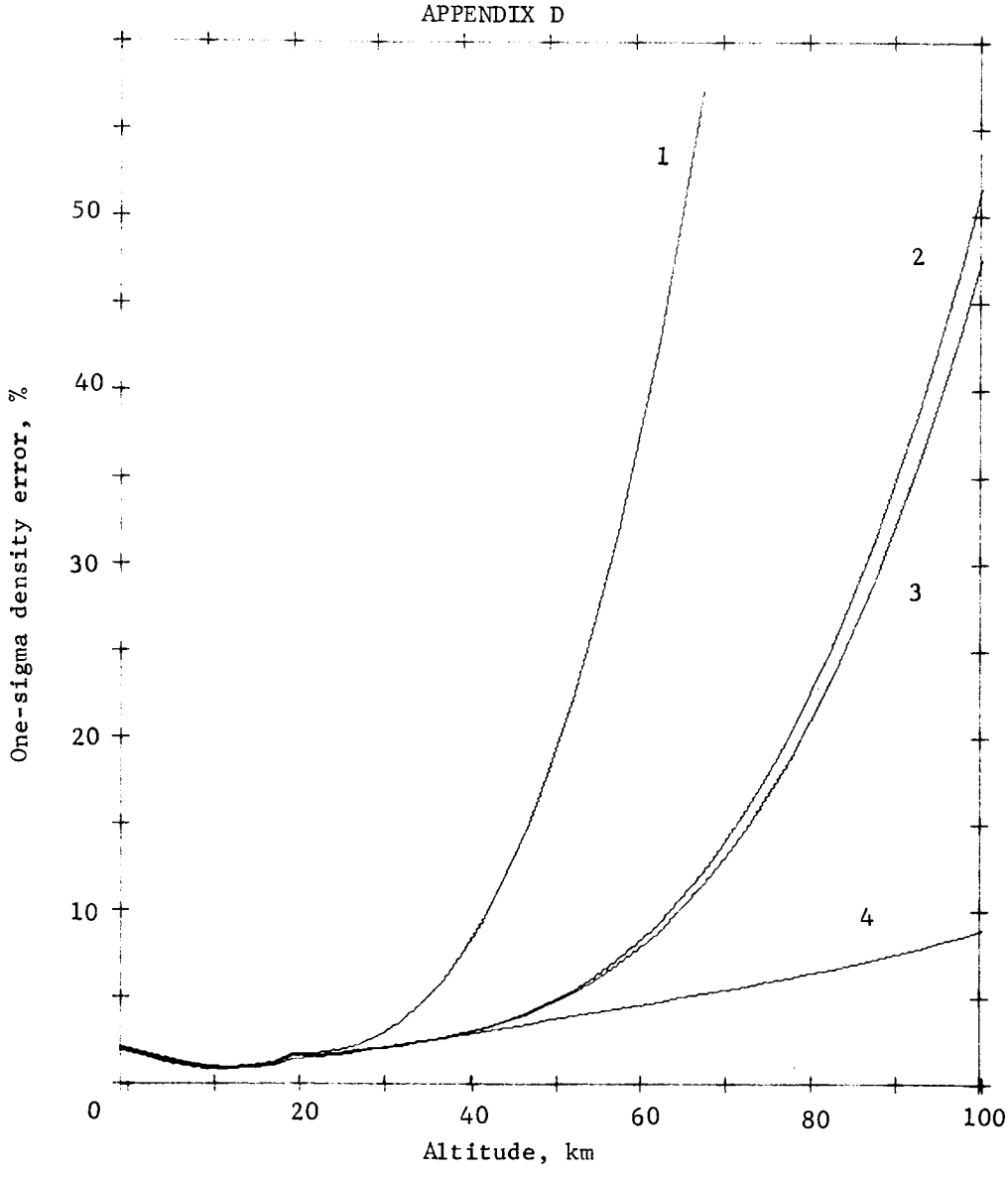

(a) Density

Curve	Measurements
1	Accelerometers (3%), AMR
2	Accelerometers (3%), AMR, and stagnation-pressure (entry from orbit)
3	Accelerometers (3%), AMR, and stagnation-pressure (direct entry)
4	Accelerometers (3), AMR, and high-altitude temperature and density

Figure D-94.- Entry into VM-8 Atmosphere, 3% Accelerometers

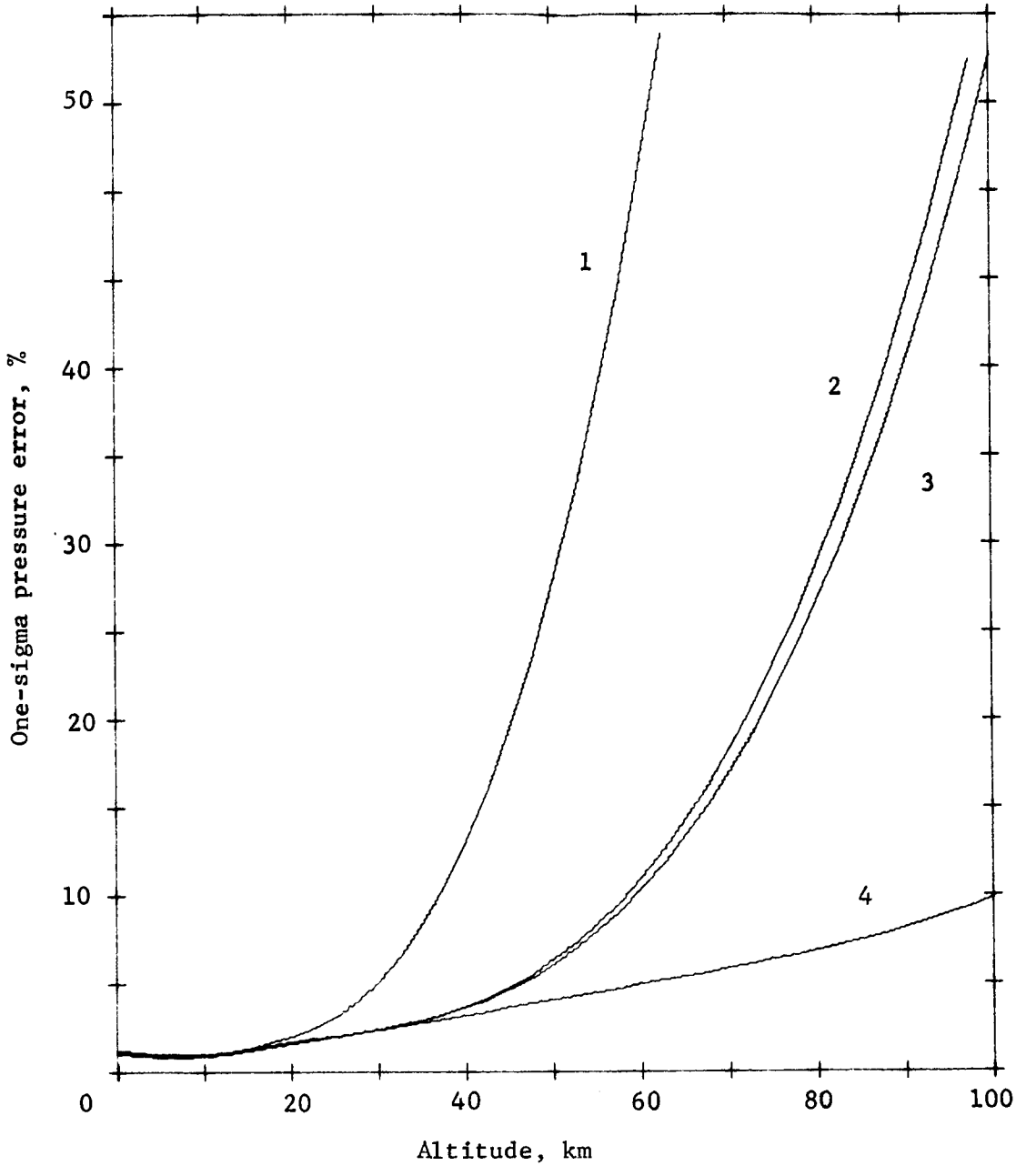

(b) Pressure

Figure D94.- Continued

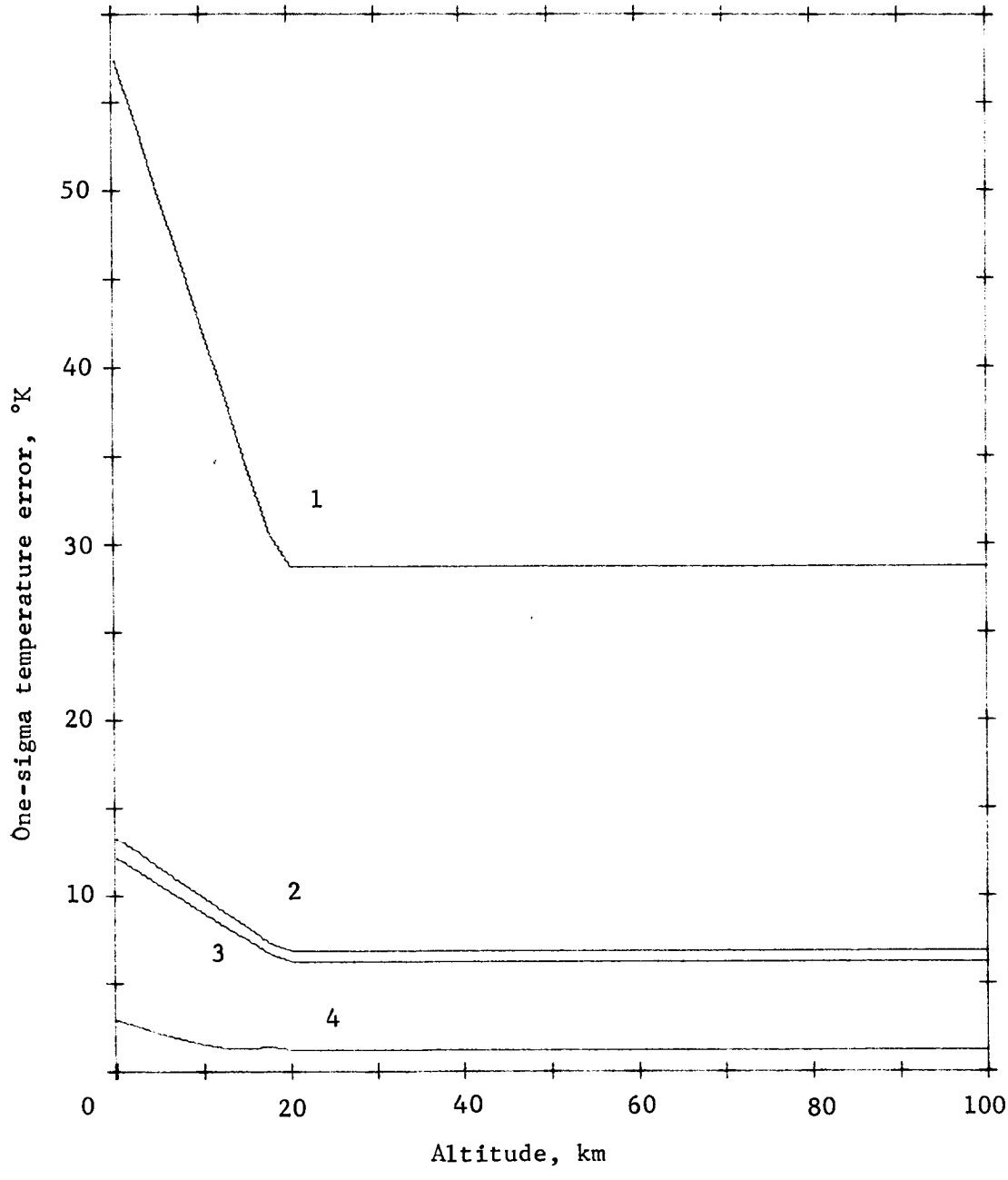

(c) Temperature

Figure D94.- Continued

Curve	Measurements
1	Accelerometers (0.1%), AMR
2	Accelerometers (0.1%), AMR and stagnation-pressure
3	Accelerometers (0.1%), AMR and high-altitude temperature and density

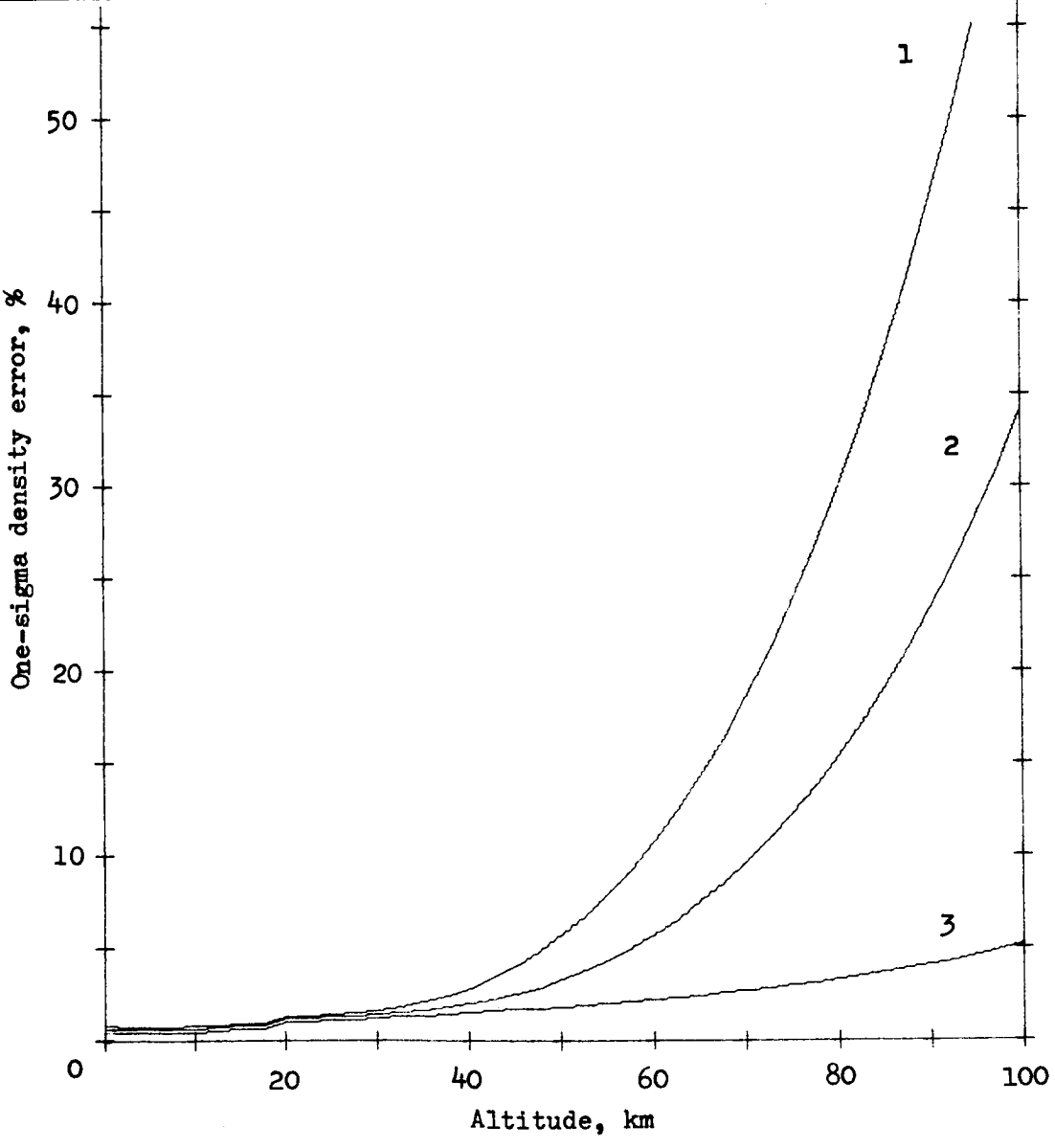

(d) Density

Figure 94.- Continued

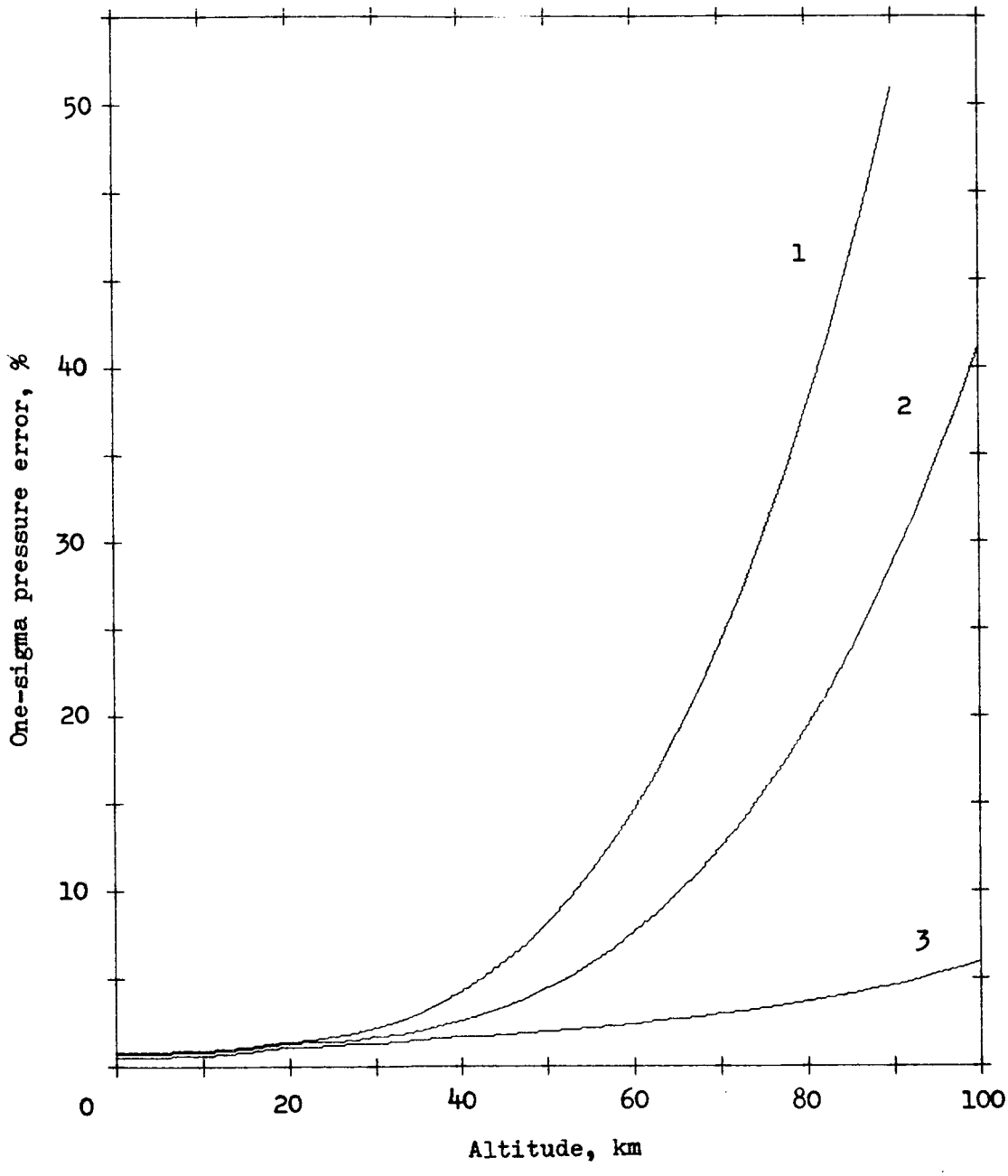

(e) Pressure

Figure 94.- Continued

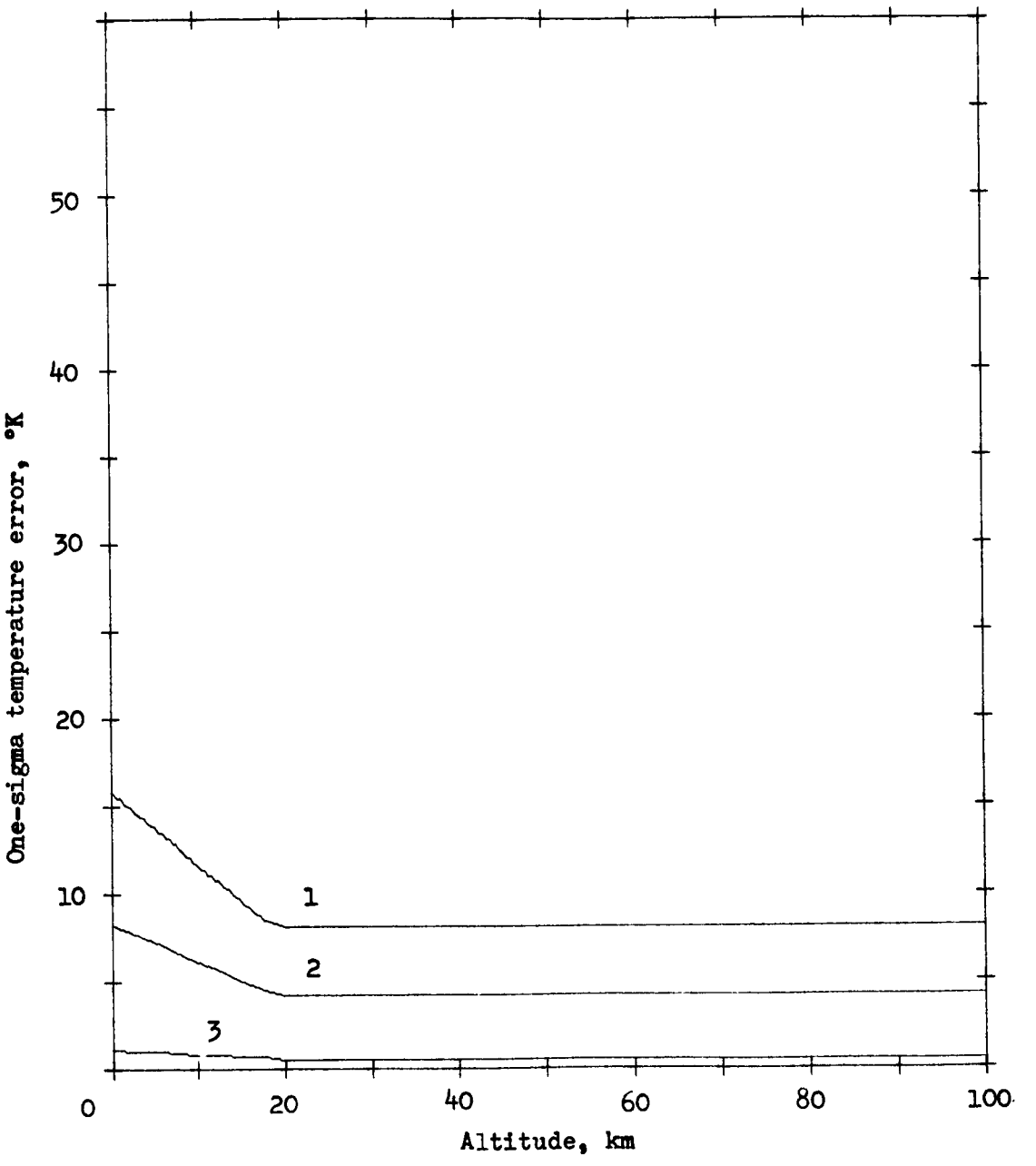

(f) Temperature

Figure 94.- Concluded

APPENDIX D

TABLE D19.- MEASUREMENT RATES AND ACCURACY

Measurement	Accuracy	Rate, sec	Altitude available, km	Number of measurements processed
For VM-5 entry				
Accelerometer triad	3% of measurement (see text)	1 sec	0 to 100	181
Stagnation pressure measurement	2% of measurement (see text)	1 sec	31 to 100	47
For VM-8 entry				
Accelerometer triad	3% or 0.1% of measurement (see text)	1 sec		81
Stagnation pressure	2% of measurement (see text)	1 sec	8 to 60	38
High-altitude density	10% of measurement	1 sec	70 to 100	21
High-altitude temperature	10% of measurement	N/A	100 only	1
Low-altitude temperature	10°K	1 sec	0 to 5	35
Low-altitude pressure	5% of measurement	1 sec	0 to 5	35

Most of the work done in the analysis assumed an entry directly from an Earth-Mars orbit.

To determine the effect of entry conditions on atmosphere determination, the entry conditions for an entry from orbit were used with onboard instrumentation of accelerometers, AMR, and stagnation pressure sensor. The errors in the atmosphere with this mode of entry were not significantly different that those resulting from an entry directly from the Earth-Mars orbit (fig. D94).

APPENDIX D

Different accuracies and data rates were considered for the more important instruments. A 10-sec data rate for the AMR was used. This resulted in altitude measurements at approximately 59.5 km, 40.0 km, 23.7 km, 11.5 km, and 6.7 km. The resulting accuracy estimate is shown in figure D95. The errors in the atmosphere estimate for the 10-sec AMR data rate are larger than for the 1-sec AMR data rate because of the poorer ability to correlate the measurements with the altitude at which they were taken.

More accurate accelerometers are also considered. The curves presented in figure D94(d), (e), and (f) show the error estimates resulting from the use of 0.1% accelerometers. These curves can be compared with those in figure D94(a), (b), and (c) to determine the significance of more accurate accelerometers.

A more accurate high altitude mass spectrometer was also used. The errors resulting from using a 5% accurate mass spectrometer (vs. 10%) are shown in figure D95. The high altitude temperature and density are computed from the neutral number densities measured by the mass spectrometer. The addition of low altitude -- low velocity ($M < 3$) measurements of pressure was included to determime what improvement could be obtained by near-surface measurements (see fig. D95).

Several entries into a VM-5 atmosphere were simulated. The obvious characteristic in this case is that both pressure and density could be determined accurately, even at the altitude above 50 km (see fig. D96). This follows from the higher density, and thus larger accelerometer and stagnation pressure measurements that occur above 50 km. Figure D97 presents axial acceleration versus altitude; the effect of the denser atmosphere is quite obvious.

Due to the simple atmosphere model, the estimated errors are probably too small. Also, sources of error such as telemetry transmission noise have been neglected. In particular, the simple temperature profile assumed for the VM atmospheres results in an estimate for the reconstructed temperature that is too low. If, instead of estimating only the surface temperature and tropopause temperature, it were necessary to determine a large number of temperature profile parameters, the estimated errors would be larger.

The information to be gained from this analysis is the relative importance of the various measurements. The relation of the various accuracy estimates should remain the same, even if the estimated errors are larger.

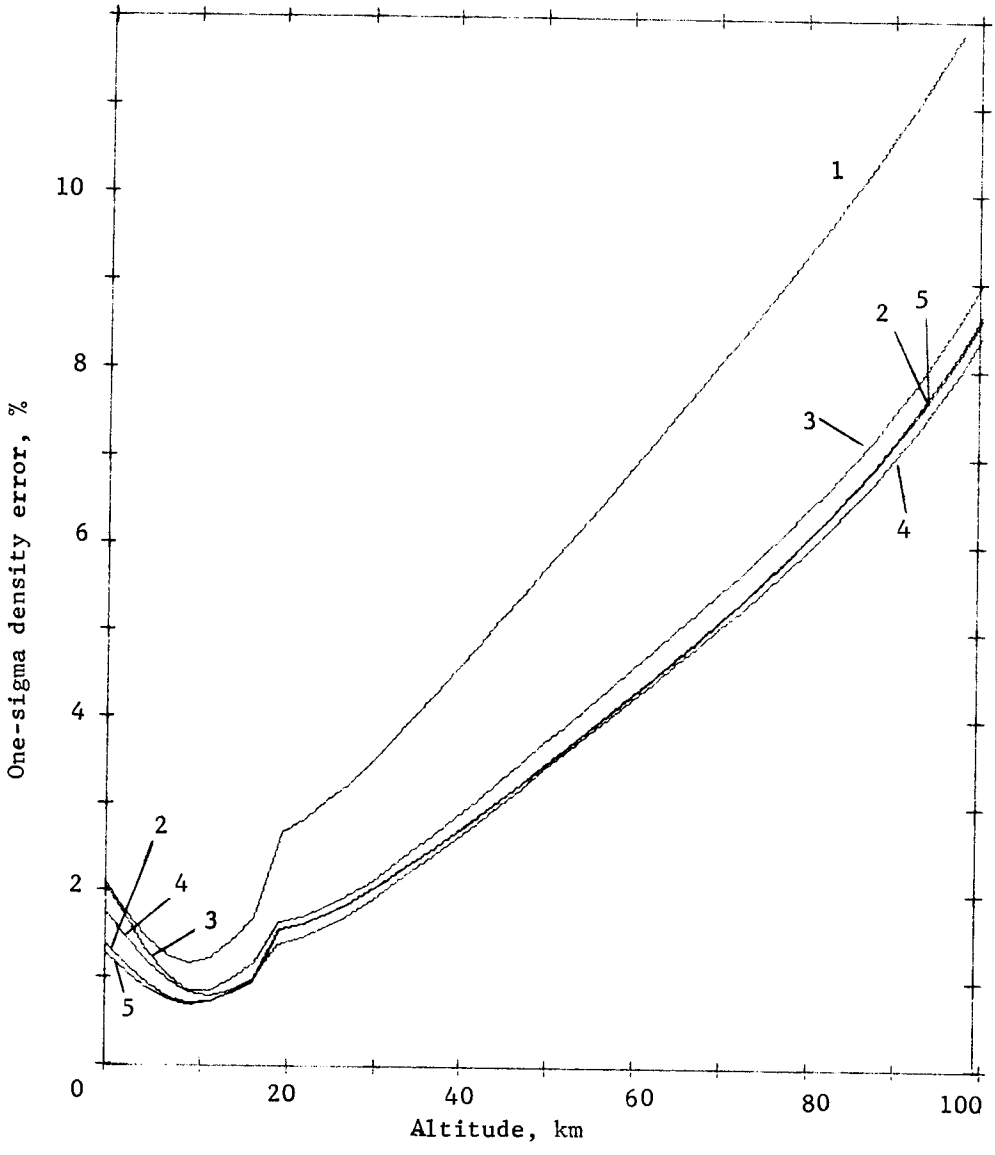

(a) Density

Curve	Measurements
1	Accelerometers, AMR (10 sec), high-altitude, temperature, and density
2	Accelerometers, AMR, high-altitude temperature (5%) and density (5%)
3	Accelerometers, AMR, and high-altitude temperature and density
4	Accelerometers, AMR, and high-altitude temperature, density, and stagnation-pressure
5	Accelerometers, AMR, and high-altitude temperature and density; low-altitude pressure

Figure D95.- Entry into VM-8 Atmosphere

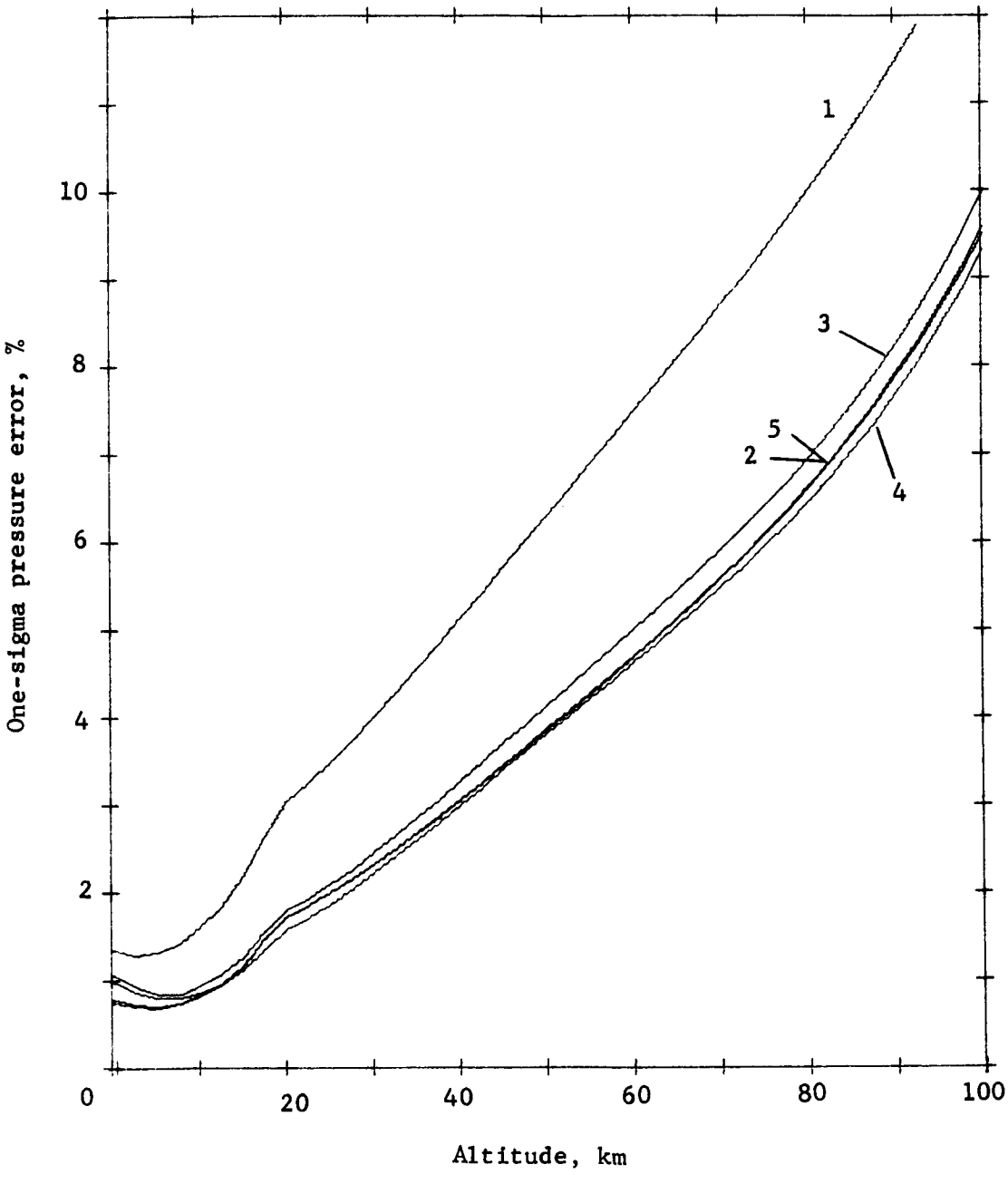

(b) Pressure

Figure D95.- Continued

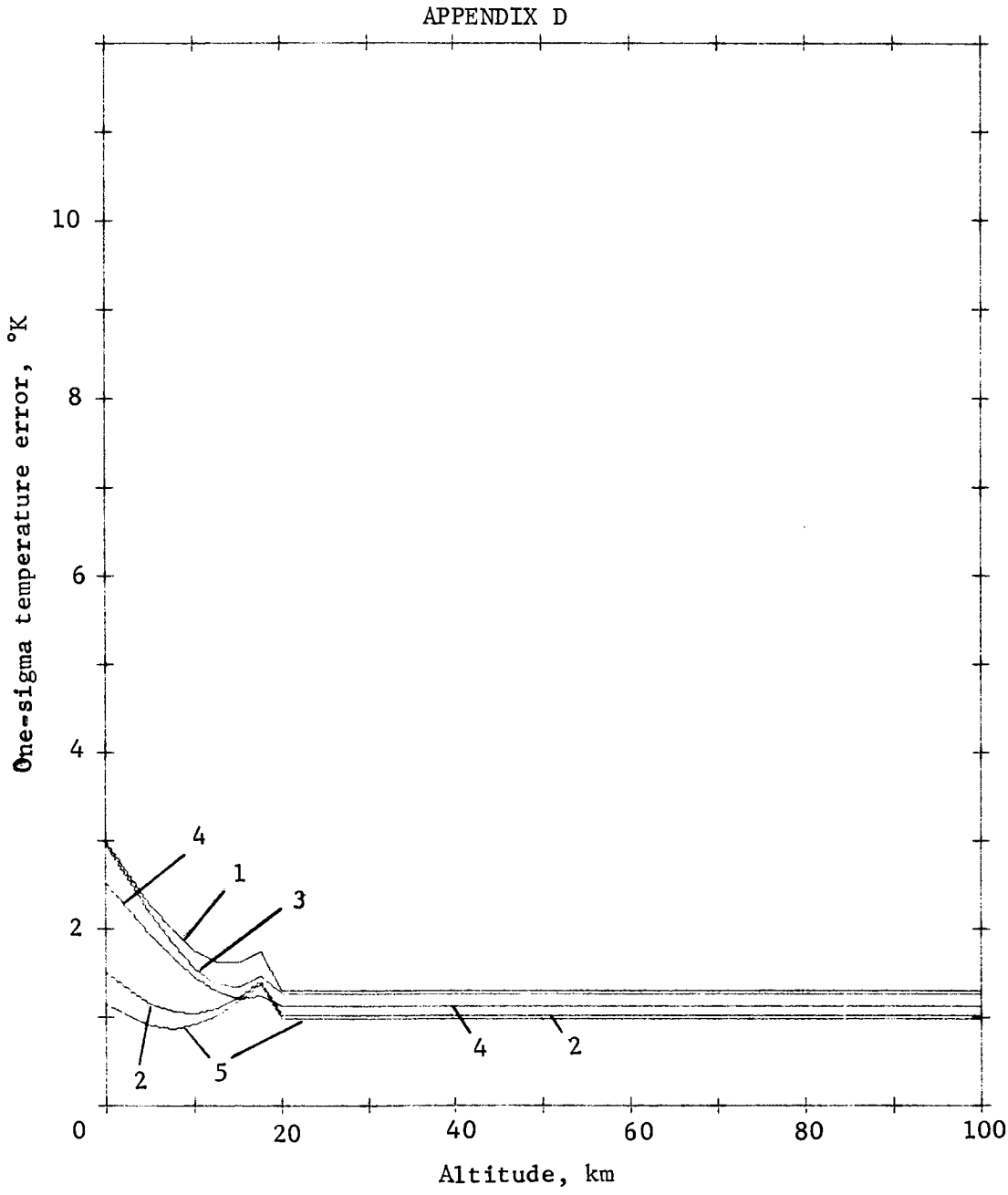

(c) Temperature

Figure D95.- Concluded

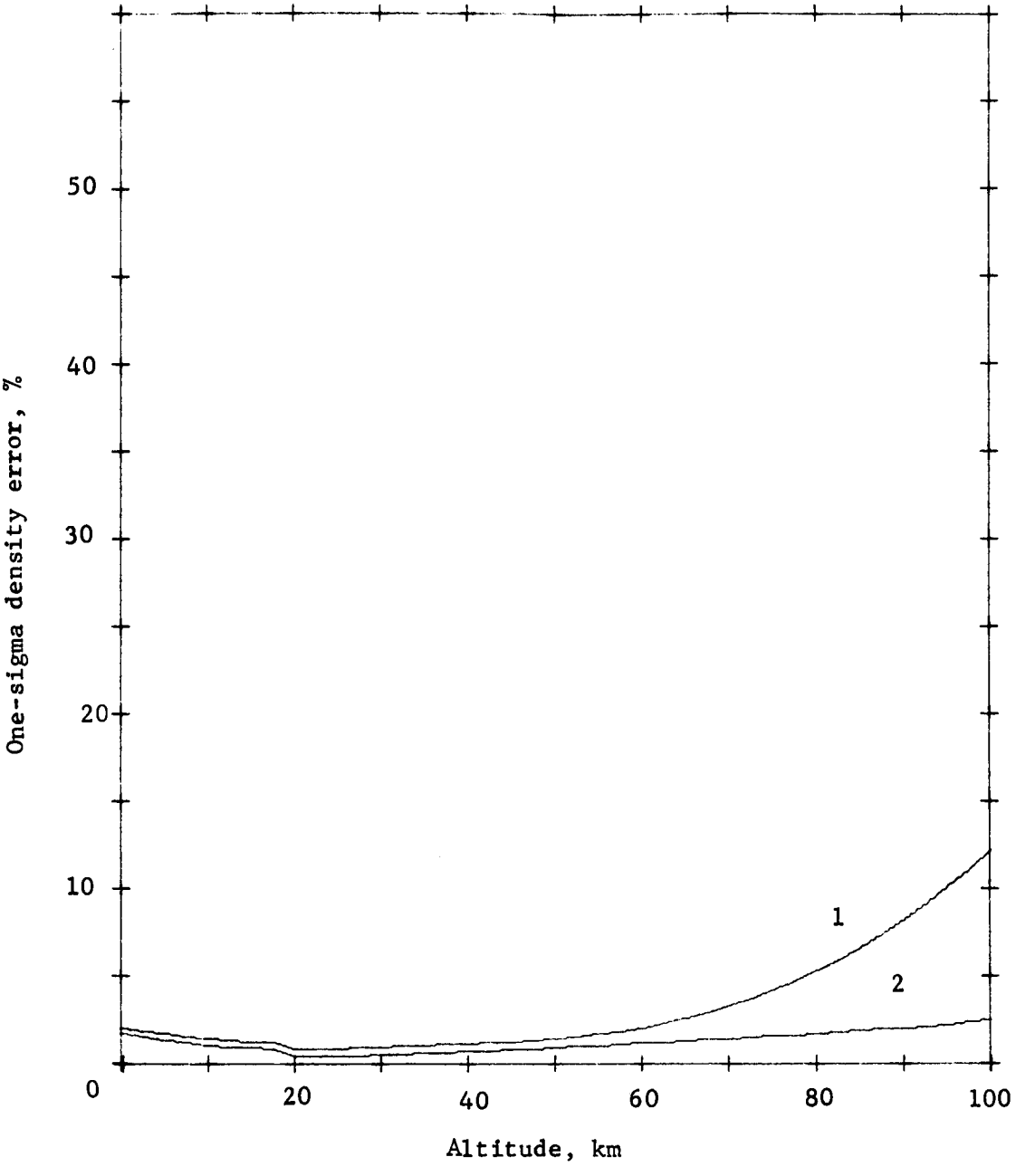

(a) Density

Curve	Measurements
1	Accelerometers, AMR
2	Accelerometers, AMR, and stagnation-pressure

Figure D96.- Entry into VM-5 Atmosphere

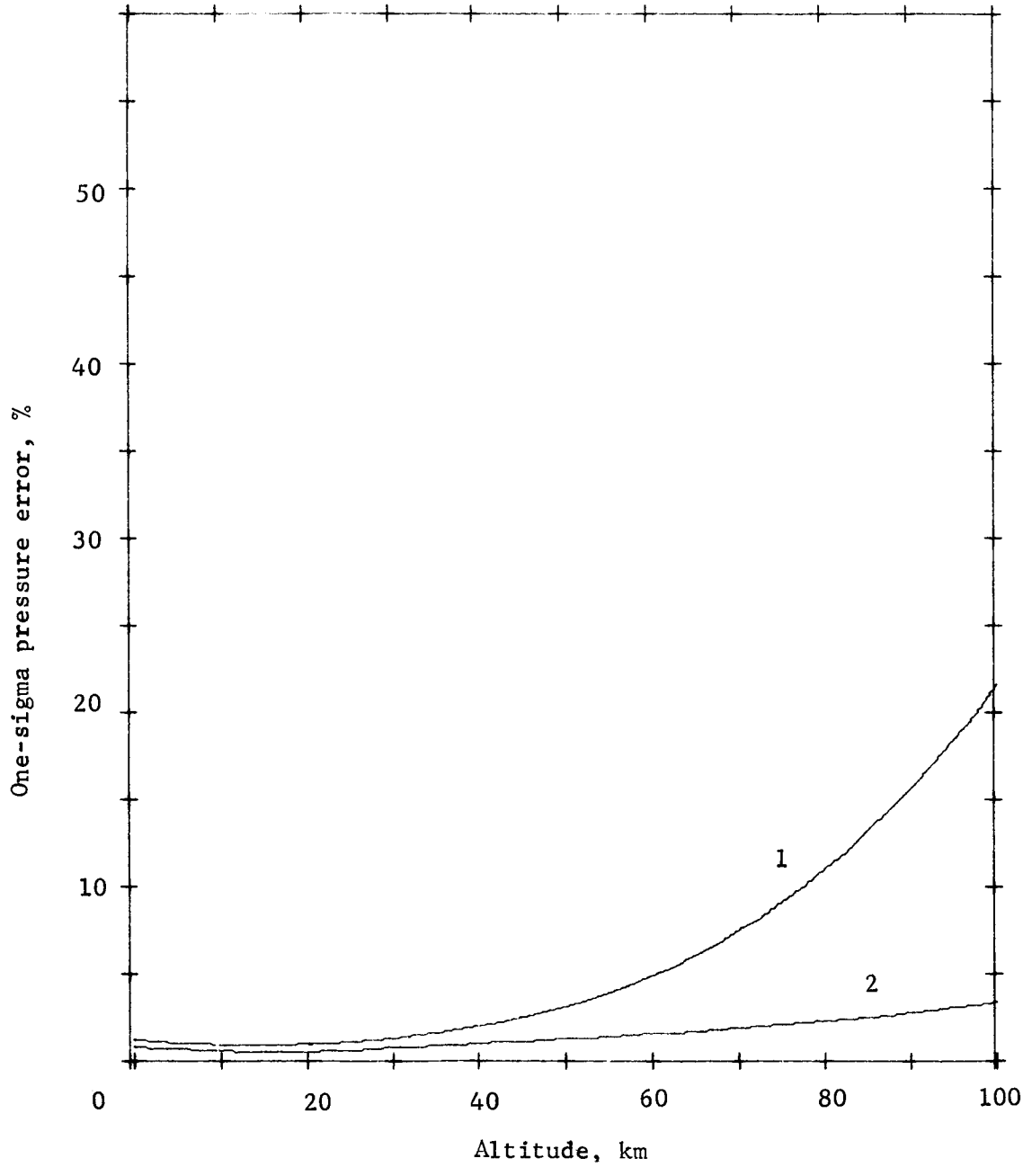

(b) Pressure

Figure D96.- Continued

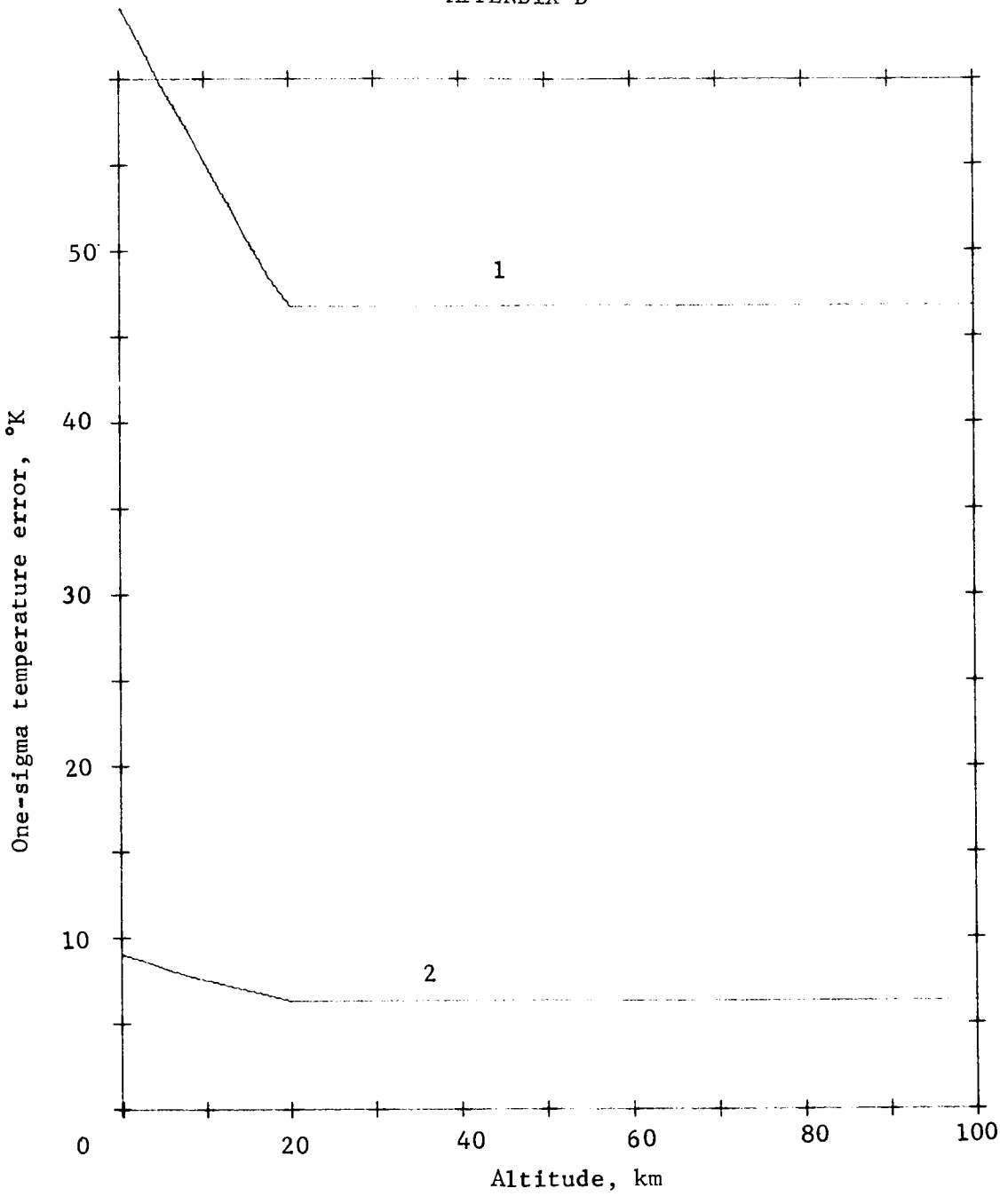

(c) Temperature

Figure D96.- Concluded

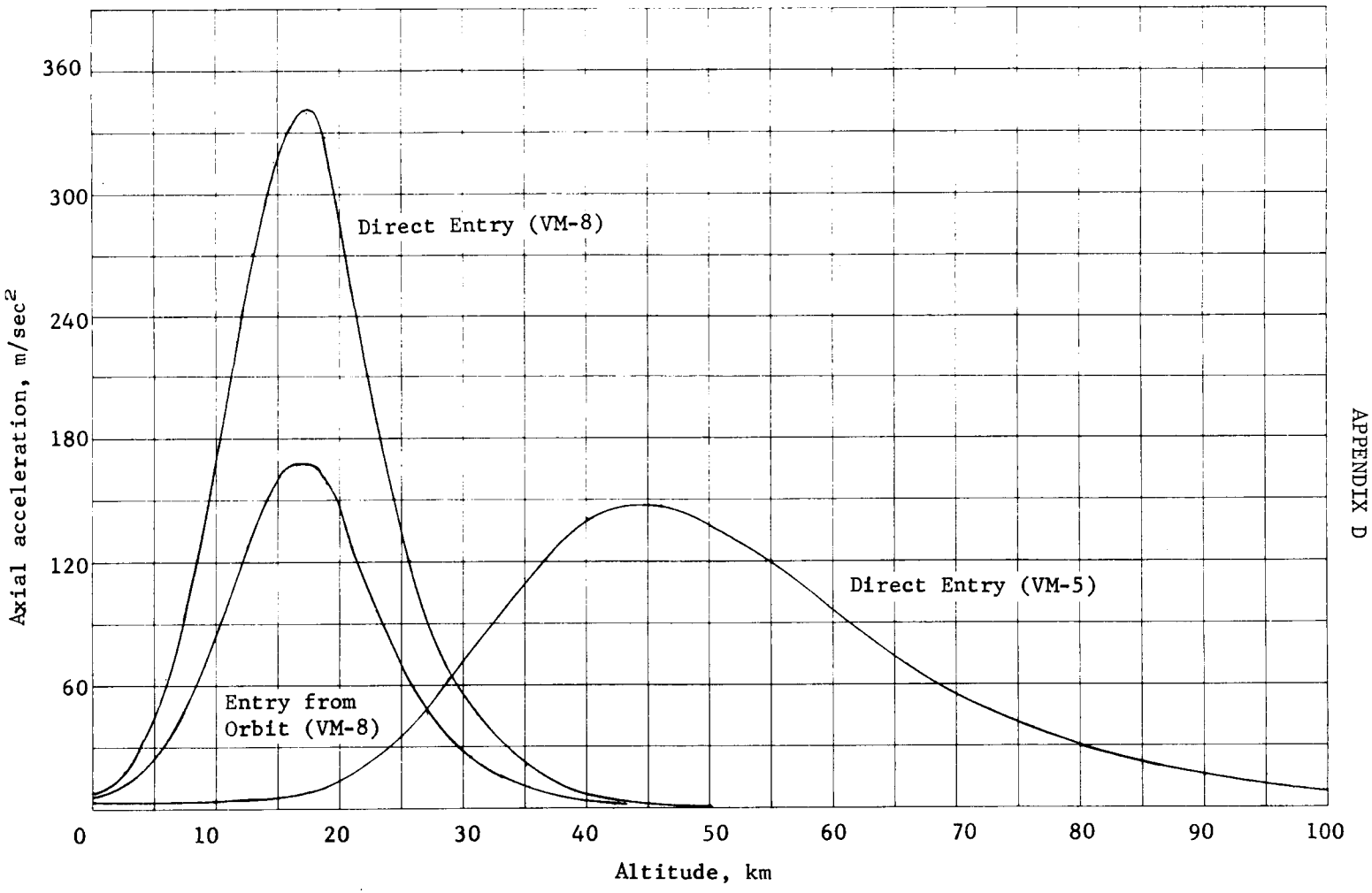

Figure D97.- Axial Acceleration versus Altitude

APPENDIX D

7. TELECOMMUNICATIONS

Direct Link S-Band Parametric Studies

Parametric weight and performance data for S-band Mars/Earth communication options must be developed in consort with technical guidelines derived from mission requirements and constraints. Because the Mars/Earth communication distance and the position of Earth in the Martian sky vary in a periodic manner, bounds on these parameters for all mission opportunities can be obtained from a consideration of the 1973 opportunity. The initial Earth/Mars communication geometry depends on the arrival date at the planet, which is determined for a given launch opportunity by the type of heliocentric transfer trajectory flown. Typical 1973 mission arrival date bands for both the Type I and Type II transfer trajectories are used to determine communication geometry parameters and the range of these parameters.

The performance capability of a given direct link communication configuration depends on the implementation of the ground receiving station. For this study, the deep space instrumentation facility (DSIF) network is considered to consist of two possible configurations. One configuration consists of three DSS, each with a 210-ft advanced antenna system. This configuration represents the projected capability of the DSIF network for the 1973 time period. The second configuration consists of one DSS at Goldstone with a 210-ft advanced antenna system and two overseas DSS, each with an 85-ft antenna system. This configuration represents the current capability of the DSIF network.

Direct link communication geometry. - The Mars/Earth communication distance for the 1974 and 1975 period is shown in figure D98. For the 1973 mission, Type I transfer trajectories result in arrival dates at the planet from 2/1/74 to 5/1/74. Arrival dates for the Type II mission lie between 5/1/74 and 7/1/74, typically. Thus, from figure D98, the communication distance, for either type of mission, is increasing and reaches its maximum value of 3.96×10^8 km around 10/1/74. The requirements that the transmission distance impose on a direct link radio subsystem design are a function of the mission life requirements.

For a mission duration of a few days, the range capability of a direct link must be from 1.68×10^3 km as a minimum to 3.60×10^8 km as a maximum to accommodate either transfer trajectory. A six month or longer mission duration requirement will necessitate a transmission capability out to the maximum Earth/Mars separation.

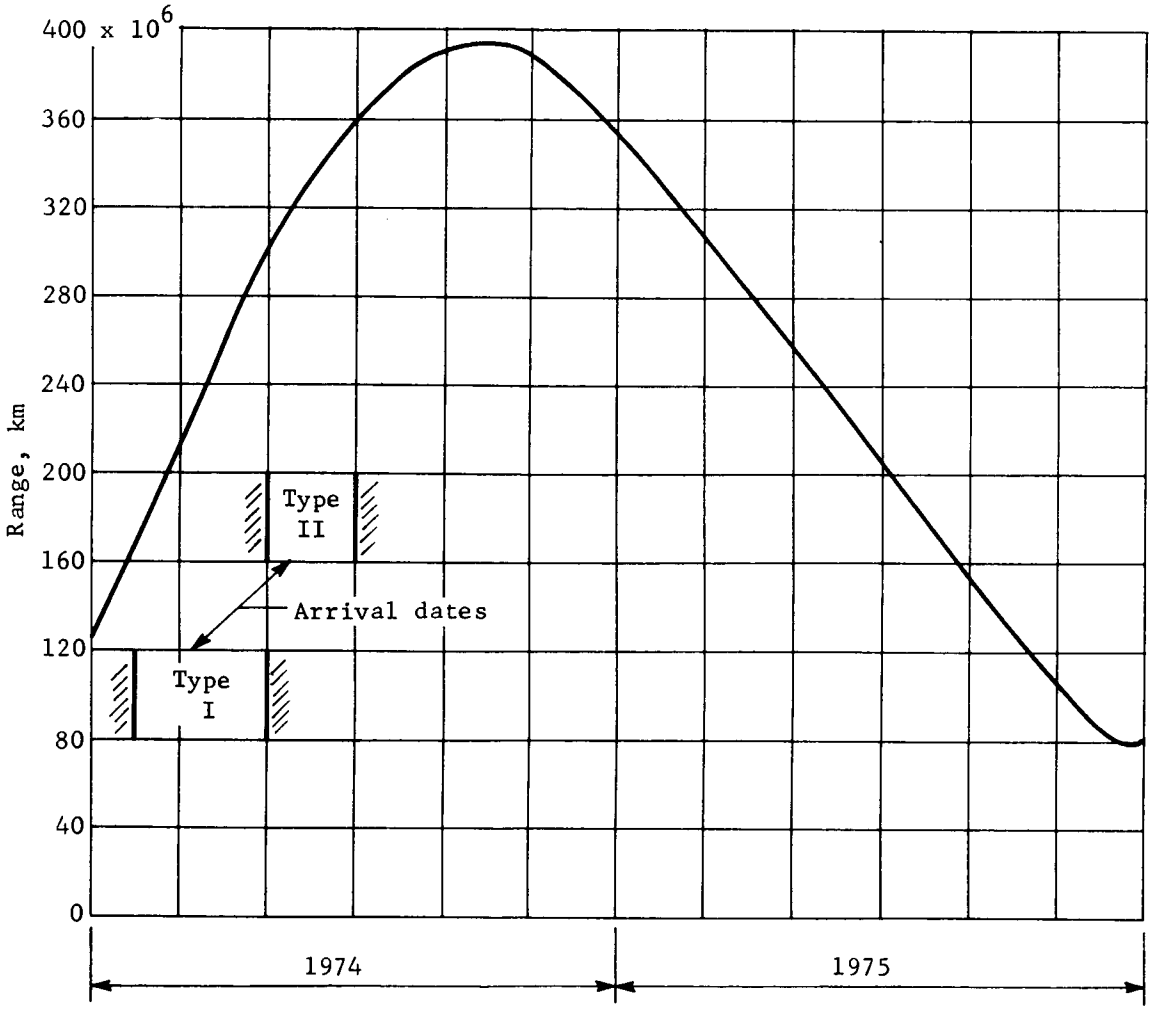

Figure D98.- Mars/Earth Communication Distance

APPENDIX D

The position of Earth with respect to the Martian equator is shown in figure D99, which shows typical arrival date bands for Type I and Type II trajectories. At the earliest arrival date possible, Type I trajectory, the Earth is 16.8° below the Martian equator and ascending northward with time. This initial declination determines the beamwidth requirements for a body-fixed antenna for either command reception of data transmission.

The contact time with Earth depends on the latitude of the landing site. For this study, the landing site latitudes were considered to lie between 20° N and 20° S. The available contact time over this latitude band considering a possible 34° surface slope and hour angle uncertainties varies between 3.9 hr/day (+20°) and 6.9 hr/day (-20°) at the earliest arrival date possible. These contact times will change over the mission life. Initially, southern latitudes are favored and provide longer view times. As time increases, contact time in the southern latitudes decrease with the northern latitudes increasing in viewing capability.

Technical considerations. - Technical considerations are discussed in the following paragraphs.

DSIF compatibility: All direct link S-band communication options will operate at a nominal frequency of 2295 MHz in the deep space telemetry band. Receiver characteristics for the standard receiver implementation and the proposed planetary receiver implementation are described in JPL Document EPD-283, Revision 2, dated Jan. 1, 1967. These characteristics will not be summarized or detailed here.

Modulation techniques: Two modulation techniques must be considered for the landed system. Low weight class landers are not capable of being designed to accommodate directive apertures. Thus, the effective radiated power (ERP) from such a lander is only about 48 or 53 dBm for a 20-W transmitter output power level and a nonarticulated antenna. Table D20 presents a telecommunication design control tabulation for a radio subsystem with an ERP of 53 dBm. For this subsystem configuration under the constraints that Earth is at its maximum range and within the 3-dB beamwidth of the transmitting antenna, the table shows that, even with all the power allocated to the carrier, not enough signal strength is available at the receiver to lock up the carrier tracking loop. Noncoherent techniques must therefore be employed for low ERP configurations. Nonbinary implementations of noncoherent modulation schemes will result in a coding power gain. For this study, the modulation choice for low ERP concepts will be multiple frequency shift keying (MFSK), in which a 5-bit binary word is converted into one of 32 frequencies or tones.

APPENDIX D

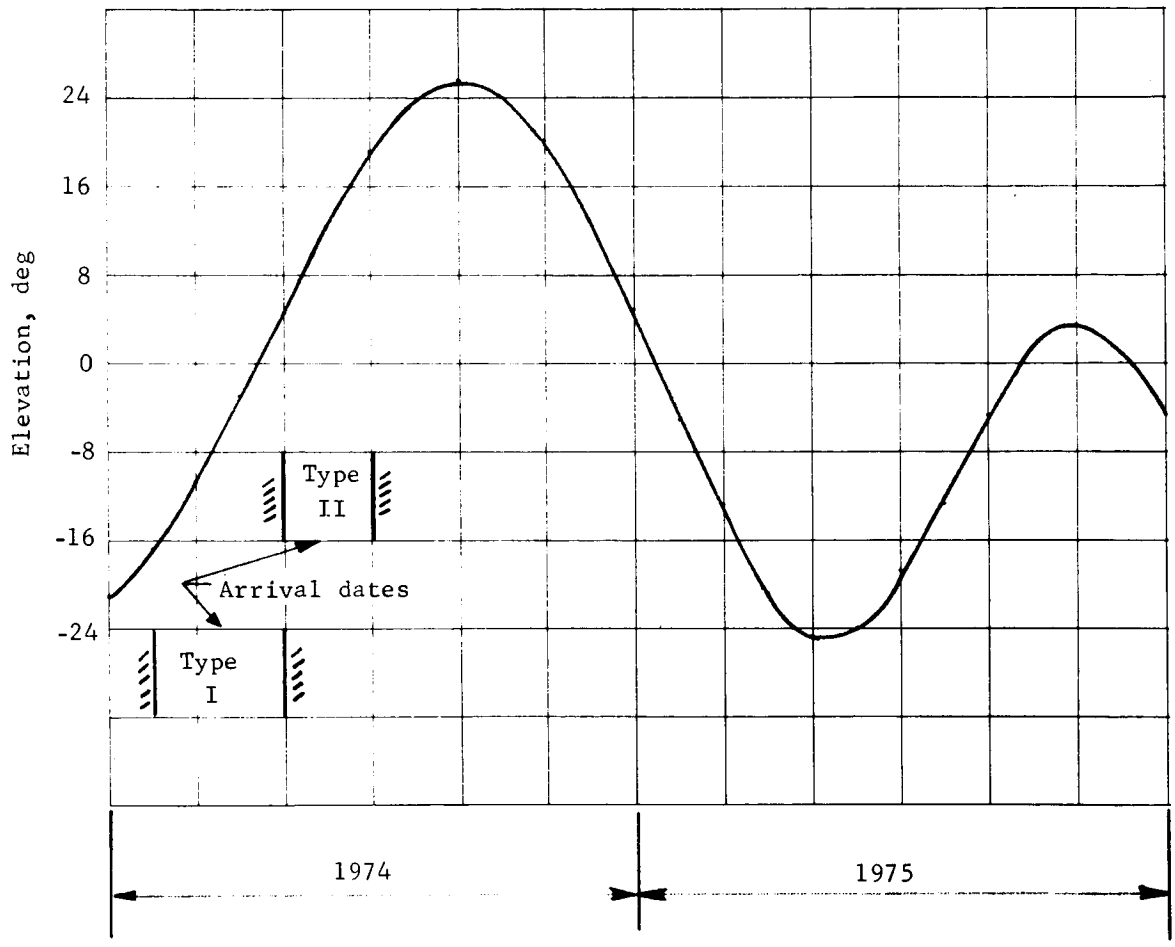

Figure D99.- Elevation of Earth above Martian Equator

TABLE D20.- COHERENT LINK (10 dB HELIX ANTENNA)

Parameter	Value	Tolerance, dB		Notes
Total transmitter power	+43.0 dBm	+1.0	-0	20 W
Transmission circuit loss	-2.0 dB	+1.0	-1.0	
Transmission antenna gain	+10.0 dB	+.5	-.5	
Transmission pointing loss	-3.0 dB	+3.0	-0	·31.5°
Space loss	-271.6 dB	----	----	Maximum range
F = 2295 MHz, R = 396 x 10^6 km				
Polarization loss	-.6 dB	----	----	
Receiver antenna gain	+61.0 dB	+1.0	-1.0	210-ft dish
Receiver antenna pointing loss	-.3 dB	+.3	-0	
Receiver circuit loss	-.2 dB	+.1	-.1	
Net circuit loss	-206.7 dB	+5.9	-2.6	
Total received power	-163.7 dBm	+6.9	-2.6	
Receiver noise spectral density	-182.1 dBm	+1.1	-.9	
T_{sys} = 45 : 10°K				
Carrier modulation loss	-0 dB			No data channel power
Receiver carrier power	-163.7 dBm	+6.9	-2.6	
Carrier APC noise BW	+10.8	+.5	-0	
$2B_{LO}$ = 12 Hz				
Carrier tracking loop				
Carrier threshold SNR in $2B_{LO}$	+6.0	+.5	-1.0	
Threshold carrier power	-165.3 dBm	+2.1	-1.9	
Performance margin	+1.6 dB	+8.0	-4.5	-2.9 dB worst case

APPENDIX D

Large weight class landers are capable of being designed with articulated directive apertures. For these configurations, ERP levels of 63 dBm or greater are possible, allowing sufficient signal strength for carrier tracking while allocating power to a data channel. The modulation choice for these concepts will be single-channel PSK/PM with sync combined with the data stream. This implementation provides greater communications efficiency because no additional power is required for synchronization. The use of a single-channel technique also provides an advantage of easier control of the transmitter modulation index.

Low gain antenna: A nonsteerable, low gain antenna with wide angular coverage requirements must be considered for command reception functions and data transmission. The command reception function applies to any class of lander system weight, while the data transmission function is applicable to the low weight class lander. Beamwidth requirements for this type of antenna are derived from the elevation angle of Earth at the earliest possible arrival date.

The geometry on the surface of Mars is shown in figure D100. From this figure, the aspect angle of Earth that is measured from the vehicle vertical axis is given by

AsAe = Lat ± Lat Uncertainty ± Surface Slope + Elev Angle of Earth

The latitude uncertainty for a 500-km landing footprint is ±8.4°. The antenna beamwidth requirement for landing latitudes within ±10° of the equator becomes 140° for a Type I trajectory and the earliest arrival date for that trajectory. The antenna gain for this coverage requirement is determined from the directivity to be 5.0 dB. For such a broad antenna pattern and the small wavelength of operation, reflections from the surrounding terrain may cause nulls or scallop the pattern. Sufficiently large ground planes on the landed system will minimize this effect.

High gain antenna: The size of the antenna reflector must be consistent with the daily data volume requirements for a given transmitter output power level and compatible with the pointing requirements. Antenna gain as a function of parabolic antenna diameter for a nominal frequency of 2295 MHz is shown in figure D101. These gains represent readily achievable values and are, therefore, consistent with conservative design practices. The 1-, 3-, and 5-dB beamwidths as a function of parabolic dish size are shown in figure D102, which also shows the angles corresponding to landing footprints of ±200 and ±500 km. The ±500-km uncertainty is typical for the 1973 missions.

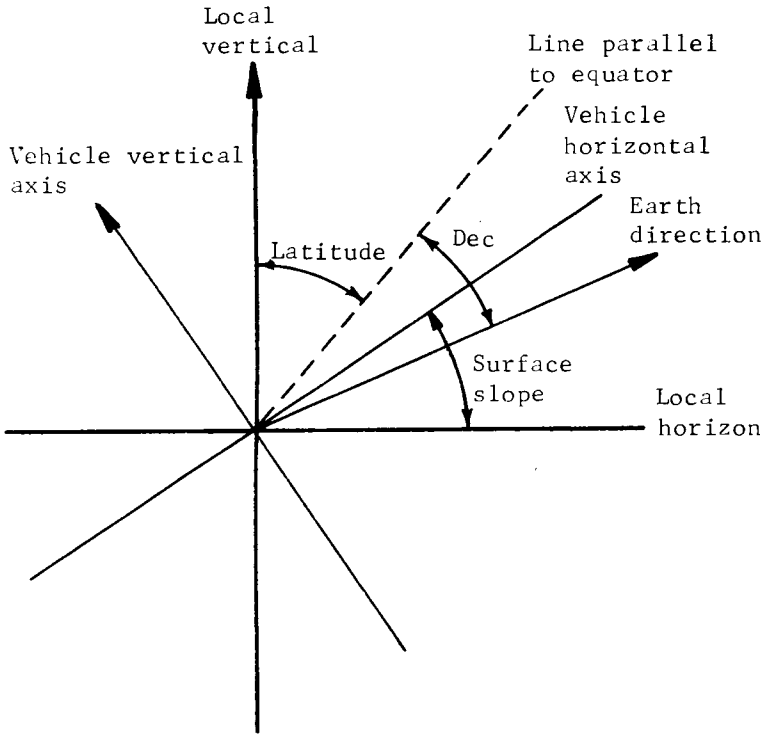

Figure D100.- Mars Lander Antenna Geometry

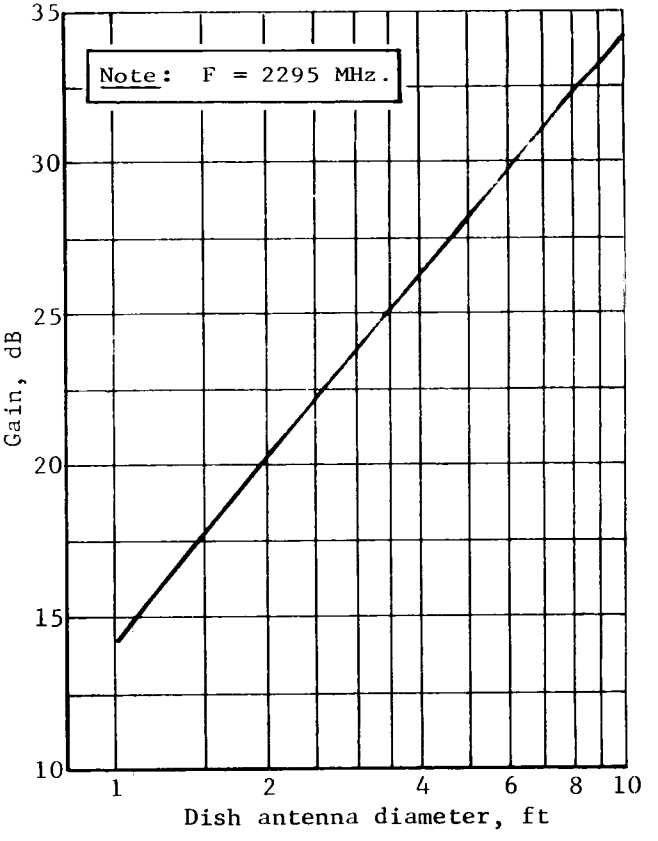

Figure D101.- Antenna Gain as a Function of Parabolic Antenna Diameter

APPENDIX D

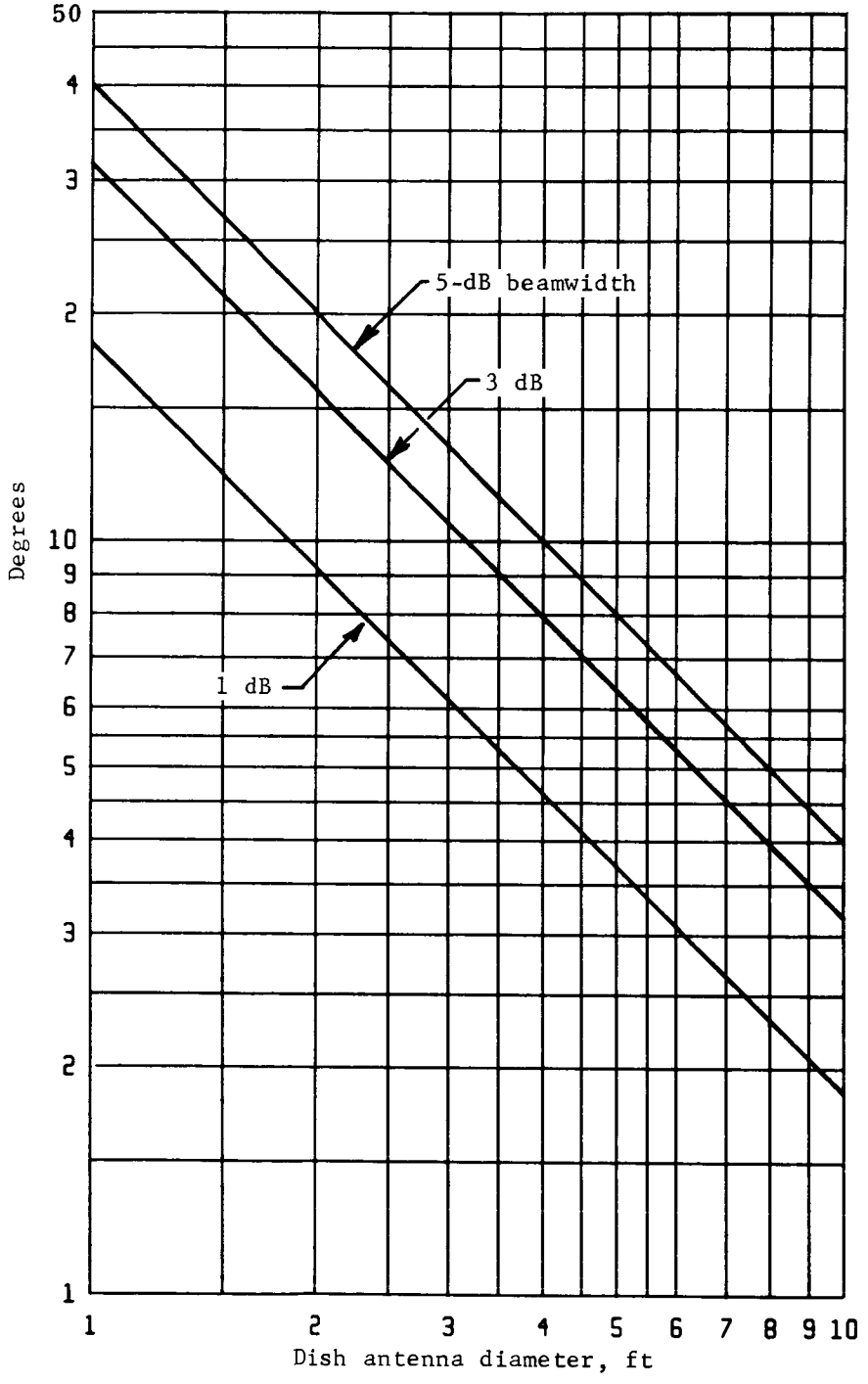

Figure D102.- Beamwidth as a Function of Parabolic Dish Size

APPENDIX D

Self-contained orientation of an equatorial system can be achieved to within ±8.4° from work performed in previous studies. With a requirement for a downlink capability without fine orientation through ground control, this pointing loss corresponds to the 5-dB beamwidth of a 2.5-ft parabolic dish. Fine orientation through ground command, after initial data transfer, can reduce the pointing loss to 1 dB. Thus, for the 1973 missions, antenna sizes are limited to about 2.5-ft for conservative design approaches. The uncertainties will be greatly reduced for the later missions, allowing the antenna size to increase to 6 or 7 ft while still maintaining a downlink capability with 5 dB of antenna pointing loss.

The effective radiated power level is the product of the transmitter output power level and the transmitting antenna gain. The effective radiated power as a function of antenna diameter with transmitter output power as a parameter is shown in figure D103.

Parametric parabolic antenna weight data was obtained from a survey of past space programs and design studies. In this survey, only the weight of the reflector, feed, and feed truss were obtained for nonerectible, solid configurations. These data are shown in figure D104. Curve fitting the data points resulted in the equation

$$W = 1.25\ D^{1.47}$$

where W is in pounds and D is in feet.

Phase lock loop bandwidth: The ground receiver tracking loop must track phase deviations of the carrier. Other considerations that also must be made are frequency acquisition range, lockup time, average in-lock time, and doppler tracking rate. The rf frequency rate (Hz/sec) capability of the loop depends on the signal level, frequency uncertainty, allowable phase error, and noise bandwidth. Acquitision time, for a given frequency/doppler shift uncertainty, will increase as the loop bandwidth is decreased. The average in-lock time is a function of the loop noise bandwidth and, hence, the received signal level. Thus, the system bandwidth is determined by oscillator instabilities, doppler and doppler rates, and operational requirements.

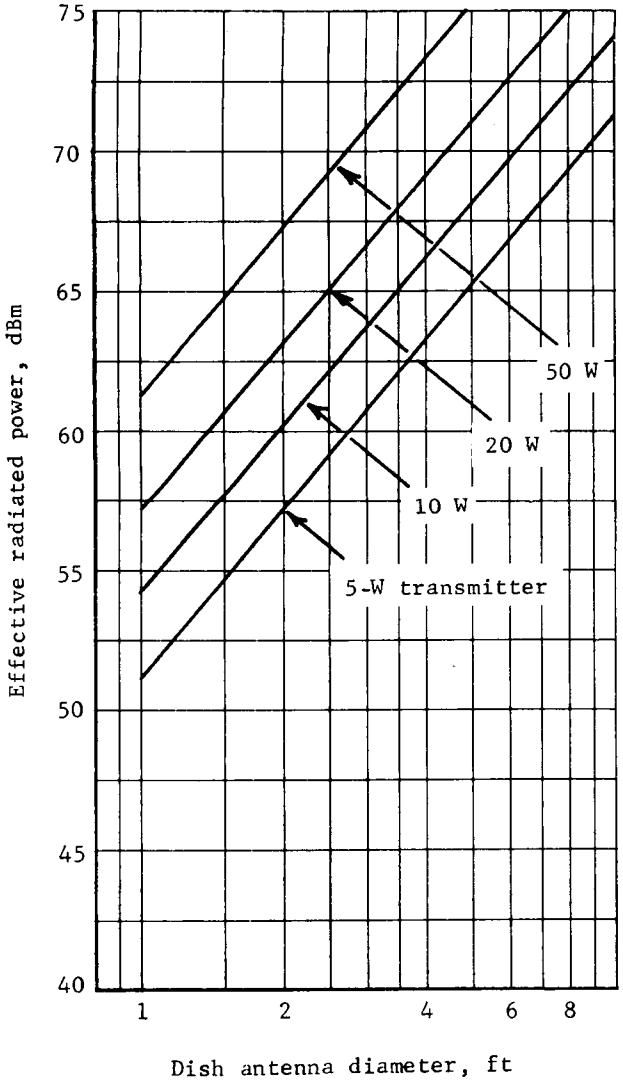

Figure D103.- Effective Radiated Power as a Function of Antenna Size

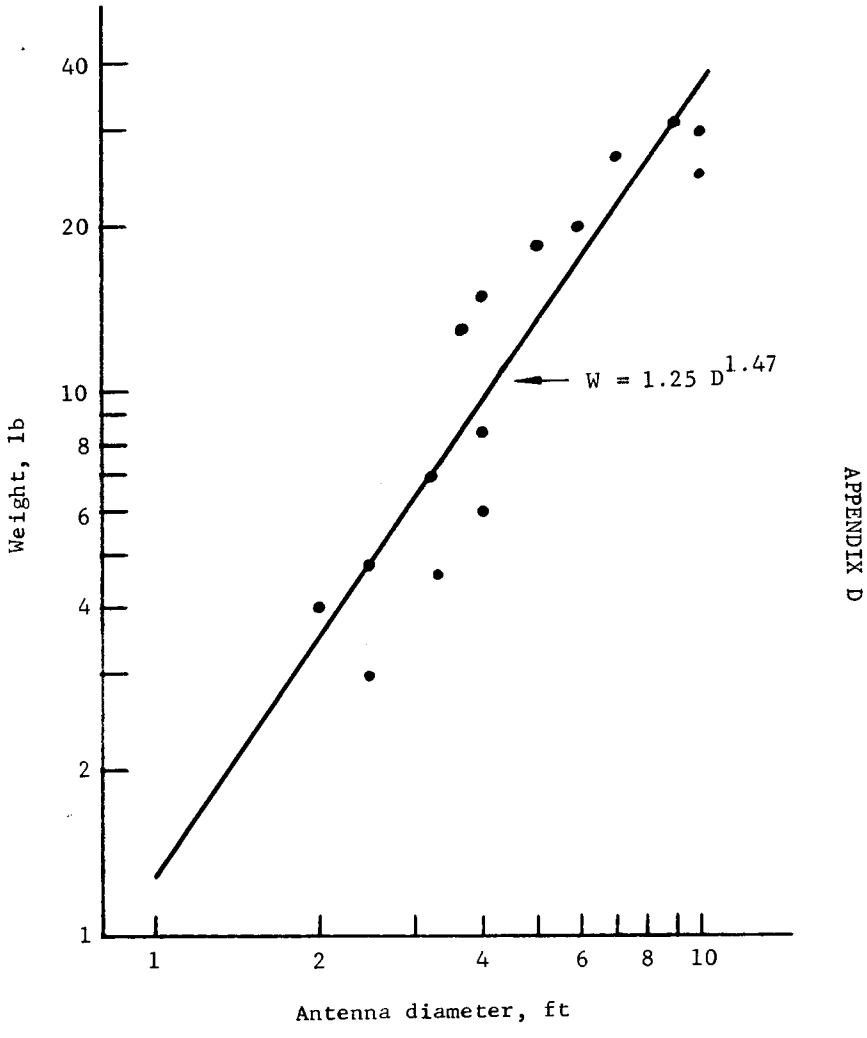

Figure D104.- Parabolic Antenna Parametric Data

APPENDIX D

The limiting factor in the design of narrowband phase-locked loops is the phase-noise inherent in the output of the voltage controlled oscillator (VCO). This noise appears as random fluctuations, drift, etc., and is usually referred to as oscillator instability. One well-known characteristic of loop bandwidth is that the output noise due to noise in the VCO increases as bandwidth decreases; whereas for output noise due to input noise, the opposite is observed. Thus, on the basis of noise output due to the VCO, there is an optimum noise bandwidth. Past studies conducted at JPL arrive at an optimum bandwidth of 13 Hz for an overdamped loop.

On the basis of the above paragraph and the requirement for accommodating the doppler and doppler rates to be experienced in the system, all performance estimates for the PSK/PM communication option are derived for a 12-Hz ground receiver. This bandwidth has been shown on the Mariner 1964 program to be capable of tracking the oscillator instabilities experienced in the system and maintaining constant carrier phase error over the bit interval. The latter is a requirement to keep system degradations within reasonable bounds.

Data rate capability. - The direct link performance capability of noncoherent MFSK and single-channel coherent PSK/PM for various ERP levels is shown in figures D105 and D106. Figure D105 presents the transmission rate that can be supported over the link with a 210-ft advanced antenna system at the ground station. On this figure, data rate is given for a nominal range of 2.6×10^8 km and a maximum range of 3.96×10^8 km. Data rate capability for single-channel coded coherent PSK/PM is also presented for the nominal and maximum range conditions. This rate capability was derived by assuming a 3-dB power advantage over an uncoded coherent system. Based on information available to date, this assumption appears to be a realistic one because coherence requirements for the carrier tracking loop and system degradations in practical implementations are unknown at this time. Figure D106 presents similar data for the 85-ft ground station antenna. MFSK direct link performance as a function of time during the 1974 time period is shown for four values of ERP in figure D107.

The assumptions and system parameters used to derive figures D105 thru D107 are presented in tables D21 thru D26. These tables are telecommunication design control tables with nominal parameter values and tolerances on the parameters identified.

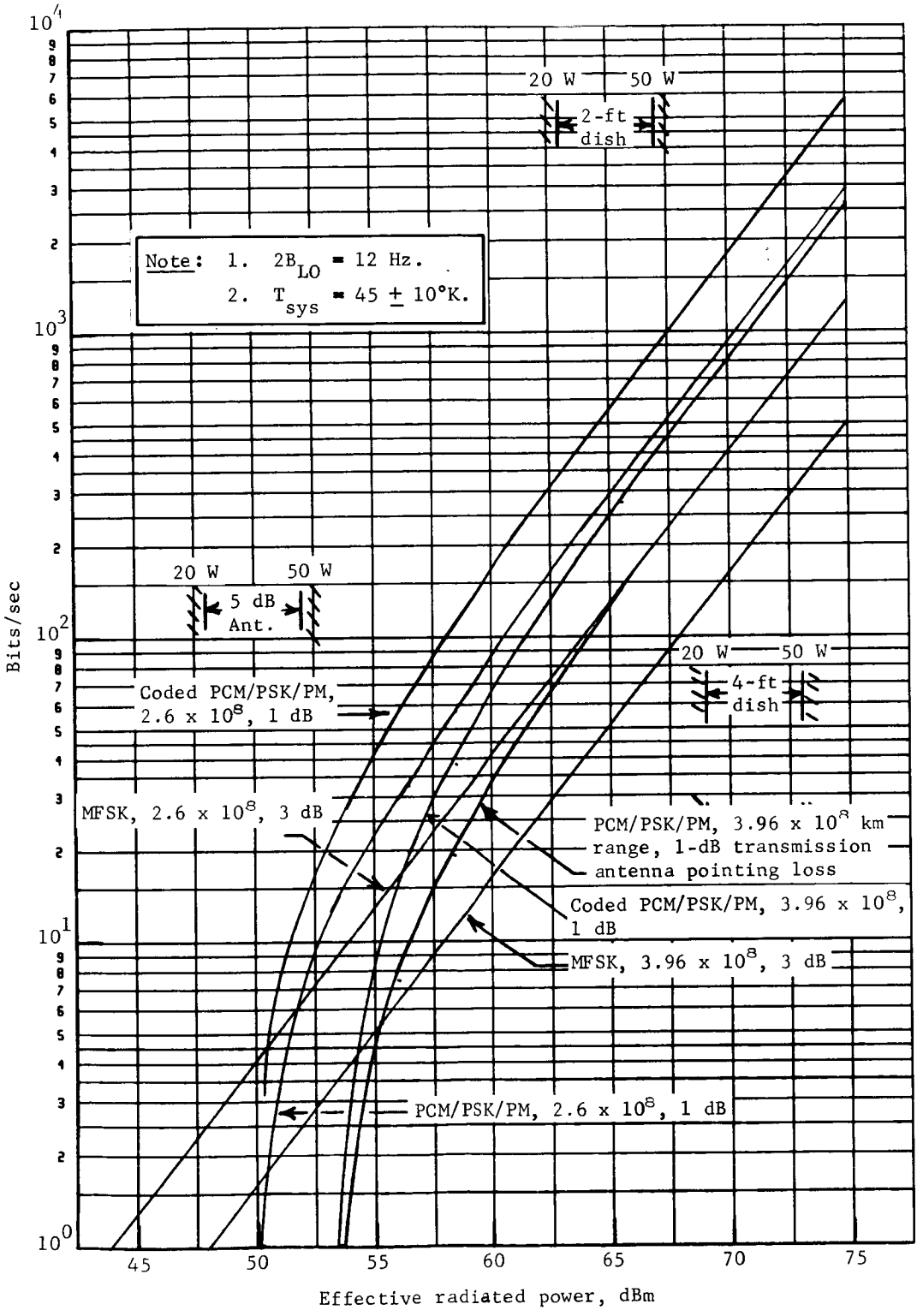

Figure D105.- Direct Link Performance, 210-ft DSIF Receiving Site

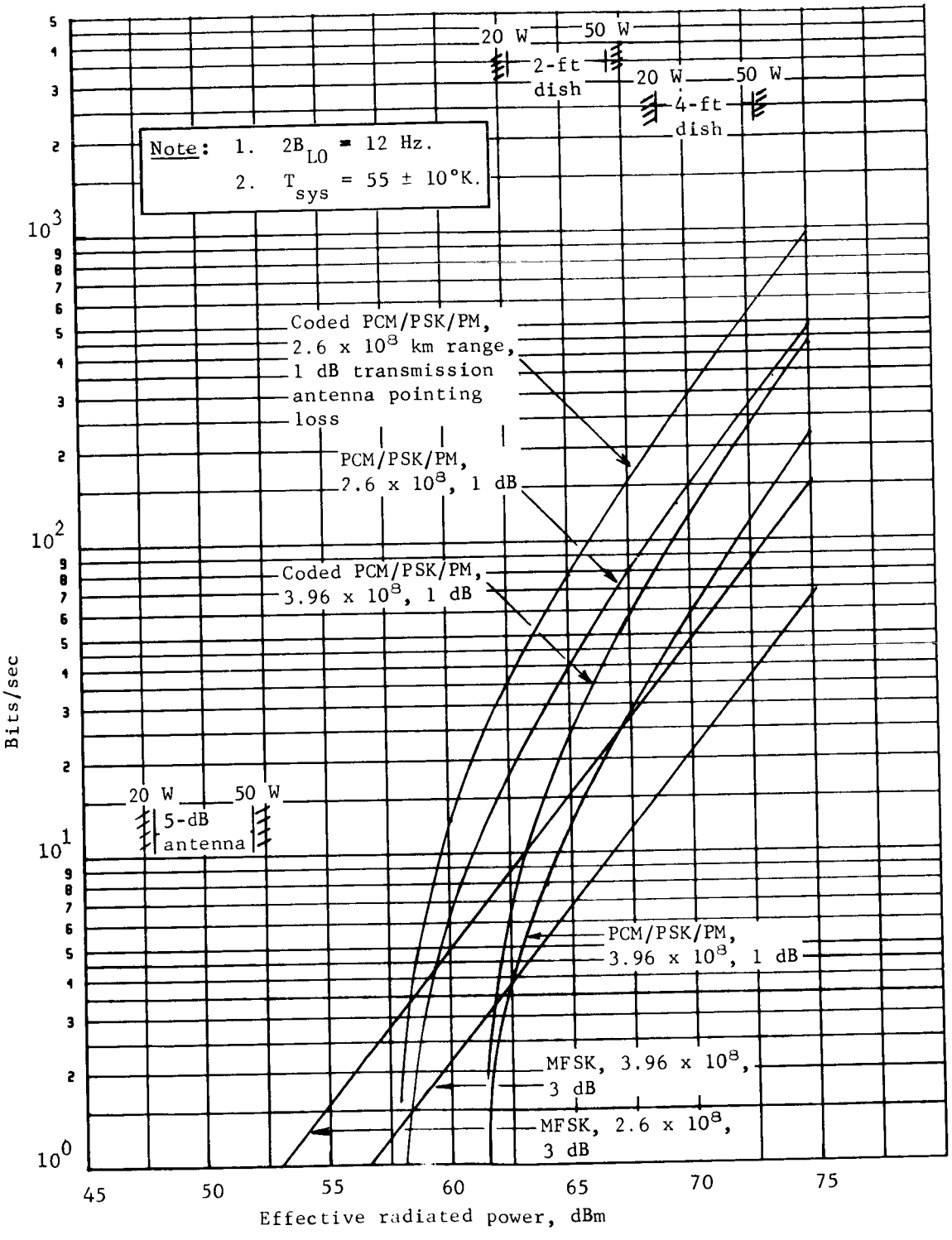

Figure D106.- Direct Link Performance, 85-ft DSIF Receiving Site

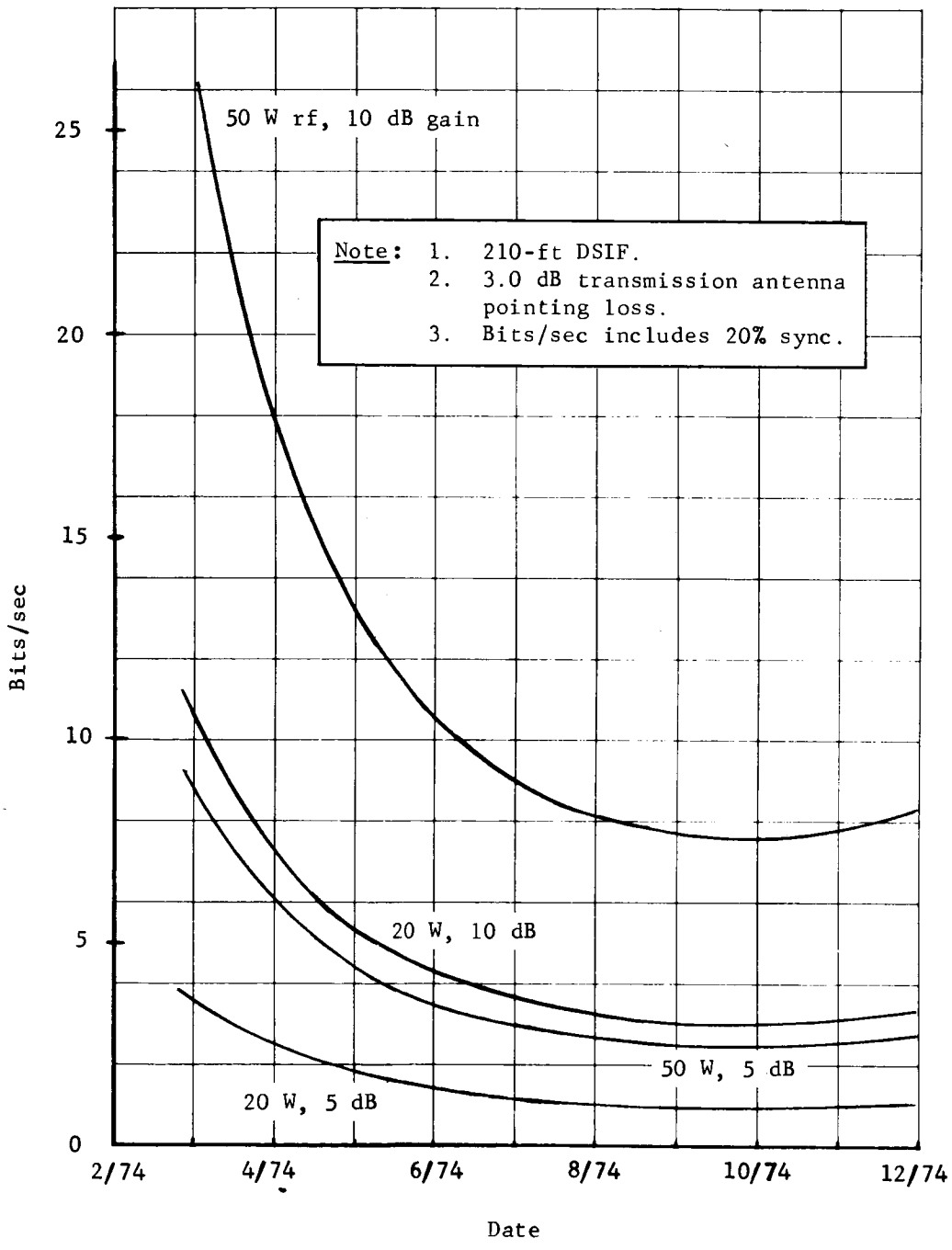

Figure D107.- MFSK Direct Link Performance

TABLE D21.- LOW DATA RATE SYSTEM, MFSK WITH 20% SYNC ALLOCATION

Parameter	Value	Tolerance, dB		Notes
Total transmitter power	+43.0 dBm	+1.0	-0	20 W
Transmission circuit loss	-1.5 dB	+.8	-0.8	
Transmission antenna gain	+5.0 dB	+.5	-0.5	
Transmission antenna pointing loss	-3.0 dB	+3.0	-0	±70°
Space loss	-271.6 dB	----	----	Maximum range
F = 2295 MHz, R = 396 x 10^6 km				
Polarization loss	-.6 dB	----	----	
S/L ϵ = 6 dB, DSIF ϵ = 0.8 dB				
Receiver antenna gain	+61.0 dB	+1.0	-1.0	210-ft dish
Receiver antenna pointing loss	-.3 dB	+.3	-0	
Receiver circuit loss	-.2 dB	+.1	-0.1	
Net circuit loss	-211.2 dB	+5.7	-2.4	
Total received power	-168.2 dBm	+6.7	-2.4	
Receiver noise spectral density	-182.1 dBm	+1.1	-0.9	
T_{sys} = 45 ± 10°K				
Required ST/N_o for $Pe^w = 10^{-2}$	+8.6 dB	----	----	
Bit rate (1/T = 1 bps)	+0 dB	----	----	Sync and information
Threshold subcarrier power	-173.5 dBm	+1.1	-0.9	
Performance margin	+5.3 dB	+7.8	-3.3	+2.0 dB worst case

TABLE D22.- HIGH GAIN DIRECT LINK, FINE POINTING AT 2.6×10^8 km

Parameter	Value	Tolerance, dB		Notes
Total transmitter power	+43.0 dBm	+1.0	-0	20 W
Transmission circuit loss	-1.5 dB	+.8	-0.8	
Transmission antenna gain	+20.3 dB	+.5	-0.5	2-ft dish
Transmission antenna pointing loss	-1.0 dB	+1.0	-0	
Space loss	-268.0 dB	----	----	
F = 2295 MHz, R = 260×10^6 km				
Polarization loss	-.6 dB	----	----	
Receiver antenna gain	+61.0 dB	+1.0	-1.0	210-ft dish
Receiver antenna pointing loss	-.3 dB	+.3	-0	
Receiver circuit loss	-.2 dB	+.1	-0.1	
Net circuit loss	-190.3 dB	+3.7	-2.4	
Total received power	-147.3 dBm	+4.7	-2.4	
Receiver noise spectral density	-182.1 dBm	+1.1	-0.9	
T_{sys} = 45 ± 10°K				
Carrier modulation loss	-10.0 dB	+1.4	-1.8	θ = 1.25 rad ± 5%
Receiver carrier power	-157.3 dBm	+6.1	-4.2	
Carrier APC noise BW	+10.8 dB	+.5	-0	
$2B_{LO}$ = 12 Hz				
Carrier tracking loop				
Carrier threshold SNR in $2B_{LO}$	6.0 dB	+0.5	-1.0	
Threshold carrier power	-165.3 dB	+2.1	-1.9	
Performance margin	+8.0 dB	+8.2	-6.1	
Data channel				
Modulation loss	-.5 dB	+.2	-0.2	
Received data subcarrier power	-147.8 dBm	+4.9	-2.6	
Bit rate (1/T = 200 bps)	+23.0 dB	----	----	Uncoded channel
Required ST/N_o for $Pe^b = 5 \times 10^{-3}$	+6.8 dB	+1.0	-1.0	
Threshold subcarrier power	-152.3 dBm	+2.1	-1.9	
Performance margin	+4.5 dB	+7.0	-4.5	

TABLE D23.- HIGH GAIN DIRECT LINK, FINE POINTING AT MAXIMUM RANGE

Parameter	Value	Tolerance, dB		Notes
Total transmitter power	+43.0 dBm	+1.0	-0	20 W
Transmission circuit loss	-1.5 dB	+.8	-0.8	
Transmission antenna gain	+20.3 dB	+.5	-0.5	2-ft dish
Transmission antenna pointing loss	-1.0 dB	+1.0	-0	
Space loss	-271.6 dB	----	----	Maximum range
F = 2295 MHz, R = 396 x 10^6 km				
Polarization loss	-.6 dB	----	----	
Receiver antenna gain	+61.0 dB	+1.0	-1.0	210-ft dish
Receiver antenna pointing loss	-.3 dB	+.3	-0	
Receiver circuit loss	-.2 dB	+.1	-0.1	
Net circuit loss	-193.9 dB	+3.7	-2.4	
Total received power	-150.9 dBm	+4.7	-2.4	
Receiver noise spectral density	-182.1 dBm	+1.1	-0.9	
T_{sys} = 45 ± 10°K				
Carrier modulation loss	-8.2 dB	+1.2	-1.3	ϑ = 1.17 rad ± 5%
Receiver carrier power	-159.1 dBm	+5.9	-3.7	
Carrier APC noise BW	+10.8 dB	+.5	-0	
2 B_{LO} = 12 Hz				
Carrier tracking loop				
Carrier threshold SNR in $2B_{LO}$	+6.0 dB	+.5	-1.0	
Threshold carrier power	-165.3 dBm	+2.1	-1.9	
Performance margin	+6.2 dB	+8.0	-5.6	
Data channel				
Modulation loss	-.7 dB	+0.2	-0.3	
Received data subcarrier power	-151.6 dBm	+4.9	-2.7	
Bit rate (1/T = 70 bps)	+18.5 dB	----	----	Uncoded channel
Required ST/N_o for Pe^b = 5 x 10^{-3}	+6.8 dB	+1.0	-1.0	
Threshold subcarrier power	-156.8 dBm	+2.1	-1.9	
Performance margin	+5.2	+7.0	-4.6	

TABLE D24.- HIGH GAIN DIRECT LINK, COURSE POINTING AT MAXIMUM RANGE

Parameter	Value	Tolerance, dB		Notes
Total transmitter power	+43.0 dBm	+1.0	-0	20 W
Transmission circuit loss	-1.5 dB	+.8	-0.8	
Transmission antenna gain	+20.3 dB	+.5	-0.5	2-ft dish
Transmission antenna pointing loss	-5.0 dB	+5.0	-0	
Space loss	-271.6 dB	----	----	
F = 2295 MHz, R = 396 x 10^6 km				
Polarization loss	-.6 dB	----	----	
Receiver antenna gain	+61.0 dB	+1.0	-1.0	210-ft dish
Receiver antenna pointing loss	-.3 dB	+.3	-0	
Receiver circuit loss	-.2 dB	+.1	-0.1	
Net circuit loss	-197.9 dB	+7.7	-2.4	
Total received power	-154.9 dBm	+8.7	-2.4	
Receiver noise spectral density	-182.1 dBm	+1.1	-0.9	
T_{sys} = 45 ± 10°K				
Carrier modulation loss	-5.3 dB	+.6	-0.8	θ = 1.00 rad ± 5%
Receiver carrier power	-160.2 dBm	+9.3	-3.2	
Carrier APC noise BW	+10.8 dB	+.5	-0	
$2B_{LO}$ = 12 Hz				
Carrier tracking loop				
Carrier threshold SNR in $2B_{LO}$	+6.0 dB	+.5	-1.0	
Threshold carrier power	-165.3 dBm	+2.1	-1.9	
Performance margin	+5.1 dB	+11.5	-5.1	
Data channel				
Modulation loss	-1.5 dB	+.3	-0.3	
Received data subcarrier power	-156.4 dBm	+9.0	-2.7	
Bit rate (1/T = 27 bps)	+14.3 dB	----	----	Uncoded channel
Required ST/N_o for $Pe^b = 5 \times 10^{-3}$	+6.8 dB	+1.0	-1.0	
Threshold subcarrier power	-161.0 dBm	+2.1	-1.9	
Performance margin	+4.6 dB	+11.1	-4.6	

TABLE D25.- HIGH GAIN DIRECT LINK, FINE POINTING AT 2.6×10^6 km

Parameter	Value	Tolerance, dB		Notes
Total transmitter power	+43.0 dBm	+1.0	-0	20 W
Transmission circuit loss	-1.5 dB	+.8	-0.8	
Transmission antenna gain	+20.3 dB	+.5	-0.5	2-ft dish
Transmission antenna pointing loss	-1.0 dB	+1.0	-0	
Space loss	-268.0 dB	----	----	
F = 2295 MHz, R = 260×10^6 km				
Polarization loss	-.6 dB	----	----	
Receiver antenna gain	+53.0 dB	+1.0	-0.5	85-ft dish
Receiver antenna pointing loss	-0 dB	+0	-0	
Receiver circuit loss	-.2 dB	+.1	-0.1	
Net circuit loss	-198.0	+3.4	-1.9	
Total received power	-155.0 dBm	+4.4	-1.9	
Receiver noise spectral density	-181.2 dBm	+.9	-0.7	
T_{sys} = 55 ± 10°K				
Carrier modulation loss	-5.1 dB	+.6	-0.7	θ = 0.98 rad ± 5%
Receiver carrier power	-160.1 dBm	+5.0	-2.6	
Carrier APC noise BW	+10.8 dB	+.5	-0	
$2B_{LO}$ = 12 Hz				
Carrier tracking loop				
Carrier threshold SNR in $2B_{LO}$	+6.0 dB	+.5	-1.0	
Threshold carrier power	-164.4 dBm	+1.9	-1.7	
Performance margin	+4.3 dB	+6.9	-4.3	
Data channel				
Modulation loss	-1.6 dB	+.3	-0.3	
Received data subcarrier power	-156.6 dBm	+4.7	-2.2	
Bit rate (1/T = 24.5 bps)	+13.9 dB	----	----	Uncoded channel
Required ST/N_o for $Pe^b = 5 \times 10^{-3}$	+6.8 dB	+1.0	-1.0	
Threshold subcarrier power	-160.5 dBm	+1.9	-1.7	
Performance margin	+3.9 dB	+6.6	-3.9	

TABLE D26.- HIGH GAIN DIRECT LINK, FINE POINTING AT MAXIMUM RANGE

Parameter	Value	Tolerance, dB		Notes
Total transmitter power	+43.0 dBm	+1.0	-0	20 W
Transmission circuit loss	-1.5 dB	+.8	-0.8	
Transmission antenna gain	+20.3 dB	+.5	-0.5	2-ft dish
Transmission antenna pointing loss	-1.0 dB	+1.0	-0	
Space loss	-271.6 dB	----	----	
F = 2295 MHz, R = 396 x 10^6 km				
Polarization loss	-.6 dB	----	----	
Receiver antenna gain	+53.0 dB	+1.0	-0.5	85-ft dish
Receiver antenna pointing loss	-0 dB	+0	-0	
Receiver circuit loss	-.2 dB	+.1	-0.1	
Net circuit loss	-201.6 dB	+3.4	-1.9	
Total received power	-158.6 dBm	+4.4	-1.9	
Receiver noise spectral density	-181.2 dBm	+.9	-0.7	
T_{sys} = 55 ± 10°K				
Carrier modulation loss	-2.0 dB	+.2	-0.2	θ = 0.65 rad ± 5%
Receiver carrier power	-160.6 dBm	+4.6	-2.1	
Carrier APC noise BW	+10.8 dB	+.5	-0	
$2B_{LO}$ = 12 Hz				
Carrier tracking loop				
Carrier threshold SNR in $2B_{LO}$	+6.0 dB	+.5	-1.0	
Threshold carrier power	-164.4 dBm	+1.9	-1.7	
Performance margin	+3.8 dB	+6.5	-3.8	
Data channel				
Modulation loss	-4.4 dB	+.4	-0.3	
Received data subcarrier power	-163.0 dB	+4.8	-2.2	
Bit rate (1/T = 5.6 bps)	+7.5 dB	----	----	Uncoded channel
Required ST/N_o for $Pe^b = 5 \times 10^{-3}$	+6.8 dB	+1.0	-1.0	
Threshold subcarrier power	-166.9 dBm	+1.9	-1.7	
Performance margin	+3.9 dB	+6.7	-3.9	

APPENDIX D

The tolerances have been assigned in such a manner that tolerances appearing in the negative column always denote a decrease in SNR, and those appearing in the positive column denote an increase. The required ST/N_o for a BER of 5×10^{-3} for an uncoded PSK/PM channel includes a degradation of 1.5 dB to account for i.f. phase error degradation, bit sync timing error, and bit detection process degradation. MFSK link performance was derived for a WER of 1×10^{-2}.

Direct link baseline configuration parametric data. - The following paragraphs discuss direct link baseline configuration parametric data.

MFSK low data rate direct communications: The baseline configuration is nonredundant and includes the following elements: (1) a 200 channel telemetry subsystem with a 50 000 bit static storage device, (2) an S-band command subsystem consisting of a receiver, detector and antenna, and (3) a radio subsystem comprised of a MFSK modulation (digit-to-tone converter), a modulator-exciter, a TWTA with an integrated power supply, and a body-fixed low gain antenna. The weight and total power requirements for this configuration as a function of transmitter power output level are shown in figure D108. Data rate capability for the range of transmitter power levels is also shown on this figure.

High gain direct communications: The baseline configuration is nonredundant and includes the following elements: (1) a 200-channel telemetry subsystem with a 50 000 bit static storage device, (2) an S-band command subsystem consisting of a receiver, detector, and antenna, (3) a radio subsystem comprised of a modulator-exciter and a TWTA with an integrated power supply, and (4) a high-gain antenna subsystem consisting of a 2-ft articulated parabolic dish and an antenna controller and pointer, which is capable of accommodating a 4-ft dish. The weight and total power requirements for this configuration as a function of transmitter power output level are shown in figure D109. Data rate capability for the range of transmitter power levels for two transmission distances is also shown on this figure.

APPENDIX D

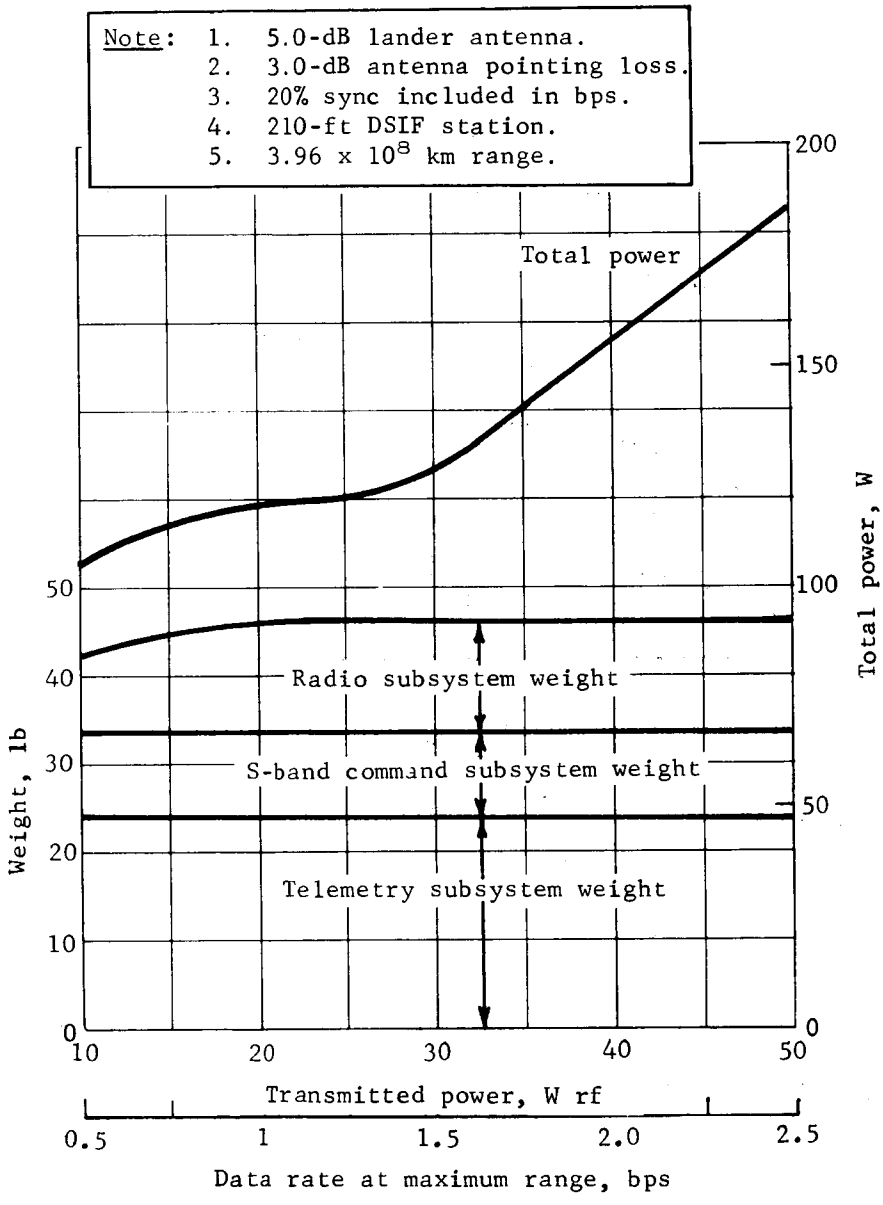

Figure D108.- MFSK Low Data Rate Direct Communications

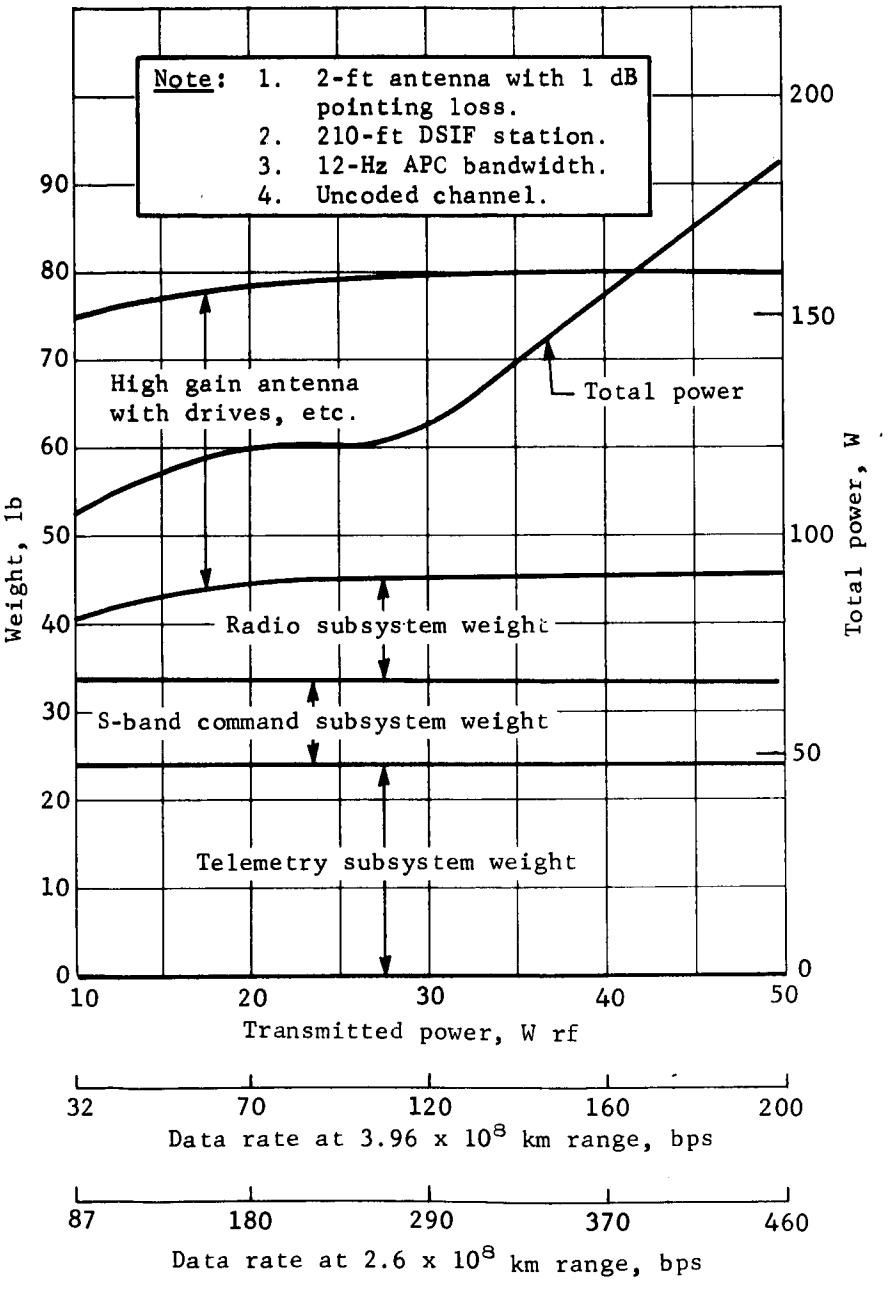

Figure D109.- High Gain Direct Communications

APPENDIX D

UHF Relay Link Parametric Studies

A radio relay link via an orbiter or a bus is used for the transmission of flight capsule engineering data, entry science status and data, and lander status from separation to shortly after touchdown. This real-time transmission capability of all data is desired to ensure the availability of data in case of failure, so that events can be reconstructed and corrective actions initiated. The geometry of the flight capsule and the spacecraft (orbiter or bus) is such that, for either mission mode and the achievable range of targeting parameters, good communications can be established between the vehicles from separation to landing. Past studies have shown that direct communications to Earth from the flight capsule are not possible because the line of sight during the latter part of the descent trajectory is not available for all flight capsule trajectories. With a relay link used for separation to landing phases of the mission, the communication geometry for both mission modes is similar because both are identically constrained by line-of-sight requirements and multipath propagation considerations.

For certain weight class landers, a radio relay link to an orbiter is required to satisfy a data volume requirement of 10^7 bits total in two days. Analysis of orbiter surface traces for the specified orbits for this study shows that an adequate number of periapsis contacts occur over the first few days to satisfy the data volume requirement. Contacts at apoapsis occur where the contact time is greater and the transmission distance is long. The use of these contacts for data transmission is restricted only by electrical energy requirements.

Technical considerations. - Technical considerations are discussed in the following paragraphs.

Frequency selection: Past trade studies have shown that the system weight for a given communication performance increases at frequencies below about 200 MHz primarily due to galactic noise and increases at frequencies above 400 MHz primarily due to path loss. Between 200 and 400 MHz, the system weight is relatively insensitive to frequency, and the selection within this range can be based on the ease of integration of the antenna design into the vehicles. For a fixed gain out of a cavity-type antenna configuration, the volume of the antenna is inversely proportional to the cube of the frequency. Thus, 400 MHz has been selected as an operating frequency band on the basis of antenna integration considerations. This frequency band is also an FCC space allocation for telemetry transmissions.

APPENDIX D

Modulation technique: Past trade studies have analyzed coherent PSK and noncoherent FSK in a multipath environment. An optimized coherent PSK has a potential 3-dB advantage but is very sensitive to accurate knowledge of the multipath environment and mission geometry. The noncoherent FSK, on the other hand, is insensitive to time varying multipath conditions and can recover more easily from entry communication blackout. Noncoherent FSK also has an added advantage of ease of combination of diversity channels to improve system performance.

Antennas: The flight capsule antenna is constrained to meet the gain and coverage requirements with a fixed, body-mounted antenna. A cavity-backed crossed-slot antenna has been selected for the baseline configuration because it has both the highest power handling ability of any of the alternatives considered and greater pattern coverage. This antenna has a gain of 5 dB on-axis. The gain is 0 dB or better over 160°.

Telemetry: Radio blackout during flight capsule entry is a distinct possibility. Rather than try to overcome the large losses associated with blackout, the telemetry subsystem circumvents the problem. The flight capsule data are delayed for a period greater than the expected blackout duration and combined with the undelayed data for transmission by the radio subsystem at a single data rate.

Data rate capability. - The data rate capability as a function of transmitter output level for various communication ranges is shown in figures D110 and D111. Figure D110 is for the entry phase of the mission, and figure D111 is for the landed phase. The parametric data for both figures were derived on worst-case design points. Thus, the data rates shown represent lower bounds on actual link performance capability. The worst-case performance margin during the descent trajectory for any possible orbit is obtained at the point of touchdown due to the aspect angle to the orbiter increasing. An entry link that has a performance margin at the point of touchdown greater than the linear summation of all negative tolerances will perform satisfactorily over the complete descent trajectory. The worst-case design point for a postland relay link is one of isotropic antenna gain at both ends of the link. For figure D111, the assumption of isotropic antenna gain for the orbiter implies that the orbiter over a long period has changed the boresight axis of the relay antenna due to its requirement to maintain a sun/Canopus reference. A requirement for a single-degree-of-freedom antenna pointing system on the orbiter that changes with time will improve the link performance considerably.

APPENDIX D

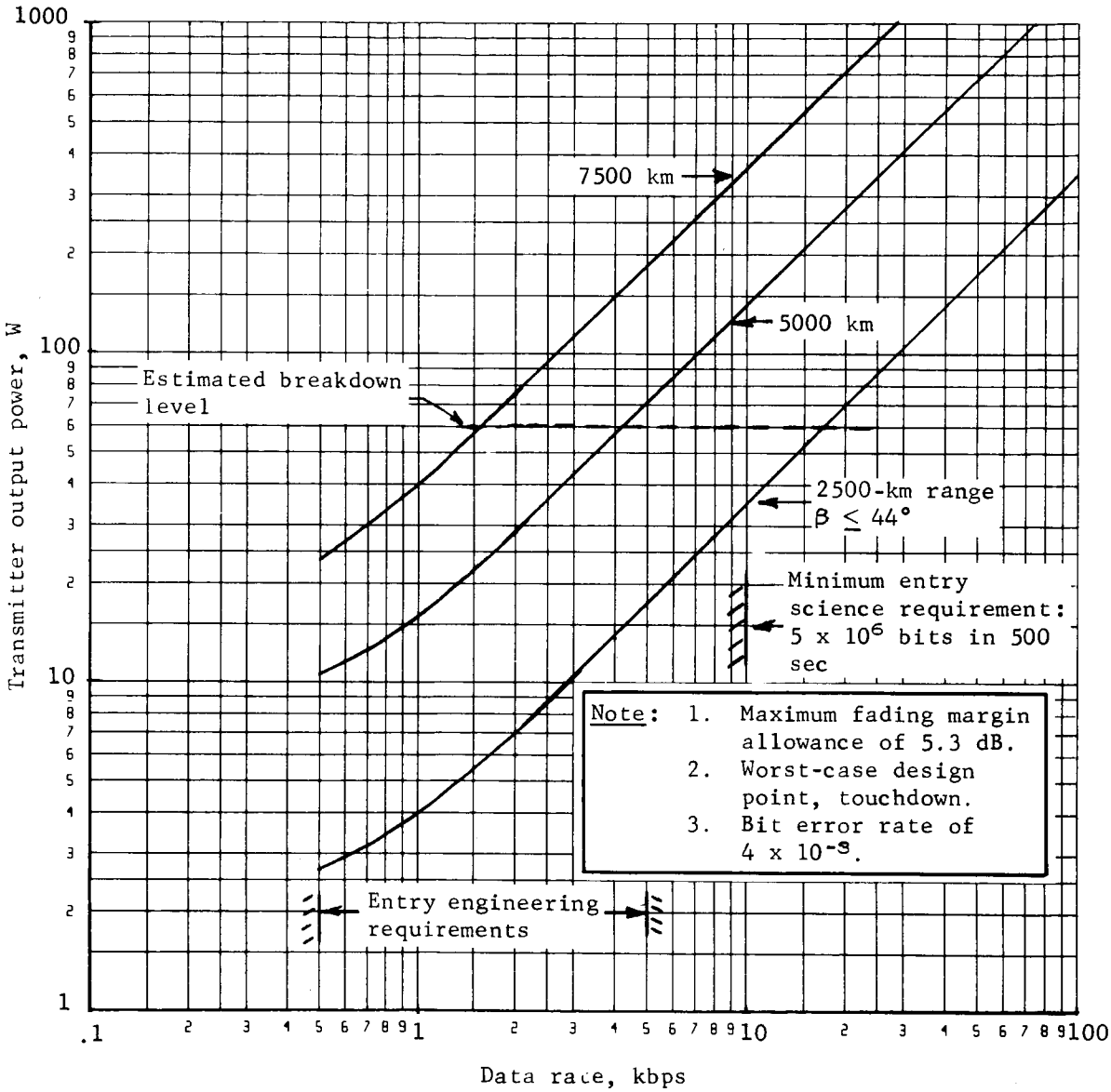

Figure D110.- Entry Relay Link, Noncoherent FSK, 400 MHz

APPENDIX D

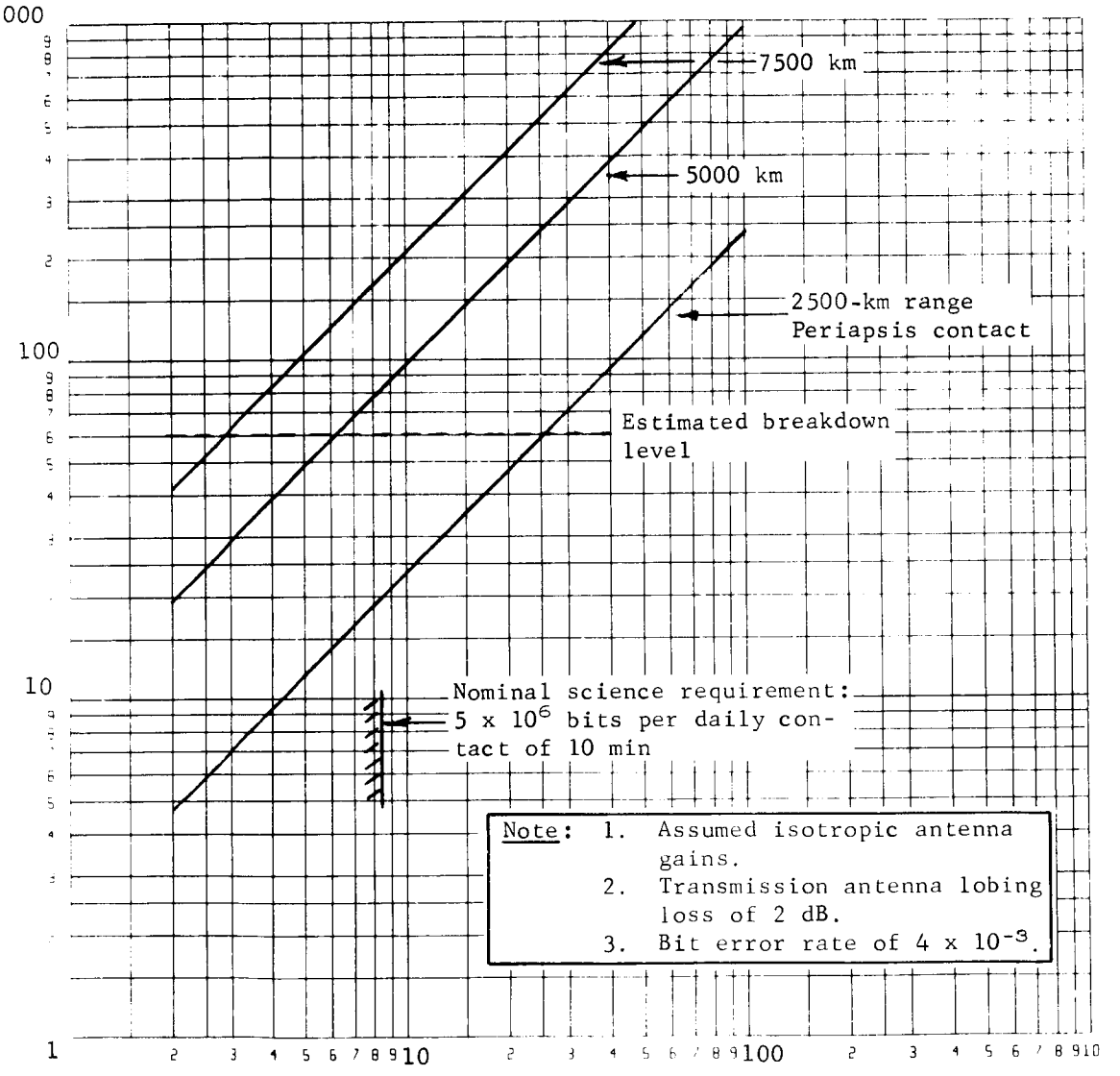

Figure D111.- Post-Land Relay Link, Noncoherent FSK, 400 MHz

TABLE D27.- ENTRY RELAY LINK, WORST CASE AT TOUCHDOWN

Parameter	Value	Tolerance, dB		Notes
Transmitter power	+47.4 dBm	+1.0	-0	55 W min.
Transmitting circuit loss	-1.0 dB	+0	-0.5	
Transmitting antenna gain	+5.0 dB	+.5	-0.5	
Transmitting antenna pointing loss	-6.0 dB	----	----	55° + 34° slope
Space loss	-158.4 dB	----	----	
F = 400 MHz, R = 5000 km				
Polarization loss	-.2 dB	+.2	-0.3	
Receiving antenna gain	+5.0 dB	+.5	-0.5	
Receiving antenna pointing Loss	-.9 dB	----	----	30°
Receiving circuit loss	-1.0 dB	+0	-0.5	
Net circuit loss	-157.5 dB	+1.2	+2.3	
Received carrier power	-110.1 dBm	+2.2	-2.3	
Receiver noise spectral density	-170.6 dBm	+1.0	-2.0	
T_{sys} = 1000°K max.				
Received S/N_0	+60.5 dB	+3.2	-4.3	
Data rate (1/T = 4000 bps)	+36.0 dB	----	----	
Received ST/N_o	+24.5 dB	+3.2	-4.3	
Data channel				
Threshold ST/N_o	+13.5 dB	+1.0	-1.0	BER = 4×10^{-3}
Performance margin	+11.0 dB	+4.2	-5.3	
Performance margin with fading allowance of 5.3 dB max.	+5.7 dB	+4.2	-5.3	

TABLE D28.- POST-LAND RELAY LINK, WORST CASE WITH ISOTROPIC GAINS

Parameter	Value	Tolerance, dB		Notes
Transmitter power	+40.8 dBm	+1.0	-0	12 W min.
Transmitting circuit loss	-1.0 dB	+0	-0.5	
Transmitting antenna gain	+5.0 dB	+.5	-0.5	
Transmitting antenna pointing loss	-4.5 dB	----	----	
Space loss	-152.4 dB	----	----	
F = 400 MHz, R = 2500 km				
Polarization loss	-.2 dB	+.2	-0.3	
Receiving antenna gain	+5.0 dB	+.5	-0.5	
Receiving antenna pointing loss	-4.5 dB	----	----	
Receiving circuit loss	-1.0 dB	+0	-0.5	
Net circuit loss	-153.6 dB	+1.2	-2.3	
Received carrier power	-112.8 dB	+2.2	-2.3	
Receiver noise spectral density	-170.6 dBm	+1.0	-2.0	
T_{sys} = 1000°K max.				
Received S/N_o	+57.8 dB	+3.2	-4.3	
Data rate (1/T = 5000 bps)	+37.0 dB	----	----	
Received ST/N_o	+20.8 dB	+3.2	-4.3	
Data channel				
Threshold ST/N_o	+13.5 dB	+1.0	-1.0	BER = 4×10^{-3}
Performance margin	+7.3 dB	+4.2	-5.3	
Performance margin with 2-dB lobing loss	+5.3 dB	+4.2	-5.3	

APPENDIX D

The assumptions and system parameters used to derive figures D110 and D111 are presented in tables D27 and D28. These tables are telecommunication design control tables with nominal parameter values and tolerances on the parameters identified. Table D27 shows that 55 W of transmitter output power is required to provide a data transmission rate capability of 4000 bps for a maximum range of 5000 km, which occurs at touchdown. At this point, the aspect angle to the orbiter is 89 deg, which includes an adverse tilt of the lander of 34 deg due to surface slope. The fading margin allowance of 5.3 db maximum is adequate for a wide range of entry conditions (spacecraft lead angles of $\pm$ 20 deg, Martin Marietta Corporation Voyager Phase B Final Report). Table D28, a link calculation, shows that 12 W of transmitter output is required to support a 5000-bps link at 2500 km. The data rate capability is derived for a BER of 4×10^{-3}.

With this allocation of error rate, the end-to-end BER of 5×10^{-3} is achieved by requiring the orbiter-to-Earth link to maintain a BER of 1×10^{-3}. The selection of the uhf relay link BER was derived from an analysis of the sensitivity of mission-dependent parameters to fading margin requirements.

The modulation technique used for relay communications to the orbiter requires a predetection bandwidth that is wide enough to accommodate the frequency uncertainty due to instability and doppler shift and the spectrum of the modulating waveform. For these studies, the total frequency uncertainty band is taken as 53 ppm, which allows 20 ppm for transmitter stability, 10 ppm for receiver stability, and 23 ppm for doppler. The mark or space channel bandwidth is given by

$$W = \frac{3}{2}\left(2f_D\right) + \Delta F = 3f_D + \Delta F \ (\text{Hz})$$

where f_D is the information rate in bits per second, and ΔF is the total frequency uncertainty. The modulating waveform is split-phase PCM, which results in a symbol rate that is twice the information rate.

The ratio of predetection bandwidth to information rate (WT) for bit rates between 4000 and 100 000 bps ranges from 8.3 to 3.2 for the frequency uncertainty used here. Past work conducted by RCA has shown good agreement between theoretical performance predictions and experimental performance for $WT \geq 10$. Also, experimental data exist for $WT = 1$, which supports theoretical analyses. Because the parametric studies are concerned with WT products for which no experimental data exist and theoretical models are not valid, the data rate capability has been derived by assuming a constant value of ST/N_o equal to 13.5 dB for $10 \cdot WT \cdot 1$. This assumption will provide some additional margin in the system design.

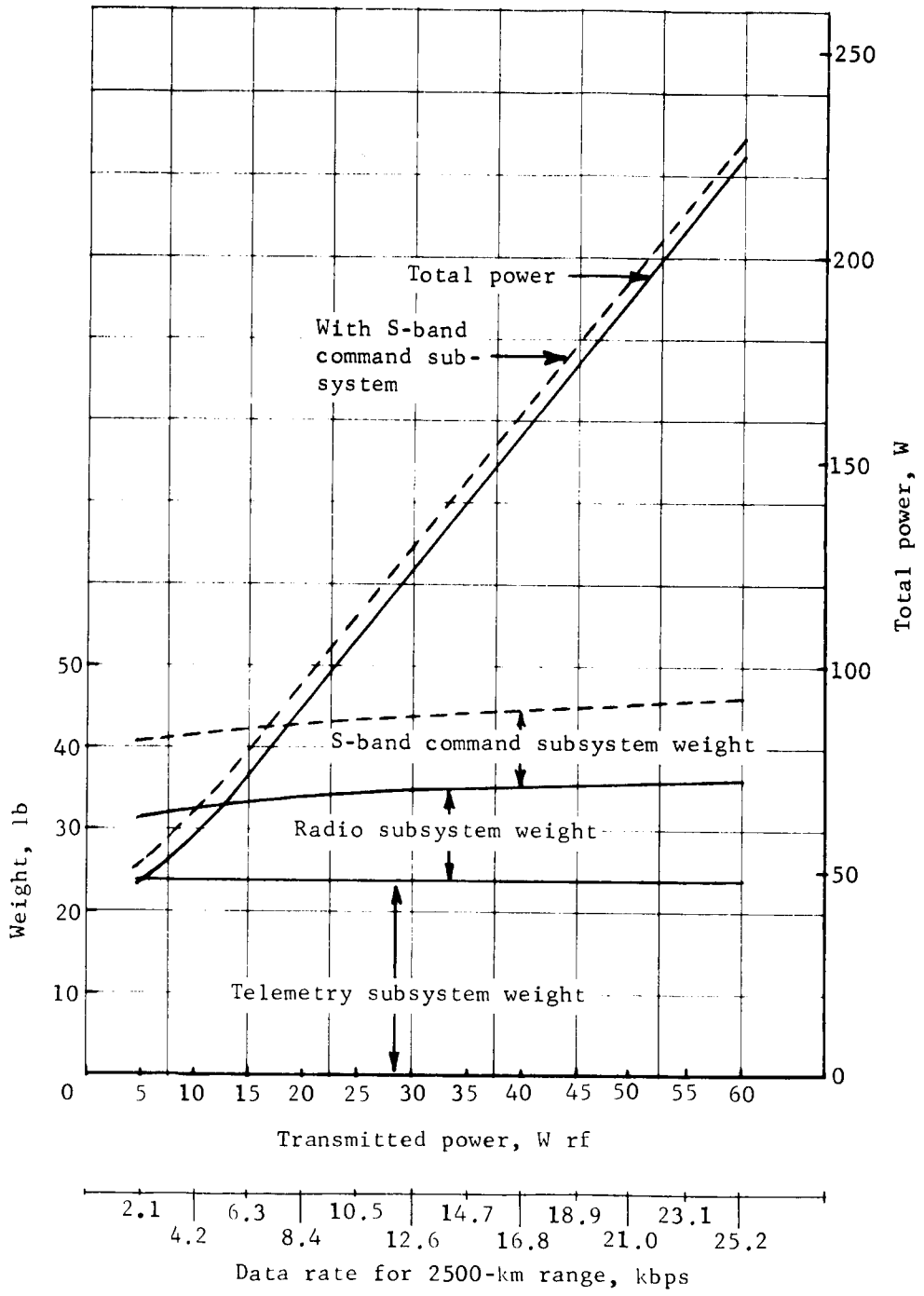

Figure D112.- Post-Land Relay Communications

APPENDIX D

Command Link Performance. - The performance of the command subsystem at a command data rate of 8-1/9 bps is shown in Table D29. This link has been designed for reception of commands at a maximum range of 4×10^8 km. At this range, the command data channel worst-case performance margin is +1.7 db.

Relay link baseline configuration parametric data. - The baseline configuration is nonredundant and includes the following elements: (1) a 200-channel telemetry subsystem with a 50 000-bit static storage device, (2) a radio subsystem comprised of a solid-state uhf transmitter, a body-fixed broadbeam antenna, and a beacon receiver for initiation and termination of data transmission to the orbiter during landed operations. The optional S-band command subsystem includes the receiver, detector, and antenna. The weight and total power requirements for this configuration as a function of transmitter power output level are shown in figure D112. The data rate capability is based on the 2500-km range indicated under the assumption that the worst-case antenna gain is 0 dB.

8. POWER AND PYROTECHNIC SUBSYSTEMS

Parametric weight and performance data for the power and pyrotechnic subsystems were developed during the first part of this study within the technical guidelines derived from mission and system requirements and constraints. Data for the power subsystem consist of curves, equations and factors which will permit determination of the subsystem weight and the size of the battery, solar array or Radioisotope Thermoelectric Generator (RTG). The pyrotechnic subsystem data consist of curves for determining the subsystem weight versus bridgewire firing requirements for capacitor energy storage with solid state firing and safe/arm circuits.

Power Subsystem

Parametric sizing and weight data for the power subsystem are presented in this section.

For power subsystem design, the power profile for a Mars lander consists of the separation to landing phase and the surface operations phase. Since the repeating profile for extended surface operations represents the larger energy requirements, the minimum weight power subsystem will normally result from designing for the landed mission and providing a supplementary battery to meet the requirements from separation through landing.

TABLE D29.- COMMAND LINK PERFORMANCE

Parameter	Value	Tolerance, dB		Notes
Total transmitter power	80.0 dBm	---	---	100 kw
Transmitting circuit loss	-.4 dB	0.1	-0.1	Estimate
Transmitting antenna gain	60.0 dB	0.8	-0.8	EPD-283
Transmitting antenna pointing loss	-.3 dB	0.3	-0.	$\pm$.02°
Space loss F = 2115 MHz, R = 2.9 x 10^{11} km	-268.2 dB	---	---	
Polarization loss Lander ϵ = 6 dB, DSIF ϵ = 0.8 dB	-.6 dB	---	---	Maximum
Receiving antenna gain	5.0 dB	0.5	-0.5	
Receiving antenna pointing loss	-5.0 dB	5.0	-0.	$\pm$65°
Receiving circuit loss	-1.5 dB	0.2	-0.2	
Net circuit loss	-211.0 dB	6.9	-1.6	
Total received power	-131.0 dBm	6.9	-1.6	
Receiver noise spectral density T_{system} = 1750°K	-166.2 dBm	1.1	-1.1	Low noise mixer
Carrier modulation loss	-4.8 dB	0.5	-0.6	θ_D = 1.12 rad $\pm$5% θ_S = .63 rad
Received carrier power	-135.8 dBm	7.4	-2.2	
Carrier APC noise BW $2B_{LO}$ = 20 Hz	13.0 dB	0.5	-0.4	
Carrier performance-command				
Threshold SNR in $2B_{LO}$	8.0 dB	1.0	-1.0	MC-4-310A
Threshold carrier power	-145.2 dBm	2.6	-2.5	
Performance margin	9.4 dB	10.0	-4.7	
Data channel				
Modulation loss	-5.3 dB	0.5	-0.5	θ_D = 1.12 rad $\pm$5%
Received data subcarrier power	-136.3 dBm	7.4	-2.1	
Bit rate (1/T = 8-1/9 bps)	9.1 dB	---	---	
Required ST/N/B	12.1 dB	1.0	-1.0	$P_e^b = 10^{-5}$
Threshold subcarrier power	-145.0 dBm	2.1	-2.1	
Performance margin	8.7 dB	9.5	-4.2	+4.5 worst case

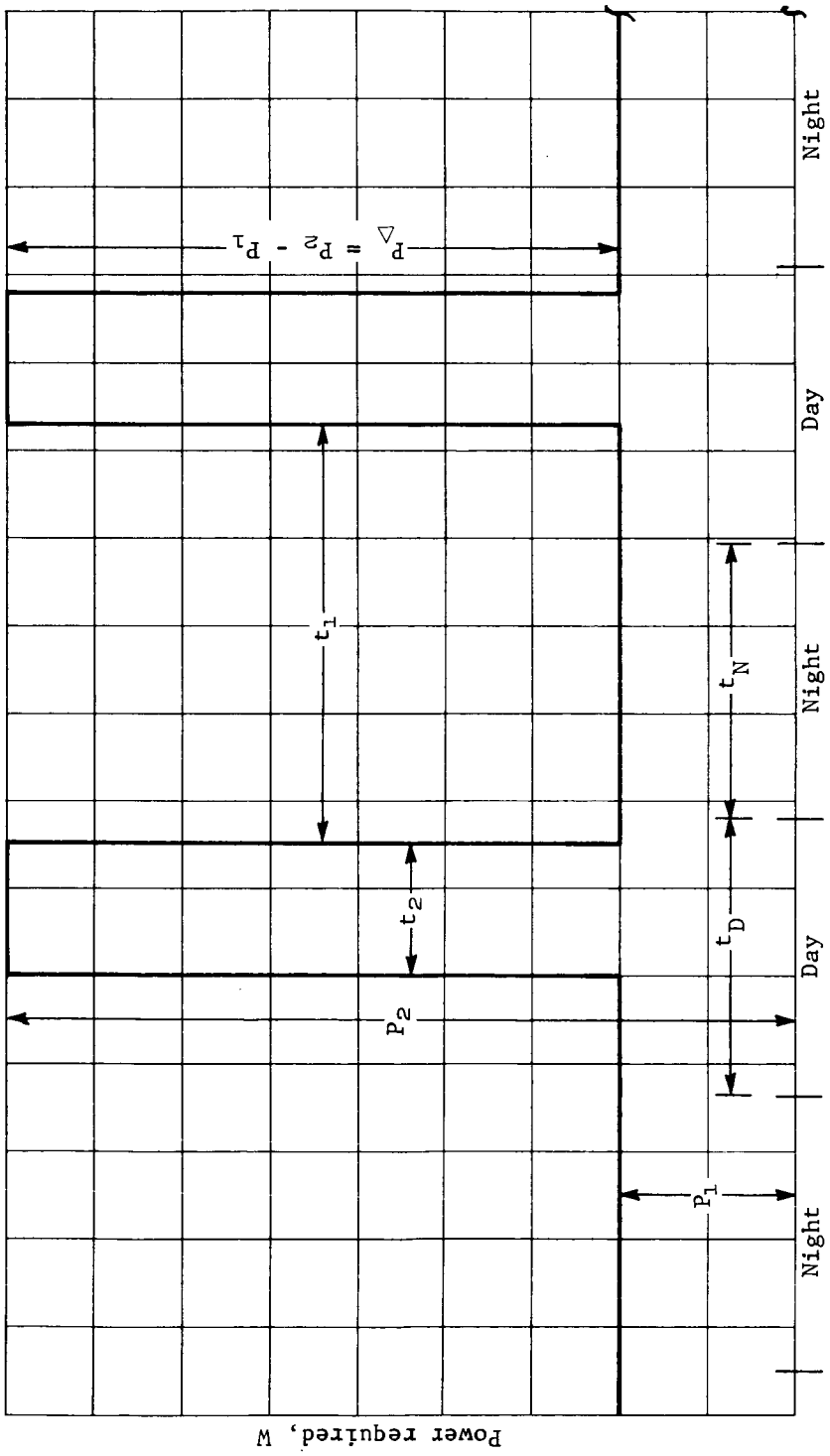

Figure D113.- Generalized Power Profile, Surface Operations

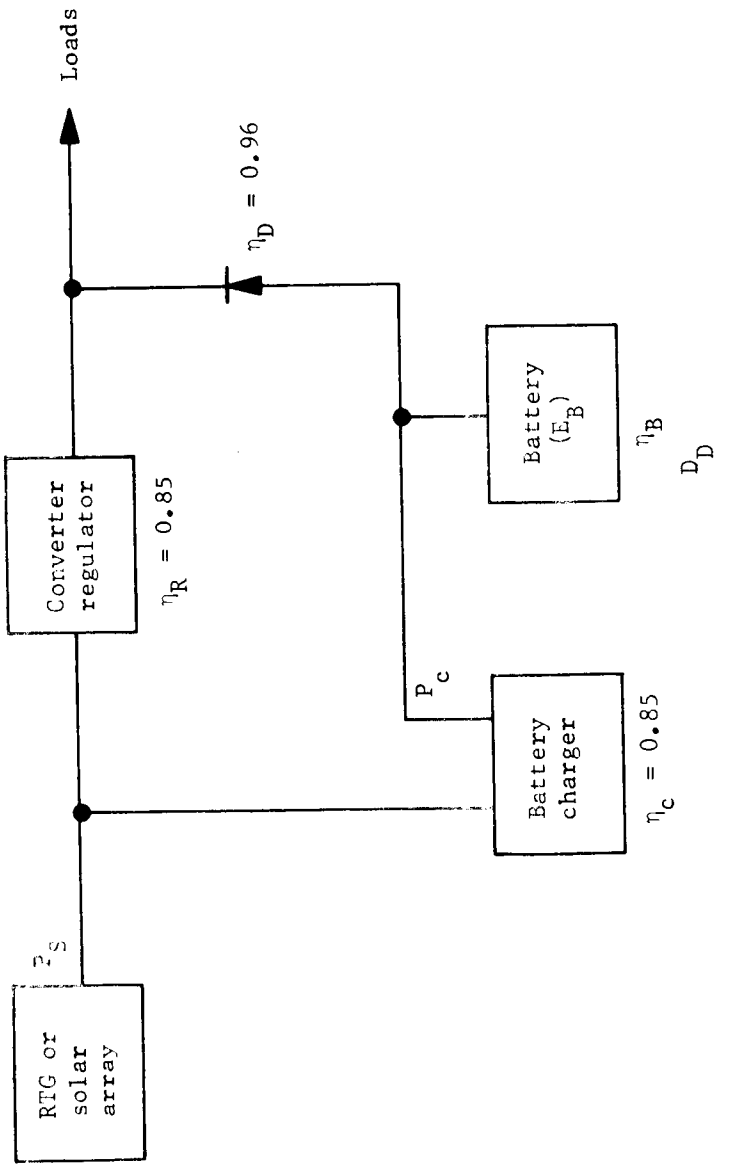

Figure D114.- Generalized Power Subsystem Block Diagram

APPENDIX D

The power subsystem parametric study considered four configurations: all-battery, RTG/Ni-Cd battery, solar array/Ni-Cd battery, and solar array/Ag-Zn battery. Limits established for the study are:

1) Continuous power level, 10 to 200 W;
2) Peak power-to-continuous power ratio, 2:1 to 20:1;
3) Maximum peak power, 600 W;
4) Data transmission duty cycle, $t_2/(t_1 + t_2)$ 0.5 to 50%.

All-battery configuration. - The all-battery configuration is presented to provide data on secondary batteries to determine the weight of a supplemental battery from separation to landing, and for use with the solar array and RTG configurations. The material also shows what can be done with batteries alone for a short-time mission. For the supplemental battery or an all-battery configuration, the Ag-Zn battery provides the minimum weight; however, if the sterilizable Ag-Zn battery has not been developed, the heavier Ni-Cd battery would be used.

To determine the source size for an all-battery system, the area under the load curve and all losses must be determined. For the power profile shown in figure D113 the battery energy, E_B, is:

$$E_B = \frac{P_1 t_1 + P_2 t_2}{\eta_D} \text{ W-h per Martian day}$$

where P_1 and P_2 are in watts and t_1 and t_2 are in hours.

The energy density of a Ag-Zn or Ni-Cd battery may be determined from figures D115 and D116, respectively. Battery weight is battery energy divided by energy density.

Figure D113 shows the repeating load profile used to determine all source and storage battery sizing equations. This generalized profile assumes a continuous nominal load, P_1, for a time period, t_1 consisting of the nighttime period, t_N, and part of the daytime period, t_D, with a period, t_2, for data transmission at some higher peak power, P_2. For simplification, the short-duration load pulses of an actual load profile must be averaged and included in the values used for continuous and peak power. The block diagram of the generalized power subsystem is shown in figure D114. The power required from the source P_S is a function of the load profile and the power efficiencies of the converter/regulator η_R, the battery charger η_C, the diode η_D,

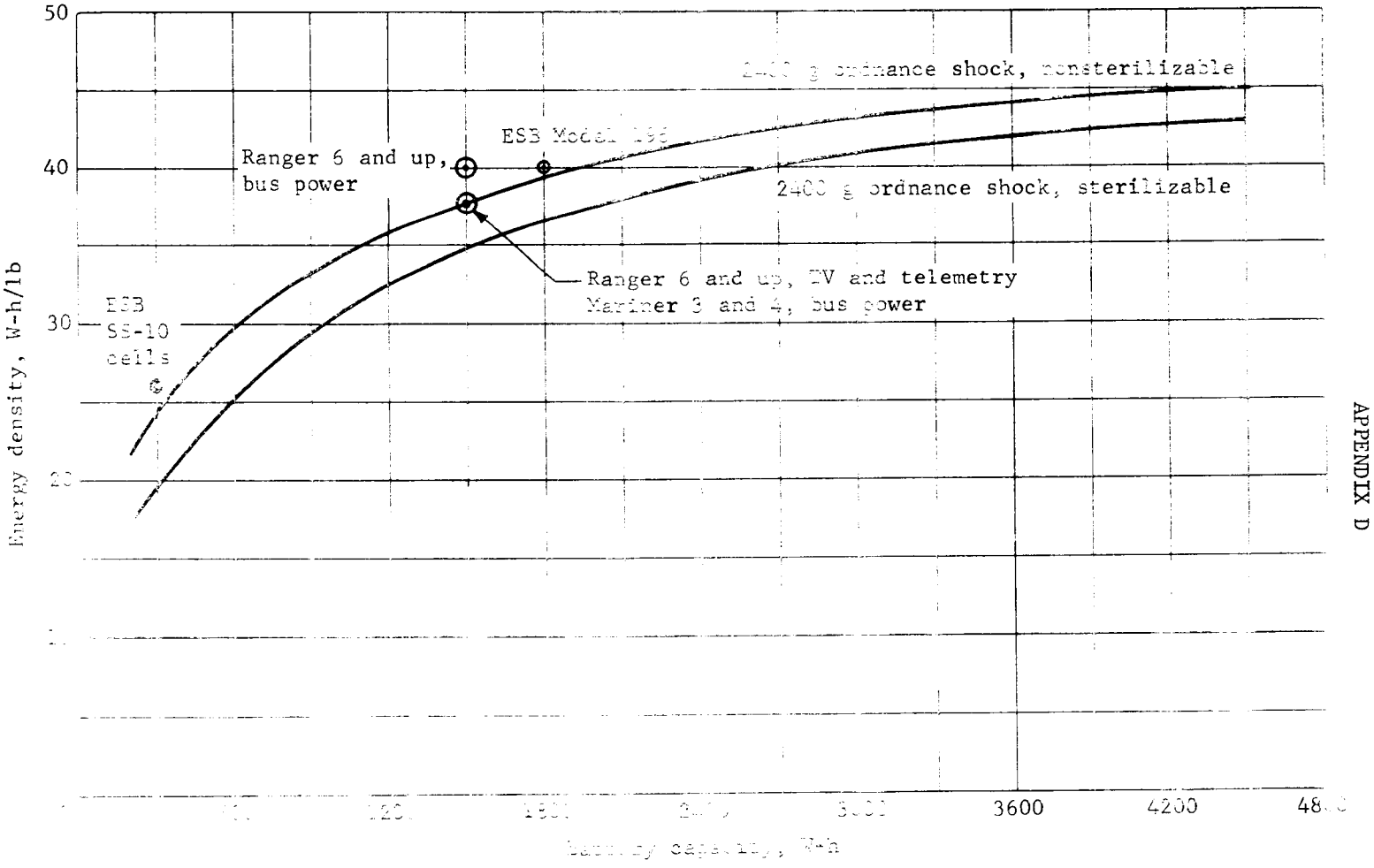

Figure D-1. - Typical Energy Density for Ag-Zn Batteries (Nominal 30 V)

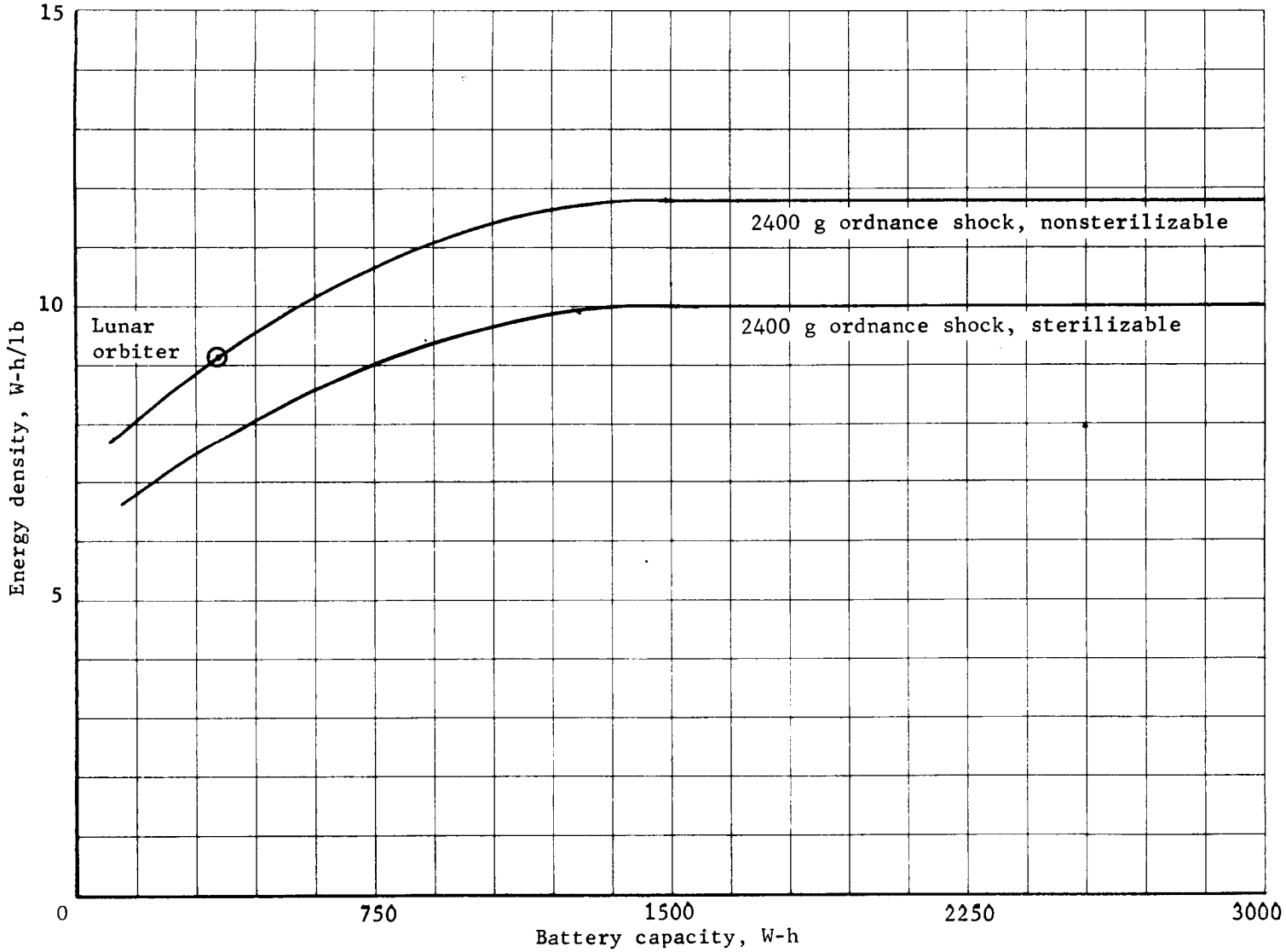

Figure D116.- Typical Energy Density for Ni-Cd Batteries (Nominal 30 V)

the charge acceptance efficiency of the battery η_B, and the depth of discharge of the battery, D_D.

The curves shown in figures D115 and D116 have been generated by the Martin Marietta Corporation for comparative purposes. These curves represent estimated energy densities for specific battery designs and include cells, battery case, potting, wiring, and connectors for a 30 V nominal battery with the following constraints:

1) Sealed cells;
2) Thin plate construction to allow good high current drain performance;
3) Shock (ordnance type) - 2400 g peak response with the peak occurring at 2000 cps (equivalent to 1500 g, 0.4 msec, half sine pulse input);
4) Vibration - random, overall 11.7 g rms with input flat 100 to 200 cps at 0.3 g^2/cps, rolloff below 100 cps at 6 dB/octave, rolloff above 200 cps at 4 dB/octave.

The nonsterilizable Ag-Zn battery curve of figure D115 is based on Electric Storage Battery (ESB) Company sealed silver-zinc cells packaged in a battery to meet the above requirements. Data from the JPL sterilizable battery contract with ESB were used to extrapolate the sterilizable battery curve, allowing for the relatively less severe ordnance shock specified above. These curves are based on limited data and should be used accordingly. They are being continuously revised as more data become available from the JPL-ESB contract and Martin Marietta in-house test programs on sterilizable silver-zinc cells.

The nonsterilizable Ni-Cd battery curve of figure D116 is based on Gulton Industries, Inc., sealed nickel-cadmium cells packaged in a battery to meet the construction and environmental requirements given above. A 15% loss due to sterilization was used to extrapolate the sterilizable battery curve. These curves are being revised as more data become available from a Martin Marietta in-house test program on sterilizable nickel-cadmium cells.

RTG/battery configuration. - The equations developed for the RTG/battery configuration are general and may be used for either Ag-Zn or Ni-Cd batteries. Because of the significantly greater cycle life of the Ni-Cd battery and the long life of the RTG, parametric data were developed for the RTG/Ni-Cd configuration only.

APPENDIX D

For the RTG/battery system, equations were developed that define the relationship of the RTG output power and the battery energy to the generalized power profile and block diagram (figs. D113 and D114). For this type system, the battery is required to supply only that portion of the load during the peak power period that is in excess of the usable power from the RTG. From the block diagram it can be seen that this usable power is represented by the product of source power and converter efficiency $\left(P_S\eta_R\right)$. The battery size required is determined by:

$$E_B = \frac{\left(P_2 - P_S\eta_R\right)t_2}{D_D\eta_D} \text{ (W-h)} \tag{D18}$$

The RTG must be sized to supply the nominal continuous load plus the power required to recharge the battery; therefore, the RTG size is determined by:

$$P_S = \frac{P_1}{\eta_R} + \frac{E_B}{\eta_C R_C} \tag{D19}$$

where R_C is the battery charge rate in hours. To determine the battery size and the RTG size as a function of the subsystem configuration and load profile, equations (D18) and (D19) are solved for E_B and P_S.

$$P_S = \frac{P_1}{\eta_R} + \frac{P_\Delta t_2}{\eta_C\eta_D R_C D_D + \eta_R t_2} \tag{D20}$$

$$E_B = \frac{\eta_C R_C P_\Delta t_2}{\eta_C\eta_D R_C D_D + \eta_R t_2} \tag{D21}$$

To minimize the size of the RTG, the relative charge rate, R_C, should be as large as possible while still permitting complete recharge of the battery. The curve of figure D117 shows the time required to replace 10% of the capacity of a Ni-Cd battery at a given charge rate. For a 50% depth of discharge the time would be five times the time for 10%. The maximum value of R_C that should be used for most applications is 15 hr. The curve of figure D118 shows the ratio of rated battery energy to P_Δ as a function of transmitting time or peak power time, t_2.

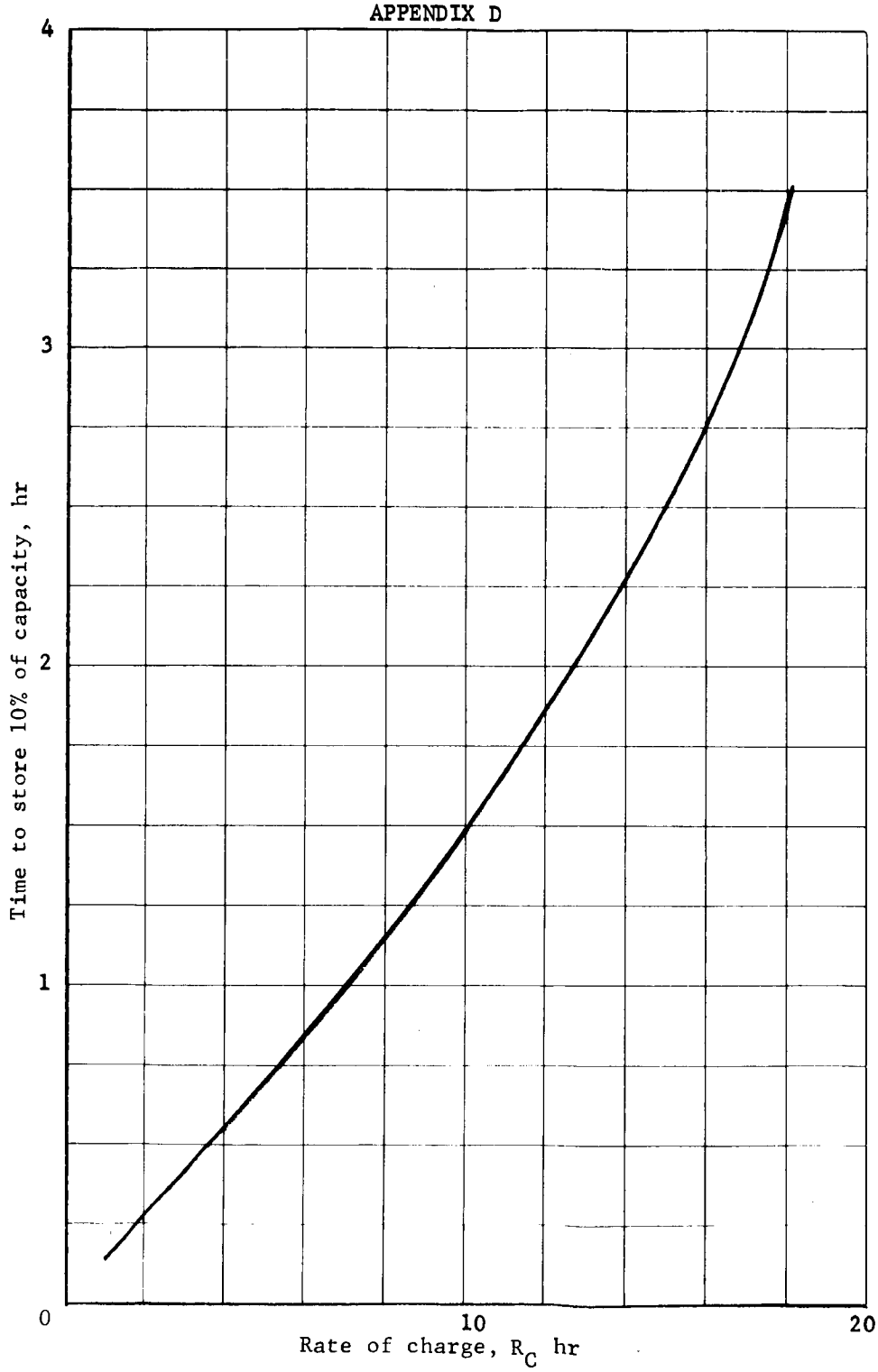

Figure D117.- Rate of Charge Effect on Charge Time for a Ni-Cd Battery

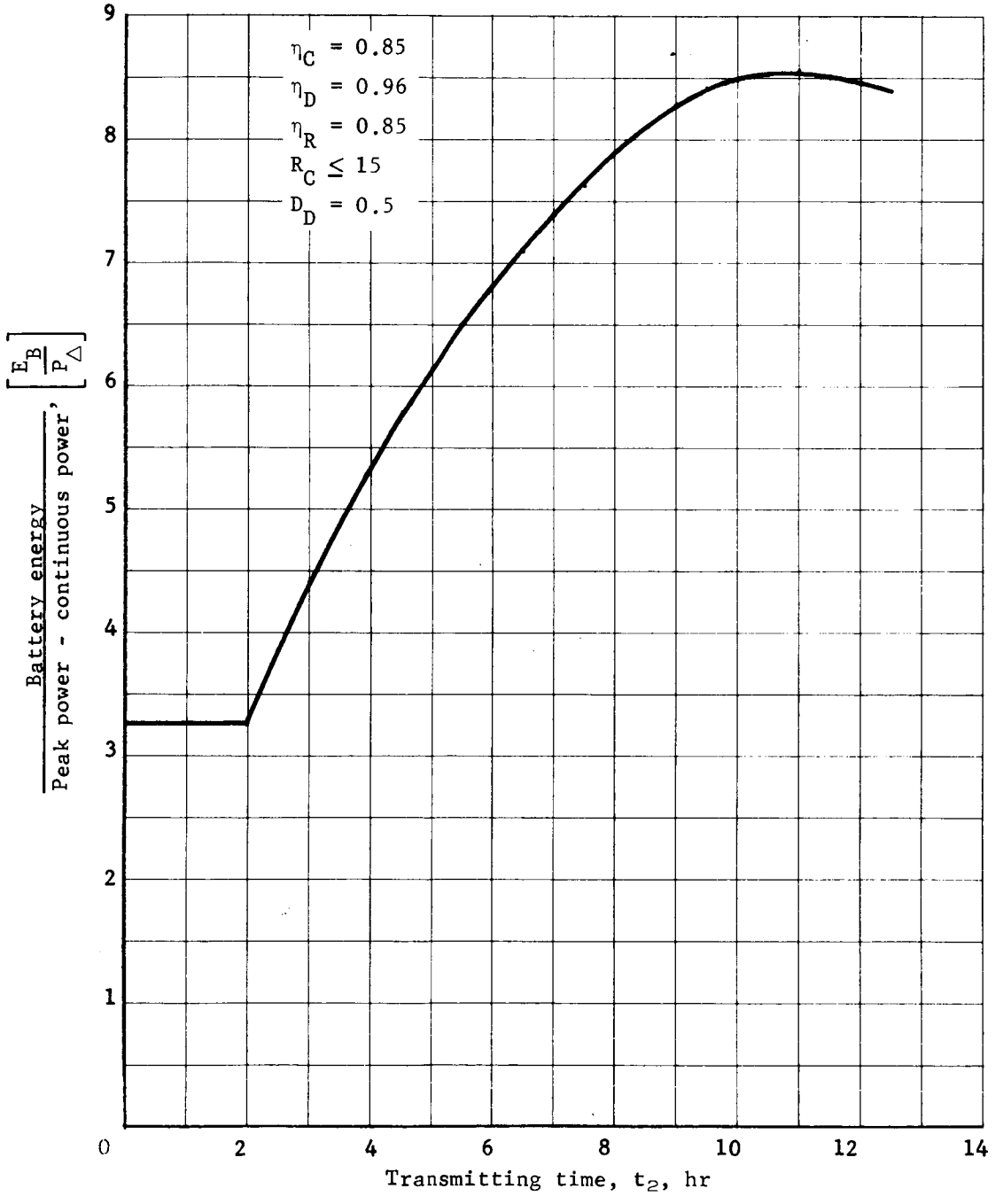

Figure D118.- Battery Size Ratio for RTG/Ni-Cd System on Mars

This curve is based on typical system efficiencies shown in the block diagram (fig. D114), a 50% depth of discharge D_D, $R_C \leq$ 15 hr as determined by figure D117, and a minimum discharge rate of 4 hr. After the battery energy is determined, the weight of the battery may be obtained from figure D116.

For the system efficiencies shown in the block diagram, and the restrictions specified for the battery, the curves of figure D119 may be used to determine the minimum end-of-life power required from the RTG. The weight of the RTG may be determined from the following power density tabulation.

Thermoelectric hot junction temperature, °F	Power density, W/lb
1250	0.54
1500	0.86

These power densities are based on the work performed by Martin Marietta Corporation during the Voyager Phase B study and are for an RTG using silicon-germanium for the thermoelectrics and capable of intact entry and intact impact. The power density is for the complete RTG and its release mechanism, but does not include the mounting structure.

Solar array/battery configuration.- For the solar array/battery configuration, equations were developed defining the relationship of the solar array output power and the battery energy to the generalized power profile and block diagram (figs. D113 and D114). For this configuration, the battery is required to supply the energy at night and also that portion of the load during the peak power period that is in excess of the usable power from the solar array. From the block diagram it can be seen that the usable array power is represented by the product of source power and converter efficiency $(P_S \eta_R)$.

When the data transmission time is long compared with the usable daylight hours, the solar array must provide enough power to meet all daytime demands plus that needed to charge the battery. For short data transmission periods the battery is also used to supplement the array during the peak power period. The equations used to determine the solar array and battery requirements are different for long data transmission times from those used when the transmission time is short. For values of P_S less than P_2/η_R obtained by solving equation (D22), equations (D25) and (D26) are used. For P_S values greater than P_2/η_R equations (D27) and (D28) are used to determine the battery and solar array size.

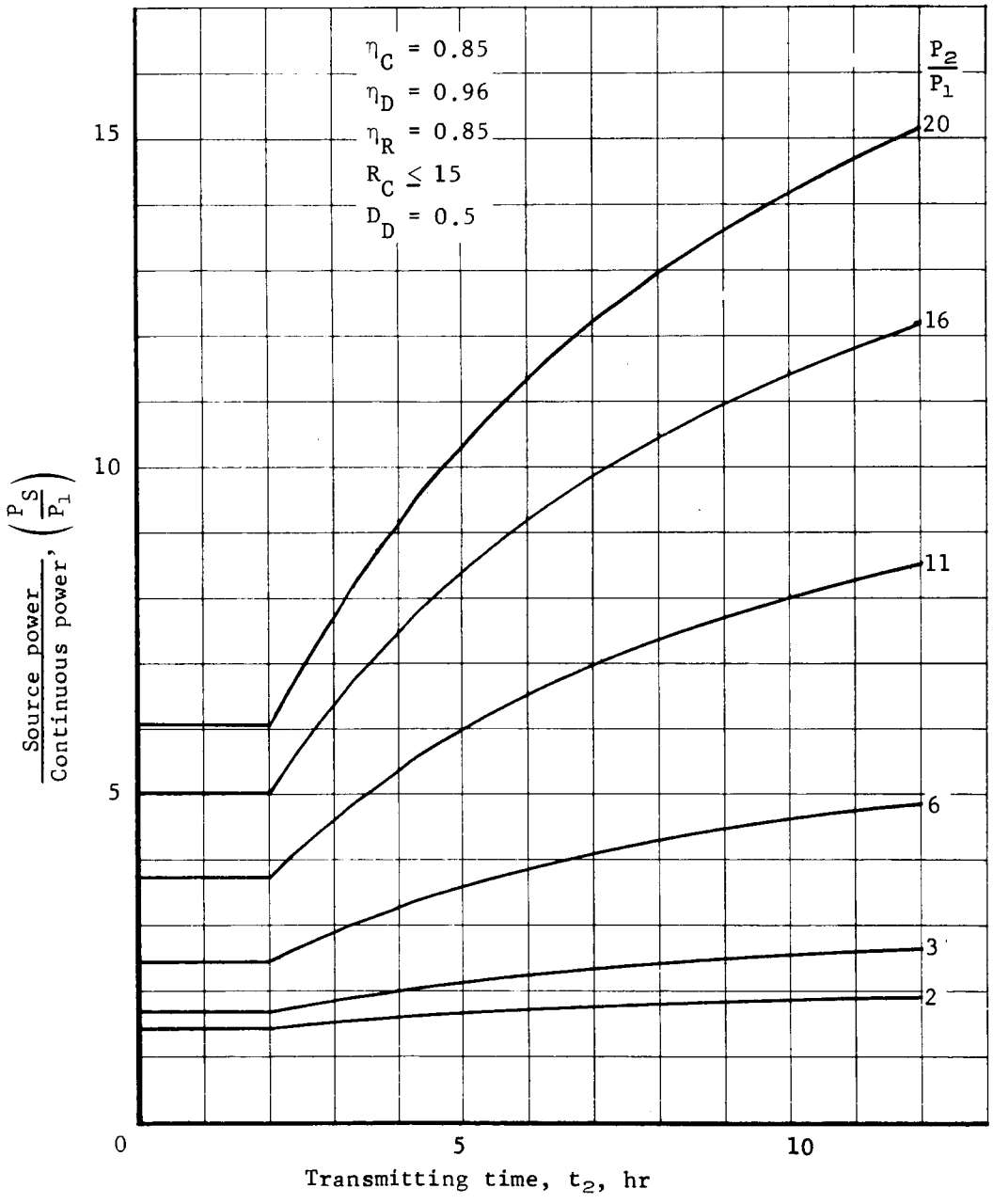

Figure D119.- RTG Size Ratio for RTG/Ni-Cd System on Mars

$$P_S = \frac{P_1}{\eta_R} + \frac{P_1 t_N}{\eta_C \eta_D R_C D_D}. \tag{D22}$$

The battery size required when the data transmission period is relatively short is determined by:

$$E_B = \frac{P_1 t_N}{\eta_D D_D} + \frac{\left(P_2 - \eta_R P_S\right) t_2}{\eta_D D_D} \tag{D23}$$

The solar array must be sized to provide the continuous load power plus the energy required to recharge the battery. Therefore, the solar array average power output is determined by:

$$P_S = \frac{P_1}{\eta_R} + \frac{E_B}{\eta_C R_C} \tag{D24}$$

where R_C is the battery charge rate, hr.

To determine the battery size and the solar array size as a function of subsystem configuration and load profile, equations (D18) and (D19) are solved for E_B and P_S.

$$P_S = \frac{P_1}{\eta_R} + \frac{P_1 t_N + P_\Delta t_2}{\eta_C \eta_D R_C D_D + \eta_R t_2} \tag{D25}$$

$$E_B = \frac{\eta_C R_C \left(P_1 t_N + P_\Delta t_2\right)}{\eta_C \eta_D R_C D_D + \eta_R t_2} \tag{D26}$$

In a similar manner the equations for the solar array size and battery size as a function of subsystem configuration and load profile for long data transmission periods may be shown to be:

$$P_S = \frac{P_1}{\eta_R} + \frac{P_1 t_N}{\eta_D \eta_C \eta_R \left[\eta_{B_1}\left(t_D - t_2\right) + \eta_{B_2} t_2\right]} + \frac{P_\Delta \eta_{B_2} t_2}{\eta_R \left[\eta_{B_1}\left(t_D - t_2\right) + \eta_{B_2} t_2\right]} \tag{D27}$$

$$E_B = \frac{P_1 t_N}{\eta_D D_D} \tag{D28}$$

where η_{B_1} is the battery charge acceptance efficiency during the period $t_D - t_2$ and η_{B_2} is the battery charge acceptance efficiency during the period t_2. The values for η_B versus R_C for typical Ni-Cd batteries are shown in figure D120.

For Ag-Zn batteries, η_B is almost constant with relative charge rates of 20 to 80 hr. Therefore equation D27 becomes:

$$P_S = \frac{P_1}{\eta_R} + \frac{P_1 t_N}{\eta_D \eta_C \eta_R \eta_B t_D} + \frac{P_\triangle \eta_B t_2}{\eta_R \eta_B t_D}. \tag{D29}$$

For Ag-Zn batteries η_B is nominally 0.87.

To minimize the size of the solar array, the relative charge rate, R_C, should be as large as possible while still permitting complete recharge of the battery. The curve of figure D117 shows the time required to replace 10% of the capacity of a Ni-Cd battery at a given charge rate. For a 50% depth of discharge the time would be five times the time for 10%. The maximum value of R_C that should be used for most applications is 15 hr. For a Ag-Zn battery this value is determined by

$$\text{Charging time} = \frac{R_C D_D}{\eta_B}. \tag{D30}$$

After the solar array average power is determined the required array size may be found by use of the curves developed in the next paragraphs. Weight of the array may be determined by multiplying the area by 1 lb/ft^2.

Solar cell panel performance calculations were performed using a computer program developed by Martin Marietta Corporation for assessing panel power characteristics during planetary missions. This program, written for the IBM 1130 computer, allows calculation of the instantaneous and daily integrated output of an arbitrarily oriented flat solar panel. The effects of latitude, ground slope, time of year, and ground mask may be considered, along with atmospheric attenuation and time-variable cloud cover. The panel temperature is calculated as a function of the time of day, and temperature corrections are applied to the panel power output.

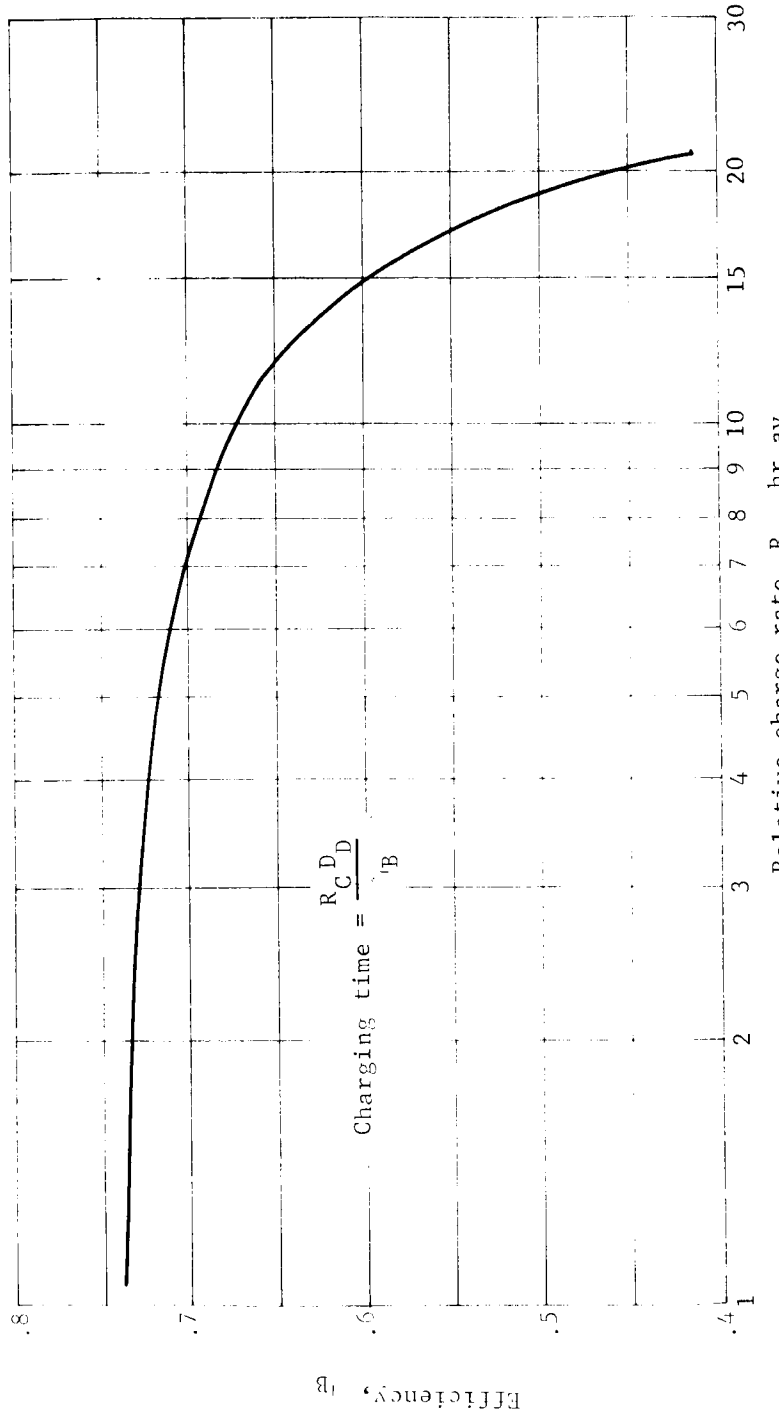

Figure DI20.- Charge Acceptance of Ni-Cd Batteries

APPENDIX D

This program has been used in establishing the performance of a directed side panel array chosen for the point designs of the lander, as shown in figure D121. One panel is horizontal and body mounted. Four side panels are adjustable in a post-land sense and have an area about twice that of the fixed panel.

In the subsequent figures, the panel temperature has been assumed to be unaffected by heat transfer from the ground, and convective effects have been neglected. Cloud cover has been assumed negligible. The power shown is after cover slide, wiring, diode, and packing losses have been accounted for, and is based on 10 W/ft^2 of usable panel area at 1 AU, air mass zero (AMO) 60°C.

Assuming a typical requirement of 15 to 20 $W\text{-}h/ft^2/day$, the performance of flat, fixed panels is satisfactory at northern near-equatorial latitudes for moderate ground slopes during the early part of 1974, as shown in figure D122 for 10° N latitude. However, at large adverse slopes and southern latitudes, power from a fixed panel drops off drastically, as shown in figure D123. It was thought that some improvement might be gained by drooping all four side panels a fixed amount. The lower curve of figure D124 shows the effect of this on the overall array output at 20° S latitude and 17° S slope. In the case shown, no significant improvement results. However, if the panels are allowed to independently take on both lift and droop angles, significant improvement in the overall array output results, as shown by the upper two curves of figure D124. Since the lander landing azimuth is not predictable, the optimum panel angles must be determined after landing. In the case considered, figure D124 shows that a landing with two of the panels on the north-south line gives slightly worse results than when all panels are 45° from the north-south line. Although figure D124 shows optimum droop and lift angles of approximately 60°, interference considerations limit the maximum droop angle to about 40°, with no such limit on the lift angle.

Figures D125 and D126 compare the output of the directed array with a horizontally fixed array. Substantial improvement results, especially at southern latitudes.

Another advantage of the directed panel concept is that it allows a significant increase in the number of hours of useful solar power per day independent of ground slope, thus minimizing the required battery size. Figure D127 shows the available daylight hours for three latitudes, as seen by the directed solar array.

APPENDIX D

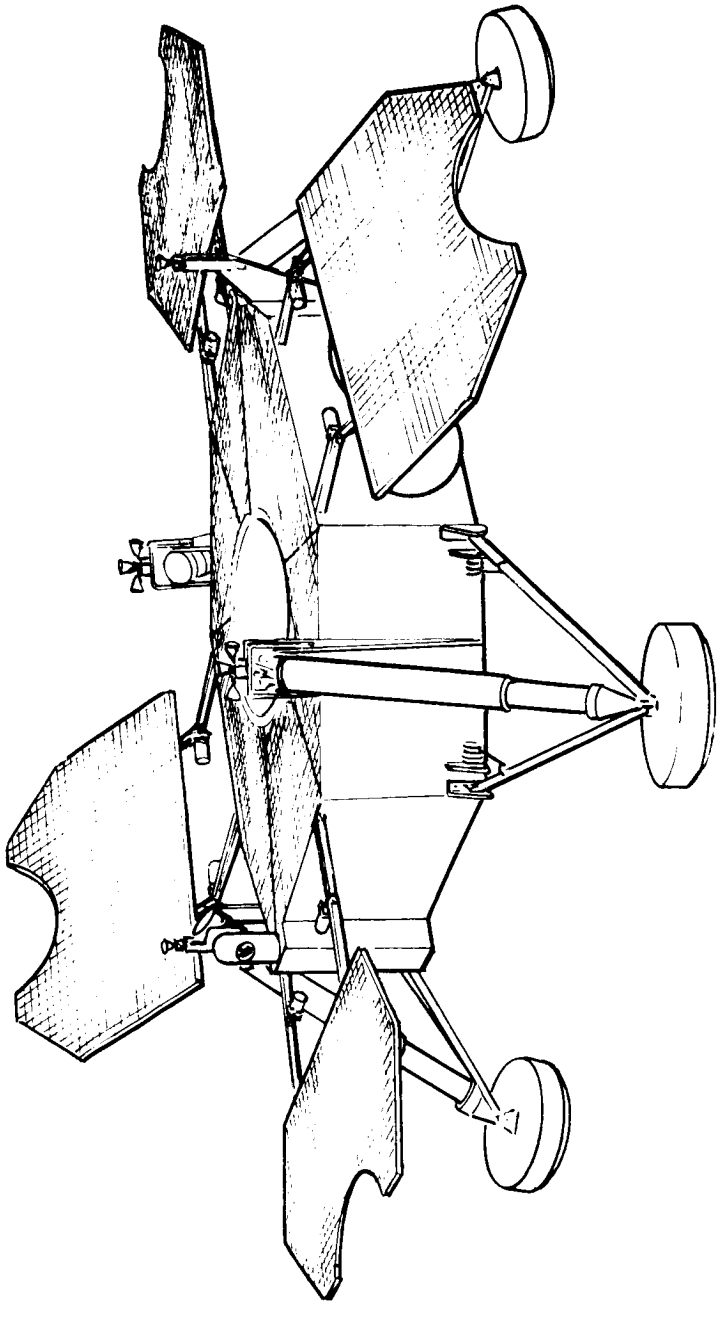

Figure D121.- Solar Panel Configuration, Deployed

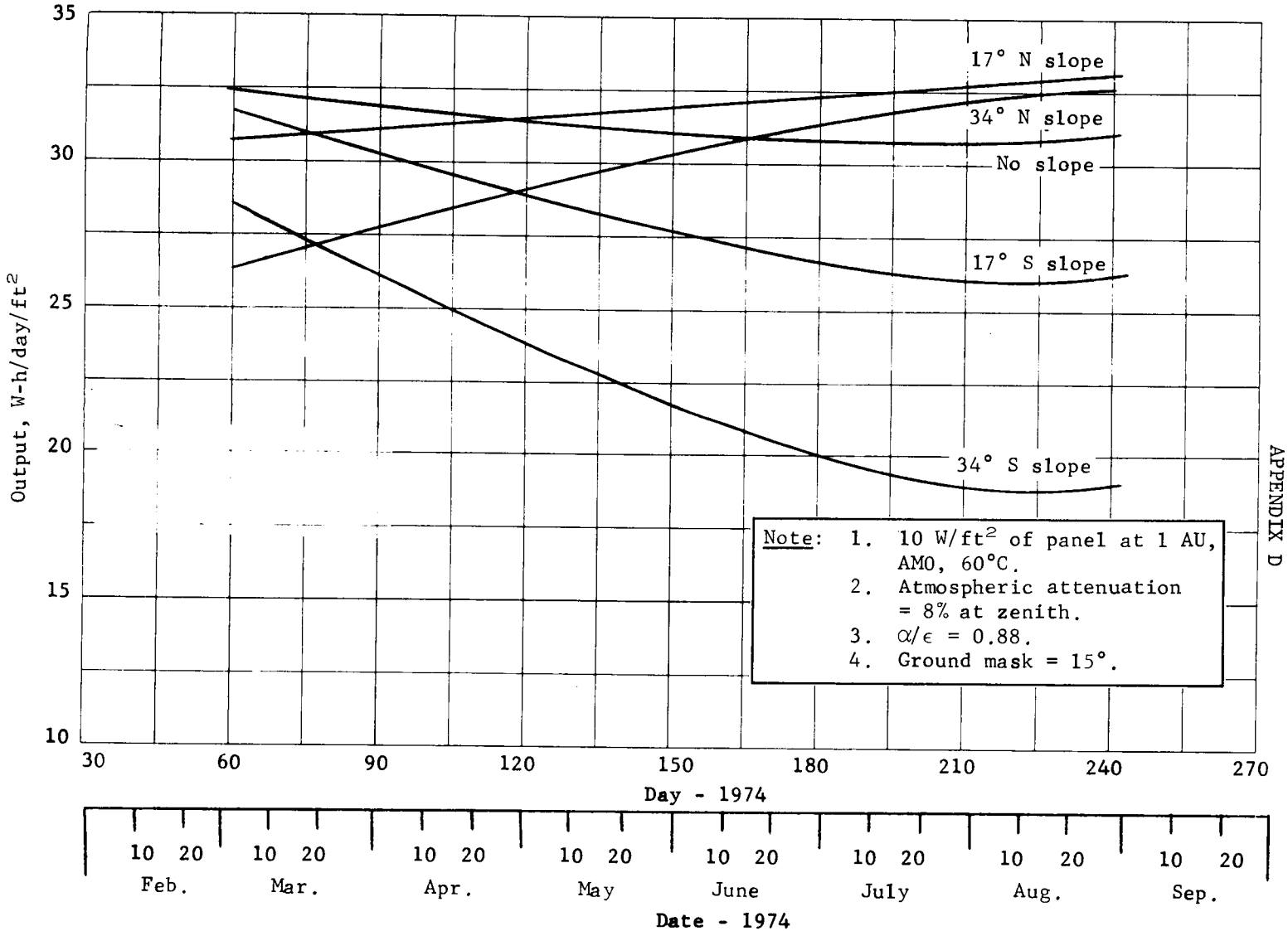

Figure D122.- Mars Lander Solar Array Output, Nonoriented Flat Panel, 10° N Latitude

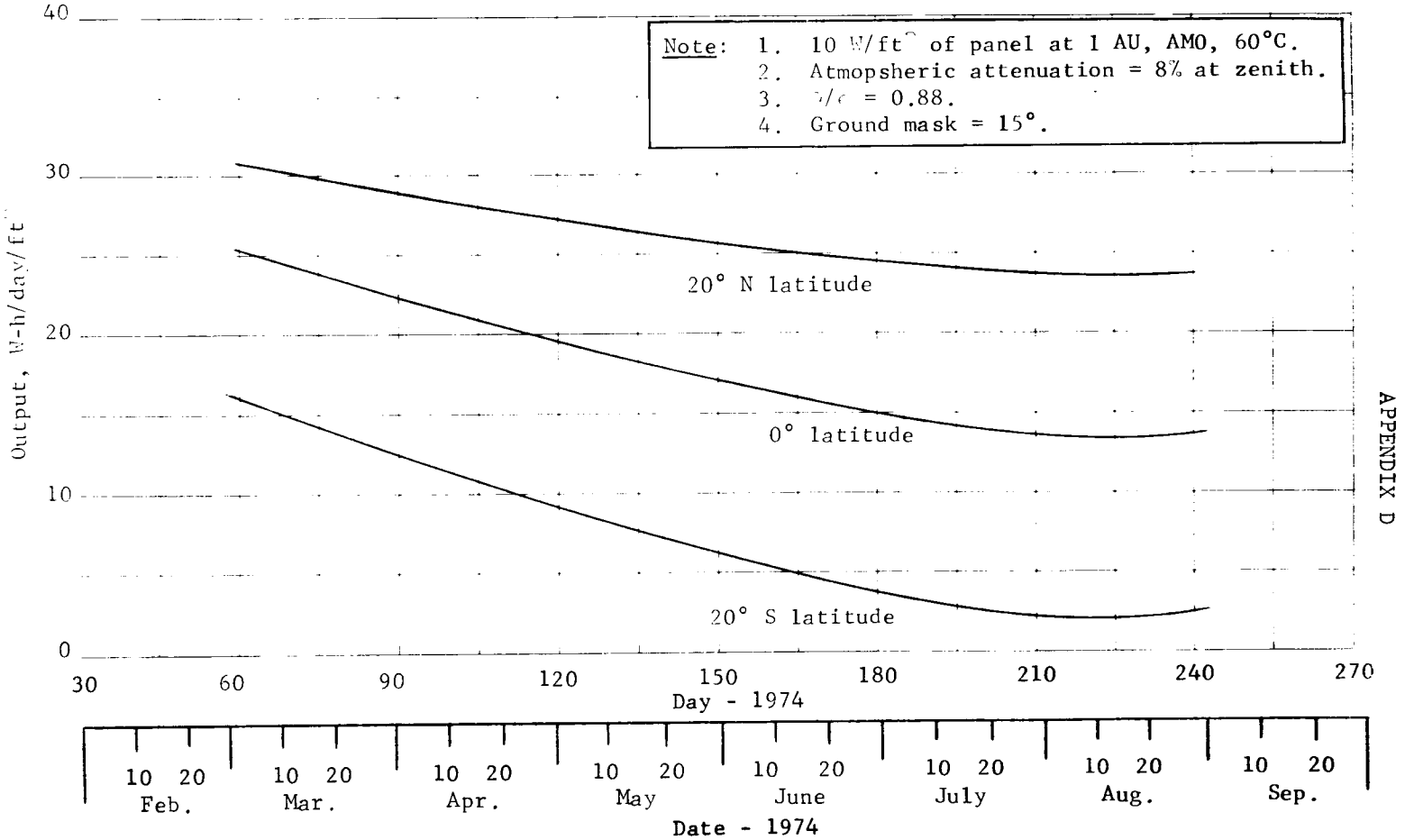

Figure D123.- Mars Lander Solar Array Output, Nonoriented Flat Panel, 34° S Slope

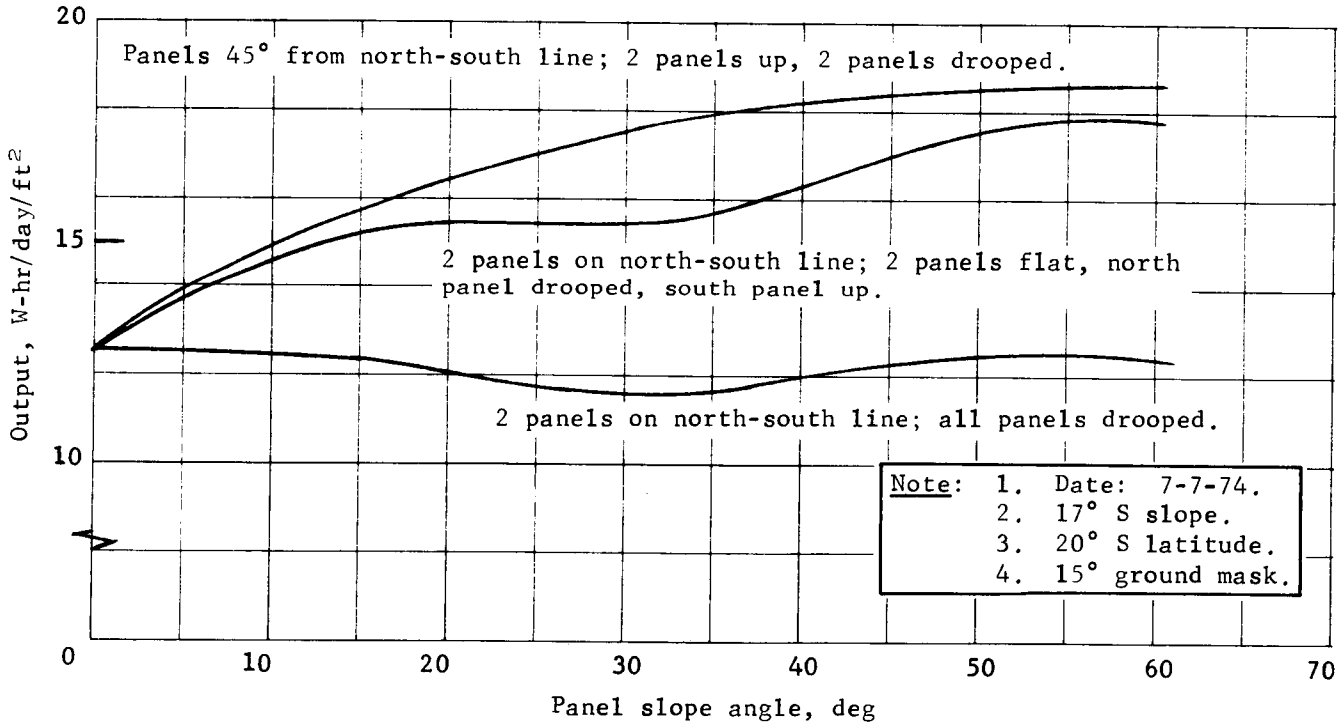

Figure D124.- Effect of Side Solar Panel Orientation on Total Array Output/ft²

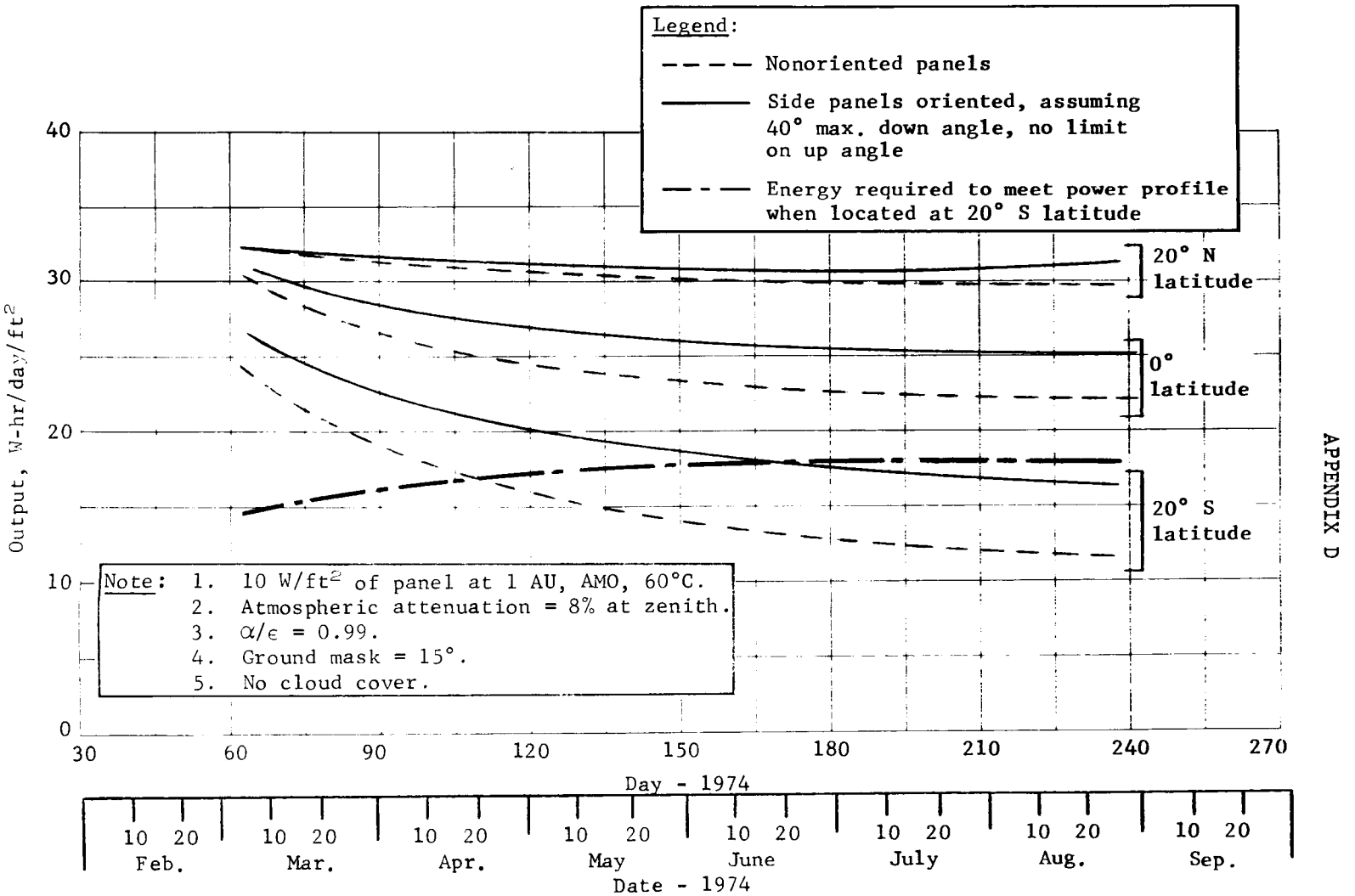

Figure D125.- Mars Lander Solar Array Output, 17° S Slope

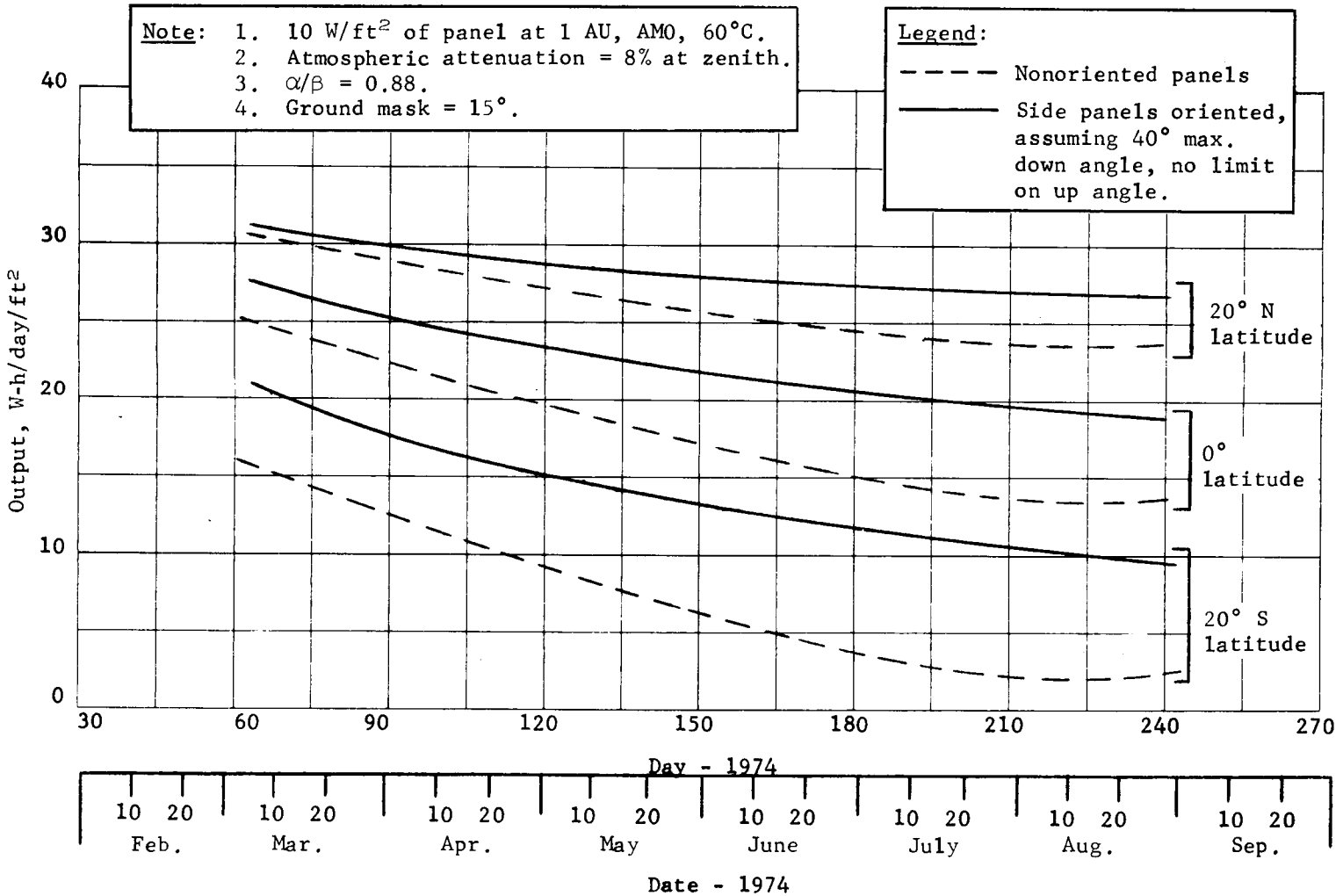

Figure D126.- Mars Lander Solar Array Output, 34° S Slope

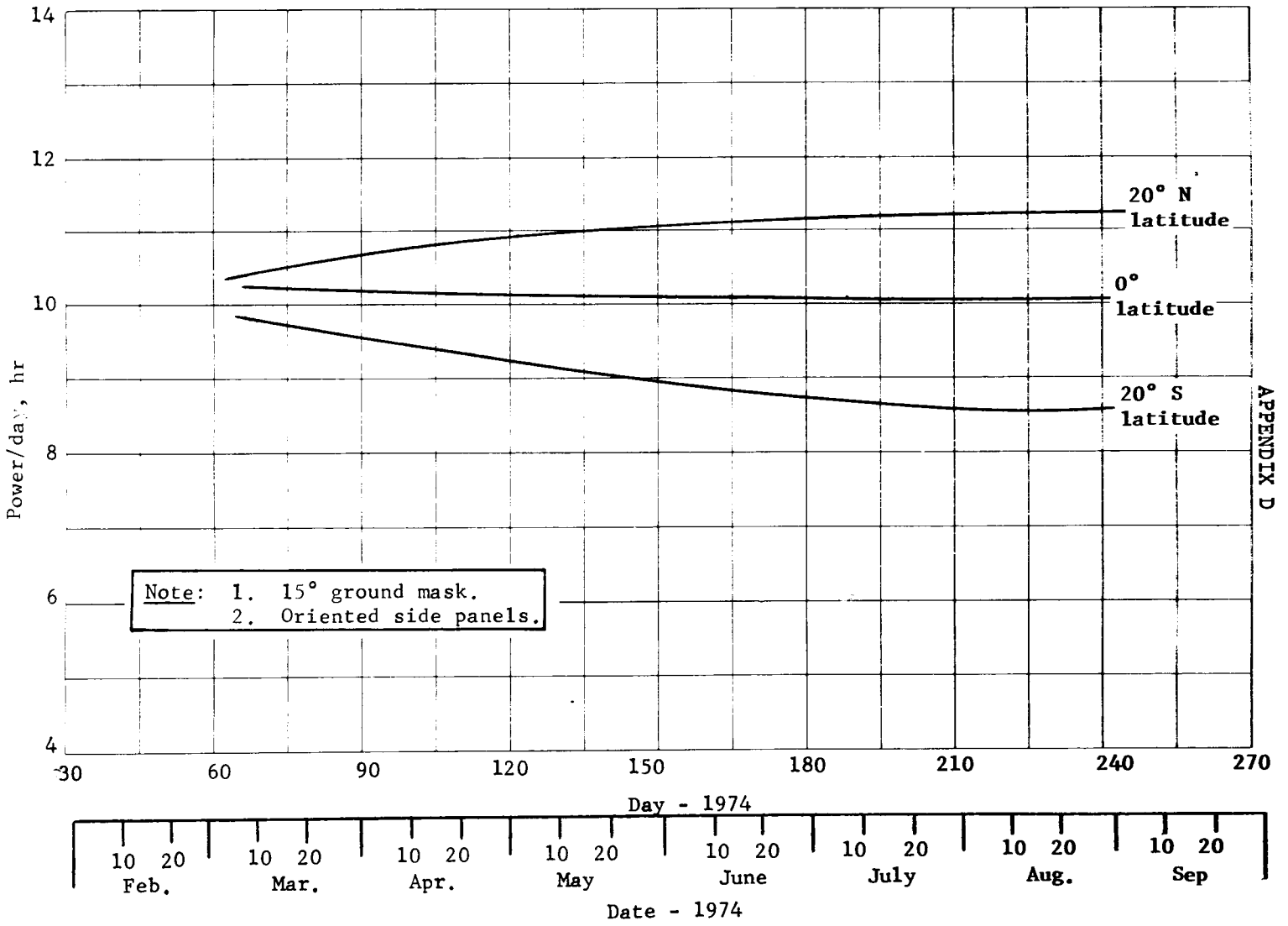

Figure D127.- Mars Lander Solar Array Hours of Usable Power

APPENDIX D

Solar cell equations: It is desirable, for computer programing purposes, to express the power output of solar panels for use in planetary missions in an analytical form as a function of solar distance, atmospheric properties, solar angle of incidence, and temperature. The simplified equations used in the calculations performed for the Mars lander solar array study are described in the following paragraphs.

The power equation is normalized to solar panel output characteristics, P_0, in W/ft^2, measured at AMO, 1 AU, at a temperature of 25°C. A value of 11.5 W/ft^2 is used for P_0 for 18 mil solar cells, based on usable total panel area. The power output at the surface of the planet may then be expressed as:

$$P = P_0 R^{-2} \left|1 + (T - 25)D\right| k_c K(\theta) \cos \theta \, e^{-\sigma m}$$

where

T = panel temperature, °C

θ = angle between panel and sun

R = solar distance, AU

k_c = factor to account for cloud cover

$K(\theta)$ = cell transmittance correction factor for oblique solar incidence

σ = atmospheric optical attenuation coefficient, cm^2/g

m = mass integral of atmosphere along the line from panel to sun, g/cm^2

D = slope of maximum power versus temperature curve of cell type of interest, divided by P_0, $°C^{-1}$.

The factor $K(\theta)$ accounts for departure of the cell power versus solar angle of incidence curve from a simple cos θ law. Typical values are:

θ(deg)	0	50	60	70	80
$K(\theta)$	1.0	0.95	0.90	0.80	0.55

APPENDIX D

The temperature parameter, D, is typically 0.0043 $°C^{-1}$ for 18 mil n-on-p silicon solar cells. If convective effects and heat transfer from the ground are neglected, the panel temperature, T may be expressed in terms of the absorptance (α) and emittance (ϵ) of the panel surface as:

$$T = 0.555 \left| 1.99 \times 10^{9} (\alpha/\epsilon) k_c S_0 R^{-2} K(\theta) \cos\theta \, e^{-\sigma m} \right|^{\frac{1}{4}} - 273$$

where

S_0 is the solar constant at 1.0 AU (130 W/ft^2).

Assuming that an exponential atmospheric density model is valid at altitudes less than a few density scale heights of the planet's atmosphere, the mass integral, m, is given by:

$$m = \frac{\rho_o}{\alpha \cos\psi}, \quad 0 \leqq \psi \leqq 75°$$

$$m = \rho_o \sqrt{\frac{r\pi}{2\alpha}} \exp\left(\tfrac{1}{2}\alpha r \cos^2\psi\right) \left| 1 - \operatorname{erf}\left(\cos\psi \sqrt{\tfrac{1}{2}\alpha r}\right) \right|, \quad 75° \leqq \psi \leqq 90°$$

where

ρ_o = surface atmospheric density, g/cm^3

$1/\alpha$ = atmospheric density scale height, cm

r = radius of planet, cm

ψ = angle between zenith and sun

erf(X) = error function.

The angular parameters θ and ψ shown throughout the preceding expression are related by the computer program to landing latitude, surface slope, panel orientation, date, and time.

APPENDIX D

Pyrotechnic Subsystem

Parametric weight data and definition of the subsystem design consistent with the data are presented in this subsection.

Weight data. - The weight of the pyrotechnic subsystem was determined as a function of the total number of bridgewires and the maximum number of bridgewires to be fired in a 20-sec period by a system using capacitors for energy storage and solid-state switches for safe/arm and firing functions. To meet the requirements of small to large landers the curves were developed for systems with 8 to 100 bridgewires that are fired in groups of 8 to 40 within a 20-sec period. For systems requiring more than about 150 bridgewires, the use of a separate battery for energy storage becomes more weight effective.

The design uses one capacitor assembly for each bridgewire fired in a 20-sec period, but reuses the capacitors for subsequent functions. One safe/arm switch and squib firing circuit (SFC) are required for each bridgewire to permit separate arming and firing of each function while retaining the capacitor isolation.

Figure D128 shows the weight of the pyrotechnic subsystem versus the number of bridgewires to be fired. The curves include allowance for an enclosing case for the electronics and the cabling internal to the case.

Subsystem design. - The pyrotechnic subsystem used in this study consists of the equipment shown in figure D129. Power to the pyrotechnic subsystem is provided from the power subsystem and control signals are received from the guidance and control subsystem.

Capacitor assemblies provide the energy storage for firing each bridgewire at its prescribed time. Capacitor assembly charging is initiated at power transfer and within about 12 sec the capacitors are ready for use. A minimum of 20 sec between subsequent events allows the squib load to be removed by safing of the safe/arm circuit and the capacitor assemblies to be recharged and used again. Each capacitor assembly provides the required energy to fire one bridgewire in a given event. The number of capacitor assemblies required is established by the maximum number of bridgewires required in any 20-sec period.

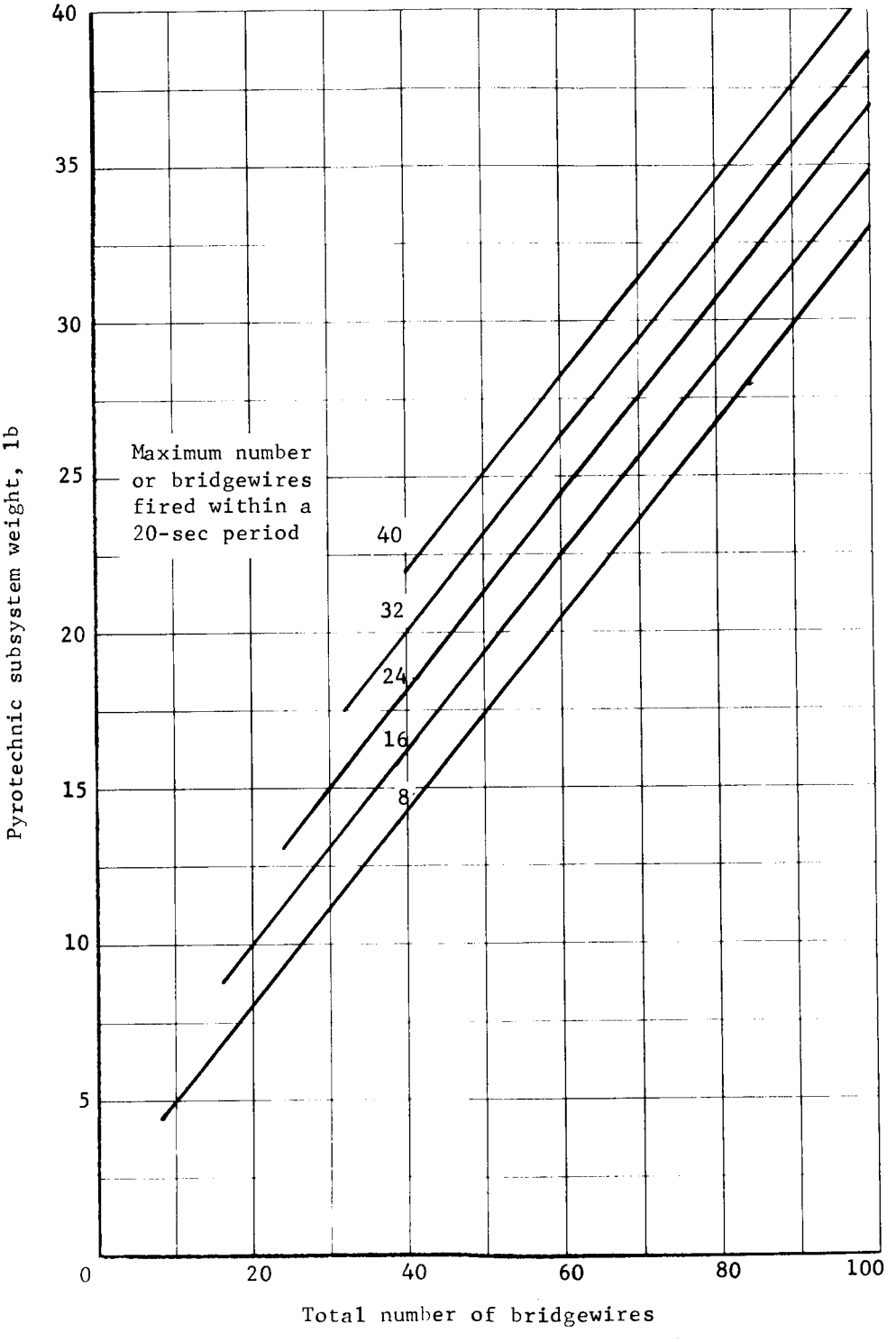

Figure D128.- Weight of the Pyrotechnic Subsystem Using Capacitor Energy Storage

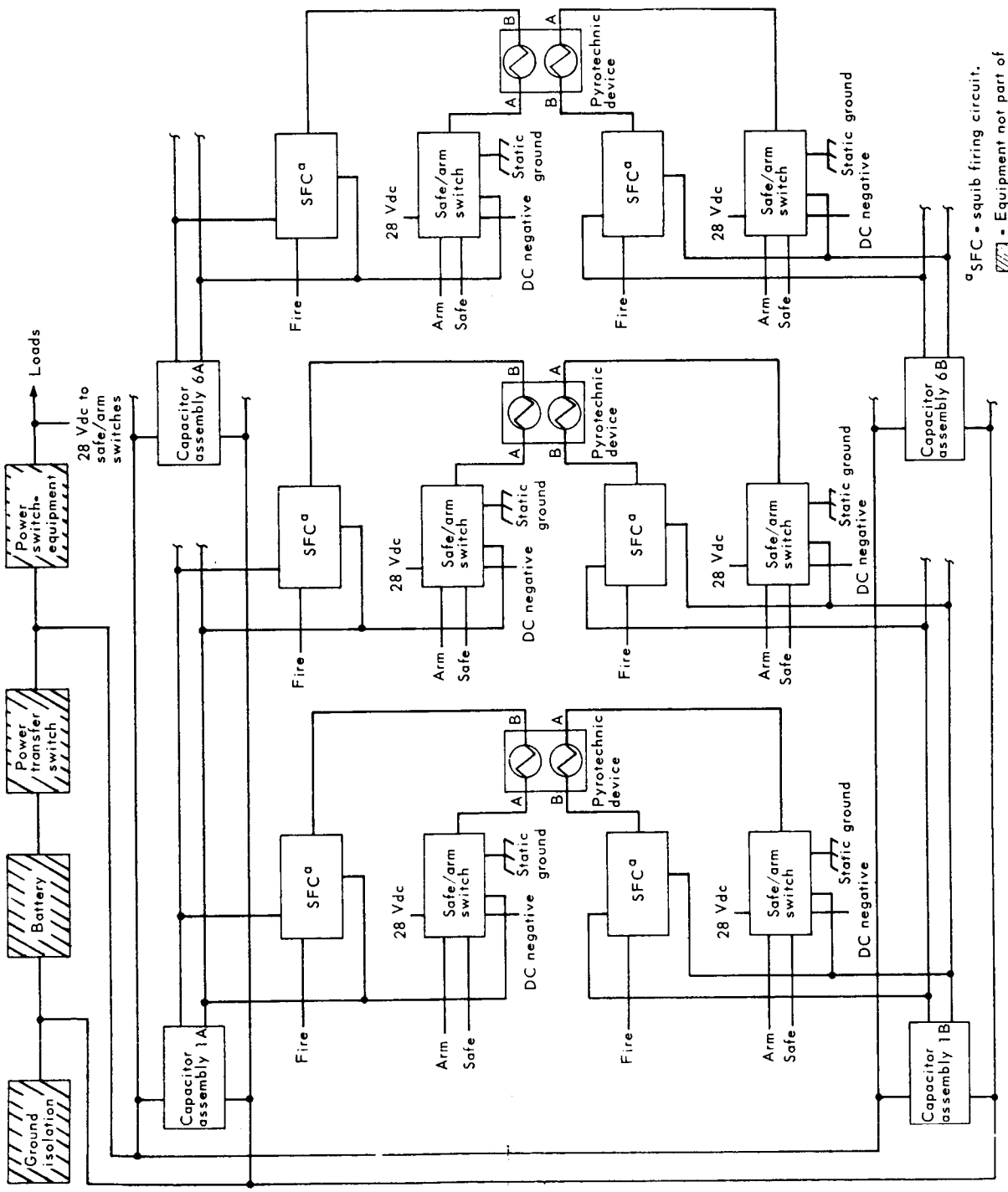

Figure D129.- Simplified Block Diagram, Lander Pyrotechnic Subsystem

APPENDIX D

The use of a small capacitor assembly to fire each bridgewire instead of a larger capacitor bank to fire all bridgewires in a given event eliminates the need for current-limiting resistors in each bridgewire circuit, and consequently a larger capacitor bank to provide for resistor losses. A minimum firing energy of approximately 0.150 J per bridgewire is provided to ensure firing within an allowable time period.

A safe/arm switch provides arming and safing of each pyrotechnic circuit. The events may be arranged so that no function need be armed more than one minute before firing. After all pyrotechnic functions in an event are fired, the switches are reset to the safe position, thus opening the power circuit and removing any load caused by a bridgewire short.

The safe/arm switch contains a 100 000 ohm resistor connected from the negative bridgewire lead to structure. This provides a ground reference for the bridgewires to prevent a static charge buildup before the bridgewire is fired.

The final switch between the energy source and the squib is the solid-state squib firing circuit, which receives its fire control signal from the sequencing subsystem.

The squibs provide gas pressure to operate valves, cable cutter, and separation nuts, or initiate linear-shaped charges for canister separation.

The block diagram (fig. D129) shows the typical redundancy provided for each function. Parallel circuits are provided from the power subsystem through redundant capacitor assemblies, safe/arm switches, squib firing circuits, and to one of two squibs in each pyrotechnic device. Two squibs with one bridgewire each are used for each function. With this arrangement, the proper functioning of either circuit branch will fire all associated pyrotechnic devices.

APPENDIX D

Safe/arm switch: A schematic of the safe/arm switch is shown in figure D130. This switch is turned on by applying a 28 V, 150 mA pulse for 100 msec to the ARM input. The switch then latches up and keeps the SCR (Q5) turned on until a similar input signal is applied to the SAFE input. The SAFE signal saturates Q1, causing the switch to unlatch. It also saturates Q3, thereby putting a negative voltage from C4 on the gate of Q5 and turning off Q5. Resistor R13 is used to provide a ground reference for the bridgewires before firing. A 100 000-ohm resistor will be used for this purpose, which will present negligible load on the capacitor assembly during bridgewire firing. This switch will safely handle current pulses with peaks of 20 A. It will operate over a temperature range from -15°F to +145°F. The leakage current is less than 1 mA at 145°F and the estimated weight is 0.19 lb.

Squib firing circuit (SFC): A schematic of the squib firing circuit is shown in figure D131. A silicon controlled rectifier (SCR) is used as the switching element. The circuit is turned on by applying a 28 V, 150 mA pulse to the input for 100 msec. Since the circuit is used in series with the safe/arm circuit, it will turn off when the current is interrupted by the safe/arm circuit turning off. Resistor R3 is provided to limit dv/dt across Q1 when the safe/arm switch is armed. The estimated weight is 0.06 lb.

This circuit will also handle current pulses with peaks of 20 A over a temperature range from -15°F to +145°F.

Capacitor assembly: Figure D132 shows a schematic of the capacitor assembly.

The capacitor assembly consists of three GE 16 K series capacitors, and current-limiting resistors in the positive and negative leads to restrict the instantaneous load on the power bus. Allowing for low temperature, minimum bus voltage, losses through the solid-state switches, and providing a minimum of 0.150 J of energy to the bridgewires, three 225 μf capacitors are connected in parallel to provide the total required energy.

The GE 16 K series capacitors are hermetically sealed, have been extensively tested and proven, and are on the JPL sterilizable approved parts list. The estimated weight is 0.16 lb.

Squibs: The weight of the squib is included in the incorporating device and is not included in the pyrotechnic subsystem weight.

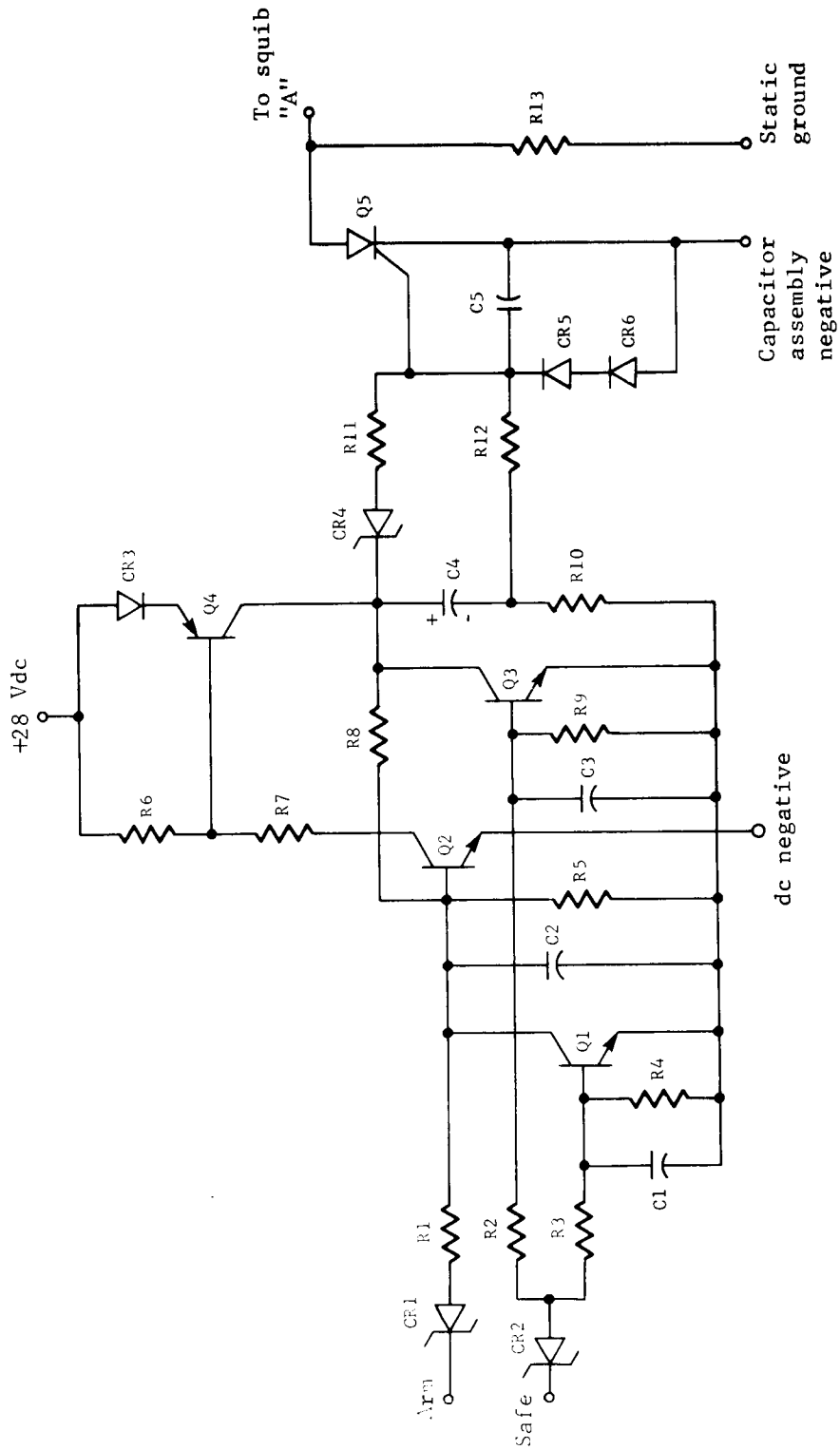

Figure D130.- Safe/Arm Circuit

APPENDIX D

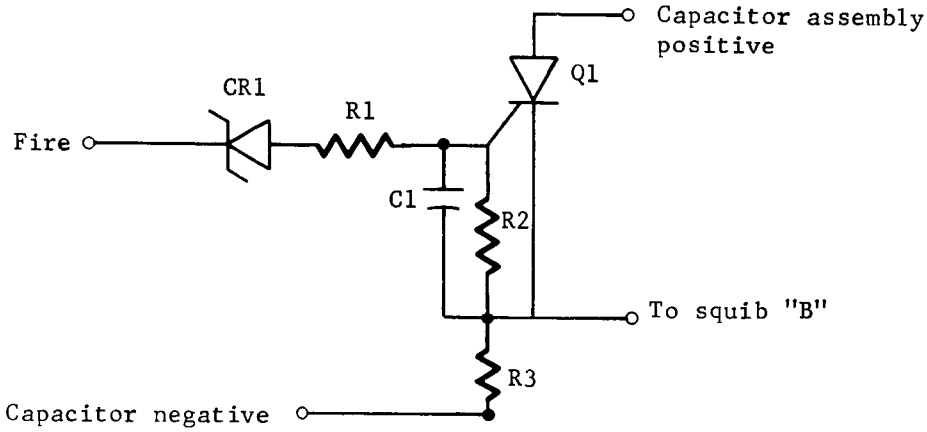

Figure D131.- Squib Fire Circuit

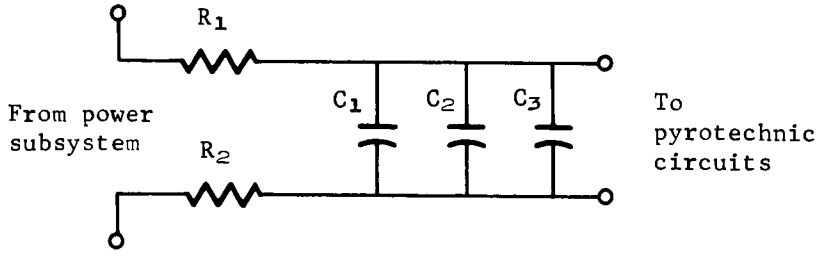

Figure D132.- Capacitor Assembly

APPENDIX D

9. SELECTION OF HUMIDITY AND WIND INSTRUMENTS

References D19 and D20 contain the information on which the selection of instruments for the meteorology package was based. These are the trade studies conducted for the Voyager Phase B preliminary design to define atmospheric instruments for the science payload. The information the references present is based on an extensive survey of the state of the art in instrumentation for measuring atmospheric pressure, temperature, humidity, and wind. A review of these documents for use in the present study showed that the information they contain is still valid and complete and is a reliable basis for payload definition.

It is the conclusion of Martin Marietta Corporation that pressure and temperature instruments can be obtained by modifying existing designs, and that the pacing items in development of a meteorology package are the instruments for the humidity and wind measurements. As stated in Part I of this report, an aluminum oxide hygrometer and a sonic anemometer, respectively, have been chosen for these measurements. Because of the significant influence of these choices on the course of a program for development of a meteorology package, the preference for these instruments is explained in detail in this section of Appendix D.

Surface Atmosphere Hygrometer

The selection of an instrument for measuring surface humidity was preceeded by a review of present knowledge regarding moisture content in the Martian atmosphere. This was necessary to determine an expected operating range and to develop a basis for setting the limits for instrument accuracy. The information required for this purpose is contained in references D21 and D22.

The range of present estimates for water vapor on Mars is given in table 21-1 of reference D21. Although the results given in reference D22 are more recent, the amount of water estimated is within the extremes of the ranges given in the table. In Part I of this report, extremes of specific humidity versus frost point are presented graphically. The range is from 1 to 60 mg/cm^2 of precipitable water, a spread of more than one and one-half orders of magnitude.

APPENDIX D

As shown in Part I of this report, the expected operating range of specific humidities for a hygrometer will start at about 20 ppm and extend past 5000 ppm. In terms of frost points, this corresponds to a minimum of -80°C, which appears to be a reasonable lower limit for calibrated performance.

The specified error band of 4°C is also shown in Part I. Typically, this will result in determination of specific humidity within a factor of 2 over the expected range of values. This error band is more than adequate for comparing accuracies of the predictions tabulated in reference D21. On the basis of resolving differences between these observations and estimates, an error band of 8°C would appear adequate and would still permit specific humidity determinations within a factor of 4.

In view of the results reported in reference D22, accuracies in this range will be satisfactory for a first landing mission and at a single site. In reporting the results of their extensive observing program over a nine-month period in 1964 and 1965, these authors make the following statement:

> "The present work indicates that H_2O does exist in the atmosphere of Mars and that the amount present varies significantly with time and place on the planet. Furthermore, the mass motion of H_2O in the atmosphere of Mars appears to be correlated with polar cap recession and growth, and possibly with the frequency of appearance of white clouds and intensification of dark features on the surface."

Instrument selection.- There are three main considerations that form the basis for selecting a surface atmosphere hygrometer.

First, the instrument should not require a flowing sample into an internal measuring system. This usually implies a fan and drive motor, and such mechanization is not easily made compatible with the dry heat and the 90-day surface life requirements. Also, when detecting part per million moisture in the dry Martian air, the problem is complicated by the fact that everything that contacts the gaseous sample tends to change it. Thus, maximum instrument accuracy demands that the sensor be exposed directly to the free atmospheric environment to minimize adsorption and desorption effects from surrounding surfaces.

Second, as shown in Part I of this report, the instrument must be sensitive to specific humidities on the order of 20 to 30 ppm. Accuracies within 10°C at frost points near -80°C are essential.

Third, consider the universal requirements for Mars lander instruments: that they be compatible with dry heat sterilization (six cycles to 275°C at 76 hr/cycle); that they perform their function for a minimum of weight, volume, and power; and that their selection be preceeded by proof of principle in similar application on Earth or in other space programs.

Based on these factors, and in light of the information given in the trade studies discussed above, the preferred instrument for the Mars 1973 lander is the aluminum oxide hygrometer. In addition to the information presented in references D19 and D20, the aluminum oxide device is described in detail in the very excellent review of the state of the art in humidity measurement given in reference D23.

The aluminum oxide element is the only type of high-sensitivity water vapor sensor that does not require sample flow into an internal measuring system. Its great advantage is that it can be exposed to the free atmospheric environment. Performance of the sensor in detecting humidity on the order of 10 to 20 ppm has been demonstrated in laboratory tests and in numerous balloon soundings in the Earth's atmosphere (ref. D24). The instrument weighs about 1½ lb and draws less than 1 w of power. Although no sterilization work is known to have been performed, the sensor materials are inherently stable at dry heat sterilization temperature, and no problems are expected.

Effort for the direct versus orbital entry study has been to reassess the conclusion of the Voyager work. In doing this, a number of organizations making basic contributions in atmospheric humidity instrumentation were visited for discussions of the Mars surface problem. These organizations included the National Bureau of Standards, the Naval Research Laboratory, the Air Force Cambridge Research Laboratories, NASA-Goddard Space Flight Center, and JPL. Commercial establishments visited included Panametrics, Inc., and Cambridge Systems, Inc.

Results of these contacts show no appreciable change in the technology base for humidity instrumentation since the trade studies reported in references D19 and D20 were completed or since the survey document (ref. D23) was published. There was general consensus among the instrument engineers contacted that the aluminum oxide sensor is the proper choice provided that accuracies of ±5°C and response times of 20 to 30 sec can be tolerated at the very low frost points. Basic work in developing a controlled process for producing the sensor has been started by ARCRL (ref. D25). Also, work on the electronics package for the aluminum oxide sensor has been conducted at JPL (ref. D26).

Surface Anemometer

Four basic types of wind velocity sensors were considered for the meteorology package. These were the sonic, hot wire, drag body, and rotating cup anemometers. Following are brief discussions of the main features of each type considered in evaluating suitability for the Mars lander application.

Sonic anemometer.- The sonic anemometer uses acoustic transducers to measure the wind velocity in each of three mutually orthogonal directions. A single component of this anemometer consists of two acoustic transducers separated by a small distance, approximately 6 in. First, one of the transducers is used as a source and the other as a detector of acoustic waves, and the travel time of acoustic waves between the transducers is measured. Then the procedure is reversed, and the travel time in the opposite direction is measured. The wind velocity in that direction can then be computed from the travel time in each direction and the distance between the transducers. This technique has not been widely used in wind velocity measurements on Earth. However, recent work by the Air Force Cambridge Research Laboratory has shown that this technique can be used to make very accurate measurements of wind velocity (refs. D27 thru D29).

The sensor for the acoustic transducer could probably be developed within a weight of about 1 lb. The reliability of the device should be good, although it may be sensitive to dust in the Martian atmosphere. The main problem is adapting the present design for use on Mars is modifying the transducers to improve energy coupling with a low pressure atmosphere.

APPENDIX D

One of the advantages of this technique is that it measures wind velocity directly, not some other wind property such as force or mass flow. Also, the resulting data will provide information on the velocity of sound in the Martian atmosphere. This, when combined with atmospheric temperature data, will enable estimates of $\overline{\gamma}/\overline{M}$, where $\overline{\gamma}$ is the specific heat ratio and $\overline{M}$ is the mean molecular weight. Another advantage is that the device inherently measures the total wind velocity vector -- both speed and direction -- when three sets of transducers are used in orthogonal planes.

Hot wire anemometer.- A hot wire anemometer uses the cooling effect of the wind flowing over a wire to measure the velocity of the wind. The results are dependent on the value of atmospheric density (ref. D30). Thus, the density must be known to derive wind velocity from the measurement result. This device can be operated in either a constant current mode or a constant temperature mode. In the constant current mode, a fixed current is passed through the wire, and the change in wire resistance (or wire temperature) gives a measure of the cooling effect of the wind. In the constant temperature mode, the temperature and resistance of the wire are maintained constant by varying the amount of current through the wire. The amount of current required is then a measure of the wind velocity.

The use of this device would require three wires oriented in mutually orthogonal directions because the wire is mainly sensitive to the wind component normal to the length of the wire. Also, one of the drawbacks of this technique is that the wires are insensitive to the direction of the wind by a factor of π (e.g., a hot wire anemometer could not uniquely distinguish between an easterly wind and a westerly wind).

Hot wire anemometers have been used extensively for wind and gas velocity measurements on Earth. Reference D31 cites a number of sources on the subject. The wires are usually made from either tungsten or platinum-iridium. The tungsten wires are more rugged and less susceptible to physical damage; however, they can be affected by atmospheric contaminants and tend to require frequent recalibration. The platinum-iridium wires are more fragile but retain their calibration better. The wires themselves are very small, typically less than an inch long by a mil or less in diameter. Much of the sensor weight would be in the probes required as mounts for the wires.

One of the severe problems associated with this technique would be the effects of wind-blown dust. Dust accretion on the wires will change the cooling effect, and thus after the calibration. There is no easy way to shield the wires from dust because they must be exposed to the atmosphere to measure wind velocity.

This anemometer technique would be compatible with the Mars lander weight constraints. It appears also to be compatible with the sterilization requirements, although the effects of the sterilization process on the calibration of the wires would have to be carefully evaluated. However, the ability of the wires to operate reliably in a dust-laden atmosphere is very questionable.

Drag body anemometer.- The drag body anemometer uses the force exerted by the wind on a body of known geometry as a measure of wind velocity. The force is measured by strain gages at the mounting of the drag body. The drag force depends on the air density times the velocity squared. Thus (like the hot wire anemometer), the effective use of a drag body to measure wind velocity requires that the atmospheric density be known.

The drag body is primarily sensitive to wind in a horizontal plane, assuming the drag body is mounted vertically. A vertical wind component may alter the response, but is difficult to separate from changes in horizontal winds. Semiconductor strain gages can be used to measure the forces, and provide a large enough signal output that amplification may not be necessary (ref. D32). However, extreme temperature sensitivity of semiconductor strain gages will create a major problem in controlling the accuracy of the instrument.

The weight of the drag body anemometer would probably be comparable to the sonic anemometer. It should be capable of being sterilized and should have good reliability, although its mounting and deployment might cause problems. It may also be sensitive to the Martian environment, particularly to dust storms that might exert a significant perturbation in the force on the body. This device can operate with adequate accuracy over a very wide range of wind speeds.

APPENDIX D

Rotating cup anemometer.- This familiar type of device is not considered a serious contender for the Mars lander application for two reasons. First, to have the response rate necessary for desired accuracies (10% accuracy specified for the Mars Mission Mode Study), the rotating portion must be lightweight. Second, the mechanization of moving components involving shafts, bearings, lubricants, and seals is not easily made compatible with the constraints of dry heat sterilization and 90-day surface lifetimes.

Instrument selection.- The sonic anemometer is the preferred instrument for three reasons. First, it requires no moving parts and is, therefore, well-suited for long-life application and for compatibility with dry heat sterilization and an uncertain operating environment. Second, a rugged sensor can be built because there is no effect of mass on speed of response to wind variations. Third, the instrument yields complete information on the wind vector.

This instrument is a recent development by Cambridge Systems, Inc., for the AFCRL and is described in detail in references D33 and D34. Martin Marietta Corporation personnel have visited both AFCRL and Cambridge Systems to discuss the application of this instrument in the Mars 1973 mission. Actual hardware was witnessed in operation, and possible modifications were discussed. The main question at the time of the visits was whether the low surface pressures expected on Mars would make it impractical to use the sonic detector principle of operation.

Cambridge Systems has since operated a sensor in a 5-mb chamber. Although this instrument was designed for Earth surface conditions, its performance in the range of Mars surface pressure demonstrated the feasibility of developing a sonic anemometer for the meteorology package.

APPENDIX D

10. MARS SURFACE SAMPLE ACQUISITION

This section of Appendix D is a report of work conducted for Martin Marietta by Dr. Ronald F. Scott on a consulting basis. Dr. Scott is a member of the faculty at the California Institute of Technology and was Principal Investigator on the Surveyor Lunar Soil Mechanics experiment. The objectives of this study were to develop the reasoning on which to base the design of a Mars soil sampler and to propose a tentative concept for such a device.

Nature of Martian Surface

The report on the Mariner Mars 1964 Project by Leighton et al. (ref. D35) discussed the possible nature of the Martian surface on the basis of previous Earth-based observations and the photographic results of the Mariner flyby. The photographs taken by the Mariner IV spacecraft showed a cratered Martian surface in which the crater density per unit area was only slightly less than that observed in lunar highland areas. However, the craters on Mars appeared more subdued than on the moon and relatively few sharply outlined (which is usually interpreted as fresh-appearing) craters were observed. This was taken by the authors to indicate that surface-modifying processes are at work on Mars, which are relatively more effective than modifying processes on the moon but less effective than on the earth.

Although direct evidence is lacking, it is assumed that the craters on Mars, as on the moon, are formed by meteorite impacts. Because it is estimated that the meteoroidal flux at Mars is from 4 to 25 times that at the moon, the lower incidence of craters observed on Mars reinforces the inference that crater modification and subsequent elimination have occurred at a faster rate on Mars than on the moon.

With meteorite impacts being the crater-forming agent, a Mars surface model is suggested analogous to that observed by the Surveyor spacecraft (ref. D36) on the moon. The surface material to a depth of at least 10 m, but varying from place to place, consists of a granular material with a wide range of sizes but possessing a substantial proportion (possibly greater than 50%) of fine material in the tens of microns size range. On the moon (ref. D36) the surface soil possesses a small but effective amount of cohesion between the particles, and the writer has interpreted this as being possibly due to the presence of Van Der Waals forces between the relatively clean grains.

APPENDIX D

The existence of a significant atmosphere on Mars, compared to the moon, would imply that the surfaces of mineral grains would become contaminated on breaking up of the parent rocks, and it might, therefore, be expected that cohesion between grains of Martian soil would be lacking, unless other forms of cementation are present.

Yellow clouds have frequently been observed on Mars both visually and photographically. Observation of the properties of these clouds suggest that they may be composed of windborne fine mineral particles (ref. D35). Thus, Leighton et al. (ref. D35) conclude that deposition of these clouds of particles would mantle and soften the outlines of craters. They also consider that the craters might be modified by thermal and vibrational creep of the granular material on slopes.

Consequently, if this is correct, blankets of relatively uniformly fine-grained soil may cover areas of Mars. With the experience developed by lunar surface investigations, and considering the low probability that Martian soil is cohesive, there is little likelihood that these fine-grained deposits will be extremely loose or highly porous. As Leighton et al. pointed out, an exception to this model may occur in those areas, if such exist, where permafrost exists at the surface. Temperatures favorable for the production of permanently frozen water in the soil (permafrost) if the water supply is sufficient, only occur between latitudes of 40 to 50° N and S and the poles. The writer understands that only near-equatorial sites are presently being considered for spacecraft landings. In this region, temperatures exceed 0°C daily for 10 Martian months. It is therefore considered that there is essentially no possibility of encountering permafrost at the spacecraft's landing site.

In summary, the surface existing at a Martian equatorial landing site has a high probability of consisting of fine-grained cohesionless mineral particles, with a density of around 1.5 g/cc (terrestrial basis) and a porosity in the neighborhood of 50%. Larger particles in the millimeter to centimeter or larger range may be encountered, although it is considered that there is a high probability that some fine-grained soil can be reached.

APPENDIX D

Sample Acquisition

With a Martian soil model as outlined above, a sampling device does not need to have a rock-coring, sampling, or grinding capability. Considering the soil analysis requirement, there are two possible approaches to the experiment: (1) deploying the soil analysis equipment from the spacecraft to the Martian surface; and (2) bringing a soil sample to an analytical device mounted on the spacecraft. These will be discussed in turn. Certain problems, such as sterilization, launch, flight, and landing survival arise with both approaches.

Analysis at surface.- It is visualized in this case, that an experiment similar in nature to the alpha-scattering experiment of Surveyor spacecraft will be employed to carry out the required analysis of the Martian soil composition. An attachment will be necessary to determine the water content of the soil. It is not the purpose of this appendix section to determine the means by which these experiments will be performed. With this technique, a sensor head will be lowered or extended to the surface for the purpose of obtaining the appropriate measurements. The soil's mechanical properties do not enter into such a deployment technique, whose advantages and disadvantages only will be listed here (this approach has essentially one degree of freedom in sampling):

1) Advantages,
   a) Requires no imagery of test area (although such imagery might be useful for interpreting the results of the experiment),
   b) Deployment has minimal power requirements,
   c) Automatic on receipt of deployment signal,
   d) Operation and performance of test have minimum interaction with other devices,
   e) Type of surface (rock, soil) relatively unimportant for compositional analysis;
2) Disadvantages,
   a) One-shot test,
   b) Sample cannot be selected,
   c) Deployment failure cancels test,
   d) Shape of surface (large rock) may tip sensor or otherwise render test ineffective,
   e) Sensor head requires mounting bracket, interface harness, etc.

APPENDIX D

Soil sample retrieval.- This approach, in general, has the following advantages and disadvantages:

1) Advantages,
   a) Degree of flexibility in sample selection (if imaging capability present),
   b) Gain in other information, such as strength, physical composition of Martian soil, variability with depth, etc.,
   c) Chemical compositional experiment remains fixed to spacecraft,
   d) Analysis of more than one sample facilitated (depth variation);
2) Disadvantages,
   a) Power requirement,
   b) Weight may be somewhat greater than deployment mechanism for composition experiment alone,
   c) Failure leads to no compositional analysis,
   d) Imaging desired,
   e) Command complexity,
   f) Location on spacecraft restricted with respect to both the imaging system and the analysis experiment,
   g) Analysis experiment requires sample receiver.

In taking the sample retrieval approach, there are three classes of mechanism which may be employed to obtain a sample of Martian soil for delivery to an onboard sensing device.

Automatic: This class of device would be preprogramed to extend until an obstacle (presumably the surface) was encountered by a force or motor current sensor, which would activate a sample bucket or scoop to retrieve a sample. Next the sampler would be withdrawn from the surface and the program would initiate motions to cause the soil sample to be placed in the analysis apparatus. No Earth commands, except for initiation, are required in this operation.

The advantages and disadvantages of this approach are almost the same as those for deployment of the chemical compositional equipment itself, except that a sample may be retrieved further from the spacecraft and the sample site may be arranged to appear in the imaging system's field of view. This equipment would also have one degree of freedom in obtaining a sample.

Manual: In this category may be placed the type of surface sampler employed on Surveyor lunar spacecraft (ref. D36). The advantages in sample selection and manipulation are obvious, and additional information may be obtained by rock and soil manipulation. However, on Mars, there are considerable disadvantages in the use of such a device. Many pictures of the sampler and the area of operation are required so that, although power requirements for the device itself may be low, more work is required of the imaging system. The time delay for signals to and from Mars makes such an operation extremely time-consuming in view of the decisions required. A command system is required. An apparatus of this kind would possess at least three degrees of freedom in movement.

Semiautomatic: In this category is visualized a surface sampling device that would be preprogramed as with the entirely automatic system, to obtain a soil sample and deposit it in the analytical experiment, but whose operations could be interrupted on Earth command to permit certain simple decisions to be made. Two degrees of freedom would have to be incorporated in the apparatus to make the response to decisions meaningful. All the disadvantages associated with the sample retrieval function are inherent in this approach, but there are a number of advantages over the other techniques suggested. The probability of sample retrieval is good, almost regardless of the nature of the surface. Multiple samples might be possible with suitable design of the analytical sensor. Additional information on the physical nature of the surface would be obtained. Belowsurface samples might be possible. One, or at most two, pictures from the imaging system would be sufficient for the operation.

APPENDIX D

Tentative Conclusion

It is considered that a fully manually controlled sample-acquiring mechanism is not feasible for the proposed Mars landing spacecraft. The alternatives are deployment of the soil analysis sensor or sensors to the surface or some form of automatic sample retrieval. If the sample retrieval is to be fully automatic (i.e., no Earth command or decision-making involved except for initiating a sequence), there appear to be few advantages in providing a separate sample-retrieval device over simply deploying the compositional analyzer to the surface. A fully automatic sample retriever is, therefore, not recommended. There are distinct advantages in some form of sampling device, however, over the deployment of an analyzer to the surface, as indicated above. It is suggested, therefore, that consideration be given to a semiautomatic sampling device. One approach to the design of such a piece of equipment is given in the following subsection.

Tentative Design of Semiautomatic Soil Sample Retrival Apparatus

The design will consist of an extendible device, such as a furlable tube, possessing a sample retrieval container at its extremity. The entire sequence of desired operations will be performed by an onboard program. The sample container will be designed to be open when the apparatus is being extended, and closed when it is retracted. On receipt of an extension command, the retrieval container will extend an inch or two, during which it opens and extension continues. On receiving a retraction command, the container will first retract about ½ in. before it closes and retraction continues.

The apparatus will be mounted on the spacecraft and oriented so that the elevation of the extension device is fixed. Its elevation altitude will be established before flight so that intersection of the sampling device with the nominal Martian surface occurs when extension is approximately two-thirds of the maximum possible. At this distance, the contact with the Martian surface will be within the field of view of the imaging system of the spacecraft. The device will be rotated in azimuth by an electric motor or other means, and will so rotate automatically, except that it may be stopped at an azimuth position that is stored in the onboard program on Earth command. When this direction has been entered in the sampler command sequence, power-on and execute commands to the sampling device will cause it to rotate to

the selected azimuth position, extend to the surface until a force-limiting device stops its extension (in the Martian soil). It will then retract (closing the soil container) and rotate to the position required for the sample to be placed in the soil processing apparatus. At this time, it will be given an extend command so that the container will open and the soil sample be ejected in the processing apparatus. The device will return to its starting point and switch off. It is desirable that it be possible to reactivate the device, having stored a different azimuth angle to perform the whole sequence again.

A tentative design is shown in figure D133. Furlable tubes are described in references D37 and D38. The weight of the sampling device alone may be in the range of 3 to 4 lb. Electric motors working on 20 to 30 Vdc are used to move the device; it is expected that they will require ¼ to ½ A of current during the operating cycle. The entire sampling cycle should occupy a few minutes of time.

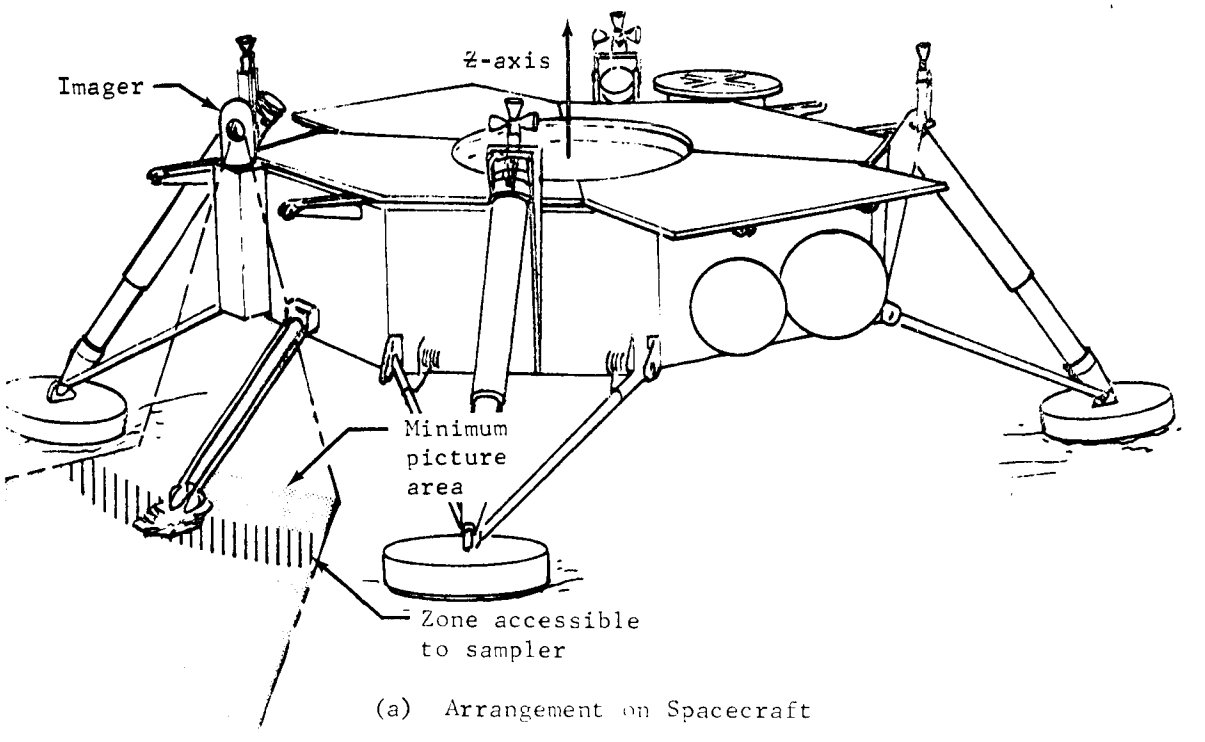

(a) Arrangement on Spacecraft

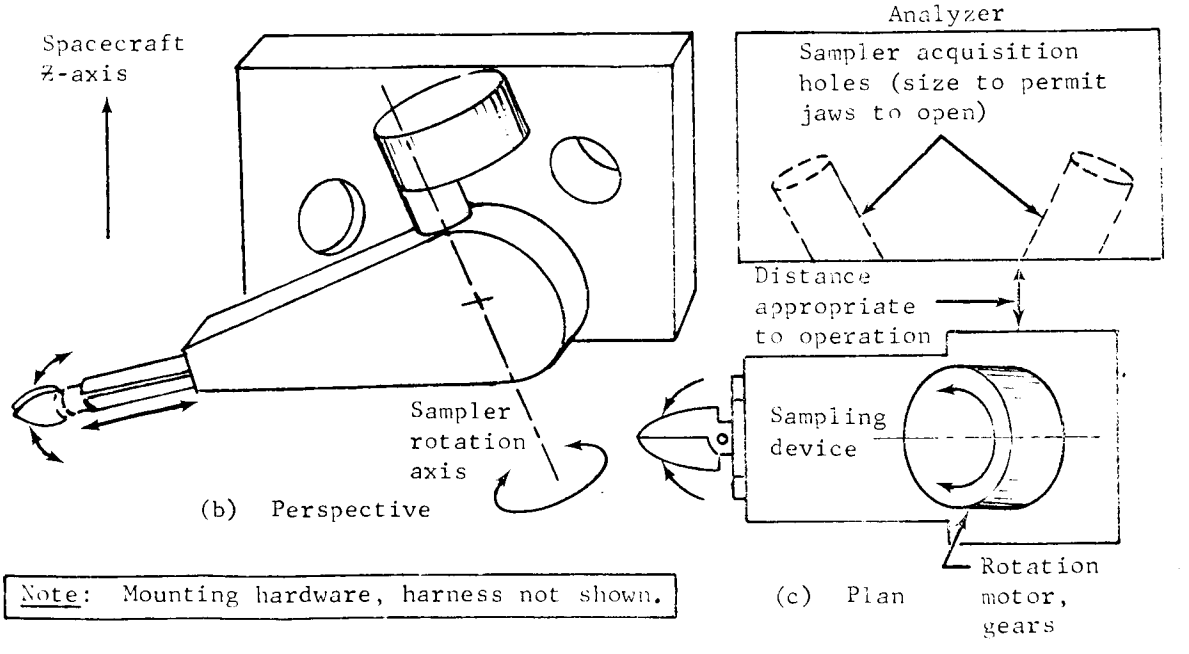

(b) Perspective

(c) Plan

Note: Mounting hardware, harness not shown.

Figure D133.- Sampler and Analyzer Arrangement

APPENDIX D

11. REFERENCES

D1. Christiansen, R. M.; and Hollingsworth, M., Jr.: The Performance of Glass Fiber Insulation under High Vacuum. Advances in Cryogenic Engineering, vol. 4, 1958, pp. 141-153.

D2. Bentilla, E. W.; Sterrett, K. F.; and Karre, L. E.: Research and Development Study on Thermal Control by Use of Fusible Materials, Final Report. (NAS8-11163), Northrup Space Laboratories, Apr. 1966.

D3. Stenger, F. J.: Experimental Feasibility Study of a Water-Filled Capillary-Pumped Heat-Transfer Loops. NASA TM X-1310, Lewis Research Center, Nov. 1966.

D4. Anon.: Technology Feasibility Spacecraft Technology Report. R-68-2 (Vol III), Martin Marietta Corporation, Denver, Colorado, Feb. 1968.

D5. Anon.: Planetary Vehicle Thermal Insulation Study. General Electric Missile and Space Division, Mar. 1968.

D6. Anon.: Voyager Capsule Preliminary Design (Phase B) Final Report. FR-22-103 (Contract 952001), Martin Marietta Corporation, Denver, Colorado, Aug. 1967.

D7. Harry, D. P.; and Friedlander, A. L.: Exploratory Statistical Analysis of Planet Approach Phase Guidance Schemes Using Range, Range Rate, and Angular Rate Measurements. NASA TN D-268.

D8. Battin, R.: Astronautical Guidance. McGraw-Hill Book Co., New York, 1964.

D9. Hartwell, Danby, Jones: Planetary Approach Navigation. Journal of the Institute of Navigation, vol. 11, No. 2, 1964.

D10. Danby: Matrizant of Keplerian Motion. AIAA J., vol. 3, No. 4, Apr. 1965, p. 769.

D11. Ingoldby, R. N.; and Seibel, R. P.: Thermal Descent Control System Analysis. PR-22-10-94-21, Martin Marietta Corporation, Denver, Colorado, Jan. 22, 1968.

APPENDIX D

D12. Anon.: JPL Space Programs Summary No. 37-37, vol. IV, Feb. 28, 1966.

D13. Anon.: JPL Space Programs Summary No. 37-41, vol. IV, Oct. 31, 1966.

D14. Anon.: JPL Request for Proposal, Sterilizable Magnetic Tape Recorder Development. BY-4-5363, July 1967.

D15. Anon.: JPL Specification No. ES503656.

D16. Mendez, W. H.: Study and Analysis of Sterilizable Tape Re-Corders, Report no. 100032-A(VCB-153), RCA, Aug. 1967.

D17. Anon.: Technology Survey, Magnetic Tape Recording. NASA SP-5038, Jan. 1966.

D18. Anon.: Sterilizable Magnetic Tape Recorder Development. Report no. 532712, Leach Corporation, Sep. 1967.

D19. Wolfert, L.: Selection of Instruments for Measurement of Atmospheric Structure of the Martian Atmosphere. ED-22-6-102, Martin Marietta Corporation, Denver, Colorado, June 1967.

D20. Magee, R.: Selection of Instruments for Atmospheric Measurements. ED-22-6-106, Martin Marietta Corporation, Denver, Colorado, Sep. 1967.

D21. Michaux, C. M.: Handbook of the Physical Properties of the Planet Mars, NASA SP-3030, 1967.

D22. Schorn, R.; Spinrad, H.; Moore, R.; Smith, H.; Giver, L.: High-Dispersion Spectroscopic Observations of Mars II. The Water-Vapor Variations. Astrophys. J., vol. 147, no. 2, Feb. 1967, p. 743-752.

D23. Wexler, A.; and Ruskin, R., ed.: Humidity and Moisture, vol. 1, Reinhold, 1965.

D24. Chleck, D.: Aluminum Oxide Hygrometer: Laboratory Performance and Flight Results. J. Appl. Meteorology, vol. 5, no. 6, Dec. 1966, p. 878-886.

D25. Del Pico, J.: Performance of Thin Film Humidity Sensors. AFCRL-67-0543, Dept. of Meteorology, Massachusetts Institute of Technology (Contract F19628-67-0228) 15 Oct. 1967.

APPENDIX D

D26. Locke, J. R.: Electronics for a Martian Water Vapor Detection System. NASA TR32-1114, Jet Propulsion Laboratory, Aug. 15, 1967.

D27. Kaimal, J. C.; and Businger, J. A.: A Continuous Wave Sonic Anemometer-Thermometer. J. Appl. Meteorology, vol.2, Feb. 1963, pp. 156-164.

D28. Kaimal, J. C.: An Analysis of Sonic Anemometer Measurements from the Cedar Hill Tower. AFCRL-66-542, Air Force Cambridge Research Laboratories, Aug. 1966.

D29. Haugen, P. A.; and Kaimal, J. C.: Momentum Flux Studies over a Horizontally Homogeneous Site. American Meteorological Society Meeting on Physical Processes in the Lower Atmosphere, Mar. 20-22, 1967.

D30. Anon.: Hot Wire Probe Calibration Equations for Air Velocity, Direction, and Temperature. Bull. 11D, Flow Corporation, Dec. 1964.

D31. Anon.: Hot Film and Hot Wire Anemometry, Theory and Application, Bull. TB5, Thermo-Systems, Inc.

D32. Norwood, M. H.; Caniffe, A. E.; and Olszewski, V. E.: Drag Force Solid State Anemometer and Vane. J. Appl. Meteorology, vol. 5, Dec. 1966, pp. 887-892.

D33. Peirce, R. M.; and Bisberg, A.: Applications of Pulse Techniques to Sonic Anemometry. To be published by the ISA.

D34. Anon.: The Sonic Anemometer--A New Instrument for Wind Measurements. Cambridge Systems, Inc., Aug. 1967.

D35. Leighton, R. B.; Murray, B. C.; et al.: Mariner Mars 1964 Project Report: Television Experiment, Part I. Investigators Report. NASA JPL TR 32-884, Dec. 1967.

D36. Scott, R. F.; and Roberson, F. I.: Soil Mechanics Surface Sampler: Lunar Surface Tests, Results and Analyses. (Chapter IV of Surveyor III Mission Report, Part II. Scientific Results), NASA JPL TR 32-1177, June 1967.

APPENDIX D

D37. MacNaughton, J. D.: Unfurlable Metal Structures for Spacecraft. Canadian Aeron. and Space J., no. 4, Apr. 1963, pp. 103-116.

D38. Anon.: Drum Rolled Space Tubes. Experimental Mech., Oct. 1966, p. 64.